CENTRAL RESEARCH LIBRARY

ORNL-5106

Cy 1

Mechanical Properties Test Data for Structural Materials Quarterly Progress Report for Period Ending July 31, 1975

[redacted]

OAK RIDGE NATIONAL LABORATORY
CENTRAL RESEARCH LIBRARY
DOCUMENT COLLECTION
LIBRARY LOAN COPY
DO NOT TRANSFER TO ANOTHER PERSON
If you wish someone else to see this document, send in name with document and the library will arrange a loan.
UCN-7969
(3 3-67)

OAK RIDGE NATIONAL LABORATORY
OPERATED BY UNION CARBIDE CORPORATION • FOR THE U.S. ATOMIC ENERGY COMMISSION

Printed in the United States of America. Available from
National Technical Information Service
U.S. Department of Commerce
5285 Port Royal Road, Springfield, Virginia 22161
Price: Printed Copy $10.60; Microfiche $2.25

This report was prepared as an account of work sponsored by the United States Government. Neither the United States nor the Energy Research and Development Administration, nor any of their employees, nor any of their contractors, subcontractors, or their employees, makes any warranty, express or implied, or assumes any legal liability or responsibility for the accuracy, completeness or usefulness of any information, apparatus, product or process disclosed, or represents that its use would not infringe privately owned rights.

ORNL-5106
UC-79b, -h, -k
(Liquid Metal Fast
Breeder Reactors)

Contract No. W-7405-eng-26

METALS AND CERAMICS DIVISION

MECHANICAL PROPERTIES TEST DATA FOR STRUCTURAL MATERIALS QUARTERLY PROGRESS REPORT FOR PERIOD ENDING JULY 31, 1975

Aerojet Nuclear Company
Argonne National Laboratory
Oak Ridge National Laboratory
Naval Research Laboratory
Hanford Engineering Development Laboratory
Westinghouse Advanced Reactors Division
University of Cincinnati
University of California at Los Angeles
General Electric Company

Compiled by M. R. Hill

SEPTEMBER 1975

OAK RIDGE NATIONAL LABORATORY
Oak Ridge, Tennessee 37830
operated by
UNION CARBIDE CORPORATION
for the
U.S. ENERGY RESEARCH AND DEVELOPMENT ADMINISTRATION

FOREWORD

This is the eighth in a series of progress reports, the purpose of which is to record and distribute quarterly the collected results of all structural materials mechanical properties test programs sponsored by the Reactor Research and Development Division of the USERDA.

To be useful as resource documents, the reports in this series must be published and distributed in a timely manner to those in the reactor design and materials technology community who have a need of mechanical property test data for nuclear reactor and power plant applications. A test and material index is included to increase the effectiveness of the report.

Reports previously issued in this series are as follows: ORNL-4936, period ending October 31, 1973; ORNL-4948, period ending January 31, 1974; ORNL-4963, period ending April 30, 1974; ORNL-4998, period ending July 31, 1974; ORNL-5103, period ending October 31, 1974; ORNL-5104, period ending January 31, 1975; and ORNL-5105 for period ending April 30, 1975. The next quarterly report will be for the period ending October 31, 1975, and contributions are due at ORNL by November 15, 1975.

W. R. Martin
Metals and Ceramics Division
Oak Ridge National Laboratory

CONTENTS

SUMMARY ix

1. AEROJET NUCLEAR COMPANY 1

1.1 INTRODUCTION 1

1.2 FATIGUE TESTS ON CLADDING AND STRUCTURAL MATERIALS . . 2

1.2.1 Fatigue Properties of CRE Type 308 Stainless Steel Weld Metal Aged at 482°C. 2

1.3 ALLOY 718 MECHANICAL PROPERTY PROGRAM 2

1.3.1 Confirmation of INEL Heat Treatment 2

1.3.2 Influence of Cooling Procedures Upon Weld Properties 5

1.3.3 Scoping Mechanical Tests for INEL Heat Treatment 7

1.3.3.1 Tensile Properties of Base and Weld Metal 7

1.3.3.2 Impact Resistance of Base and Weld Metal 10

1.3.3.3 Fatigue Properties of Base and Weld Metal 12

1.3.3.4 Stress Rupture Life of Base Metal . . 14

1.3.3.5 Stability Check of Base Metal Stressed at 650°C. 15

1.4 REFERENCES 17

2. ARGONNE NATIONAL LABORATORY 19

2.1 INTRODUCTION 19

2.2 FRACTURE AND FATIGUE STUDIES ON STAINLESS STEEL . . . 19

2.2.1 Statistical Analysis of Low-Cycle Fatigue Data Scatter 19

2.3 SODIUM EFFECTS OF LMFBR MATERIALS 24

2.3.1 Influence of Sodium Environment on Tensile Behavior of Austenitic Stainless Steels 24

2.3.2 Influence of Sodium Environment on the Low-Cycle Fatigue Behavior of Austenitic Stainless Steels 36

2.4 REFERENCES 40

3. OAK RIDGE NATIONAL LABORATORY 41

3.1 INTRODUCTION 41

3.2 MECHANICAL PROPERTIES AND BEHAVIOR FOR STRUCTURAL MATERIALS 41

3.2.1 Mechanical Property Characterization of Type 304 Stainless Steel Reference Heat 41

3.2.1.1 Creep and Rupture Properties of the 2-in. (51-mm) Plate of Reference Heat . 41

3.2.2 Mechanical Property Characterization of Type 316 Stainless Steel Reference Heat 50

3.2.2.1 Heat Treatment 51

3.2.2.2 Tensile Data 62

3.2.2.3 Creep Properties 64

3.2.3 Heat-to-Heat Variation of Mechanical Properties of Types 304 and 316 Stainless Steel 64

3.2.3.1 Relation Between Tensile and Creep Properties in the As-Received (Mill-Annealed) and Reannealed (Laboratory-Annealed) Conditions for Types 304 and 316 Stainless Steel 64

3.2.3.2 Effect of Thermal Aging on Tensile Creep Properties of Types 304 and 316 Stainless Steels 72

3.2.4 Materials Behavior in Support of Development and Evaluation of Failure Criteria for Materials. 87

3.2.4.1 Methods for Analysis of Creep and Creep-Rupture Data 87

3.2.4.2 Complex Loading Behavior of LMFBR Structural and Component Materials . . . 96

3.2.5 Material Data Processing 100

3.2.6 Elastic Properties of Engineering Construction Materials 100

3.2.6.1 Elastic Properties Determined by Dynamic Tests 104

3.3 MECHANICAL AND METALLURGICAL BEHAVIOR OF WELDMENTS FOR LMFBR 112

3.3.1 Studies of Strain Distribution in Weldments and Room-Temperature Elastic Constants 112

3.3.1.1 Elastic Compliances 112

3.3.1.2 Interpretation of Results 114

3.3.2 Task Force on Alternate Structural Materials for Liquid Metal Fast Breeder Reactors 114

3.3.2.1 Summary of Phase I Findings 116

3.3.2.2 Summary of Phase II Findings 119

3.4 MECHANICAL PROPERTIES OF STEAM GENERATOR AND HEAT EXCHANGER MATERIALS 121

3.4.1 High-Strain-Rate Tensile Properties of 2 1/4 Cr-1 Mo Steel 121

3.4.2 Heat-to-Heat Variations of 2 1/4 Cr-1 Mo Steel. . 131

3.4.2.1 Tensile Properties 134

3.4.2.2 Discussion 142

3.4.3 Fatigue Behavior of 2 1/4 Cr-1 Mo Steel 144

3.4.3.1 Creep-Fatigue Data Analysis 144

3.4.3.2 Subcritical Crack Growth of 2 1/4 Cr-1 Mo Steel. 147

3.4.4 Mechanical Property Correlations of 2 1/4 Cr-1 Mo Steel for LMFBR Steam Generators 155

3.4.4.1 Rupture Life 155

3.4.4.2 Comparison of Lower Stress Limits with Code Case 1592 161

3.4.4.3 Time to Start of Tertiary Creep 162

3.4.5 Mechanical Properties of a Weld-Overlaid Stainless Steel Forging 165

3.5 HIGH-TEMPERATURE DESIGN 171

3.5.1 Exploratory Studies in Support of Structural Design Methods. 171

3.5.1.1 Characterization of the Product Forms of the Reference Heat of Type 304 Stainless Steel 171

3.5.1.2 Exploratory Testing to Identify Behavioral Features 174

3.5.1.3 Exploratory Testing of 2 1/4 Cr-1 Mo Steel. 179

3.5.2 Investigations of Creep Failure under Uniaxial and Multiaxial Conditions (No report) 185

3.6 MECHANICAL PROPERTIES OF HTGR STEAM GENERATOR AND PRIMARY CIRCUIT MATERIALS 185

3.6.1 Tensile Testing 185

3.6.2 Environmental Creep Testing 187

3.6.3 Subcritical Crack Growth Studies 188

3.6.4 Fatigue Life Testing 189

3.7 REFERENCES 189

4. NAVAL RESEARCH LABORATORY 197

4.1 INTRODUCTION 197

4.2 ELASTIC PLASTIC TOUGHNESS OF TYPE 316 STAINLESS STEEL FORGING 197

4.2.1 Introduction 197

4.2.2 Experimental Procedure 198

4.2.3 Fracture Morphology 199

4.2.4 J-Integral Determinations 204

4.3 INFLUENCE OF DELTA FERRITE CONTENT ON NOTCH TOUGHNESS OF AUSTENITIC STAINLESS STEEL WELDMENTS 207

4.3.1 Background 207

4.3.2 Materials 209

4.3.3 Experimental Results 213

4.4 THE EFFECT OF AGING ON HOLD-TIME EFFECTS IN SOLUTION ANNEALED TYPE 316 STAINLESS STEEL 216

4.4.1 Background 216

4.4.2 Materials and Test Procedures 216

4.4.3 Results and Discussion 217

4.5 REFERENCES 220

5. HANFORD ENGINEERING DEVELOPMENT LABORATORY (No report) . . . 223

6. WESTINGHOUSE ADVANCED REACTORS DIVISION 225

6.1 INTRODUCTION 225

6.2 BASIC SPECIMEN TESTING 225

6.2.1 Uniaxially Loaded Specimens with Uniform Gage Sections (Types A, B, and G) 233

6.2.2 Plate Specimens Under Tension and Bending (Type E). 238

6.2.3 Specimens with Welds 238

6.2.3.1 Transverse Welds in Specimens B and G. . 238

6.2.3.2 Axial Welds in Specimens B and G 238

6.2.3.3 Transverse Weld Specimens with Notches in the Weld 240

6.2.3.4 Transverse Welds with Notches at the HAZ 240

6.3 TUBULAR SPECIMEN TESTING 240

6.3.1 Test Piece Description 240

6.3.2 Test Matrix 241

6.3.3 Test Equipment and Measurement 241
6.3.4 Data Reduction 248
6.4 REFERENCES 255
7. UNIVERSITIES 257
7.1 UNIVERSITY OF CINCINNATI 257
7.1.1 Introduction 257
7.1.2 Experimental Program 257
7.1.2.1 Characterization of the Creep and Tensile Substructure of 304 Stainless Steel, Reference Heat 9T2796 259
7.1.2.2 Characterization of the Dislocation Substructure in Creep Mode of AISI 304 Stainless Steel, UC Heat G8607 . . . 268
7.1.2.3 Analysis of Relationships of Deformation Rate, Stress and Temperature for 304 Stainless Steel 272
7.1.2.4 Change in Stress Experiments on 304 Stainless Steel, Reference Heat 9T2796 . 272
7.1.2.5 Substructure Development During Low Cycle Fatigue of AISI 304 Stainless Steel at 649°C 272
7.1.3 References 285
7.2 UNIVERSITY OF CALIFORNIA, LOS ANGELES 287
7.2.1 Microstructure and High Temperature Deformation of Cr-Mo Steels for LMFBR Heat Exchanger. 287
7.2.2 Creep Studies in Stainless Steels 291
7.2.2.1 Rupture Life, t_R 293
7.2.2.2 Steady State Creep Rate, $\dot{\varepsilon}_s$. 293
7.2.2.3 Primary Creep 293
7.2.3 The Effect of Carbon on the Elevated Temperature Tensile Properties and Fracture Behavior of Type 304L Stainless Steel 298
7.2.3.1 Mechanical Properties vs. Volume Fracture of Case 299
7.2.3.2 Fracture Model 302
7.2.3.3 Fracture Mode 302
7.2.4 References 305
8. GENERAL ELECTRIC COMPANY 307
8.1 INTRODUCTION 307

8.2 MECHANICAL PROPERTIES OF STAINLESS STEEL IN CARBURIZING SODIUM 307

8.2.1 Background 307

8.2.2 Current Progress 308

8.3 DECARBURIZATION KINETICS AND DESIGN METHODS VERIFICATION TESTING 316

8.3.1 Background 316

8.3.2 Current Progress 321

8.4 REFERENCES 322

INDEX 325

SUMMARY

1. AEROJET NUCLEAR COMPANY

Fatigue tests of Type 308 CRE stainless steel weld metal aged and tested at 482°C are reported. No significant difference was noted in the fatigue life of the aged material, but stress levels were slightly lower when compared with unaged weld metal.

Test programs have been conducted to verify that the proposed INEL Heat Treatment will produce ductile Alloy 718 weldments. Tensile, Charpy impact, fatigue, stress rupture and stability scoping tests of base metal have been performed as well as tests checking the tensile, Charpy impact, and fatigue properties of weld metal heat treated according to the INEL procedure. Results of these studies are herein reported.

2. ARGONNE NATIONAL LABORATORY

Two series of ten identical elevated-temperature (593°C) low-cycle fatigue tests on Type 304 stainless steel have been completed, and a statistical analysis of the results is reported. The scatter in both data sets displayed no obvious correlation with minor fluctuations in experimental parameters, and both populations could be described reasonably well by Weibull distribution functions. The 1-min tension-hole-time data at 1% were distributed fairly symmetrically about the sample mean, and the corresponding distribution function had 95% confidence limits of 930 and 2370 cycles. The zero-hold-time 0.5% data were distributed quite unsymmetrically about the sample mean, and the 95% confidence limits for the distribution function were 27,420 and 114,500 cycles.

True stress-true strain tensile data have been obtained for AISI Types 304 and 316 stainless steel in the annealed condition and after exposure to a flowing sodium environment at temperatures of 700, 650, 600, and 550°C. The specimens were exposed to sodium for periods between 120 and 5012 hr to produce carbon penetration depths of ∿0.01, 0.020, and 0.038 cm in the steels. These data showed that, as the depth of carbon penetration and the average carbon concentration in the material increase, the yield strength and ultimate tensile strength increase and the elongation decreases at 550 and 600°C. This effect is less pronounced at 650 and 700°C. The results also showed that neither carbon penetration depth nor the average carbon concentration in the steel had a significant influence on the strength coefficient (K) or strain-hardening exponent (n).

Low-cycle fatigue data have been obtained on annealed Type 316 stainless steel specimens after exposure to sodium (1512 hr at 600°C) that resulted in surface carburization of the material to a depth of 0.01 cm. The results indicate that the applied stress range for the sodium-exposed specimens decreased by 15—20% relative to the annealed specimens tested in sodium at 600°C. For total strain ranges below ∿1%, the fatigue life

was enhanced by the 1500-hr sodium exposure. Metallographic examination of the specimens after testing revealed a lower density of surface cracks in the sodium-exposed material relative to the "as-received" specimens. This suggests that carburization of Type 316 stainless steel in sodium to moderate levels (<0.5 wt% at the surface) tends to inhibit crack initiation.

3. OAK RIDGE NATIONAL LABORATORY

Elevated-temperature creep testing of the ORNL reference heat of type 304 stainless steel is continuing, and data have been updated. The creep rupture data bank has been updated, and comparisons have been made with the ASME Code Case minimums. Several ductility measures have been plotted as a function of time to rupture. Stress was plotted against rupture elongation and reduction of area. Plots of stress against creep strain showed a break at a critical stress, which was shown to be related to the transition from an intragranular process to one controlled by grain boundary sliding.

Heat treatment procedures and conditions have been determined for the reference heat of type 316 stainless steel. Elevated-temperature tensile and creep testing of this heat has begun, and tensile results for the reannealed condition are presented.

Tensile and creep properties of various products of types 304 and 316 stainless steel, in reannealed (laboratory-annealed) and as-received (mill-annealed) conditions, have been related by linear relationships. As-received plate and pipe of these steels contain approximately 3 to 4% residual cold-work strain, as opposed to 10% contained in the bar product. Residual cold work decreased minimum creep rate and increased time to rupture for low-stress or long-term tests.

Highlights of effect of thermal aging on tensile and creep properties of types 304 and 316 stainless steel are presented. The changes observed in yield strength resulted from both inter- and intragranular precipitates. The creep properties were shown to be affected most by matrix or matrix and grain boundary precipitates as opposed to only grain boundary precipitates.

A parametric method for the prediction of creep ductility has been applied to data for types 304 and 316 stainless steel, 2 1/4 Cr-1 Mo steel, and Inconel Alloy 718. The method predicts reasonable results, although the data exhibit a large amount of scatter. Design lower limits on ductility have been calculated, however.

Complex loading material behavior studies will be conducted on three LMFBR-related materials. Tests under other than constant uniaxial tensile loading are described. Testing facility requirements are being met, and our complex loading testing machine is described.

Data input to the Mechanical Properties Data Storage and Retrieval System continued, with the results from over 6000 tests now on file. In addition, computer programs to aid in the processing of raw data have been expanded and improved.

Dynamic elastic constants (E, G, and ν) were reestablished for 2 1/4 Cr-1 Mo steel, heat 20017 (0.135% C, isothermally annealed) from room temperature to 649°C (1200°F). Cubic polynomials are presented for the individual constants, and estimates of the properties at 28°C (50°F) increments are tabulated.

The present elastic property data do not differ substantially from our earlier data, which had been determined on a swaged specimen with a pronounced crystallographic texture. The underlying reason for this is being investigated.

Static Young's moduli were determined for the same 2 1/4 Cr-1 Mo steel from room temperature to 732°C (1350°F) by use of LVDTs as strain sensors. The resulting time-dependent static modulus curve fell intermediate to our dynamic curve and the ASME Code Case 1592 (static) values. Whereas our static values did not differ from the code values very appreciably at low temperatures, the difference began to become significant above about 482°C (900°F).

Strain gage rosette data from a room-temperature tensile test performed on a whole-weld cross section of an FFTF vessel test weld have been analyzed. While the entire elastic compliance matrix cannot be determined from such tests, the elements that were estimated indicate significant differences between base metal and weld metal behavior. The consequences of this behavior are that mechanical tests on specimens containing welds, where either the weld or the specimen is not of simple geometry, are difficult to interpret.

Preliminary reports summarizing the findings of the Task Force on Alternate Structural Materials for Liquid Metal Fast Breeder Reactors have been completed. The use of types 304 and 316 stainless steel is found to reflect sound engineering judgment at this time, but some difficulties with these alloys make desirable the selection of alternate candidate alloys to be explored and developed for future reactor systems. Materials recommended for further consideration included 8–14% Cr, 1–2% Mo stabilized transformable steels, austenitic steels in the 15 Cr-15 Ni range, partially stabilized austenitic steels, and the nickel-bearing alloys 600, 800, and 800H.

High-strain-rate tensile tests were conducted on normalized-and-tempered 2 1/4 Cr-1 Mo steel over the range 25 to 566°C. With the completion of these tests, we can now describe the tensile behavior over this temperature range and the strain rate range of 2.67×10^{-6} to 144/sec. Three-dimensional plots of yield stress, ultimate tensile strength, total elongation, and reduction of area are given.

The effect of heat treatment on the tensile properties of annealed 2 1/4 Cr-1 Mo steel has been investigated. Cooling rate significantly affected the dynamic strain aging effects in the range 300–450°C. These differences are attributed to differences in the proeutectoid ferrite, and not in the amounts of bainite in the microstructures.

Calculations of creep-fatigue damage for 2 1/4 Cr-1 Mo steel by the linear summation of damage approach have been made, including values obtained using design safety factors. These results are being compared with current design rules.

Subcritical crack-growth test types and material tested are described. Limiting test conditions, which are valid for analysis under LEFM (Linear Elastic Fracture Mechanics), are described, along with several approaches for their determination. Mean stress studies at 510°C (950°F) and room temperature are reported and discussed. Environmental effects of steam at 510°C (950°F) are discussed.

Mathematical descriptions of rupture life and times to start of tertiary creep are given for annealed 2 1/4 Cr-1 Mo steel. The lower limit of rupture life is defined and minimum stress values are compared with corresponding stresses from Code Case 1592.

Experimental studies on the creep-rupture properties of the type 304 stainless steel forging overlaid with type 308 stainless steel weld metal have been completed. Examination of the fractured specimens by metallography indicates that grain boundary cracks form for all tests. With two exceptions, failures of the composite specimens that contained both forging and weld metal in the specimen gage section occurred in the weld metal. In two specimens, failure was initiated at the fusion line at defects introduced during the forging process.

Tensile characterization tests on the different product forms of the reference heat of type 304 stainless steel have been completed, and curves at 593°C are presented in graphical and analytical forms. Efforts to describe the primary creep behavior of the 25-mm (1-in.) plate of the reference heat of type 304 stainless steel are described; two transient components are required to represent the behavior. In relaxation tests on 2 1/4 Cr-1 Mo, for multiple loadings the relaxation rate for short times was increased.

Tensile properties of Hastelloy S are reported from room temperature to 871°C (1600°F). Progress is reported on creep tests of Hastelloy X, 2 1/4 Cr-1 Mo, and 9 Cr-1 Mo in simulated HTGR coolant.

Subcritical crack growth tests on 2 1/4 Cr-1 Mo in air and steam at 510°C (950°F) are discussed. Equipment for similar tests in simulated HTGR coolant are discussed along with preliminary results.

An environmental chamber was designed for strain-controlled fatigue tests, and Hastelloy X specimens are being prepared.

4. NAVAL RESEARCH LABORATORY

The toughness of Type 316 stainless steel forging was evaluated using the J-Integral approach. Notched, three-point bend specimens were statically loaded at 500°F (260°C) to different fractions of the maximum load in order to define R curves for three different thicknesses. To assess the J_{Ic} value at crack initiation, different techniques were explored to separate the region of stable (rising load) crack extension from the stretch zone at the tip of the fatigue precrack. A size effect in J_{Ic} was noted between 1 in. (25 mm) thick specimens and those of smaller thicknesses (0.2 and 0.4 in., 5 and 10 mm). This size effect is expected for the extremely high toughness of the forging (3200 in.lb/in.^{2}) and it appears that small specimens can be used only at lower levels of toughness such as can be exhibited by irradiated material.

A series of four AISI Type 308 austenitic stainless steel weld deposits was fabricated to explore the contribution of delta ferrite content to apparent notch toughness. The 2 1/2 in. thick welds were made by the shielded metal arc method and exhibited delta ferrite contents ranging from 2.9 to 13.7%. Charpy-V and dynamic tear test determinations for the unirradiated condition are reported. Within the range investigated variations in delta ferrite content did not appear to be a major factor in observed toughness trends for 75°F (24°C) to 1100°F (593°C).

The effect of hold time was examined at 1100°F (593°C) for solution annealed Type 316 stainless steel thermally aged at 1100°F (593°C) for 5000 hr and in the unaged condition. For the unaged material, fatigue crack growth rates were increased by periods of static loading of 0.1 and 1.0 min during cycling. It was found that thermal aging eliminated the small hold-time effects observed in the unaged material. In addition, thermal aging decreased crack growth rates in the annealed steel for all hold times. Evaluations using single-edge-notched and 1/2 T compact tension specimens were performed on annealed Type 316 stainless steel at 1100°F (593°C). The preliminary data comparisons of the two specimen types appear to be in reasonable agreement, and it is expected that 1/2 T compact tension specimens will be satisfactory for pre- and postirradiation comparisons of Type 316 stainless steel at 1100°F (593°C).

5. HANFORD ENGINEERING DEVELOPMENT LABORATORY

(No Report)

6. WESTINGHOUSE ADVANCED REACTORS DIVISION

Creep testing of bar, plate, and tube specimens was continued using material from the ORNL Type 304 stainless steel reference heat (9T2796).

A plate test under combined tension and bending has accumulated 10.8 percent permanent strain with the creep rate continuing to decrease. Test results for welded plates and bars have been compared to unwelded specimens. The rupture strength of the transverse weld plate specimens is slightly less than that for base metal under plane stress. Similar specimens with axial welds indicate that the rupture life at comparable stress is about three times that of the base metal and about 60 percent that of all-weld-metal specimens under plane stress. Results for notched bar specimens with transverse welds indicate notch insensitivity in the weld metal and notch weakening in the heat affected zone.

Data reduction on results obtained from the tubular specimen creep tests continued. Master equations were derived for these tests. For the multiaxial creep testing, a master equation was derived for a given stress ratio for the effective stress range in the present study. For uniaxial creep tests, the master equation described the experimental results very well; while in the case of multiaxial creep tests, the agreement is less satisfactory, particularly for the transient creep stage. Factors which may contribute to this discrepancy have been outlined.

7. UNIVERSITIES

UNIVERSITY OF CINCINNATI

Work on the preliminary evaluation of the dislocation substructure of the creep and tensile tested specimens from the reference heat 9T2796 of AISI 304 stainless steel is nearly completed. These specimens were tested at temperatures ranging from 538 to 816°C and strain rates from 9.7×10^{-9} sec^{-1} to 8.3×10^{-2} sec^{-1}. TEM observations suggest that well developed subgrains are formed at higher temperatures and lower stress levels. At high stresses and low temperatures, the substructure consisted of cells. At 593°C, the presence of carbides influences the formation of cells or subgrains. The analysis of the creep and tensile test results of these specimens and its correlation with the corresponding substructure is now being documented.

TEM evaluations of the substructure were performed on a set of specimens of 304 stainless steel tested in creep to study the development of the substructure as a function of creep strain. Well developed subgrains were observed for specimens tested till rupture and the subgrain size — stress relationship determined for the reference heat adequately describes the results from this heat.

A family of creep tests has been performed on 304 stainless steel reference heat (9T2796) in which the stresses were changed during steady state creep to obtain the strain time behavior after the stress changes. In this manner the influence of the microstructure developed with the initial stress on the subsequent creep behavior may be determined. Work is continuing on the evaluation of the dislocation substructure of these specimens.

In the study of high temperature fatigue substructure development in AISI 304 stainless steel under a total strain range of 2% at 649°C it was found that the saturation state is reached within the initial 4% of the fatigue life and that cells form in the initial 0.4% of the fatigue life. The cell intercept size decreases until the saturation is reached and the misorientation angle increases throughout the fatigue life. Based on TEM observations, subboundary movement was suggested to account for the accumulated cyclic strain.

Work on the substructural evaluation in Incoloy 800 tested in fatigue mode at elevated temperature is being continued.

UNIVERSITY OF CALIFORNIA, LOS ANGELES

The creep study of 2 1/4 Cr-1 Mo was extended to a low-carbon heat. Short-term creep of type 316 stainless steel was studied at 649 to 760°C (1200–1400°F) as affected by prior cold work and aging at the test temperature. The effect of a carbon case on tensile properties was compared for types 304L and 316 stainless steel.

8. GENERAL ELECTRIC COMPANY

Programs for defining the effects of high temperature sodium environments on the mechanical properties of 2 1/4 Cr-1 Mo steel and stainless steels were initiated. The effect of a carburizing sodium environment on creep rupture, creep rate, and creep-fatigue properties of Type 316 stainless steel is being determined. The test facilities for automatic load interruptions and data accumulation have been completed. In addition, the effect of carburizing sodium on the fatigue crack propagation rate will be determined using a fracture mechanics approach. Pre-exposed specimens will be subjected to continuous carburization during testing. A matrix of tests to be conducted in this program is presented; currently, the fabrication of the experimental apparatus is nearing completion, and specimens are being pre-exposed in Loop A.

The effect of decarburization on creep and creep-fatigue properties of 2 1/4 Cr-1 Mo base metal and weld metal is being studied. Uniaxial testing of sodium and gas filled pipe samples is under way. The test facility for the determination of creep-fatigue interaction effects under decarburizing sodium is virtually complete. Effects of cycling on the rupture life of 2 1/4 Cr-1 Mo tubing and weld metal will be determined in this rig.

1. AEROJET NUCLEAR COMPANY

D. D. KEISER

1.1 INTRODUCTION

Aerojet Nuclear Company is conducting mechanical properties investigations under two programs sponsored by ERDA Division of Reactor Research and Development. Program 06031, Fatigue Tests on Cladding and Structural Materials, involves experimental fatigue tests on stainless steel Types 304 and 316 as well as Type 304/308 weldments. These tests are intended to determine the influence of irradiation, cold work, heat treatment, heat-to-heat property variations, and temperature on fatigue behavior. Irradiated, thermal control, as-received, and annealed specimens are being tested at 427 to 700C (800 to 1292F). Current work on irradiated material is reported in the Semi-Annual Progress Report for the Irradiation Effects on Reactor Structural Materials Program compiled at HEDL. Unirradiated work reported in this document involves fatigue tests performed on Type 308 weld metal aged 5923 hours at 482C (900F). This program terminated June 30, 1975, and therefore, no further progress will be reported in this document.

Program 06084, Alloy 718 Mechanical Property Program, has as its primary objective the acquisition of the necessary mechanical property data to permit safe, efficient use of this material in LMFBR service. The specific immediate application is for selected structural components of the Clinch River Breeder Reactor Project. Other reactor service applications which require high levels of mechanical properties at temperatures up to 649C (1200F) are also expected to make use of this material.

What have been considered standard heat treatments for Inconel 718 have not consistently yielded acceptable ductility values for the welded material. Current work involves scoping tests on material subjected to modified thermal treatments in an effort to optimize the heat treatment that will yield the best mechanical properties of both base and weld metal. A modified heat treatment (designated the INEL Heat Treatment) has been chosen and data generation of base and weld metal given this treatment has begun. The first strain fatigue tests of weld metal

are reported.

1.2 FATIGUE TESTS ON CLADDING AND STRUCTURAL MATERIALS - G. E. Korth and M. D. Harper

1.2.1 Fatigue Properties of CRE Type 308 Stainless Steel Weld Metal Aged at 482C

Test specimens of Type 308 stainless steel weld metal with controlled residual elements (CRE) were aged in helium at 482C (900F) for 5923 hours to investigate effects of thermal aging on low cycle fatigue properties. ORNL did find some effects on tensile and creep properties of this same weld metal aged at 482C for up to 10,000 hours [1,2]. The fatigue test data is tabulated in Table 1.1 and plotted in Figure 1.1. The values obtained for both weld metal and base metal prior to aging are also shown in the plot for comparison. Test data show that the cyclic life of the aged material is well within the normal data scatter and no significant effect of aging on cycles to fail was evident. However, when comparing the stress data of unaged weld metal tested and reported previously[3], it was noted that with very few exceptions, the aged weld metal exhibited lower stress values for given strain ranges. This softening was also noted by ORNL[1] in their tensile testing.

1.3 ALLOY 718 MECHANICAL PROPERTY PROGRAM - G. E. Korth and G. R. Smolik

1.3.1 Confirmation of INEL Heat Treatment

The previous quarterly report has identified a modified (INEL) heat treatment for welded structures of Alloy 718. This heat treatment consists of a one hour 1095C (2000F) solution anneal, a furnace cool to 540C (1000F) at a rate of 83 $\pm$ 28C/hr (150 $\pm$ 50F/hr), and an age harden of 4 hours at 720C (1325F) plus 16 hours at 620C (1150F). The 1095C solution anneal was incorporated to obtain better ductility resulting from the dissolution of Laves phase in weld deposits as experienced in other investigations[4,5,6]. The furnace cool from the solution anneal was established as a result of ANC experience in fabricating Power Burst Facility components. The slow cool reduces thermal stresses and improves ductility around 760C (1400F) thereby assisting in the

Table 1.1 Strain Fatigue Behavior of Aged Type 308 Stainless Steel Weld Metal Tested[a] at 482oC.

Specimen No.	Condition[b]	$\Delta\varepsilon_t$, %	$\Delta\varepsilon_p$, %	$\Delta\sigma$ at 1st Cycle, MPa	$\Delta\sigma$ max, MPa	Cycle at $\Delta\sigma$ max	$\Delta\sigma$ of $N_f/2$, MPa	σ_t at $N_f/2$, MPa	$\Delta\sigma$ at 3/4 N_f, MPa	Cycles to Fail N_f	Time to Fail t_f, hr
WT-50	Weld 2x-T-S	2.00	1.52	648.1	728.1	5	648.1	324.0	635.0	388	1.05
WT-15	Weld 2x-T-C	2.00	1.44	706.0	783.9	4	689.5	348.9	681.9	361	0.96
WP-50	Weld 2x-P-S	2.00	1.50	577.1	657.8	4	598.5	302.0	589.5	413	1.10
WP-73	Weld 2x-P-C	2.00	1.48	655.0	725.3	5	626.0	307.5	617.1	623	1.67
WT-51	Weld 2x-T-S	1.00	0.58	551.6	652.2	9	529.5	258.5	516.4	2079	2.81
WT-14	Weld 2x-T-C	1.00	0.56	730.2	730.2	1	589.5	291.0	575.7	1317	1.84
WP-53	Weld 2x-P-S	1.00	0.60	491.6	521.9	11	431.6	212.4	424.7	3940	5.05
WP-74	Weld 2x-P-C	0.99	0.54	659.1	684.0	9	537.8	266.8	526.1	2577	3.60
WP-55	Weld 2x-P-S	0.52	0.17	487.5	497.8	17	406.8	180.6	398.5	24,790	16.74
WP-75	Weld 2x-P-C	0.50	0.15	536.4	539.9	15	444.7	150.3	444.0	101,648	69.02
WT-18	Weld 2x-T-C	0.52	0.16	619.2	644.7	27	496.4	198.6	482.6	12,431	8.36
WT-52	Weld 2x-T-S	0.52	0.17	613.6	622.6	2	488.2	217.9	478.5	9,794	6.56

[a]Triangular wave form with strain rate of $4 \times 10^{-3} s^{-1}$

[b]2 = Base metal heat 600414
x = As welded condition plus 5923 hour age at 482°C
T = Specimen taken transverse to weld seam
P = Specimen taken parallel to weld seam
S = Taken from section near surface of weldment
C = Taken from section near center of weldment

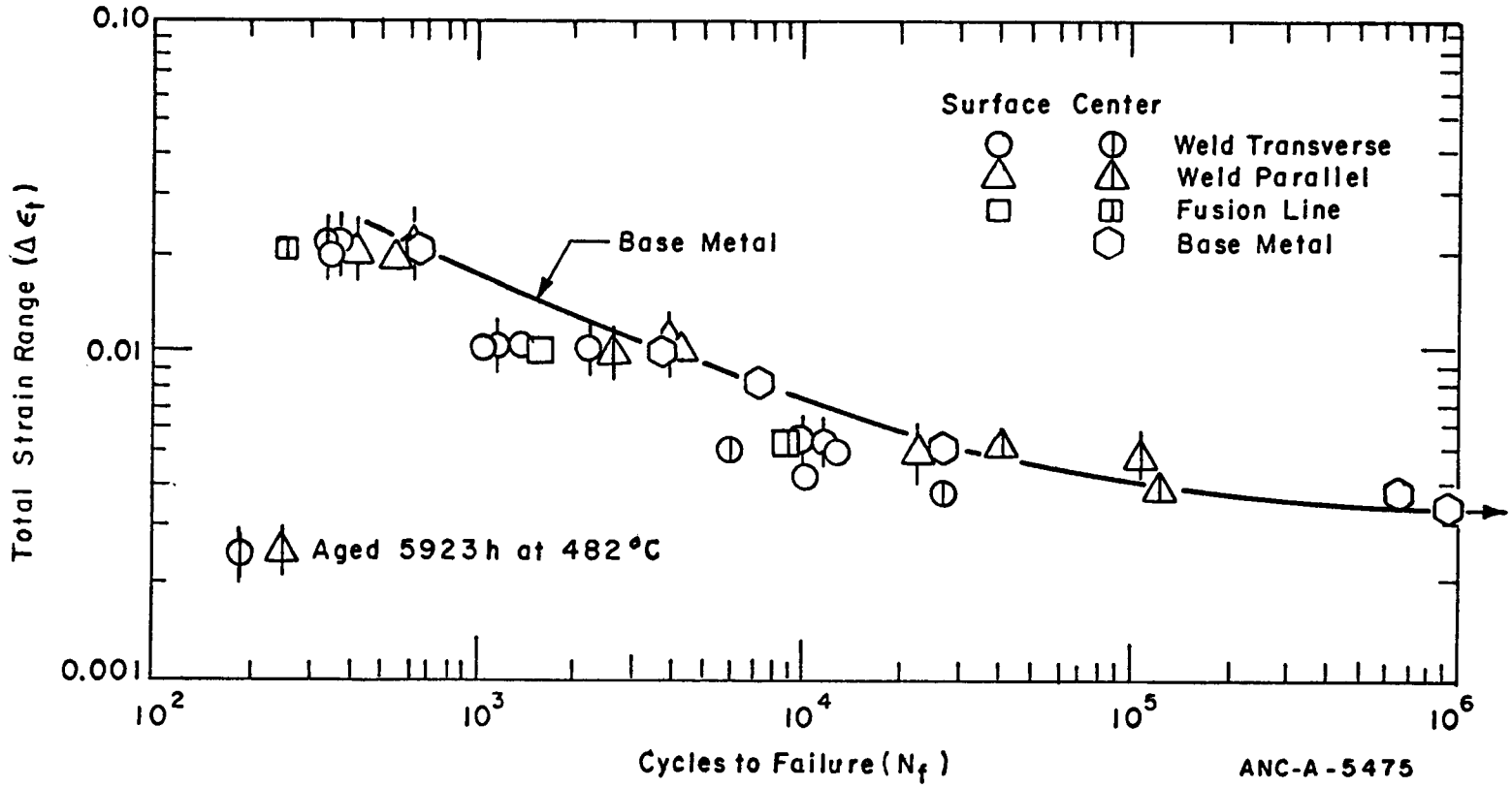

Figure 1.1 - Strain fatigue behavior of unirradiated Type 304/308 stainless steel weldment material tested at 482C (900F).

prevention of heat treat cracking.

Investigations have been performed to confirm the INEL heat treatment before proceeding with an expanded test program for LMFBR design data. An examination of the time-temperature-precipitation curves shows that a cooling curve at 56C/hr (100F/hr) passes through the nose of the Laves phase precipitation curve (see Figure 1.2). Investigations have therefore been performed to determine if any reduction of weld metal ductility results from Laves phase reprecipitation. In addition, scoping tests of mechanical properties resulting from the modified heat treatment have been conducted. These preliminary checks have included tensile, impact resistance, and side bend investigations at room temperature; fatigue tests at 540C (1000F); and tensile, stress rupture, and stability investigations at 650C (1200F).

1.3.2 Influence of Cooling Procedures Upon Weld Properties

A program investigating the possibility of Lave phase precipitation which would cause reduced weld ductility has been reported[7]. Various types of cooling procedures were applied to transverse tensile specimens consisting of weld metal-heat affected zone-base metal. Two step-type cooling curves using rates of 667C/hr (1200F/hr) and 222C/hr (400F/hr) were evaluated and compared with the INEL heat treatment employing a cooling rate of 56C/hr (100F/hr). Specimens prepared by the INEL heat treatment failed in the weld metal while specimens cooled by the two step-type processes fractured in base metal. The composite specimens made interpretation difficult.

A second investigation checking the influence of cooling procedures upon weld properties has been performed. This investigation was extended to include Charpy impact resistance and side bend behavior in addition to tensile properties. A uniform gage fatigue specimen configuration was used for the tensile tests. This specimen used a 1.02 cm (0.4 inch) reduced gage length which was located in the weld metal. The cooling procedures checked were a 56C/hr (100F/hr) representing the lowest limit (worst case) in the INEL process, a 167C/hr (300F/hr) cool, and a step-type cool of 167C/hr from 1095C (2000F) to 925C (1700F) and then a 56C/hr to 540C (1000F). The 167C/hr and the 167C/hr - 56C/hr step cooling

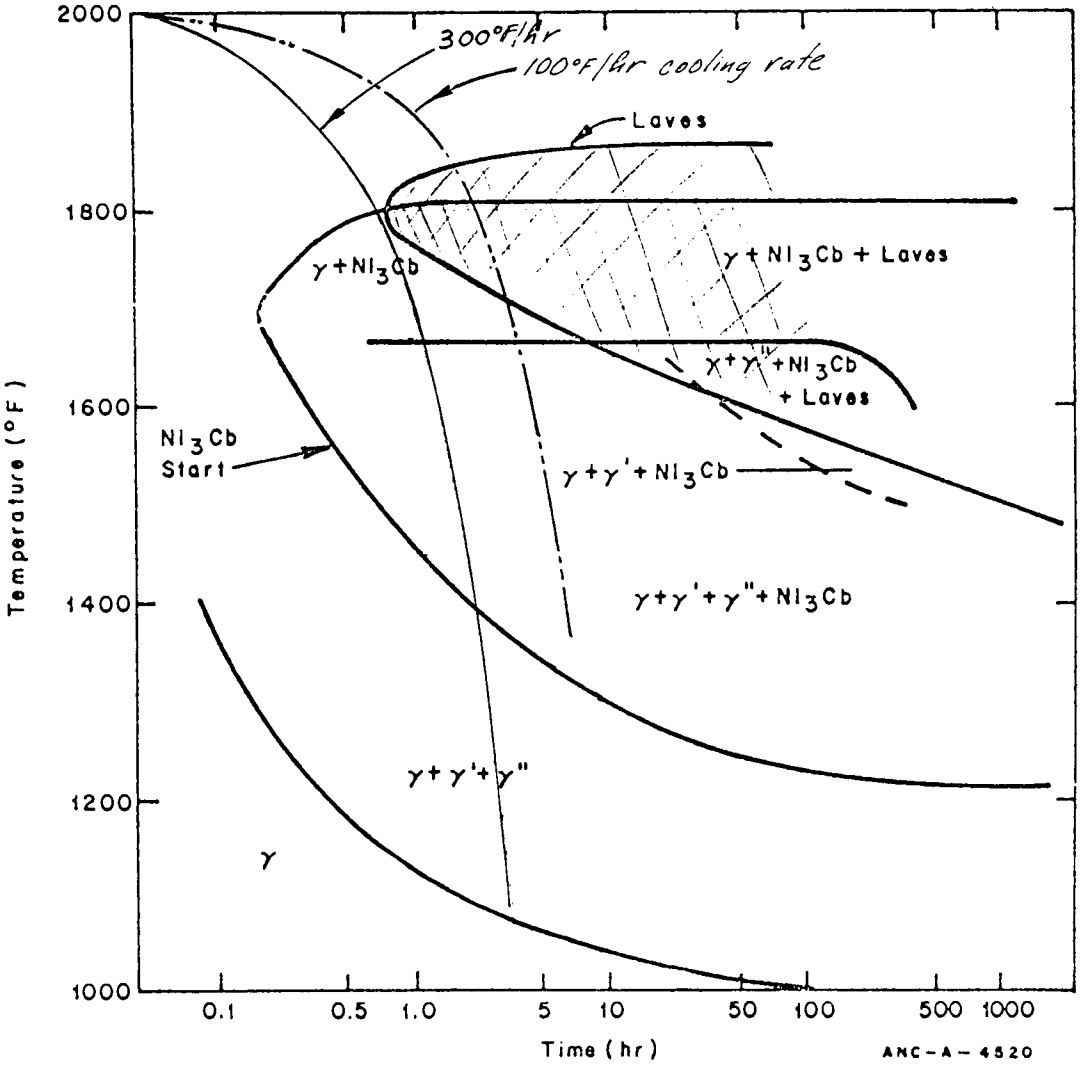

Figure 1.2 Time-temperature-precipitation curves for phases in Alloy 718.

rates were chosen to miss the Laves phase precipitation region (see Figure 1.2). The results of the tests are shown in Table 1.2.

Test results show no significant difference between the INEL heat treatment with the 56C/hr cool and the 167C/hr or the step cool which misses the Laves phase precipitation curve except for room temperature yield strength. The faster cooling rate (167C/hr) showed approximately a 69-83 MPa (10-12 ksi) higher yield strength. Dynamic yield strengths from the instrumented Charpy tests also confirmed the higher values for the faster cooling rate. The impact resistance was quite similar for all heat treatments. From the results of these tests and previous base metal work, it can be concluded that ductility is not very sensitive to cooling rates within the 56-167C/hr range when cooled from 1095C. Yield strength can be increased somewhat by employing cooling rates near the upper range but this rate is probably not practicable in large furnaces. In conclusion, the recommended cooling rate of the INEL heat treatment from the 1095C solution anneal is 83C/hr ± 28C/hr (150F/hr ± 50F/hr). All test specimens for mechanical property generation will use the 83C/hr cooling rate but a ± 6C/hr (± 10F/hr) tolerance will be utilized.

1.3.3 Scoping Mechanical Tests for INEL Heat Treatment

1.3.3.1 Tensile Properties of Base and Weld Metal

Tensile data for the modified INEL heat treatment collected from PBF related projects has been listed in Table 1.3.

The data show an average RT yield strength of 1007 MPa for the plate material tested in the longitudinal direction. The yield strength was slightly lower (965 MPa) for the same material tested in the transverse direction. This represents a compromise from 1038 MPa room temperature yield strengths reported elsewhere[8] for the more conventional heat treatments employing 1038C and 940C solution anneals and faster cooling rates. The yield strength for heat 92514 was significantly higher than the other materials tested. This may be the consequence of either a heat-to-heat variance or a different forming history. The room temperature ductilities are similar for all cases except heat 83C2EK which appears lower.

Yield strengths, ultimate tensile strengths, and reductions in area shown for heat 83C2EK at 650C are comparable to Heat 3 reported by Brinkman and Korth[8]. The heats are similar in that they were both pro-

Table 1.2 Tensile, Side Bend, and Charpy Data of Alloy 718 Weld Metal Given Various Heat Treatments

Tensile Tests

Specimen No.	Heat Treat[a]	Test Temp. C	Yield Strength, MPa	Ultimate Strength, MPa	Total Elong. %	Reduction in Area, %
1-A-1-156	A	24	989	1368	20.0	31.5
1-A-1-157	A	24	983	1378	22.4	33.2
1-A-1-147*	B	24	1076	1382	13.7	21.0
1-A-1-148	B	24	1080	1387	21.8	29.9
1-A-1-167	C	24	1025	1369	21.4	33.3
1-A-1-168	C	24	998	1373	21.6	31.2
1-A-1-160**	A[b]	760	605	716	17.7	21.2
1-A-1-161	A[b]	760	625	747	32.4	35.3
1-A-1-169	C[b]	760	615	733	23.1	27.0
1-A-1-170	C[b]	760	651	758	19.9	24.7

*Small weld flaw noted on fracture surface
**Fracture outside weld metal gage length (in HAZ or base metal)

Charpy Tests (24C)

Specimen No.	Heat Treat[a]	Energy Absorbed, Joule: Crack Initation	Crack Propagation	Total Energy	Dynamic Yield Strength, MPa
1-A-1-136	A	11.9	14.5	26.4	1124
1-A-1-137	A	11.5	12.9	24.4	1103
1-A-1-138	A	12.2	13.6	25.8	1151
1-A-1-145	B	12.9	11.8	24.7	1241
1-A-1-146	B	12.5	12.6	25.1	1241
1-A-1-149	C	-	-	23.0	-
1-A-1-150	C	12.2	12.2	24.4	1093
1-A-1-151	C	12.2	10.2	22.4	1072

Side Bend Tests (24C)

Specimen No.	Heat Treat[a]	Bend Radius: 5t	3.3t	2.8t
1-A-1-129	A	Pass	Fail	-
1-A-1-130	A	Pass	Pass	Pass
1-A-1-131	A	Pass	Pass	Pass
1-A-1-143	B	Pass	Pass	Pass
1-A-1-144	B	Pass	Pass	Pass
1-A-1-164	C	Pass	Pass	Pass
1-A-1-165	C	Pass	Pass	Pass
1-A-1-166	C	Pass	Fail	-

[a]A - 1095C solution anneal for 1 hr cool to 540C at 56C/hr; age at 720C for 4 hr and 620C for 16 hr.
B - 1095C solution anneal for 1 hr; cool to 540C at 167C/hr; age at 720C for 4 hr and 620C 16 hr.
C - 1095C solution anneal for 1 hr; cool to 925C at 167C/hr; cool to 540C at 56C/hr; age at 720C for 4 hr and 620C for 16 hr.

[b] - Same solution anneal and cooling to 540C as footnote (a) but not aged.

Table 1.3 Tensile Properties of Alloy 718 Base

Metal Heat Treated by the INEL Process[a]

Heat	Test Temp. C	Spec. Ident.	0.2% Yield Strength MPa	Ultimate Strength MPa	Total Elong. % (1 in. G.L.)	Red. in Area, %
83C2EK[b]	24	BB6	993	1351	17	17
"	24	BB5	1020[e]	1358	16	14
87C0EK1[b]	24	FS7	986	1372	20	31
"	24	FS8	1000	1386	20	29
"	24	FS9	1007	1393	20	29
87C0EK1[b]	24	AFU1-1	1014	1276	27	33
"	24	AFU1-8	965	1248	26	31
"	24	AFU1-10	993	1303	27	33
87C0EK1[c]	24	AFU1-2	1000	1248	25	31
"	24	AFU1-9	965	1234	26	30
"	24	AFU1-12	910	1276	23	26
87C0EK1[b]	24	AFU2-2	1027	1386	22	33
"	24	AFU2-3	1007	1372	22	30
"	24	AFU2-9	1048	1379	23	33
87C0EK1[c]	24	AFU2-6	985	1289	24	30
"	24	AFU2-7	951	1276	22	29
"	24	AFU2-12	965	1344	23	30
92514[d]	24	4-1Hd-1	1075	1248	19	30
"	24	4-1Hd-2	1110	1282	24	35
"	24	4-1Hd-3	1110	1276	21	30
"	24	4-1Hd-4	1110	1255	18	32
"	24	2-Hd-1	1055	1303	25	34
"	24	2-Hd-2	1069	1310	24	35
83C2EK[b]	650	PS3	814	1040	16	18
"	650	PS4	814	1068	13	16

[a] 1095C solution anneal, cool to 540C at 56-66C/hr; age at 720C for 4 hours plus 16 hours at 620C.

[b] Oriented longitudinal to the rolling direction of one inch thick plate prepared per AMS 5596C.

[c] Oriented transverse to the rolling direction of one inch thick plate prepared per AMS 5596C.

[d] Tangential orientation in a ten inch diameter forging prepared per AMS 5662C.

[e] The value reported is questionable as a result of the extensometer slipping.

cessed by Vacuum Induction Melting-Vacuum Arc Melting sequences. Heat 3, however, had been solution annealed at 940C for 2 hours, air cooled, and duplex aged 8 hours at 720C plus 8 hours at 620C.

Tensile properties for weld metal have been reported in Section 1.3.2.

1.3.3.2 Impact Resistance of Base and Weld Metal

Impact resistance measurements for base metal and weld metal having received the modified INEL heat are listed in Table 1.4.

Table 1.4 Room Temperature Impact Properties for Alloy 718 Base and Weld Metal Having Received the INEL Heat Treat[a]

Heat	Specimen No.	Energy for Crack Initiation, Joule	Energy for Crack Propagation, Joule	Total Energy, J Joule	Dynamic Yield Strength, MPa
87COEK1	FS10[b]	--	--	66.4	--
	FS11[b]	--	--	69.8	--
	FS12[b]	--	--	72.5	--
60C7E	1-A-1-136[c]	11.9	14.5	26.4	1124
	1-A-1-137[c]	11.5	12.9	24.4	1103
	1-A-1-138[c]	12.2	13.6	25.8	1151

[a] 1095C solution anneal, cool to 540C at 56C/hr; age at 720C for 4 hours plus 16 hours at 620C.

[b] Specimen was removed from one thick thick plate and had the L-S orientation.

[c] Specimen was removed from a weldment such that the orientation was identified as T-S (see Figure 1.3).

The average Charpy V-notch strength of greater than 68 J for the base material is superior to any values reported by Huntington Alloys[9] in their Inconel 718 data book. This source has reported average room temperature impact strengths of 27 J for plates solution annealed at 954C and duplex aged at 720-620C. Impact strengths reported for hot rolled product solution annealed at 1038C and duplex aged at 760-650C ranged from 35 to 53 J.

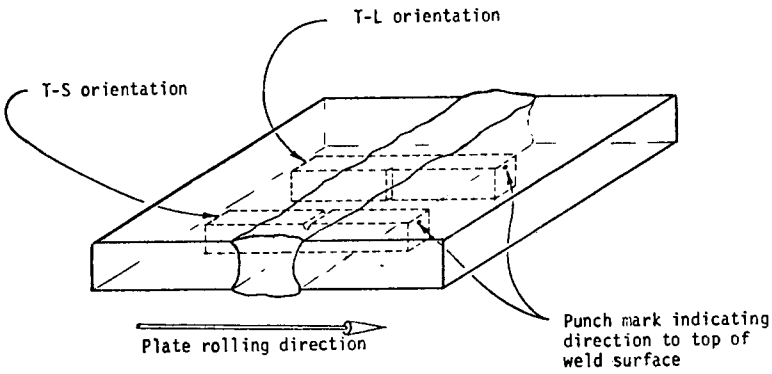

TRANSVERSE WELD CHARPY

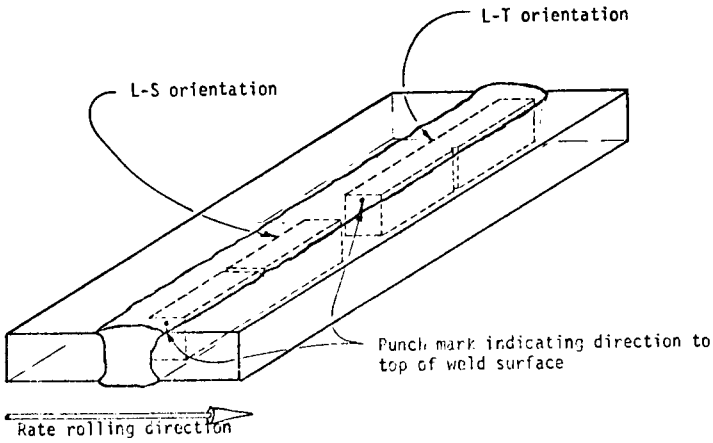

LONGITUDINAL WELD CHARPY

Figure 1.3 Orientation of Charpy impact specimens with respect to weldments.

The absorbed energy of 26 J for weld metal agrees very well with the 28 J reported by Gordine[4] for weld metal solution annealed at 1095C and aged. This also illustrates the improvement resulting from higher solution temperatures since Gordine reported impact strengths of only 8 J when the post weld solution anneals were 927 or 1038C.

1.3.3.3 Fatigue Properties of Base and Weld Metal

Strain controlled fatigue tests have been conducted at 540C. Test data for base metal has been previously reported[10]. Additional data for weld metal are tabulated in Table 1.5. Sufficient base metal specimens have been tested to establish the fatigue curve shown in Figure 1.4. The three data points for weld metal are also plotted in Figure 1.4 to provide a comparison with base metal given the INEL heat treat and other conventional heat treatments.

Table 1.5 Fatigue Data Generated for Weld Metal of Alloy 718 at 540C[a]

Spec. No.	Type	$\Delta\varepsilon_t$, %	Properties at $N_f/2$			N_f	$\dot{\varepsilon}$, s^{-1}
			$\Delta\varepsilon_p$, %	$\Delta\sigma$, MPa	σ_t, MPa		
1-A-1-158	Weld	0.98	0.09	1586	655	4549	4×10^{-3}
1-A-1-162	Weld	0.77	0.01	1400	686	11,767	4×10^{-3}
1-A-1-175	Weld	1.70	0.65	1862	917	775	4×10^{-3}

[a] 1095C solution anneal, cool to 540C at 56C/hr; age at 720C for 4 hours plus 16 hours at 620C.

The fatigue specimens were taken from a transverse orientation of the weldment, i.e. axial gage length was perpendicular to the welding direction. The entire gage section was located in the weld deposit. The base metal specimens were oriented such that the longitudinal axes of the specimens were aligned with the working direction of the plate. The fatigue curve for base metal treated by the INEL process is essentially the same as that shown for the conventional 1040C solution anneal plus 760-650C age.

The weld metal test compares well with the base metal. Very slight hardening (approximately 2% stress increase) occurred during the first

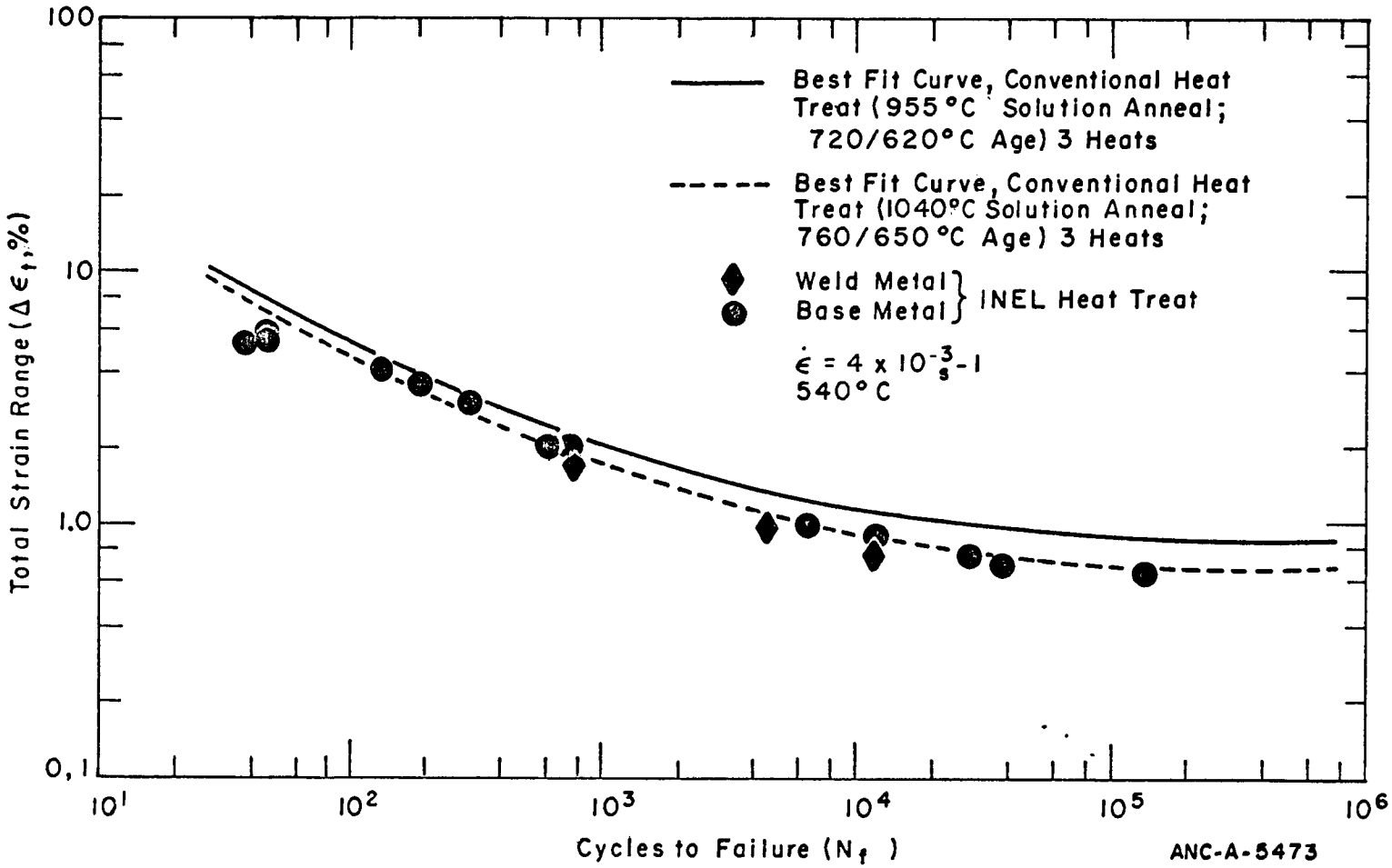

Figure 1.4 Strain fatigue of base and weld Inconel 718 with the INEL heat treat compared to conventional heat treatments. Test temperature:

few cycles and then a small amount of strain softening was observed (<4% stress range) from the peak stress to the end of the test. The softening was negligible in comparison to stainless steel weld metal[11]. The post-weld-solution anneal must completely stress relieve the weldment.

1.3.3.4 Stress Rupture Life of Base Metal

Some 650C stress rupture tests were conducted upon base metal heat treated by the INEL process. The results of these tests are listed in Table 1.6. The notched specimens were prepared per AMS 4928G (Spec. No. 5). This provided a stress concentration factor, K_t, equal to 3.2.

Table 1.6 Stress Rupture Properties of Alloy 718 Base Metal: Heat 52C9EK.

Spec. No.	Spec. Type	Stress MPa	Time to Failure, hr	Total Elong., % (1 in. G.L.)
3AS-2	Smooth	675.9	204.1	6
3AS-9	Smooth	661.2	26.5	3
3AS-12	Smooth	689.5	54.3	4
3AS-5	Notched	744.6	6040	
3AS-8	Notched	715.0	2950	
3AS-11	Notched	857.9	1775	
3AS-7	Notched	960.9	1.4	
3AS-6	Notched	704.0	5240 then discontinued[b]	
3AS-10	Notched	731.5	5180 then discontinued[b]	

[a] 1095C solution anneal, cool to 540C at 56C/hr; age at 720C for 4 hours plus 16 hours at 620C.

[b] Specimens from the discontinued tests were machined into specimens for 650C tensile tests.

The preliminary data points from Table 1.6 are plotted in Figure 1.5 and compared with base metal of Alloy 718 heat treated by conventional methods. The GE data represent round smooth bar specimens removed tangentially from a pancake forging. Smooth and notch rupture life at 650C for hot-rolled bar is shown by the Huntington data.

1.3.3.5 Stability Check of Base Metal Stressed at 650C

The stability of two Inconel 718 base metal specimens stressed at 650C were checked. Specimens 3AS-6 and 3AS-10 listed in Table 1.6 were machined into tensile specimens and tested at 650C. The results are as follows:

Specimen No.	Test Temp. C	0.2% Yield Strength, MPa	Ultimate Strength, MPa	Total Elong., % (1" G.L.)	Red. in Area, %
3AS-6	650	866.7	946.0	12	15
3AS-10	650	921.8	1100.4	18	17

A comparison may be made with the 650C tensile properties reported in Table 1.3. The samples were all removed longitudinally from plate materials melted by similar VIM-ESR processes. The yield strengths for the specimens stressed at 650C were higher than those reported in Table 1.3 obtained from tests subsequent to the aging cycle. This may indicate that additional age hardening is occurring at 650C or it may be reflecting a heat-to-heat variance. No significant differences were observed for the elongations and reductions in area.

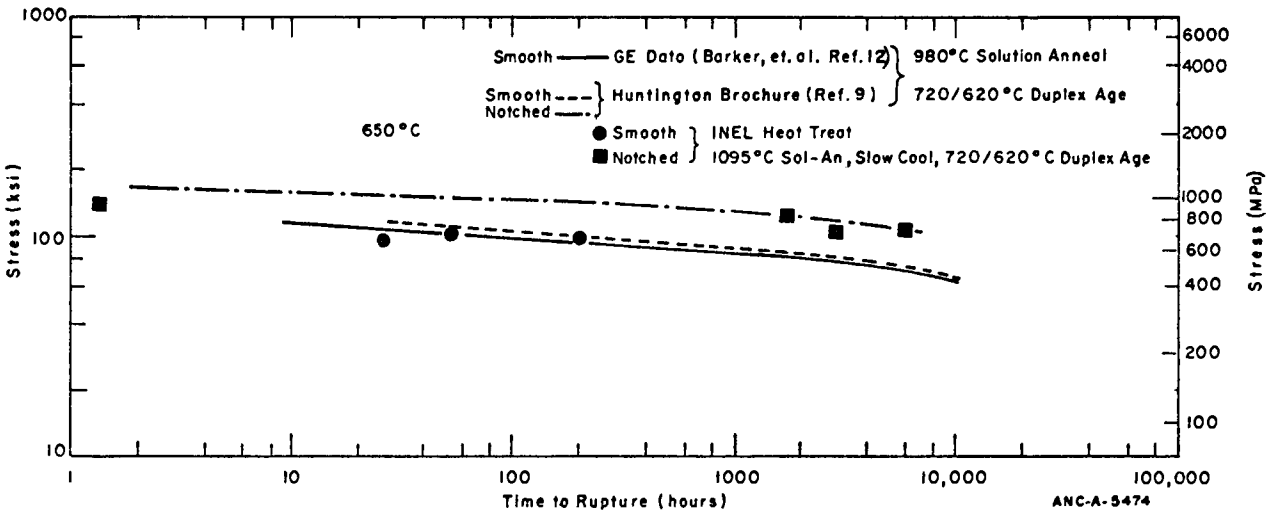

Figure 1.5 650C stress rupture scoping tests of Inconel 718 comparing conventional and INEL heat treatments.

1.4 REFERENCES

1. R. T. King and J. O. Stiegler, "Effects of Thermal Aging on the Properties and Structure of Type 308 CRE Stainless Steel Weld Metal," Fuels and Materials Development Program Quarterly Progress for the Period Ending Sept. 30, 1973, ORNL-TM-4405, (155-162).
2. R. T. King and E. Bolling, "Effect of Thermal Aging on the Creep and Creep-Rupture Behavior of CRE Type 308 Stainless Steel SMA Welds," Mechanical Properties Test Data for Structural Materials Quarterly Progress Report for period ending April 30, 1975, ORNL-5105 (178-181).
3. G. E. Korth and M. D. Harper, "Low Cycle Fatigue Behavior of SMA Type 304/308 Stainless Steel Weldments," Mechanical Properties Test Data for Structural Materials Quarterly Progress Report for period ending January 31, 1974, ORNL-4948 (2-5).
4. J. Gordine, Welding JOurnal Research Supplement, p 531-s, (1972).
5. M. J. Graber, C. R. Brinkman, and R. R. Hobbins, "Metallurgical Evaluation of Welding and Heat Treating Procedures for the Inconel 718 PBF In-Pile Tube," ANCR-1087 (1972).
6. G. R. Smolik, Aerojet Nuclear Company, unpublished data.
7. G. E. Korth and G. R. Smolik, ANC contribution to Mechanical Properties Test Data for Structural Materials Quarterly Progress Report ending July 30, 1975, ORNL-5105.
8. C. R. Brinkman and G. E. Korth, "Strain Fatigue and Tensile Behavior of Inconel 718 from Room Temperature to 650C," J. Test. Eval. 2, 249-259 (1974).
9. Huntington Alloys brochure 10M 10-73 T-39.
10. D. D. Keiser, et. al., ANC contribution to Mechanical Properties Test Data for Structural Materials Quarterly Progress Report for period ending July 31, 1974, ORNL 4998.
11. C. R. Brinkman and G. E. Korth, "Heat-to-Heat Variations in the Fatigue and Creep-Fatigue Behavior of AISI Type 304 Stainless Steel, and the Fatigue Behavior of Type 308 Stainless Steel Weld Material," Aerojet Nuclear Co. Report ANCR-1097, May, 1973, p 34-36.
12. J. F. Barker, E. W. Ross, and J. F. Radavich, "Long Time Stability of Inconel 718", G. E. Report R67FPD379 (1968).

2. ARGONNE NATIONAL LABORATORY

R. W. Weeks

2.1 INTRODUCTION

Argonne National Laboratory (ANL) is conducting extensive programs to provide elevated-temperature, low-cycle fatigue data on Types 304 and 316 stainless steel and to study the effects of sodium environment on the elevated-temperature mechanical properties of these materials. Both programs are in support of the LMFBR component design. The present report describes a brief statistical analysis of data scatter observed in low-cycle fatigue tests of Type 304 stainless steel, presents elevated-temperature true stress-true strain tensile data obtained for Types 304 and 316 stainless steel after extended exposure to flowing sodium, and describes the effects of a flowing-sodium test environment on the low-cycle fatigue behavior of Type 304 stainless steel.

2.2 FRACTURE AND FATIGUE STUDIES ON STAINLESS STEEL -- D. R. Diercks

2.2.1 Statistical Analysis of Low-cycle Fatigue Data Scatter -- D. R. Diercks

Two series of ten identical elevated-temperature low-cycle fatigue tests on Type 304 stainless steel have been completed, and the results are reported in Tables 2.1 and 2.2. These tests were conducted to determine the extent of data scatter present for two test conditions. The data of Table 2.1 were generated at a total strain range of 1%, with a 1-min tension-hold time per cycle. The total strain range for the data of Table 2.2 was 0.5%, and no hold time was present. The test temperature was 593°C (1100°F) in all cases, and the total strain rate was 4×10^{-3} sec^{-1}. All specimens were from heat 9T2796 and were solution annealed and aged for 1000 hr at 593°C (1100°F) before testing.

The cyclic-life data of Table 2.1 may be seen to have an approximately symmetrical distribution about the sample mean of 1711 cycles, and the extreme values of the sample differ from each other by about a factor of two. However, these data in Table 2.2 are obviously quite

Table 2.1. Fatigue Data for Type 304 Stainless Steel Cycled at 593°C (1100°F) and $\Delta\varepsilon_t$ = 1%, with a 1-min Tension Hold Time

Test No.	Specimen No.	Strain Range Total, %	Strain Range Plastic, %	Total Stress Range, MPa	Machine No.	Machine Operator	Cycles to Failure	Time to Failure, min
629	T-282	1.009	0.688	507	7	1	1171	1240
656	T-308	0.995	0.700	481	2	4	1528	1657
631	T-275	0.998	0.684	500	2	4	1560	1680
633	T-285	1.004	0.689	514	2	4	1593	1723
135	AA-10	0.997	0.704	483	3	3	1664	1730
682	T-315	1.010	0.704	499	1	4	1670	1769
655	T-307	1.002	0.698	485	7	1	1748	1880
698	T-331	1.049	0.753	477	1	4	1824	1973
695	T-326	0.996	0.699	477	6	5	2099	2257
663	T-309	1.006	0.722	457	7	1	2255	2425

Table 2.2. Fatigue Data for Type 304 Stainless Steel Cycled at 593°C (1100°F) and $\Delta\varepsilon_t$ = 0.5%, with Zero Hold Time

Test No.	Specimen No.	Strain Range Total, %	Strain Range Plastic, %	Total Stress Range, MPa	Machine No.	Machine Operator	Cycles to Failure	Time to Failure, min
683	T-316	0.499	0.268	352	1	4	27,552	1147
696	T-329	0.527	0.299	346	1	4	27,980	1164
701	T-334	0.493	0.262	352	2	4	29,386	1222
134	AA-8	0.512	0.307	312	1	6	30,498	1272
700	T-333	0.499	0.272	345	6	5	30,507	1269
691	T-323	0.504	0.285	332	6	5	34,052	1417
697	T-330	0.502	0.275	346	6	5	34,626	1441
638	T-302	0.517	0.281	359	7	1	37,819	1574
685	T-319	0.496	0.269	344	1	4	47,003	1956
703	T-335	0.528	0.308	334	1	2	73,752	3074

nonsymmetrical, with most of the cyclic lives clustered below the sample mean value of 37,318 cycles and one extremely high value exceeding the mean by almost a factor of two. The data scatter within a sample shows no obvious relationship to total or plastic strain range, total stress amplitude, the machine on which the test was run, nor to the individual responsible for setting up and operating the test.

Data of Tables 2.1 and 2.2 were found to behave according to a Weibull distribution function, a distribution frequently used to describe fatigue data scatter.[1,2] The Weibull distribution is characterized by a probability function f(N) that has the form

$$f(N) = \frac{b}{N_a - N_o} \left(\frac{N - N_o}{N_a - N_o} \right)^{b-1} \exp\left[- \left(\frac{N - N_o}{N_a - N_o} \right)^{b} \right], \tag{1}$$

where N is the cyclic life, and N_o, N_a, and b are constants. The fraction F(N) of a given population that may be expected to fail prior to life N is given by

$$F(N) = 1 - \exp\left[- \left(\frac{N - N_o}{N_a - N_o} \right)^{b} \right]. \tag{2}$$

Equation (2) may be transformed to the form

$$\ln \ln\left[\frac{1}{1 - F(N)} \right] = b \ln(N - N_o) - b \ln(N_a - N_o). \tag{3}$$

Thus, from Eq. (3), a suitable choice for N_o will yield a linear plot of $\ln \ln \{1/[1 - F(N)]\}$ versus $\ln (N - N_o)$ that has a slope b and a value of N equal to N_a at $\ln \ln \{1/[1 - F(N)]\} = 0$, or $F(N) = 0.632$. The constant N_o is referred to as the "minimum life parameter" and has a value greater than or equal to zero. For a distribution with a nonzero value of N_o, failure prior to $N - N_o$ has zero probability.

Figure 2.1 shows the data of Tables 2.1 and 2.2 plotted according to Eq. (3) with $N_o = 0$. Values of the percent of the sample failed [F(N) x 100] were obtained using a mean-rank estimate.[1] A best straight-line fit to these data was obtained using a least-squares analysis, minimizing the errors in the y-direction. The values obtained for

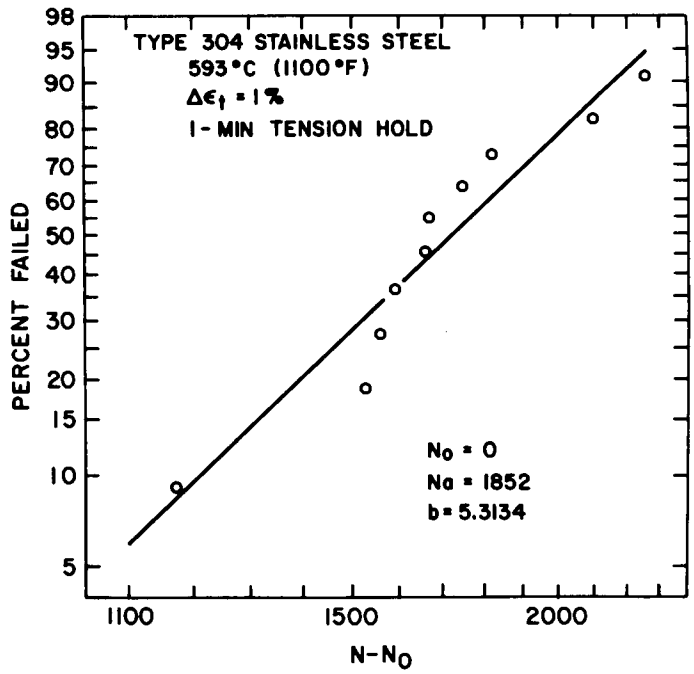

Fig. 2.1. Fit of Weibull Distribution Function to Data of Table 2.1. Neg. No. MSD-61436.

b and N_a are indicated in Fig. 2.1. From the values of the constants, one computes[1] a mean value μ of 1706 cycles for the distribution function fit to the sample compared with a sample mean of 1711 cycles. The variance σ^2 of the distribution function is 1.341×10^5 (σ = 366 cycles).

A nonzero value for N_o was required to fit a Weibull distribution to the data sample of Table 2.2. Figure 2.2 shows the fit to Eq. (3), which was obtained assuming N_o = 27,400 cycles. A value of 41,024 cycles is computed for the mean of the distribution function as compared with a sample mean of 37,318 cycles. The variance σ^2 of the distribution function about the mean has a rather large value of 5.893×10^8 (σ = 24,276 cycles).

Employing numerical integration techniques, 95% confidence intervals were determined for the two distribution functions obtained above. The lower and upper bounds, N_1 and N_2, respectively, for the intervals were chosen such that

$$\int_0^{N_1} f(N)\, dN = \int_{N_2}^{\infty} f(N)\, dN = 0.025. \tag{4}$$

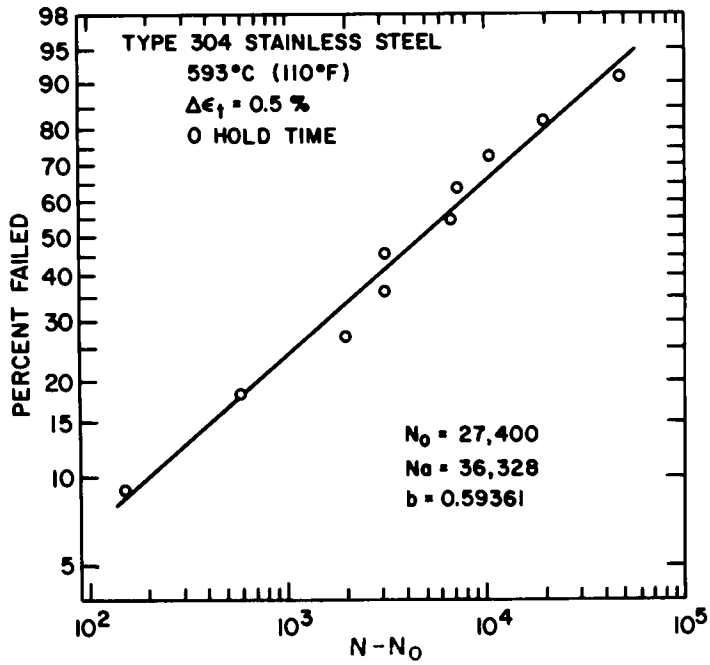

Fig. 2.2. Fit of Weibull Distribution Function to Data of Table 2.2. Neg. No. MSD-61435.

Note that the confidence intervals thus obtained are not necessarily symmetric about the mean of the distribution function. For the distribution function fitted to the data of Table 2.1, the 95% confidence interval lies between 930 and 2370 cycles. For the function corresponding to the data of Table 2.2, the interval lies in the broad range between 27,420 and 114,500 cycles. The large value of N_2 for the second case is associated with the long tail on the corresponding distribution function. The 90% confidence limits for the same function are 27,460 and 85,060 cycles, and the 80% confidence limits are 27,600 and 64,000 cycles.

2.3 SODIUM EFFECTS ON LMFBR MATERIALS -- T. F. Kassner

2.3.1 Influence of Sodium Environment on Tensile Behavior of Austenitic Stainless Steels -- K. Natesan and O. K. Chopra

The effect of carburization on the tensile properties of Types 304, 316, and Ti-modified 316 stainless steel is being determined after

exposure of the materials to well-characterized sodium at temperatures between 550 and 700°C. Since the composition and microstructure of the material in the vicinity of the sodium-steel interface can have a strong influence on crack initiation and propagation, the degree of carburization that results from the sodium environment needs to be correlated with the mechanical-property changes in the material. Because of the relatively low operating temperatures and large thickness of materials in structural components, carbon concentration profiles rather than a uniform equilibrium carbon distribution in the material will result during their service in reactor systems. Thus, it is essential to obtain mechanical-property data on materials with specific carbon penetration depths and to correlate the property changes with the penetration depth and surface carbon concentration in the material. In the present report, data are presented on the effect of carburization on the tensile behavior of Types 304 and 316 stainless steel for temperatures between 550 and 700°C.

The experimental procedure detailing specimen preparation, sodium-exposure conditions, and tensile test conditions is discussed elsewhere.[3-5] Load-elongation data from the tensile tests were converted to true stress-true strain curves by assuming a constant volume approximation. Figure 2.3 shows the true stress-true strain curves for Types 304 and 316 stainless steel in the solution-annealed condition at test temperatures of 25, 550, 600, 650, 700, and 750°C. It is evident that the flow stress at a given strain tends to decrease with an increase in test temperature. The curves also indicate that Type 316 stainless steel is stronger than Type 304 in the temperature range of our investigation. The true stress-true plastic strain data were fitted by the Holloman equation[6,7]

$$\sigma = K \varepsilon_p^n , \tag{5}$$

where

σ = true stress,

ε_p = true axial plastic strain,

K = strength coefficient,

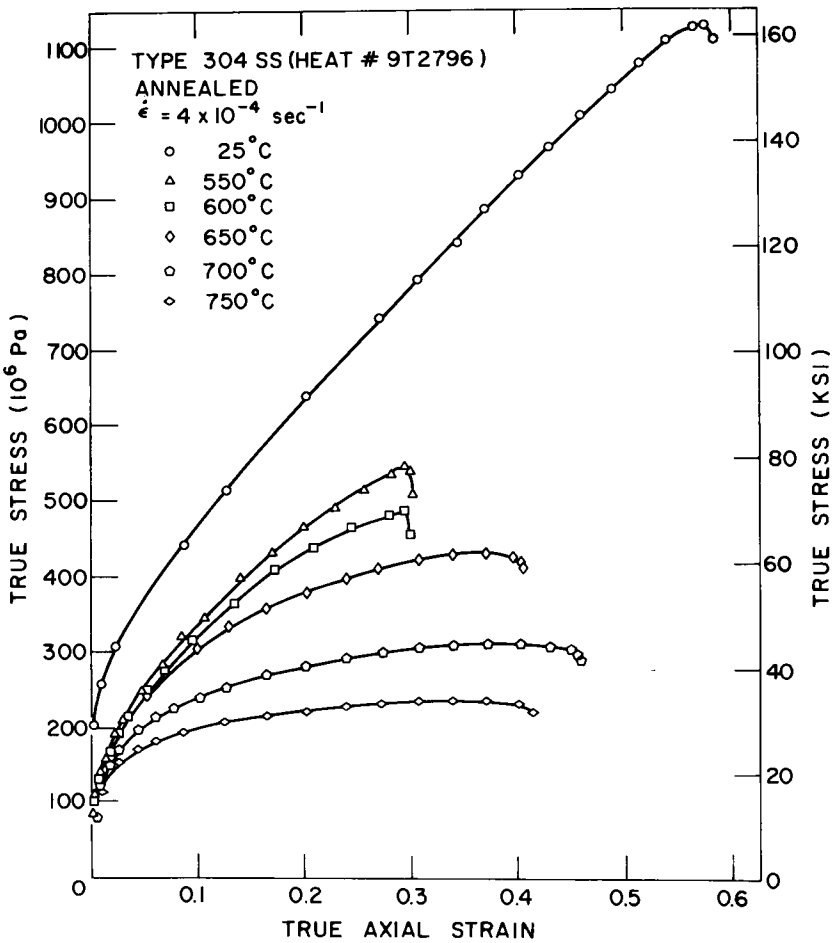

(a)

Fig. 2.3. True Stress-True Strain Behavior of Types 304 and 316 Stainless Steel in the Annealed Condition at Various Temperatures. Neg. Nos. MSD-60135 and MSD-60142.

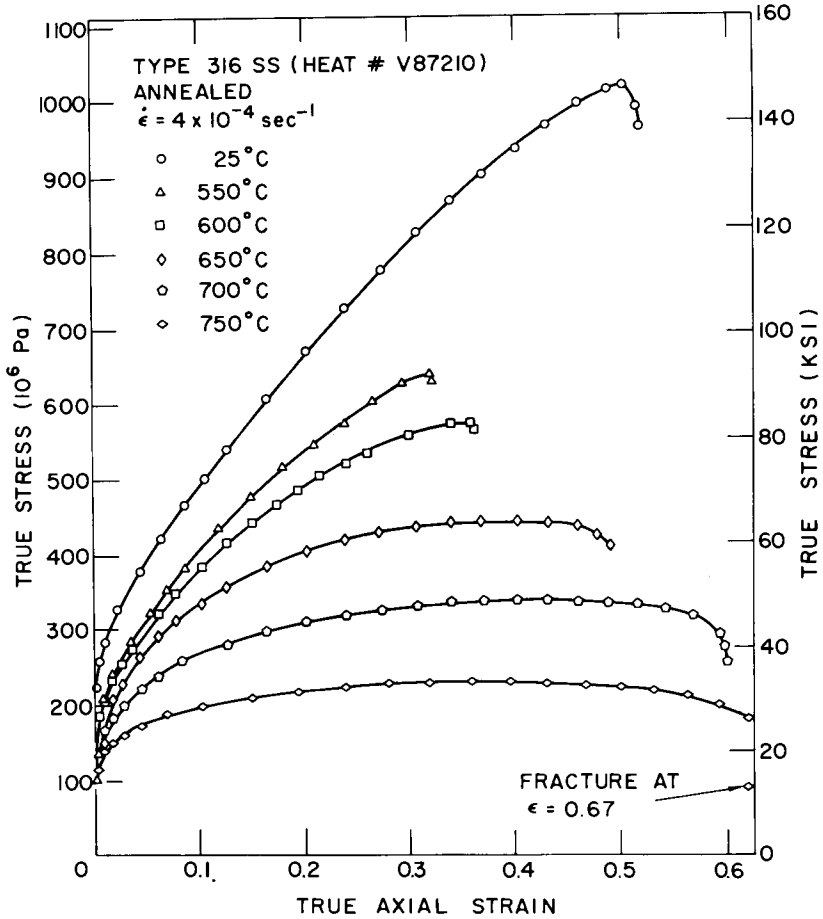

(b)

and

n = strain-hardening exponent

The results shown in Table 2.3 indicate that both K and n increase as the temperature decreases. The yield stress (0.2% offset value) and ultimate tensile strength increased, whereas the tensile elongation decreased as the test temperature decreased. Data listed in Table 2.4 for Type 316 stainless steel also indicate the same behavior. These data at 550 and 600°C were not linear when plotted as log σ versus log ε_p, and thus the calculated n values are applicable only in the true-strain range between 5 and 30%. The influence of lowering the strain rate is to lower the ultimate tensile strength and increase the tensile elongation.

The test data on specimens with various carbon penetration depths at different temperatures are shown in Fig. 2.4 along with curves for the

Table 2.3. Tensile Behavior of AISI Type 304 Stainless Steel upon Exposure to Sodium Environment

Strain Rate, sec^{-1}	Temperature, °C	Sodium-exposure Time, hr	Carbon Penetration Depths, cm	Carbon Penetration Depths, (mils)	Surface Carbon Concentration, wt%	Average Carbon Concentration, wt%	0.2% Yield Stress, MPa	0.2% Yield Stress, (ksi)	Ultimate Tensile Strength, MPa	Ultimate Tensile Strength, (ksi)	Total Elongation, %	K, MPa	K, (ksi)	n
4×10^{-4}	700	0	0	(0)	0.046	0.046	70.1	(10.1)	234.0	(33.7)	58	434.0	(62.5)	0.264
		120	-	-	↕	↕	72.9	(10.5)	217.4	(31.3)	71	413.2	(59.5)	0.253
		504	-	-		0.043-0.046	70.8	(10.2)	213.2	(30.7)	68	411.8	(59.3)	0.265
		1512	-	-			71.5	(10.3)	211.8	(30.5)	71	424.3	(61.1)	0.265
	650	0	0	(0)	0.046	0.046	83.3	(12.0)	311.8	(44.9)	50	623.6	(89.8)	0.320
		312	0.01	(∿4)	0.095	0.078	78.5	(11.3)	302.8	(43.6)	52	581.9	(83.8)	0.300
		1512	0.020	(∿8)	0.25	0.122	78.5	(11.3)	297.2	(42.8)	58	593.0	(85.4)	0.303
	600	0	0	(0)	0.046	0.046	90.3	(13.0)	363.2	(52.3)	34	738.2	(106.3)	0.364[a]
		1512	0.010	(∿4)	0.30	0.145	96.5	(13.9)	377.8	(54.4)	26	760.4	(109.5)	0.328
	550	0	0	(0)	0.046	0.046	88.2	(12.7)	406.2	(58.5)	35	815.3	(117.4)	0.384[a]
		5012	0.010	(∿4)	0.207	0.207	109.0	(15.7)	444.4	(64.0)	20	950.0	(136.8)	0.358
4×10^{-5}	700	0	0	(0)	0.046	0.046	83.3	(12.0)	176.4	(25.4)	61	284.7	(41.0)	0.190
		1512	-	-	0.046	∿0.046	70.1	(10.1)	163.9	(23.6)	69	316.7	(45.6)	0.241
	650	0	0	(0)	0.046	0.046	85.4	(12.3)	241.0	(34.7)	53	442.4	(63.7)	0.265
		1512	0.010	(∿8)	0.25	0.122	84.0	(12.1)	241.0	(34.7)	63	484.0	(69.7)	0.281
	600	0	0	(0)	0.046	0.046	81.2	(11.7)	320.1	(46.1)	45	600.0	(86.4)	0.313
		1512	0.010	(∿4)	0.30	0.145	85.4	(12.3)	332.6	(47.9)	39	737.5	(106.2)	0.377[a]
	550	0	0	(0)	0.046	0.046	91.0	(13.1)	401.4	(57.8)	41	743.7	(107.1)	0.372[a]
		5012	0.010	(∿4)	0.60	0.207	95.1	(13.7)	-	-	30	-	-	-

[a]The n values are applicable in the strain range between 5 and 30%.

Table 2.4. Tensile Behavior of AISI Type 316 Stainless Steel upon Exposure to Sodium Environment

Strain Rate, sec^{-1}	Temperature, °C	Sodium-exposure Time, hr	Carbon Penetration Depths, cm	(mils)	Surface Carbon Concentration, wt%	Average Carbon Concentration, wt%	0.2% Yield Stress, MPa	(ksi)	Ultimate Tensile Strength, MPa	(ksi)	Total Elongation, %	K, MPa	(ksi)	n
4×10^{-4}	700	0	0	(0)	0.058	0.058	91.7	(13.2)	236.1	(34.0)	82	404.1	(58.2)	0.185
		120	0.010	(∿4)		0.063	91.0	(13.1)	233.3	(33.6)	70	370.8	(53.4)	0.171
		504	0.020	(∿8)	0.16 ±0.1	0.068	86.8	(12.5)	241.7	(34.8)	69	401.4	(57.8)	0.190
		1512	0.0375	(∿15)		0.075	75.0	(10.8)	243.0	(35.0)	72	435.4	(62.7)	0.225
	650	0	0	(0)	0.058	0.058	104.2	(15.0)	330.5	(47.6)	63	586.1	(84.4)	0.247
		312	0.010	(∿4)	0.26	0.085	91.0	(13.1)	317.4	(45.7)	57	560.4	(80.7)	0.246
		1512	0.020	(∿8)	0.34	0.145	95.1	(13.7)	317.4	(45.7)	59	572.2	(82.4)	0.236
	600	0	0	(0)	0.058	0.058	114.6	(16.5)	420.0	(60.5)	40	829.2	(119.4)	0.337[a]
		1512	0.010	(∿4)	0.52	0.153	121.5	(17.5)	394.4	(56.8)	37	765.3	(110.2)	0.300[a]
	550	0	0	(0)	0.058	0.058	121.5	(17.5)	449.0	(64.5)	37	835.4	(120.3)	0.344[a]
		5012	0.010	(∿4)	0.65	0.259	131.9	(19.0)	499.3	(71.9)	32	909.7	(131.0)	0.308[a]

[a]The n values are applicable in the strain range between 5 and 30%.

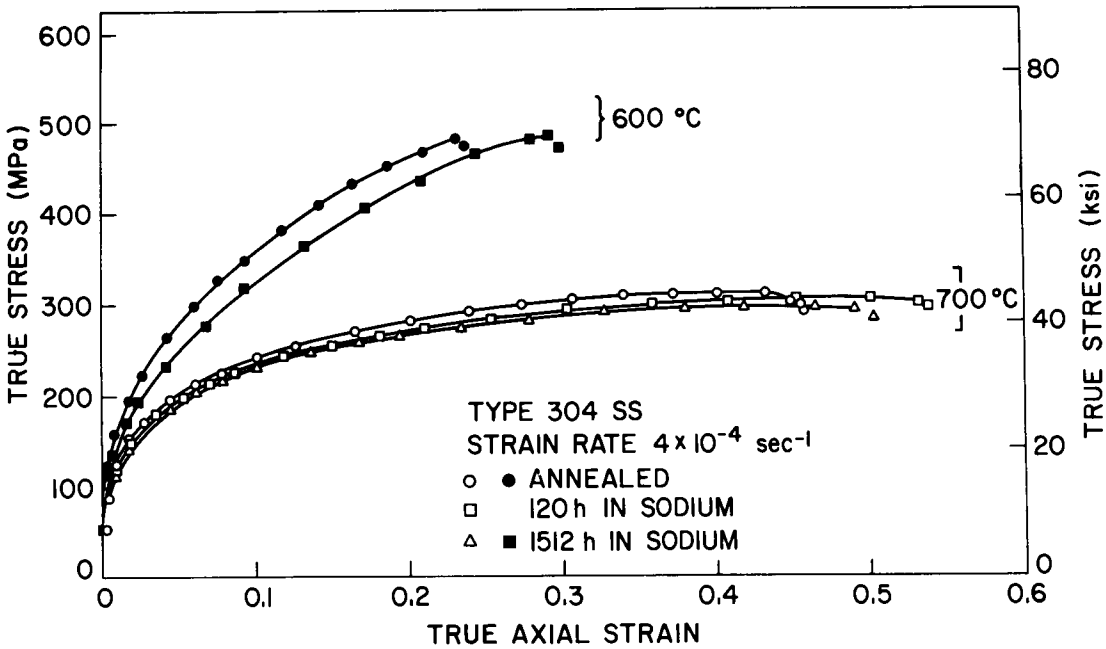

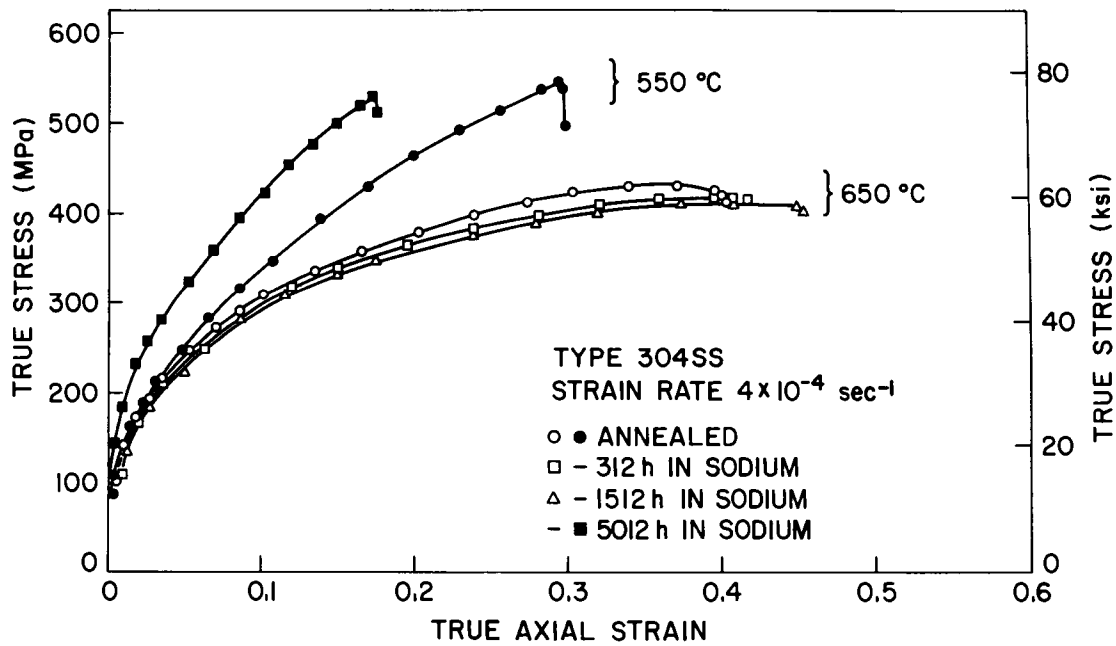

(b)

Fig. 2.4. True Stress-True Strain Curves for Type 304 Stainless Steel in the Annealed and Carburized Conditions at 550, 600, 650, and 700°C. Neg. Nos. MSD-61183 and MSD-61178.

solution-annealed material. These data indicate that, for the conditions of temperature and sodium purity in which the material undergoes minimal compositional changes (i.e., 650 and 700°C in these experiments), the environment had almost no effect on the tensile properties, whereas, in general, the strength improves and ductility decreases at 550 and 600°C. The carbon penetration depths and average carbon concentrations in the sodium-exposed specimens are shown in Table 2.3 along with the property data.

Figure 2.5 shows the true stress-true strain behavior of Type 304 stainless steel at strain rates of 4×10^{-4} and 4×10^{-5} sec^{-1} at 600 and 700°C. The influence of lower strain rate on the tensile properties of the sodium-exposed specimens is to shift the true stress-true strain curves to lower stress levels similar to those for solution-annealed specimens.

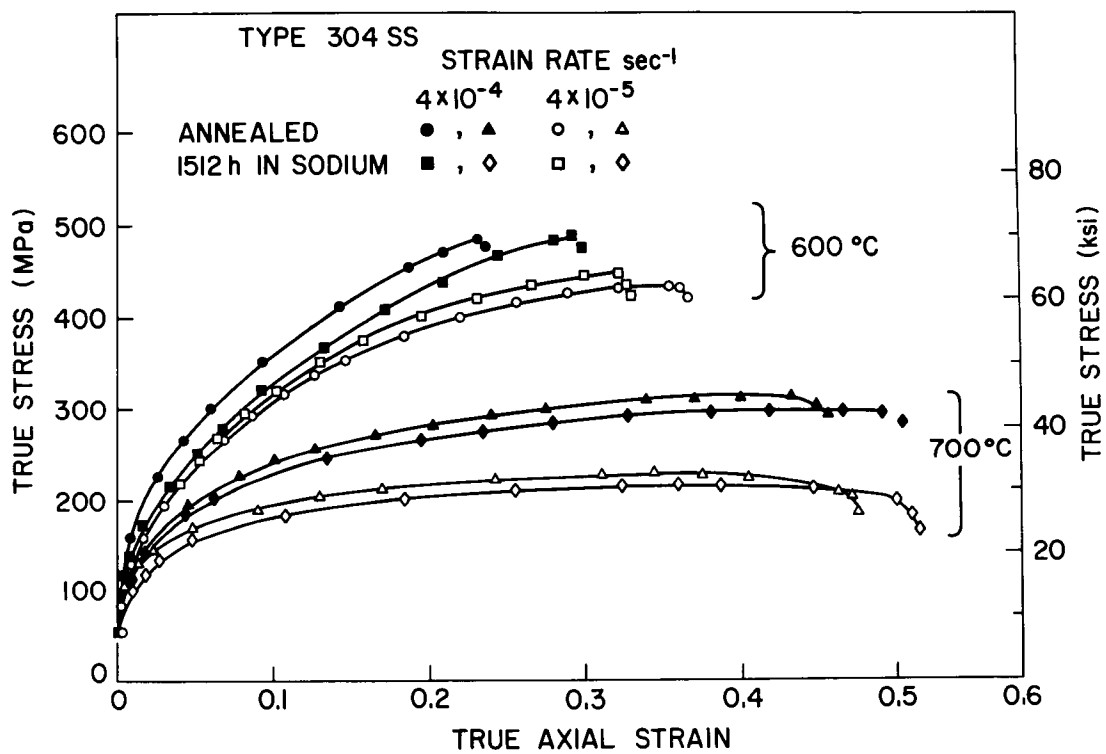

Fig. 2.5. Influence of Strain Rate on the True Stress-True Strain Behavior of Types 304 Stainless Steel in the Annealed and Carburized Conditions at 600 and 700°C. Neg. No. MSD-61182.

The application of the Holloman equation to the data for the sodium-exposed specimens indicates that the carbon concentration of the steel in the range investigated does not show any systematic variation of K or n. Figure 2.6 shows a comparison of the tensile behavior of Types 304 and 316 stainless steel in the solution-annealed and sodium-exposed conditions at 550 and 650°C at a strain rate of 4×10^{-4} sec^{-1}. The curves and the calculated values for different properties in Tables 2.3 and 2.4 indicate that Type 316 stainless steel is stronger under all conditions, and the influence of carbon penetration on the tensile properties of both materials was small for the range of conditions investigated.

Figures 2.7 and 2.8 show scanning-electron micrographs of the fracture surfaces of Types 304 and 316 stainless steel tested at a strain rate of

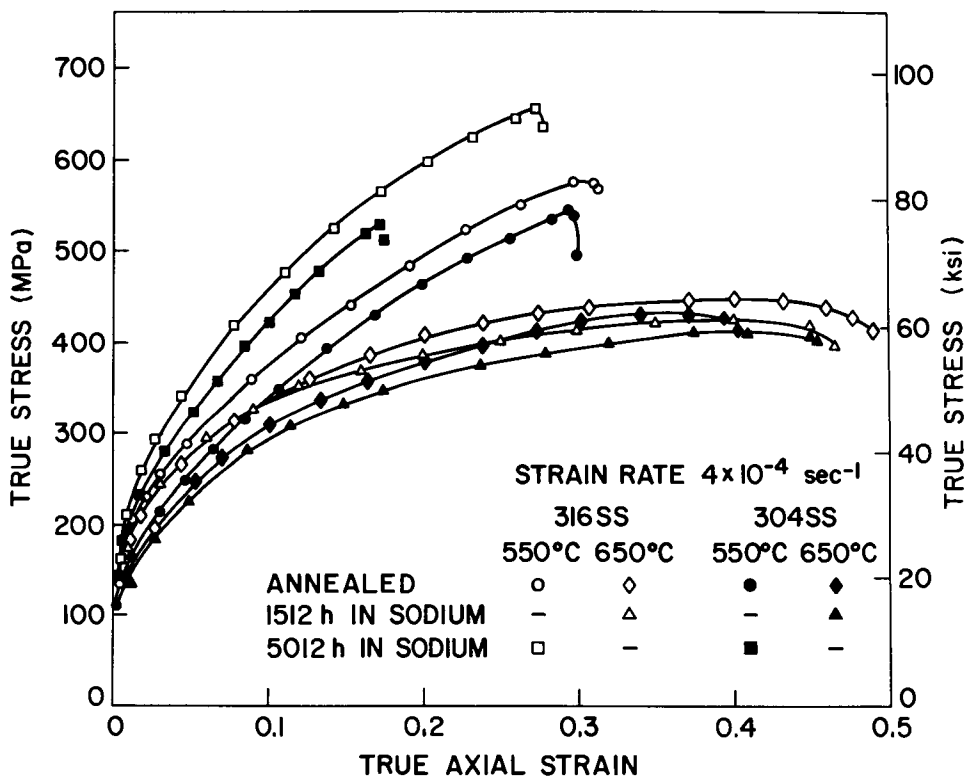

Fig. 2.6. A Comparison of the True Stress-True Strain Behavior of Types 304 and 316 Stainless Steel in the Annealed and Sodium-exposed Conditions at 550 and 650°C. Neg. No. MSD-61179.

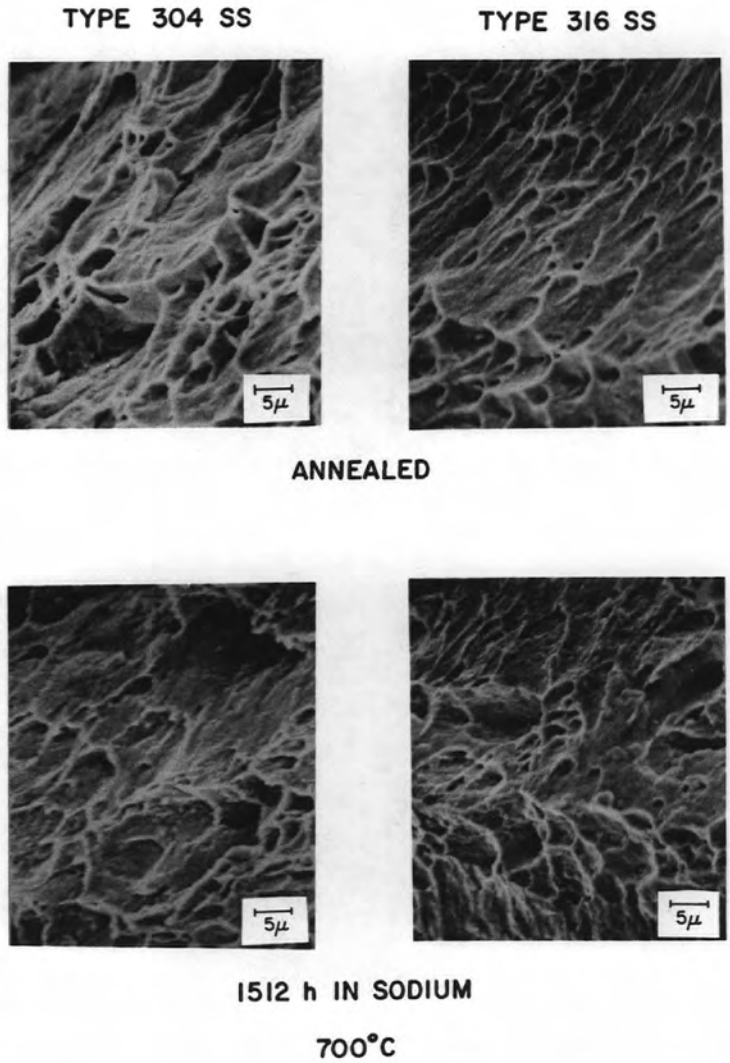

Fig. 2.7. Scanning-electron Micrographs of Fracture Surfaces of Types 304 and 316 Stainless Steel in the Annealed and Sodium-exposed Conditions at 700°C. Neg. No. MSD-61184.

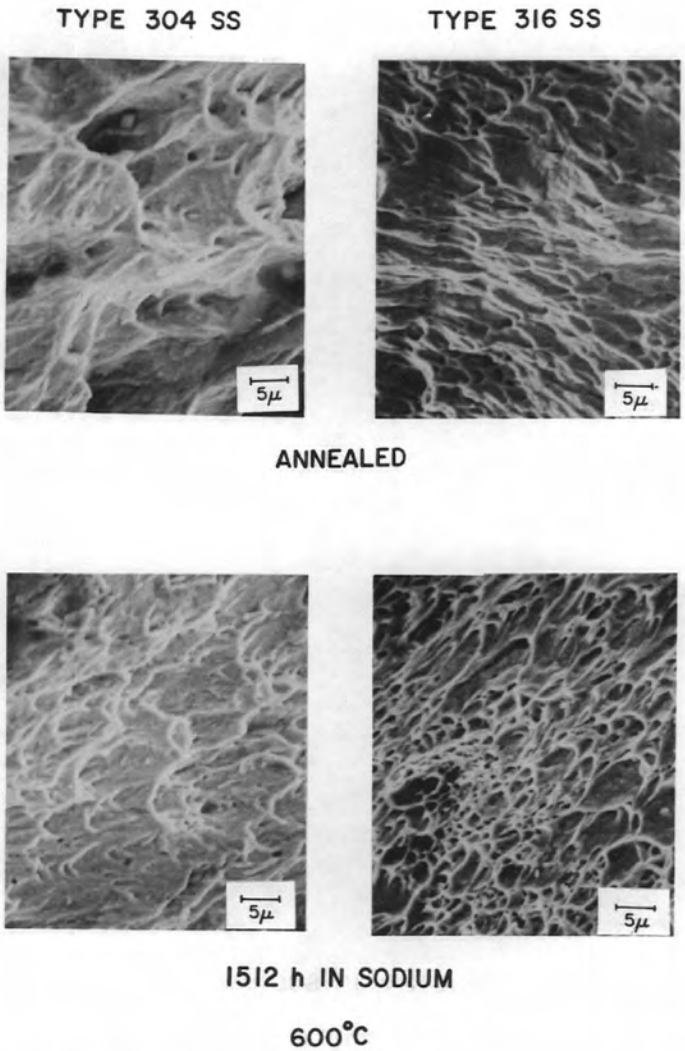

Fig. 2.8. Scanning-electron Micrographs of Fracture Surfaces of Types 304 and 316 Stainless Steel in the Annealed and Sodium-exposed Conditions at 600°C. Neg. No. MSD-61185.

4×10^{-4} sec^{-1} in the annealed condition and after a 1512-hr exposure to sodium at 700 and 600°C, respectively. The figures indicate that the fractures are dimpled, which is indicative of a ductile mode, and can be associated with the growth of internal voids or holes.

Figure 2.9 shows the variation of engineering tensile strength as a function of temperature for Types 304 and 316 stainless steel in the solution-annealed and sodium-exposed conditions. The strength decreases at 700 and 650°C, whereas a small increase can be noted at 600 and 550°C; however, the values are higher than the minimum expected values specified for these steels in the Nuclear Systems Materials Handbook.

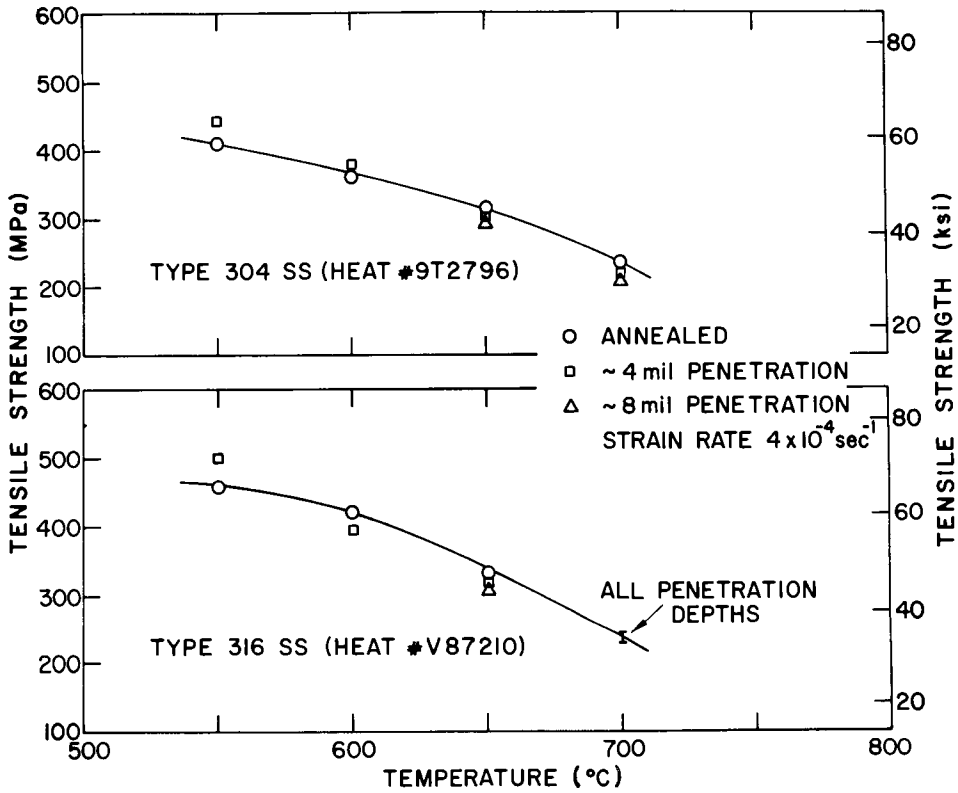

Fig. 2.9. Variation of Engineering Tensile Strength with Temperature for Types 304 and 316 Stainless Steel in the Annealed and Carburized Conditions. Neg. No. MSD-61181.

2.3.2 Influence of Sodium Environment on the Low-cycle Fatigue Behavior of Austenitic Stainless Steels -- D. L. Smith and G. J. Zeman

Fatigue tests in sodium are being conducted to investigate the influence of a high-temperature sodium environment on the low-cycle fatigue behavior of Types 304 and 316 stainless steel. Both the effect of testing in a sodium environment and the effect of long-term sodium exposure are being investigated. Data reported previously[8] indicate that the fatigue life of annealed Type 316 stainless steel tested in sodium at 600°C is a factor of four greater than when tested in air under similar conditions, vis., strain rate of 4×10^{-3} sec^{-1} and total strain range of 0.7-1.2%. However, the fatigue life of specimens tested in sodium is not substantially affected by variations of the carbon concentration in sodium in the range of 0.03-0.3 ppm. The increased fatigue life in sodium, which is attributed primarily to the low oxygen potential that exists in sodium, is in agreement with the hypothesis of enhanced crack-propagation rates caused by an "oxide wedging" effect when testing in an oxidizing atmosphere. No oxide formation occurs on stainless steel at 600°C when exposed to sodium that contains 1-ppm oxygen.

Microscopic examination of the test specimens revealed a number of surface cracks in the gauge section, ranging in depth from 1 to 20 g. Figure 2.10 is a photomicrograph of a typical surface crack observed in an annealed specimen after testing in sodium. These cracks were predominantly transgranular, which is in agreement with the fracture mode. Approximately four times as many cracks were observed in specimens tested in air as those tested in sodium. This result indicates that crack initiation is apparently more difficult in the sodium environment.

Figure 2.11 shows the fatigue data obtained on samples that were exposed to sodium for 1512 hr at 600°C prior to fatigue testing in sodium and on "as-received" specimens tested in sodium. The carbon concentrations in sodium during the 1512-hr exposure and during the fatigue test were maintained at ∿0.4 ppm. The long-term exposure was sufficient to produce a carbon gradient in the steel that varied from ∿0.3 wt% carbon at the surface to the bulk concentration of ∿0.06 wt% at

Fig. 2.10. Photomicrograph Showing Surface Crack Typical of Those Observed after Fatigue Testing Annealed Type 316 Stainless Steel Specimens in 600°C Sodium Environment ($\Delta\varepsilon_t$ = 1.11%). Mag. 400X. Neg. No. MSD-61413.

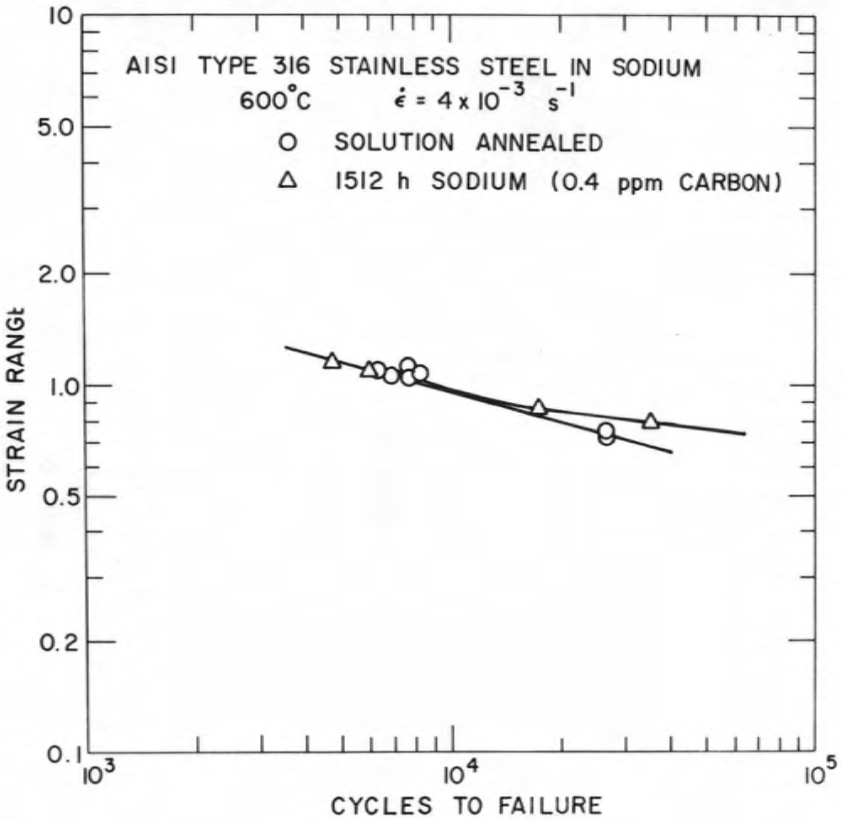

Fig. 2.11. Fatigue Data Obtained in Sodium on Annealed Type 316 Stainless Steel and Material Exposed to Sodium for 1512 hr at 600°C before Testing. Neg. No. MSD-61295.

a depth of 0.01 cm. The sodium-exposed specimens tend to have a longer fatigue life at strain ranges below ∿1%. Two phenomena, vis., the surface carburization and aging during exposure, may contribute to the difference in fatigue life. Since carburization is limited to the surface regions, it will probably have a greater effect on crack initiation than on crack propagation. Also, since crack initiation is more important at low strain ranges, the effect of the carbon gradient should be more pronounced at the lower strain ranges. One could conclude, therefore, that carburization of Type 316 stainless steel to moderate levels (<0.5 wt% carbon at the surface) tends to inhibit crack initiation. This conclusion is also supported by metallographic examination of the specimen, which indicates a lower density of surface cracks in the sodium-exposed specimens relative to the "as-received" specimens. At the higher strain ranges, the effect of sodium exposure on the fatigue life of Type 316 stainless steel becomes less pronounced. Since more surface cracks are observed in all cases at the higher strain ranges, crack initiation is less important. The effect of sodium exposure on the interior portion of the sample is primarily that of aging; however, Cheng et al.[9] have shown that aging of Type 316 stainless steel has little effect on fatigue life at 565 and 650°C.

The cyclic stress-strain response is shown in Fig. 2.12 for "as-received" specimens tested in both air and sodium and for the sodium-exposed specimens tested in sodium. The cyclic stress associated with the preexposed specimens is substantially lower than that for the "as-received" material tested in either air or sodium. When expressed in terms of the cyclic stress-strain parameters given by

$$\frac{\Delta\sigma}{2} = K\left(\frac{\Delta\varepsilon_p}{2}\right)^n , \qquad (6)$$

the cyclic strength coefficient K decreases, and the cyclic strain-hardening exponent n increases for the sodium-exposed material. The values for the two parameters are given in Table 2.5. The results for the "as-received" material agree fairly well with data from Weeks et al.[10] for annealed Type 316 stainless steel tested in air at 565 and

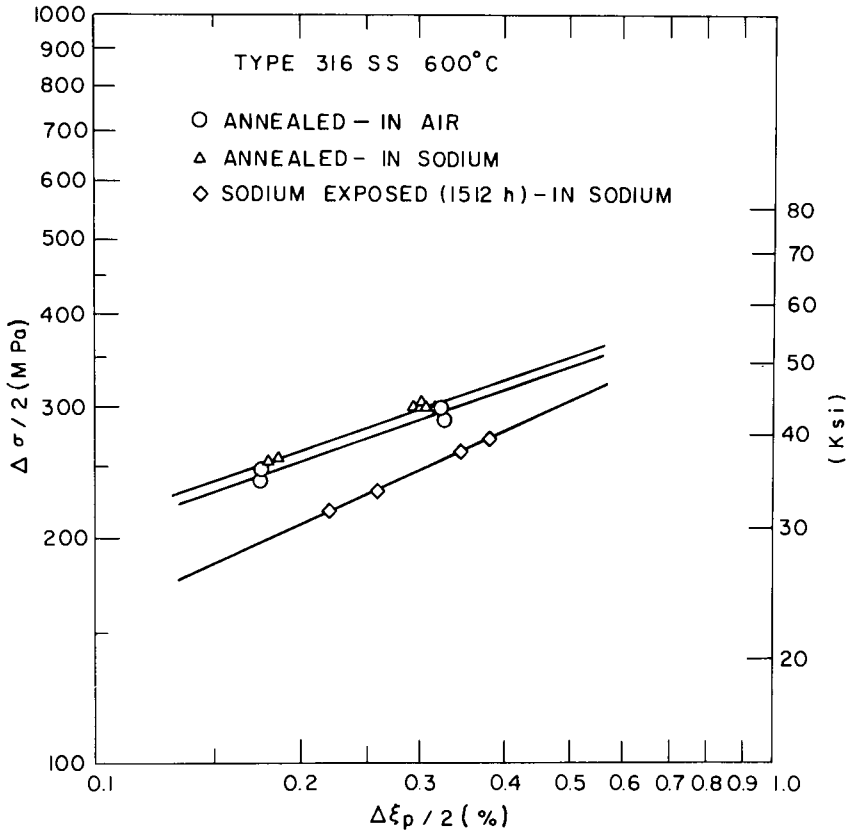

Fig. 2.12. Cyclic Stress-Strain Response for Type 316 Stainless Steel Tested in Sodium and Air at 600°C. Neg. No. MSD-61294.

Table 2.5. Cyclic Stress-Strain Parameters for Type 316 Stainless Steel at 600°C

Condition	K, MPa	n
As-received, Air	420	0.31
As-received, Sodium	430	0.31
Sodium-exposed, Sodium	410	0.41

650°C. No significant effect of aging (1000 hr at 565°C) was indicated by the data reported for the 565°C tests. (No data were reported for aged specimens at 650°C.) Based on this information, the increase in the cyclic strain-hardening exponent is attributed primarily to the surface carburization of the sodium-exposed specimens.

2.4 REFERENCES

1. "A Guide for Fatigue Testing and the Statistical Analysis of Fatigue Data," ASTM STP 91-A, American Society for Testing and Materials, Philadelphia, 1963.

2. W. Weibull, "Fatigue Testing and the Analysis of Results," Chapter 9, Pergamon Press, New York, 1961.

3. Mechanical Properties Test Data for Structural Materials Quarterly Progress Report for Period Ending July 31, 1974, Oak Ridge National Laboratory, ORNL-4998, pp. 35-53.

4. Mechanical Properties Test Data for Structural Materials Quarterly Progress Report for Period Ending January 31, 1975, Oak Ridge National Laboratory, ORNL-5104, pp. 38-45.

5. K. Natesan, D. L. Smith, T. F. Kassner, and O. K. Chopra, "Influence of Sodium Environment on the Tensile Behavior of Austenitic Stainless Steels," to be presented in ASME Winter Annual Meeting, Houston, Texas, Nov. 30-Dec. 5, 1975, and to be published in the conference proceedings.

6. J. H. Holloman, "The Effect of Heat Treatment and Carbon Content on the Work Hardening Characteristics of Several Steels," Trans. ASM 32, 123-133 (1944).

7. J. H. Holloman, "Tensile Deformation," Trans. AIME 162, 268-290 (1945).

8. Mechanical Properties Test Data for Structural Materials Quarterly Progress Report for Period Ending April 30, 1975, Oak Ridge National Laboratory, ORNL-5105, pp. 61-63.

9. C. F. Cheng, C. Y. Cheng, D. R. Diercks, and R. W. Weeks, "Low-cycle Fatigue Behavior of Types 304 and 316 Stainless Steel at LMFBR Operating Temperature," in Fatigue at Elevated Temperatures, Am. Soc. Testing, ASTM STP 520, August 1973, pp. 355-364.

10. R. W. Weeks, D. R. Diercks, and C. F. Cheng, "ANL Low-cycle Fatigue Studies--Program, Results, and Analysis," Argonne National Laboratory, ANL-8009 (November 1973).

3. OAK RIDGE NATIONAL LABORATORY

W. R. Martin

3.1 INTRODUCTION

The ORNL mechanical properties effort comprises several programs. The program Mechanical Properties and Behavior for Structural Materials deals with materials of general applicability to the LMFBR program. Other programs are concerned with the mechanical properties of weldments in LMFBR components, the specific materials of interest for LMFBR steam generators, collection and correlation of mechanical data needed for design on high-temperature LMFBR systems, and materials for the primary circuit and steam generators of HTGR systems.

3.2 MECHANICAL PROPERTIES AND BEHAVIOR FOR STRUCTURAL MATERIALS — C. R. Brinkman

The objective of this program is to collect mechanical property data and material behavior for LMFBR structural and component materials. Included in the scope of this effort are the following: (1) basic tensile, creep, creep-rupture, and relaxation base-line data that are directly applicable to design criteria and methods for types 304 and 316 stainless steel reference heats and cyclic stress-strain tests performed with emphasis on loading and aging history effects, (2) variations in properties for several heats of types 304 and 316 stainless steel determined to allow establishment of minimum and average values of specific properties and the equation parameters required for design purposes. This work will include determination of property variation of samples from different mill products within a given heat of stainless steel.

3.2.1 Mechanical Property Characterization of Type 304 Stainless Steel Reference Heat — V. K. Sikka

3.2.1.1 Creep and Rupture Properties of the 2-in. (51-mm) Plate of Reference Heat

Several creep tests on 2-in. (51-mm) plate of the reference heat of type 304 stainless steel (9T2796) continued. The test times and strains

for all tests have been updated and are summarized in Table 3.1. Several tests have approached a test time of 23,000 hr. One creep test at 649°C (1200°F) and 8 ksi (55 MPa) ruptured after 20,059 hr. The tertiary creep strain for this test was 1.20%, and time to onset of third stage creep was 12,400 hr. The rupture elongation and reduction of area were 5.1 and 6.6%, respectively.

The time-to-rupture data at 649°C (1200°F) are compared with the ASME Code Case 1592 minimum curve in Fig. 3.1. Note that the present data on the reference heat of type 304 stainless steel suggest that the code case minimum might not be conservative enough. As more long-term data become available, the code case minimum value curves will be re-examined.

The creep ductility measures — reduction of area, rupture elongation, tertiary creep strain, and plasticity resource ($e = \dot{e}_m t_r$) — are plotted as functions of time to rupture in Figs. 3.2 through 3.5. Ductility data for the 5/8-in. (15.9-mm) bar of the reference heat have also been included in the figures. Figure 3.5(b) shows a plot of plasticity resource as a function of time to rupture for data obtained from Simmons and Van Echo.[1] The visual fit in Fig. 3.2 was drawn for 649°C (1200°F) to show the ductility trend: a decrease and an increase, followed by another decrease. Similar trends were observed for rupture elongation data in Fig. 3.3. Furthermore, the breaks in ductility curves observed at 649°C (1200°F) were also observed at 593°C (1100°F). Note that although rupture elongation and reduction of area had values of 5 to 6% after rupture periods of 20,000 to 30,000 hr, the tertiary creep strain and plasticity resource were as low as 1 to 2% and 0.3 to 1%, respectively, for similar creep rupture periods (Figs. 3.4 and 3.5).

Recently Booker et al.[2] used parametric techniques to calculate the average and minimum values for various ductility measures. We have compared the experimental data with the calculated[2] range between the average and minimum values in Figs. 3.4 and 3.5(a). In Fig. 3.5(b), the calculated values are shown as ranges of minimum and average values for temperature range of 593 to 704°C (1100–1300°F). Note that the predicted values[2] show an excellent agreement with the experimental

Table 3.1 Creep Tests on Type 304 Stainless Steel Reference Heat 9T2796 2-in.-thick (51-mm) Plate[a]

Test	Temperature (°C)	Temperature (°F)	Stress (ksi)	Stress (MPa)	Time in Test (hr)	Strain, % Loading	Strain, % Creep	Ratio of Creep Stress to Yield Stress[b]	Comments[c]
11595	427	800	20.0	138	17,972	2.67	0.0073	1.57	
12368	427	800	18.0	124	14,940	1.91	0.099	1.42	
12472	427	800	16.0	110	14,071	1.17	0.063	1.26	
12570	427	800	14.0	97	13,743	0.83	0.048	1.10	
15319	482	900	30.0	207	1,650	7.86	0.071	2.54	
15268	482	900	20.0	138	2,225	3.38	0.023	1.70	
11569	482	900	20.0	138	15,455	3.27	0.141	1.70	Discontinued
12375	482	900	18.0	124	12,376	2.40	0.072	1.53	Discontinued
11675	482	900	16.0	110	2,451	1.48	0.032	1.36	Discontinued
11693	482	900	14.0	97	97	0.92	0.14	1.19	Discontinued
11830	482	900	12.0	83	83	0.35	0.04	1.02	Discontinued
13152	482	900	10.0	69	11,728	0.089	0.087	0.85	
13020	482	900	10.0	69	12,608	0.085	0.029	0.85	
10489	538	1000	20.0	138	22,977	3.80	0.678	1.80	
12250	538	1000	18.0	124	15,443	2.62	0.283	1.62	
11625	538	1000	16.0	110	17,812	1.79	0.268	1.44	
10491	538	1000	14.0	97	23,000	1.16	0.266	1.26	
12444	538	1000	14.0	97	14,412	1.18	0.201	1.26	
12445	538	1000	14.0	97	4,498	1.17	0.090	1.26	Discontinued
11568	538	1000	12.0	83	18,084	0.53	0.12	1.08	
11626	538	1000	10.0	69	17,845	0.071	0.102	0.90	
11641	538	1000	8.0	55	3,170	0.040	0.027	0.72	Discontinued
10853	593	1100	18.0	124	4,547	2.84	5.94	1.65	Ruptured
10852	593	1100	16.0	110	14,647	2.29	3.55	1.47	Ruptured
13947	593	1100	16.0	110	7,785	2.13	1.424	1.47	
10554	593	1100	14.0	97	8,710	1.40	0.65	1.28	Discontinued
11596	593	1100	12.0	83	17,941	0.52	0.435	1.10	
10490	593	1100	10.0	69	22,975	0.22	0.380	0.92	
13710	593	1100	10.0	69	2,010	0.096	0.204	0.92	Discontinued
14163	593	1100	10.0	69	6,930	0.228	0.141	0.92	
11227	593	1100	8.0	55	6,103	0.041	0.080	0.73	Discontinued
12459	593	1100	5.0	34	14,155	0.024	0.109	0.46	
10855	649	1200	16.0	110	304	2.41	12.0	1.57	Ruptured
13764	649	1200	16.0	110	244.9	2.42	14.53	1.57	Ruptured
10854	649	1200	14.0	97	761	1.60	13.0	1.37	Ruptured
11563	649	1200	12.0	83	2,674	0.59	13.0	1.18	Ruptured
11226	649	1200	10.0	69	7,278	0.18	7.0	0.98	Ruptured
10851	649	1200	8.0	55	20,059	0.044	5.03	0.78	Ruptured
12255	649	1200	5.0	34	992	0.030	0.08	0.49	Discontinued
12443	649	1200	5.0	34	14,111	0.024	0.177	0.49	
12460	649	1200	3.0	21	14,128	0.020	0.221	0.29	
10856	704	1300	10.0	69	568	0.067	15.60	0.90	Ruptured
11562	704	1300	10.0	69	653	0.12	22.50	0.90	Ruptured
11222	704	1300	8.0	55	2,760	0.031	16.40	0.72	Ruptured
12254	704	1300	5.0	34	15,305	0.030	2.29	0.45	
12461	704	1300	3.0	21	14,127	0.018	0.389	0.27	
12462	704	1300	2.0	14	13,940	0.010	0.236	0.18	

[a]Annealed 0.5 hr at 1093°C before testing. All tests loaded at a strain rate of 0.004/min.

[b]Yield stresses used in this ratio were 12,700 psi (88 MPa) at 427°C (800°F), 11,800 psi (81 MPa) at 482°C (900°F), 11,100 psi (77 MPa) at 538°C (1000°F), 10,900 psi (75 MPa) at 593°C (1100°F), 10,200 psi (70 MPa) at 649°C (1200°F). 11,000 psi (77 MPa) at 704°C (1300°F).

[c]Unless otherwise noted, tests in progress.

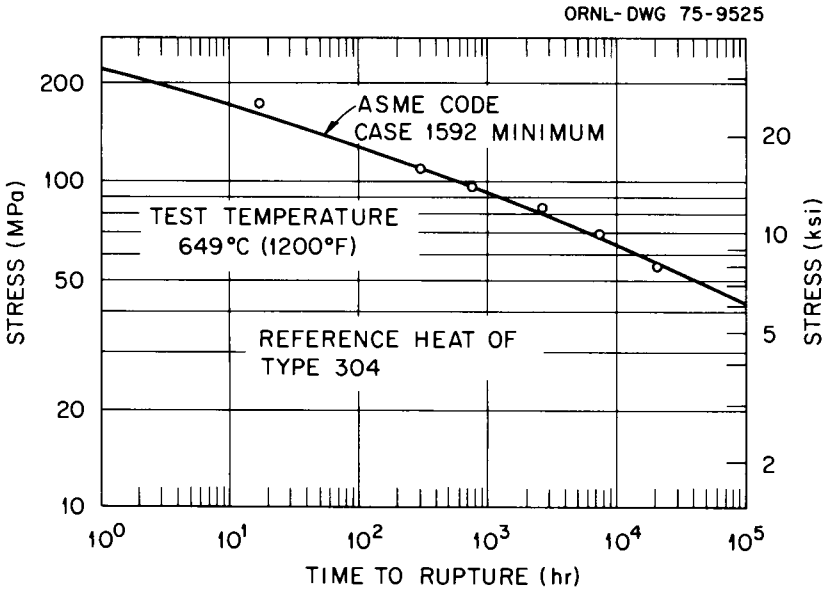

Fig. 3.1. Stress Versus Time to Rupture at 649°C (1200°F) for the Reference Heat of Type 304 Stainless Steel.

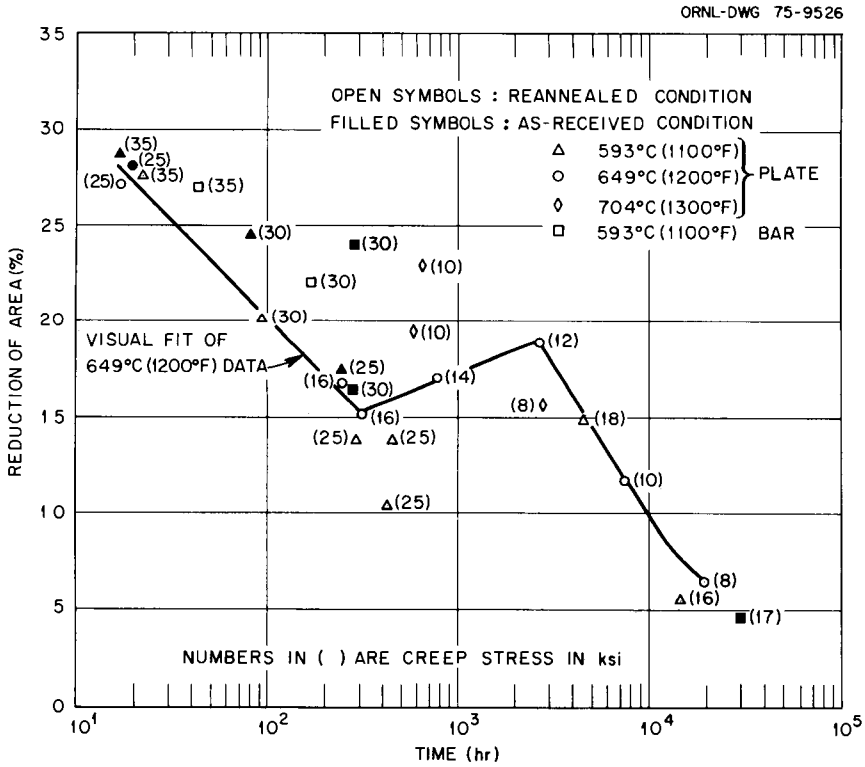

Fig. 3.2. Reduction of Area at Several Temperatures as a Function of Time to Rupture for the Reference Heat of Type 304 Stainless Steel.

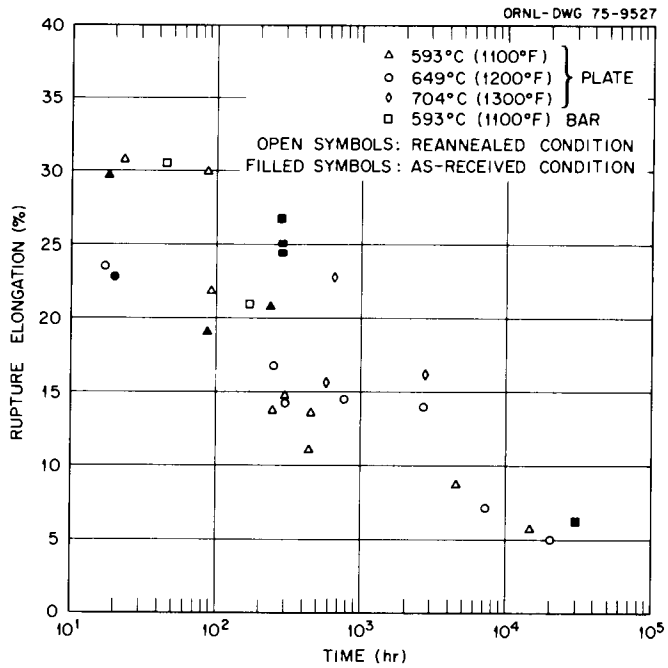

Fig. 3.3. Rupture Elongation at Several Temperatures as a Function of Time to Rupture for the Reference Heat of Type 304 Stainless Steel.

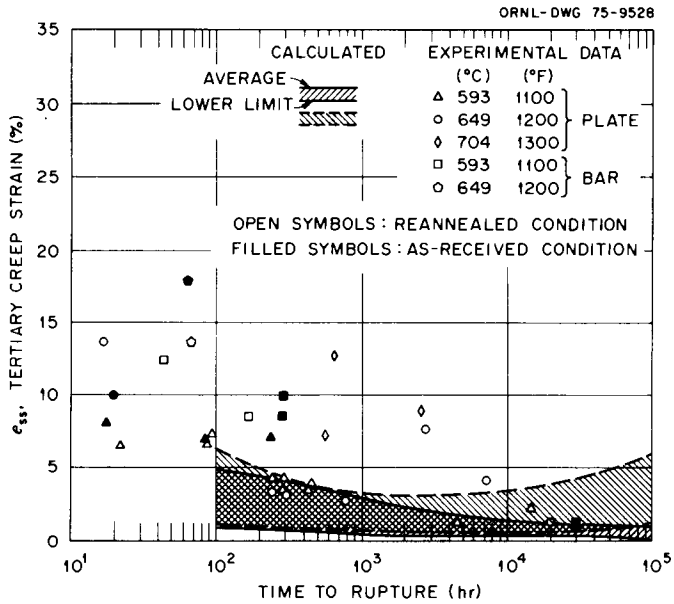

Fig. 3.4. Tertiary Creep Strain at Several Temperatures as a Function of Time to Rupture for the Reference Heat of Type 304 Stainless Steel.

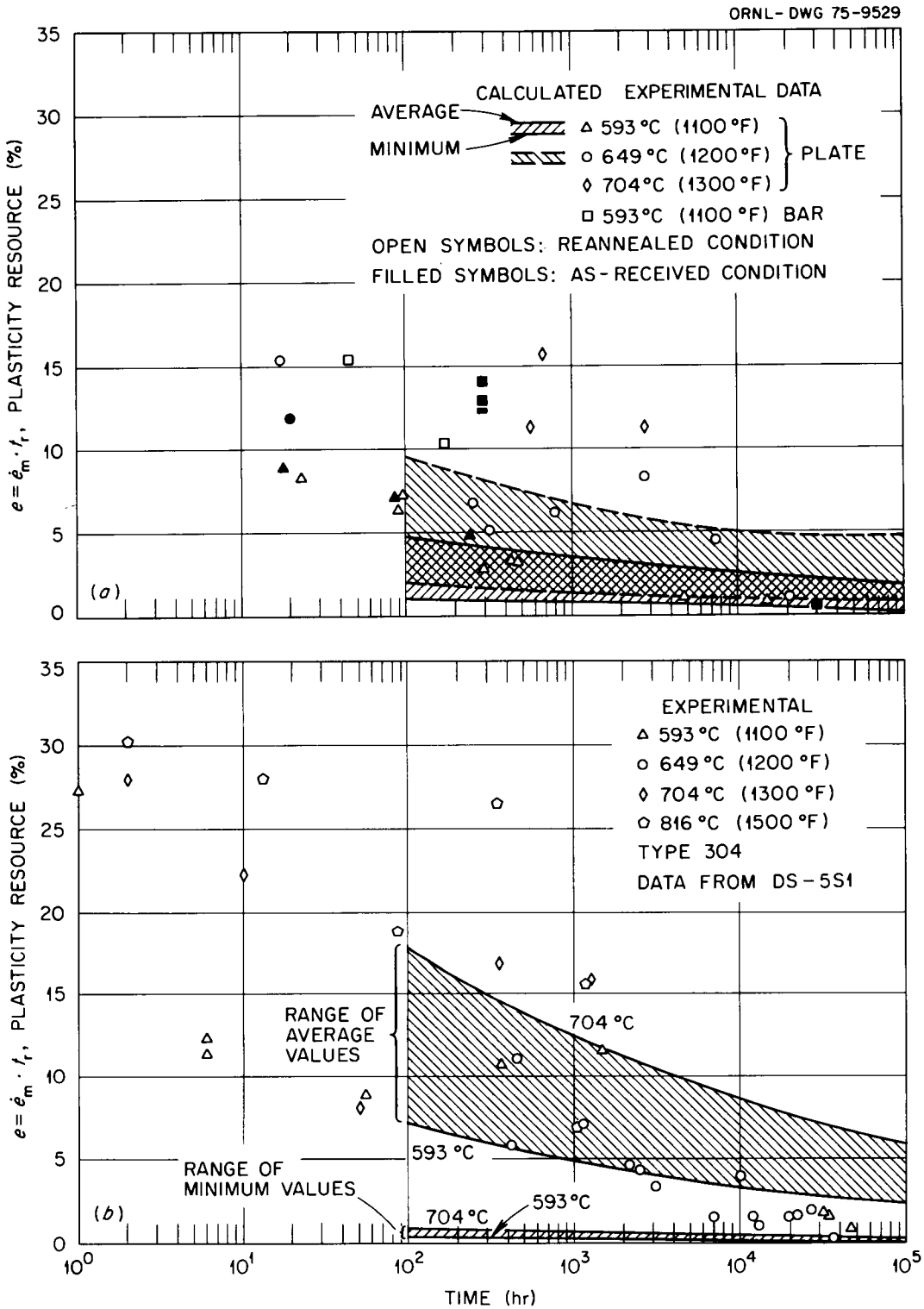

Fig. 3.5. Plasticity Resource at Several Temperatures on a Function of Time to Rupture. (a) Reference heat of type 304, ORNL data. (b) Several heats of type 304, data from DS-5S-1.

results to test periods approaching 46,000 hr. However, it should be pointed out that the long-term (>10,000 hr) experimental data are closer to the minimum ductility values than to the averages in Figs. 3.4 and 3.5.

Figure 3.6 shows stress plotted against reduction of area for the reference heat of type 304 stainless steel. Note that such a plot shows a break in the curve at a certain critical stress, S_c, which increases with decreasing test temperature. This critical stress is the stress above which the slope of the stress-strain curve changes. In Fig. 3.7, we have plotted stress versus creep-rupture elongation data[1] for type 316 stainless steel. Note that these curves show breaks similar to those observed in Fig. 3.6 for the reference heat of type 304 stainless steel.

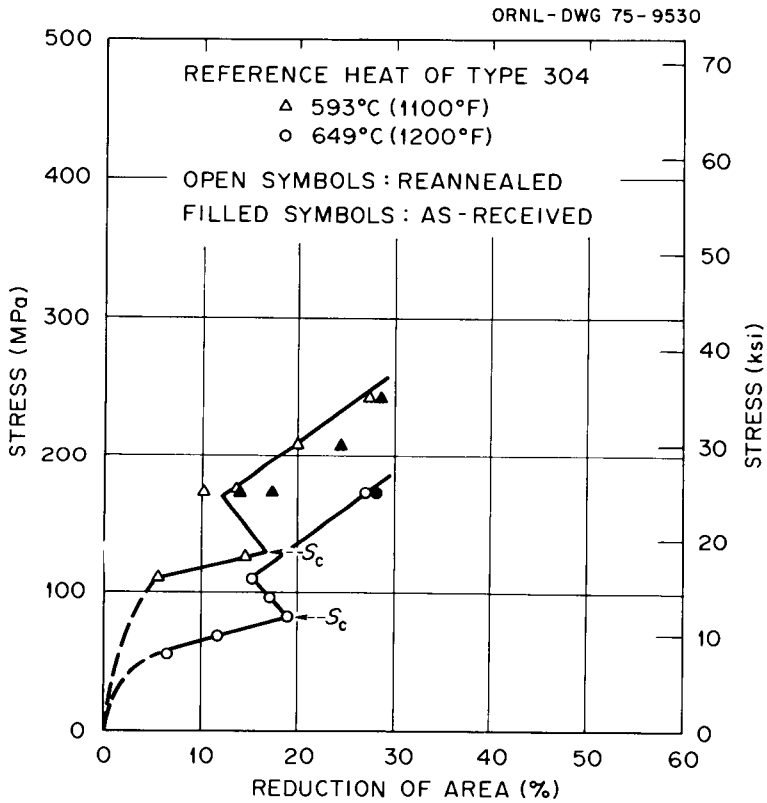

Fig. 3.6. Stress Versus Creep Reduction of Area for the Reference Heat of Type 304 Stainless Steel.

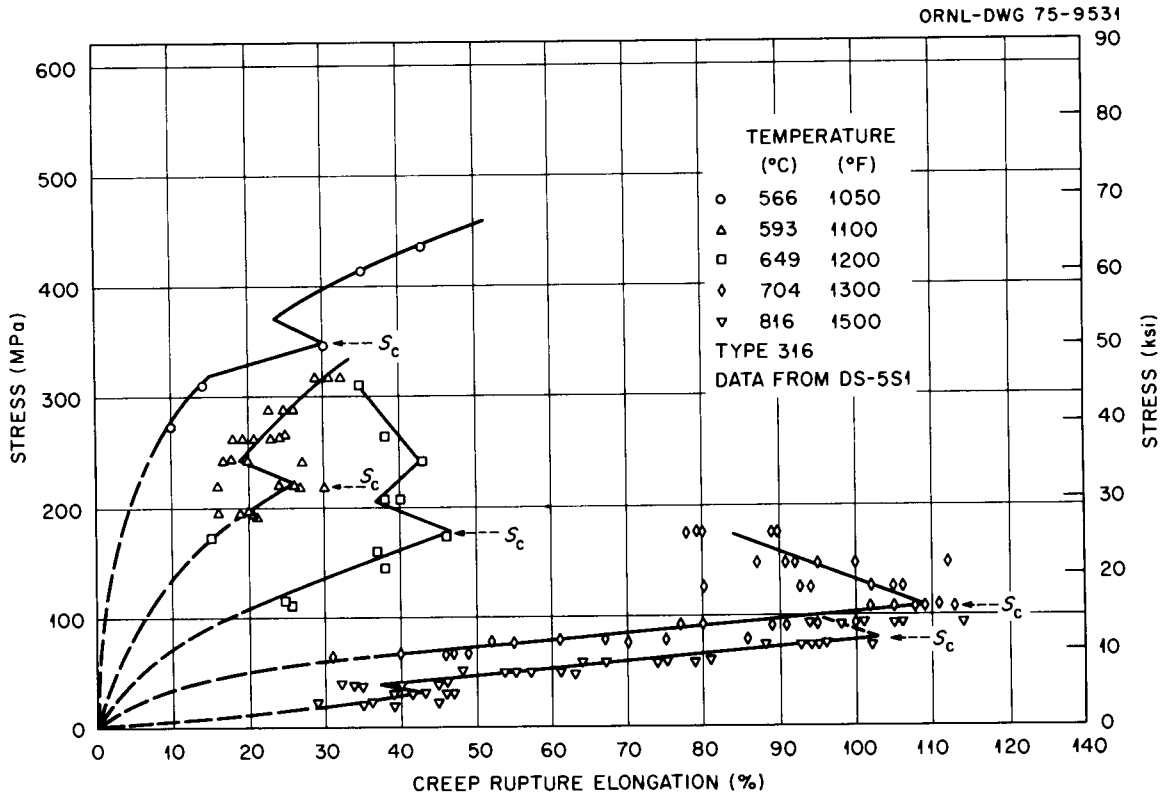

Fig. 3.7. Stress Versus Creep-Rupture Elongation for Type 316 Stainless Steel. Data were taken from Simmons and Van Echo.

The critical stress can be related to test temperature by a relationship of the form:

$$S_c = A \exp(\Delta H/RT) \ , \tag{1}$$

where

ΔH = activation energy,

A = constant related to microstructure.

The plot of S_c versus $1/T$ in Fig. 3.8 yielded an activation energy of 13.2 kcal/mole (55 kJ/mole). Such an activation energy is too low compared with the self-diffusion activation energy[3] of 75 kcal/mole (314 kJ/mole) for austenitic stainless steels.

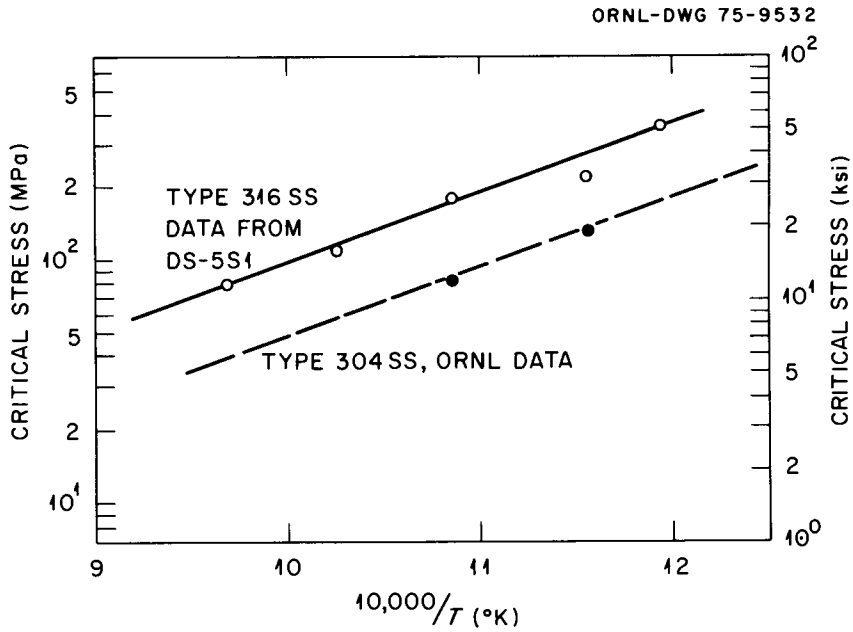

Fig. 3.8. Critical Stress as a Function of $1/T$ for Creep Data on Types 304 and 316 Stainless Steel. Critical stress is the stress at which the slope of the stress-strain (creep) plot changes.

If the critical stress corresponds to a critical grain boundary sliding rate, then Eq. (1) should be modified to take into account the stress dependence of the sliding rate. Modified Eq. (1) should take the form:

$$S_c^n = A_n \exp(\Delta H/RT) \quad . \tag{2}$$

Stevens[4] has indicated that the exponent n for grain boundary sliding is about 72% of that for the overall creep process. Austenitic stainless steels commonly show a stress exponent of about 6. Thus, n in Eq. (2) should be about 4.3, and the activation energy would then become 57 kcal/mole (238 kJ/mole). Such an activation energy is about 76% of the overall creep process and is consistent with about 72% reported[4] for grain boundary sliding of various metals. Thus, the critical stress observed in Figs. 3.6 and 3.7 could correspond to a transition from an intragranular process to one controlled by grain boundary sliding.

Garofalo[5] offered the following explanation for the break in ductility curves of type 316 stainless steel at 704 and 816°C (1300 and 1500°F) in Fig. 3.7. For stresses below the critical stress the ratio of cavity growth rate to intragranular creep rate increases as the stress is lowered and may be related to an increase in grain boundary sliding that is often observed. Thus, our explanation for breaks in stress-strain (creep) curves is in general agreement with the qualitative explanation put forth by Garofalo.[5] Metallographic examination of specimens tested at 649°C (1200°F) and different stresses are in progress. The micrographs on these specimens will be used to determine the ratio of grain boundary to intragranular deformation.

3.2.2 Mechanical Property Characterization of Type 316 Stainless Steel Reference Heat — V. K. Sikka

Various product forms of the reference heat 8092297, to be used in the product form characterization, were procured. Product forms and their dimensions are summarized in Table 3.2. The 5/8-in.-thick (15.9-mm) plate will be used for elevated-temperature mechanical property

Table 3.2 Products to be Used in Product Form Characterization of the Reference Heat of Type 316 Stainless Steel

Product Form	Dimensions	
	(in.)	(mm)
Plate	5/8	15.9
Plate	1	25.4
Plate	2	50.8
Bar	1	25.4
Bar	2	50.8
Bar	2 1/2	63.5
Pipe	0.5 × 4 1/2 OD	12.7 × 114
Pipe	0.5 × 8 5/8 OD	12.7 × 219

characterization in detail. Tensile and creep specimens were machined from this plate. Specimens from other product forms will be machined during next quarter.

3.2.2.1 Heat Treatment

The following backup work was performed to determine a suitable reannealing heat treatment. Four product forms — 5/8-in. (15.9-mm) plate, 1-in. (25.4-mm) plate, 2 1/2-in. (63.5-mm) pipe, and 8 5/8-in. (219-mm) pipe — of the reference heat were used in the program. These products were given the following reannealing treatments:

1. cold furnace + 0.5 hr at 1065°C (1950°F), followed by air cooling;
2. hot furnace at 1065°C (1950°F) + 0.5 hr at 1065°C (1950°F), followed by air cooling;
3. hot furnace at 800°C (1472°F) + 1 hr at 816°C (1500°F) + 0.5 hr at 1065°C (1950°F), followed by air cooling.

All reanneals were performed in an argon atmosphere. The air cooling rates were approximately 2000°C/hr (3600°F/hr) from 1065 to 420°C (1950 to 788°F).

Blocks of 5/8-in. (15.9-mm) plate and quadrants of 2 1/2-in. (63.5-mm) pipe were also aged 1, 10, and 100 hr at 482, 593, and 649°C (900, 1100, and 1200°F).

As-received (mill-annealed) and reannealed (laboratory-annealed) aged blocks and specimens were subjected to the following tests:

1. room-temperature hardness, Rockwell B;
2. tensile at a crosshead speed of 0.004/min;
3. optical grain size determination on specimens etched electrolytically in dilute nitric acid.

Room-temperature hardness for various reanneal and aging treatments are summarized in Tables 3.3 and 3.4. Tensile data are summarized in Table 3.5, and grain size measurements are presented in Table 3.6. The microstructure of as-received and reannealed 5/8-in. (15.9-mm) plate is shown in Figs. 3.9 and 3.10. Changes in microstructure resulting from various heat treatments of the 2 1/2-in. (63.5-mm) pipe are shown in Figs. 3.11 through 3.13. Note that the reannealing treatments produced

Table 3.3 Effect of Annealing on Room-Temperature Hardness of the Reference Heat of Type 316 Stainless Steel

Product	Hardness, R_B			
	As Received	Cold Furnace + 0.5 hr at 1065°C	Hot Furnace + 0.5 hr at 1065°C	Hot Furnace + 1 hr at 816°C +0.5 hr at 1065°C
5/8-in. (15.9-mm) plate	72.1	70.0	69.9	71.2
1-in. (25.4-mm) plate	76.6	70.7	71.7	
2 1/2-in. (63.5-mm) pipe				
wall	75.5		71.2	71.8
outer surface	81.8		59.2	64.9
inner surface	80.0		73.4	73.7
8 5/8-in. (219-mm) pipe	75.6	72.4	72.1	

Table 3.4 Effect of Aging on Hardness of the Reference Heat of Type 316 Stainless Steel

Aging Temperature		Aging Time (hr)	Room-Temperature Hardness, R_B			
			5/8-in. Plate[a]		2 1/2-in. Pipe	
(°C)	(°F)		Edge	Interior	Wall	Outer Surface
482	900	0	82.7	72.9	76.4	92.0
		1	83.4	73.4	78.2	89.5
		10	83.2	73.1	77.6	87.3
		100	82.6	72.8	77.7	90.1
593	1100	0	84.6	72.2	76.4	92.0
		1	82.6	72.2	78.1	83.1
		10	82.5	72.4	77.8	83.0
		100	81.5	72.1	77.3	83.1
649	1200	0	80.1	72.5	76.4	92.0
		1	80.6	72.8	75.4	87.8
		10	78.6	72.4	76.4	84.6
		100	80.1	72.5	77.3	88.0

[a]Aged specimens are compared with unaged specimens from the same block.

Table 3.5. Tensile Properties of 5/8-in. Plate[a] of Reference Heat 297 of Type 316 Stainless Steel, Tested at a Strain Rate of 0.004/min

Test Temperature		Stress, ksi (MPa)				Elongation, %			Reduction of Area (%)
		Proportional Limit	Yield		Tensile	Uniform	Total		
(°C)	(°F)		0.02%	0.2%			1 in.	2 in.	
25	77	24.4 (168)	28.7 (198)	30.6 (211)	82.8 (571)	62.0	83.9[b]	69.8	78.8
93	200	17.2 (119)	23.4 (161)	25.9 (179)	74.6 (514)	40.3	61.8[b]	49.4	76.9
204	400	15.5 (107)	19.3 (133)	20.9 (144)	71.1 (490)	36.7	51.4[b]	43.5	76.4
316	600	14.7 (101)	17.2 (119)	18.5 (126)	72.5 (500)	44.0	42.5[c]	45.9	71.78
371	700	13.9 (96)	15.4 (106)	17.0 (117)	72.4 (499)	40.8	39.9[c]	44.9	71.84
427	800	11.1 (77)	15.2 (105)	16.9 (117)	72.8 (502)	40.7	39.6[c]	44.7	69.75
482	900	11.2 (77)	14.3 (99)	15.4 (106)	70.8 (488)	45.3	57.0[b]	50.0	70.84
538	1000	11.4 (79)	13.4 (92)	15.2 (105)	67.3 (464)	39.2	56.95[b]	47.7	65.40
593	1100	12.8 (88)	14.3 (99)	16.0 (110)	59.9 (413)	41.7	50.4[c]	52.7	64.93
649	1200	13.0 (90)	14.0 (97)	15.9 (110)	44.1 (304)	25.0	42.3[c]	40.6	46.33
704[d]	1300			15.5 (107)	41.4 (285)	26.9	76.9[b]	62.9	60.96

[a]Reannealed for 0.5 hr at 1065°C (1950°F).

[b]Contains the necked region.

[c]Specimen broke off-center and therefore did not contain the neck.

[d]Strain rate for this test was 0.04/min.

Table 3.6. Summary of Grain Sizes for Reference Heat of Type 316 Stainless Steel

Product	Grain Size, ASTM (μm)							
	As Received		Cold Furnace Plus 0.5 hr at 1065°C		Hot Furnace Plus 0.5 hr at 1065°C		Hot Furnace Plus 1 hr at 816°C and 0.5 hr at 1065°C	
	Without Twins	With Twins	Without Twins	With Twins	Without Twins	With Twins	Without Twins	With Twins
5/8-in. Plate Longitudinal	5.3 (50)	6.2 (37)	3.7 (86)	5.6 (44)	3.6 (90)	5.5 (46)	4 (80)	5.3 (50)
5/8-in. Plate Transverse	5.4 (48)	6.4 (34)	4.6 (64)	6.1 (37)	50 (56)	5.8 (41)	5.5 (46)	6.2 (36)
2 1/2-in. Pipe Transverse								
Wall	6.7 (31)	7.5 (27)			5.4 (48)	6.2 (36)		
Outside	7.2 (24)	8.0 (19)			4.2 (74)	5.5 (46)	3.7 (85)	4.7 (60.5)
Inside	6.5 (33)	7.4 (24)			6.0 (38)	7.0 (27.5)	5.6 (44)	6.7 (31)
2 1/2-in. Pipe Longitudinal								
Outside							2.7 (122)	5.6 (45)
Inside							5.8 (42)	6.9 (28)
8 5/8-in. Pipe								
Outside	5.8 (42)	6.7 (31)	3.2 (100)	4.8 (60)	3 (110)	4.3 (70)		
Inside					5.4 (48)	6.7 (31)		

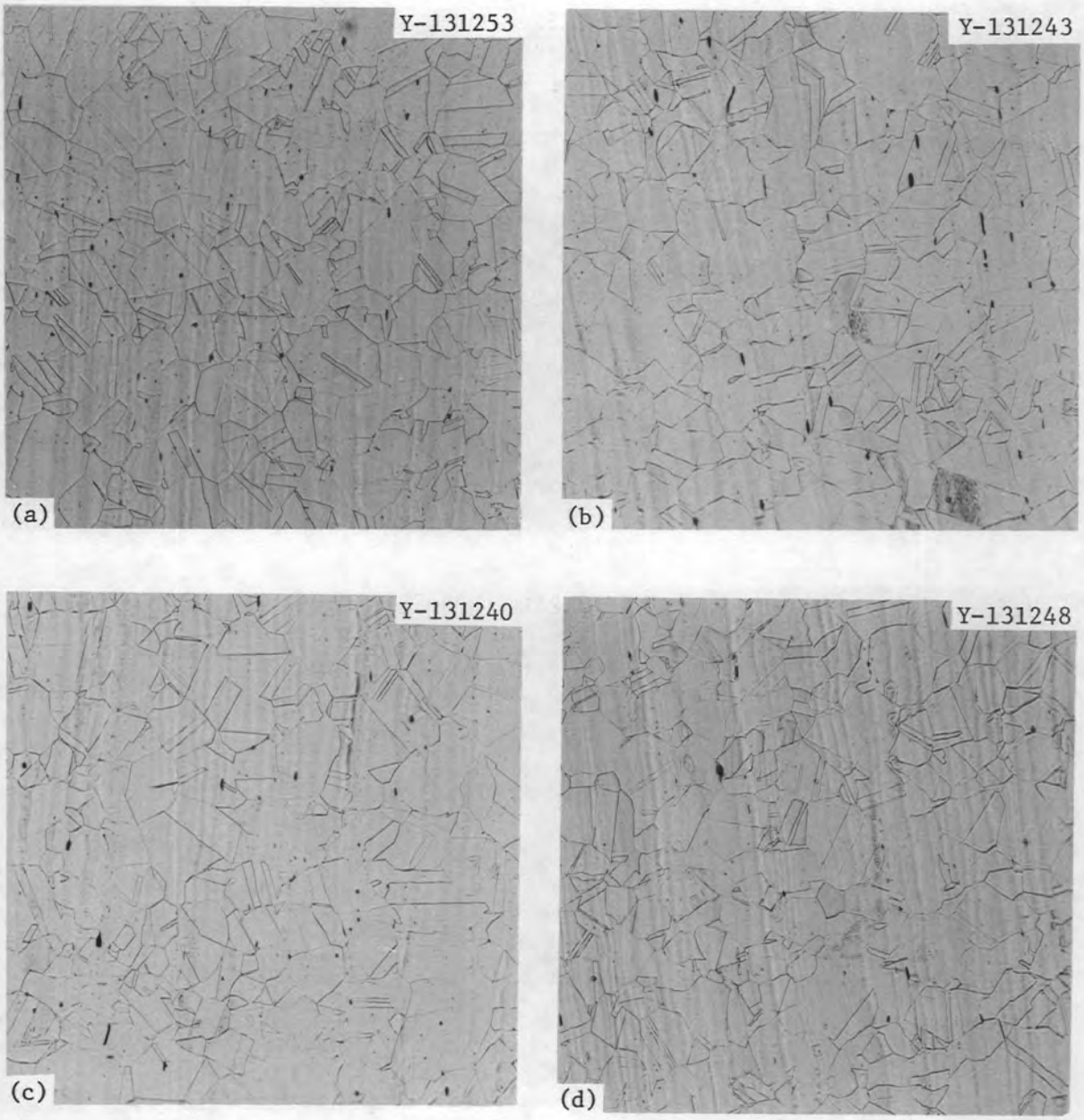

Fig. 3.9. Microstructure of As-Received and Reannealed 5/8-in. (15.9-mm) Plate of the Reference Heat of Type 316 Stainless Steel. Transverse Sections. 100×. (a) A 240. (b) A 240 + Cold Furnace + 0.5 hr at 1065°C. (c) A 240 + Hot Furnace (1065°C) + 0.5 hr at 1065°C. (d) A 240 + Hot Furnace (800°C) + 1 hr at 816°C + 0.5 hr at 1065°C.

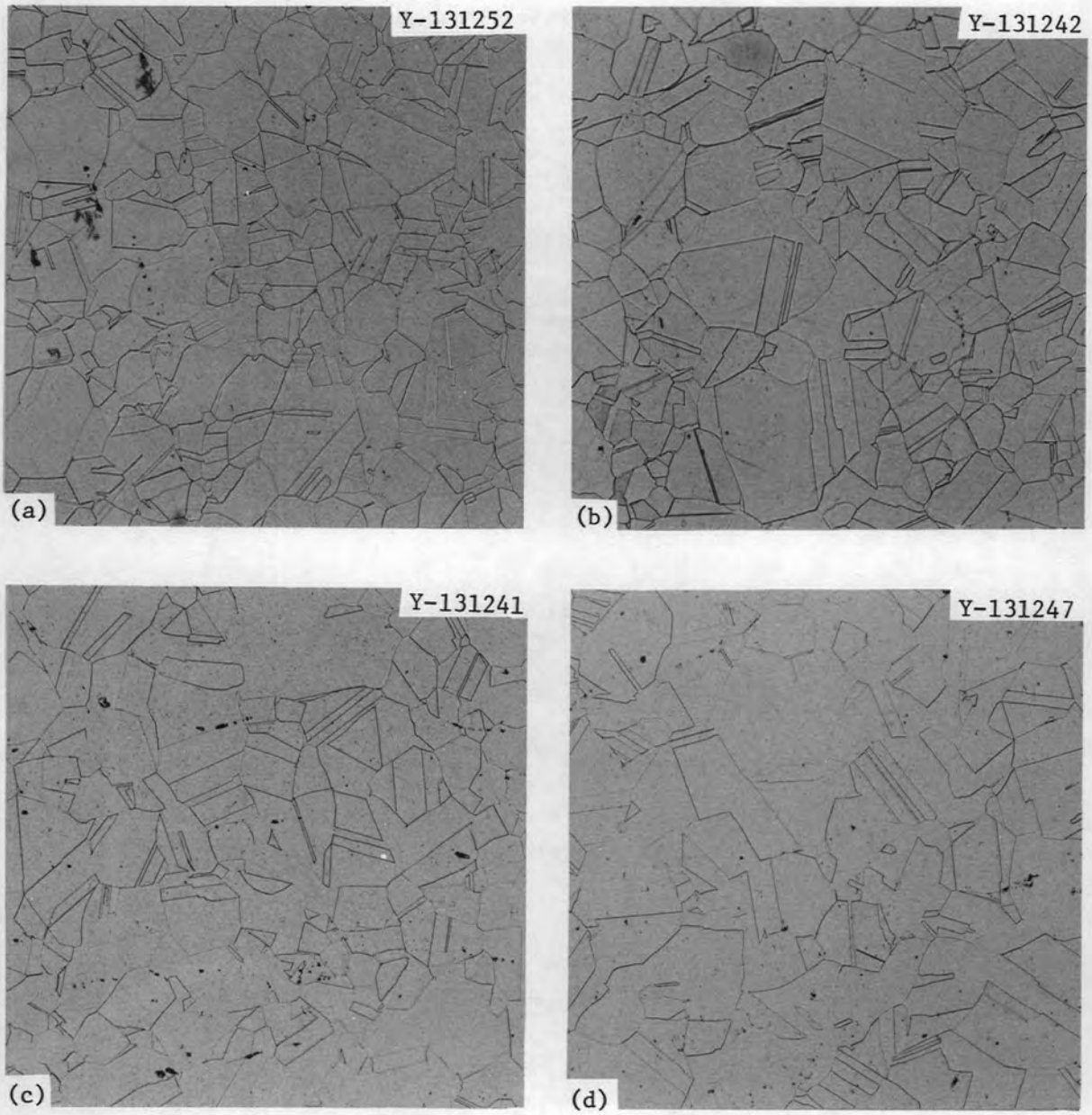

Fig. 3.10. Microstructure of As-Received and Reannealed 5/8-in-(15.9-mm) Plate of the Reference Heat of Type 316 Stainless Steel. Longitudinal Sections. 100×. (a) A 240. (b) A 240 + Cold Furnace + 0.5 hr at 1065°C. (c) A 240 + Hot Furnace (1065°C) + 0.5 hr at 1065°C. (d) A 240 + Hot Furnace (800°C) + 1 hr at 816°C + 0.5 hr at 1065°C.

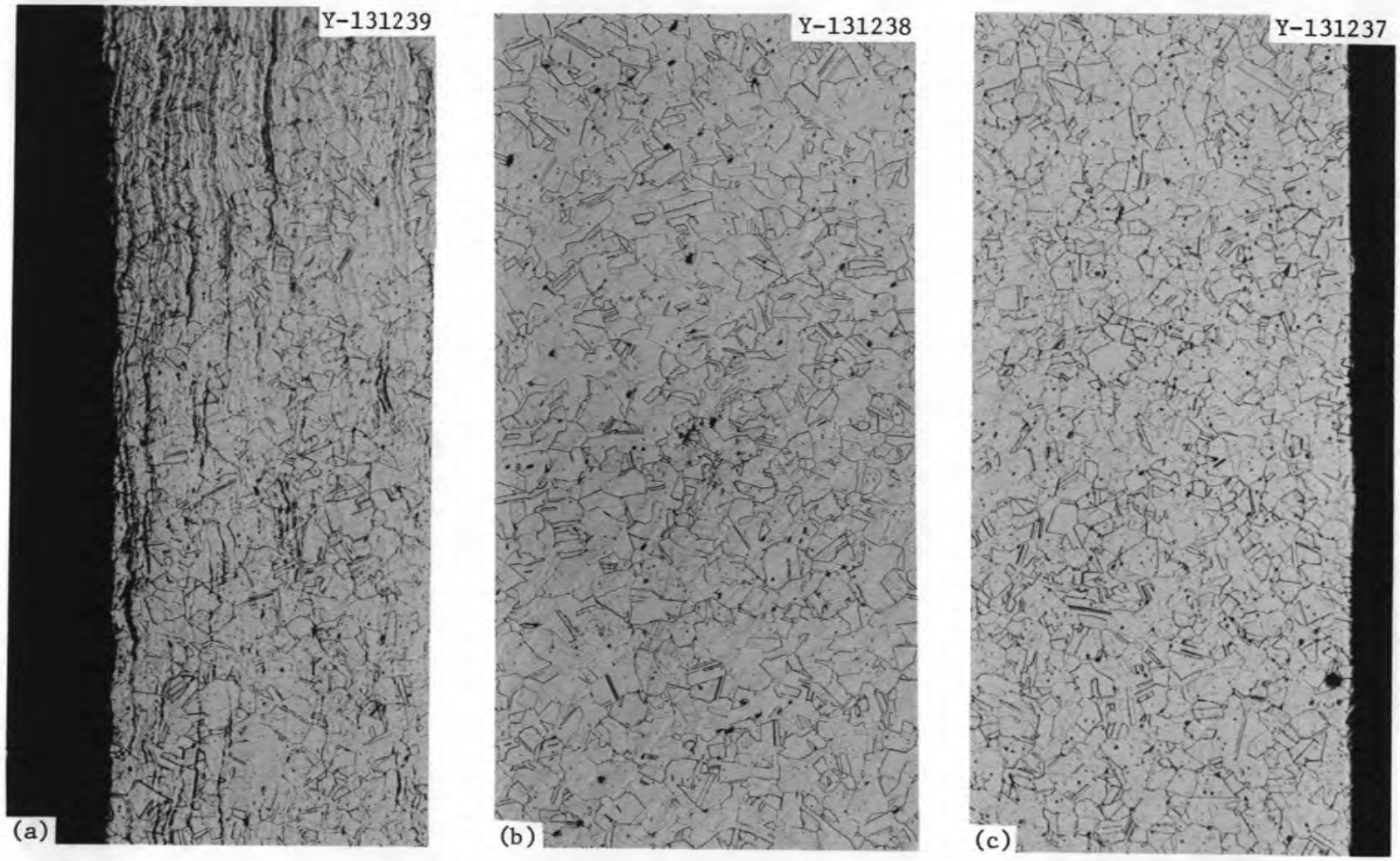

Fig. 3.11. Microstructure of As-Received 2 1/2-in. (63.5-mm) Pipe of the Reference Heat of Type 316 Stainless Steel. 100×. (a) Inside surface. (b) Midthickness. (c) Outside surface.

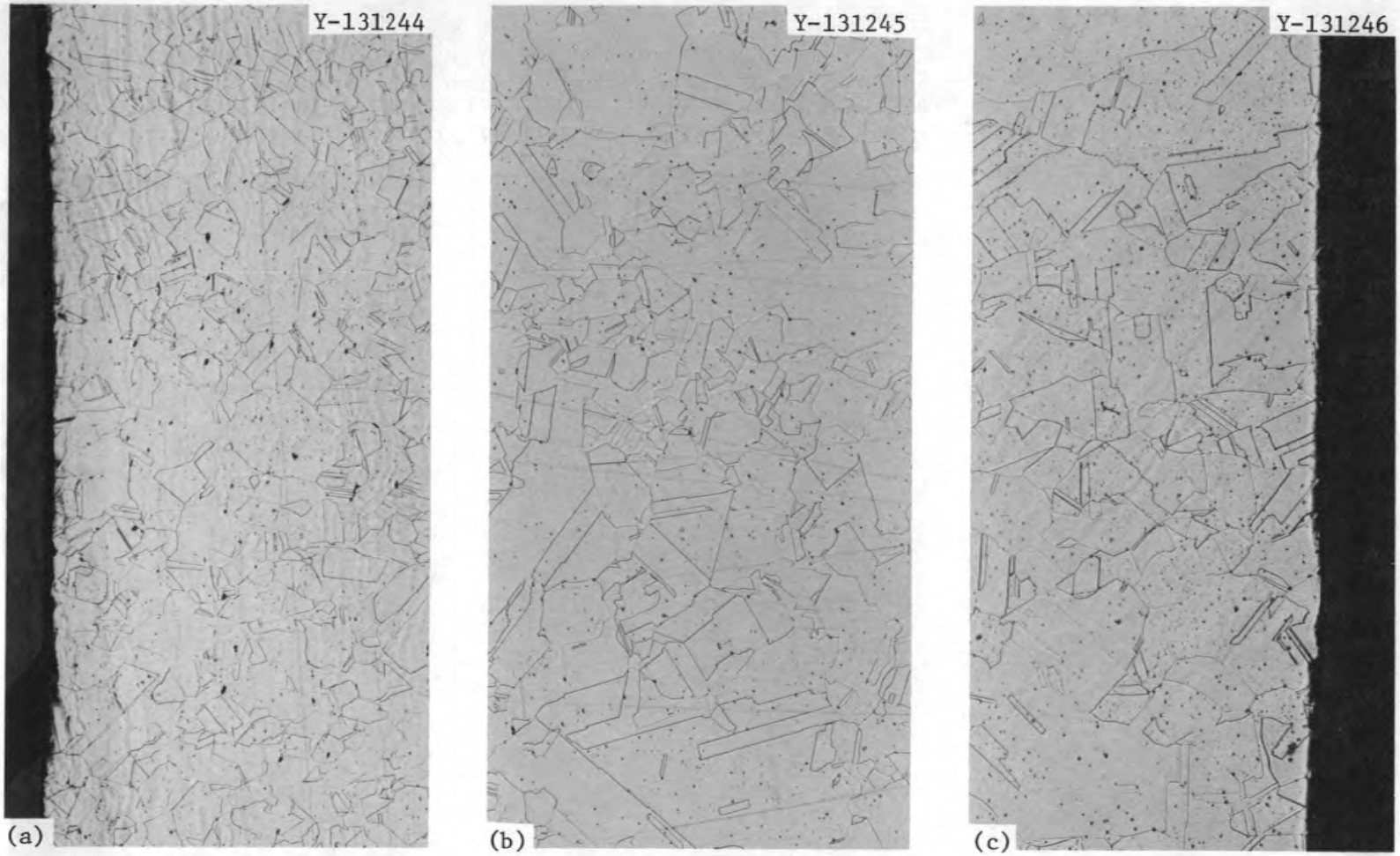

Fig. 3.12. Microstructure of Reannealed (Hot Furnace, 0.5 hr at 1065°C) 2 1/2-in. (63.5-mm) Pipe of the Reference Heat of Type 316 Stainless Steel. 100×. (a) Inside surface. (b) Mid-thickness. (c) Outside surface.

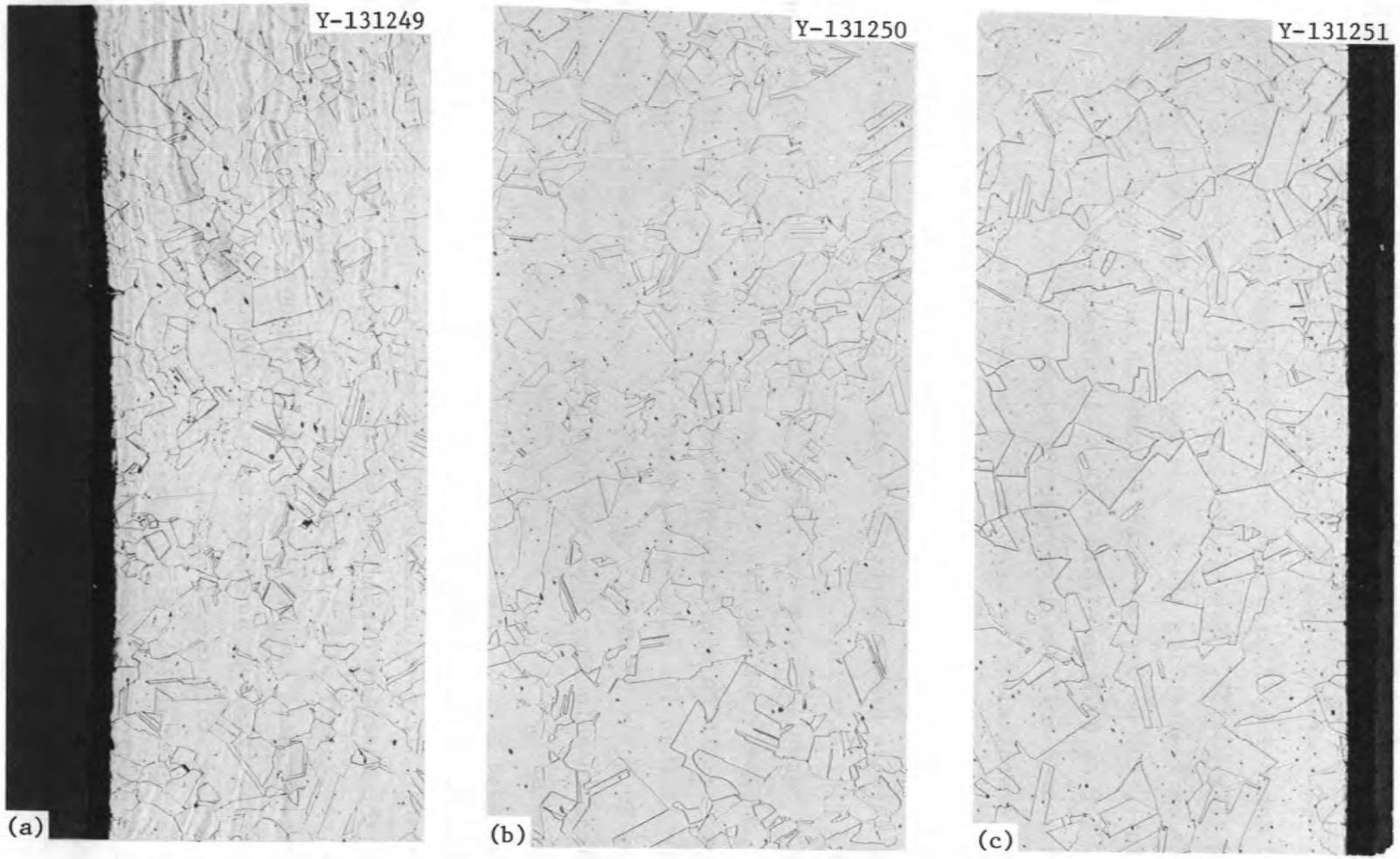

Fig. 3.13. Microstructure of Reannealed (Hot Furnace, 1 hr at 816°C + 0.5 hr at 1065°C) 2 1/2-in. (63.5-mm) Pipe of the Reference Heat of Type 316 Stainless Steel. 100×. (a) Inside surface. (b) Transition between midthickness and outside surface. (c) Outside surface.

a fairly uniform microstructure for the 5/8-in. plate, whereas the reannealed microstructure of the 2 1/2-in. pipe was nonuniform across the pipe wall. The inside surface of the pipe was highly distorted in the as-received condition (Fig. 3.11), and it developed surface cracks on reannealing (Fig. 3.13). The outside surface of the pipe showed excessive grain growth on reannealing (Figs. 3.12 and 3.13). Consistent with the microstructure, the hardness of the outside surface dropped from an average of 81.8 to 64.9 R_B (Table 3.3). All other products of the reference heat showed only small changes in hardness, and, furthermore, these changes were essentially the same for all heat treatments used. Aging treatments for periods up to 100 hr did not produce any significant changes in hardness (Table 3.4). The initial temperature (cold or hot) of the reannealing furnace head apparently little or no influence on the final hardness and microstructure.

The ASTM Material Specifications[6—8] A 240 (plate), A 312 (pipe), and A 479 (bar) suggest that the heat treatment given these products should be such as to result in specified mechanical properties. One of these requirements is that the room temperature 0.2% yield strength shall not be less than 30 ksi (207 MPa). The *Metals Handbook*[9] lists the following considerations in selecting a proper annealing temperature for austenitic stainless steels:

1. Carbides precipitate between 427 and 900°C (800—1650°F), and thus the annealing temperature should be above this range.

2. Because all carbides should be in solution before cooling begins, and because the chromium carbide dissolves slowly, the highest practical temperature consistent with limited grain growth should be selected. This temperature is in the vicinity of 1093°C (2000°F).

3. Cooling from the annealing temperature must be rapid, but not rapid enough to distort the specimen.

For type 316 stainless steel, the recommended[9] annealing temperature range is 1038 to 1121°C (1900 to 2050°F). The time at the selected annealing temperature should be 3 to 5 min per 0.10 in. (2.5 mm) of thickness.

Examination of these and other results, in light of ASTM Material Specifications[6–8] and considerations suggested in the *Metals Handbook*,[9] indicates that *an annealing treatment of 0.5 hr at 1065°C (1950°F) followed by air cooling* should be used for the reference heat of type 316 stainless steel. Since using an initial hot or cold furnace did not produce any difference in resultant room-temperature hardness and grain size, a hot furnace is preferable to cut down on the long heat-up period.

Let us examine the results of the treatment in light of ASTM Specifications and recommendations made in the *Metals Handbook*.

1. The room-temperature yield strength of the plate reannealed 0.5 hr at 1065°C (1950°F) was 30.6 ksi (211 MPa), compared with a minimum specified value of 30 ksi (207 MPa).

2. This treatment produced a uniform grain size of approximately ASTM 4 without excessive grain growth. Note in Table 3.6 that the grain size in the transverse direction is smaller (approximately ASTM 5) than in the longitudinal direction, and thus might result in some tendency toward anisotropic properties, such as yield strength. The higher annealing temperature, 1100°C (2012°F), produces a coarse grain structure, approximately ASTM 2.6.

The yield strength, S_y, of several heats of type 316 stainless steel can be related to carbon (C), nitrogen (N), and grain size intercept, D, by a relationship of the form:

$$S_y = S_0 + B(C + N)D^{-1/2} , \qquad (3)$$

where S_0 and B are constants with room-temperature values of 23.5 and 621.6, respectively. Equation (3) can be used to estimate the grain size necessary to meet the minimum yield strength of 30 ksi (207 MPa). Such a grain size for the reference heat was estimated to be ASTM 4.2 (75 μm) and is consistent with the grain size obtained by the recommended heat treatment. Any higher annealing temperature is likely to yield a coarse grain structure with resultant yield values below the specified minimum.

The 8 5/8-in. (219-mm) pipe annealed for 0.5 hr at 1065°C was subjected to the ASTM A 262-70 sensitization test, which gave negative results, indicating that the air cooling rate was sufficient to prevent any precipitation at the grain boundaries.

We can make the following conclusions concerning heat treatment:

1. The recommended heat treatment for the reference heat of type 316 stainless steel 0.5 hr at 1065°C, followed by air cooling.

2. The temperature of the furnace before reaching the annealing temperature has no influence on the final grain size or room-temperature hardness.

3. The recommended reannealing treatment gives a microstructure that meets the minimum room-temperature yield strength requirement.

4. The transverse grain size is smaller than longitudinal grain size, and this might result in anisotropic properties.

5. The outer skin of the 2 1/2-in. (63.5-mm) pipe showed more grain growth than the rest of the material, so the outer skin should be avoided in fabricating the specimens.

3.2.2.2 Tensile Data

Tensile data on 5/8-in. (15.9-mm) reannealed plate of the reference heat were completed over the range from room temperature to 649°C (1200°F) at a strain rate of 0.004/min. Similar data for the as-received condition will become available during the next quarter. Tensile data for the reannealed condition are summarized in Table 3.5 and plotted in Fig. 3.14. Minimum expected value curves for yield, ultimate tensile strength, and uniform and total elongations from *Nuclear Systems Materials Handbook*[10] have also been plotted in Fig. 3.14. Note that the yield strength of the reference heat plate is essentially coincident with the minimum expected value curve, whereas ultimate tensile strength values are above the minimum expected curve except at 649°C (1200°F). At test temperatures of 593°C (1100°F) and above, ultimate tensile strength decreases with decreasing strain rate. The minimum expected curve for ultimate tensile strength is based on data at a strain rate of 0.05/min, whereas our data are at a strain rate of 0.004/min. Thus, our tensile strength values

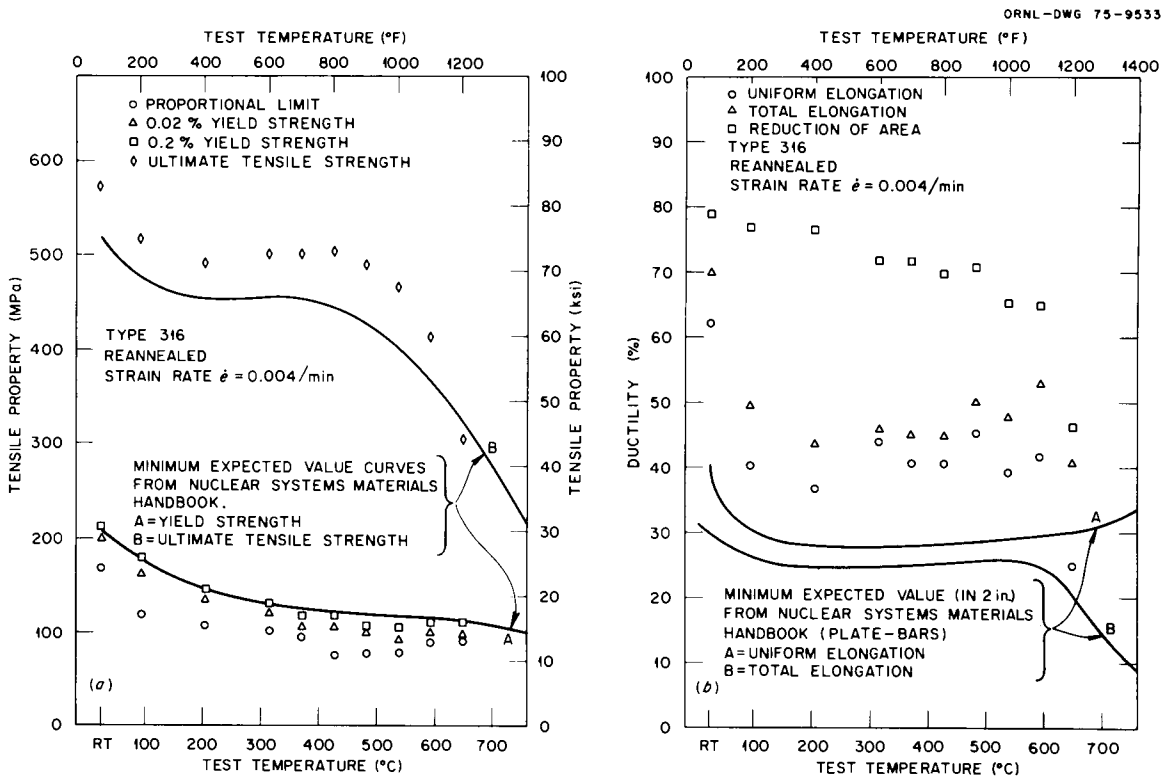

Fig. 3.14. Tensile Data as Functions of Test Temperature for 5/8-in. (15.9-mm) Reannealed Plate of the Reference Heat of Type 316 Stainless Steel at a Strain Rate of 0.004/min.

below the minimum observed at 649°C (1200°F) are apparently a consequence of our lower strain rate.

The uniform and total elongations at all temperatures were well above the minimum expected curves in Fig. 3.14. Both showed a large drop between room temperature and 212°C (400°F), remained essentially constant up to 593°C (1100°F), and dropped sharply at the higher test temperature. On the other hand, reduction of area showed almost a linear drop from room temperature to 593°C (1100°F) and dropped sharply at the higher temperature. This trend was quite similar to that observed for uniform and total elongations.

A comparison between the as-received and reannealed tensile properties should become possible during the next quarter.

3.2.2.3 Creep Properties

Creep testing of 5/8-in. (15.9-mm) plate of the reference heat of type 316 stainless steel began. Two of the creep tests have already ruptured, and the status of other tests in progress is summarized in Table 3.7.

Table 3.7. Summary of Creep Tests on Type 316 Stainless Steel Reference Heat 8092297 5/8-in.-Thick (15.9-mm) Plate[a]

Test	Temperature		Stress		Time in Test[b] (hr)	Strain (%)		Comments
	(°C)	(°F)	(ksi)	(MPa)		Loading	Creep	
15607	593	1100	30	207	117.0	3.93	1.15	
15460	649	1200	30	207	110.2	4.27	40.17	Ruptured
15538	649	1200	20	138	765.0	0.79	8.56	
15594	649	1200	18	124	325.2	0.54	2.35	
15593	760	1400	14	97	100.8	0.083	90.6	Ruptured

[a]All tests are being performed for plate in the as-received (mill-annealed) condition.

[b]Unless otherwise noted tests are in progress.

3.2.3 Heat-to-Heat Variation of Mechanical Properties of Types 304 and 316 Stainless Steel — V. K. Sikka

3.2.3.1 Relation Between Tensile and Creep Properties in the As-Received (Mill-Annealed) and Reannealed (Laboratory-Annealed) Conditions for Types 304 and 316 Stainless Steel — V. K. Sikka and T. L. Hebble*

3.2.3.1.1 Tensile Properties. Tensile Properties (0.2% yield, ultimate tensile strength, and uniform elongation) for as-received and reannealed material were related last quarter[11] by

$$P_{RA} = A + BP_{AR} , \qquad (4)$$

*Mathematics and Statistics Research Department.

where

P_{RA} = tensile property for the reannealed condition,
P_{AR} = same property for the as-received condition,
A,B = constants.

During this quarter we related total elongation and reduction of area (tensile) by Eq. (4) for plate and pipe products of 20 heats of type 304 stainless steel plate, pipe, and bar of seven heats of type 316. These relationships are shown in Figs. 3.15 through 3.17. Constants A and B for these two properties along with the properties related during the last quarter are summarized in Table 3.8. Based on room-temperature yield strength and total elongation data for two conditions, the residual cold work in terms stress and strain for various products of types 304 and 316 stainless steel can be summarized as follows:

Material and Product	Stress ksi (MPa)	Strain (%)
304 plate and pipe	3.3 (23)	3
316 plate and pipe	3.8 (26)	4
316 bar	15.0 (103)	10

Note that type 316 stainless steel bar has much more residual cold work than plate and pipe, and thus tensile properties of the bar are influenced significantly on reannealing. Equation (4) with the constants summarized in Table 3.8 may be found useful in calculating a tensile property in one condition by knowing it in the other.

3.2.3.1.2 Creep Properties. The creep properties — loading, creep, and rupture strain; reduction of area; minimum creep rate; and time to rupture — for the reannealed material were also plotted as functions of the same property for the as-received condition for test temperatures from 538 to 649°C (1000—1200°F) and stresses of 25 to 46 ksi (172—317 MPa) and are shown in Figs. 3.18 through 3.20. The strains (loading, creep, rupture, and reduction of area) were fitted to Eq. (4), whereas minimum

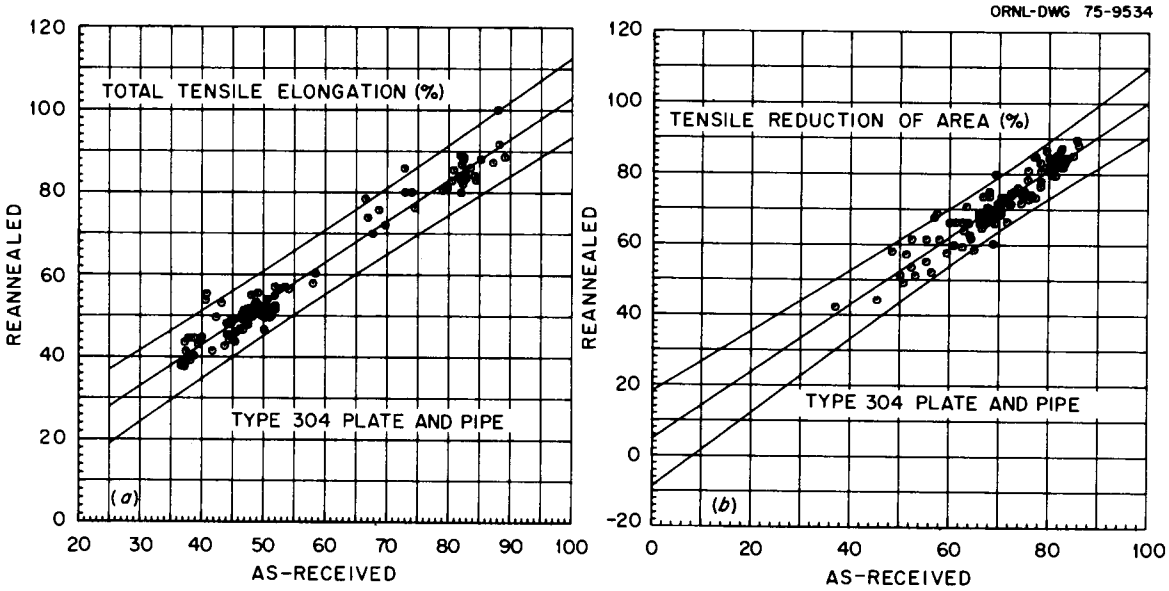

Fig. 3.15. Relation Between Tensile Properties of Plate and Pipe of 20 Heats of Type 304 Stainless Steel in the As-Received (Mill-Annealed) and Reannealed (Laboratory-Annealed) Conditions. (a) Total elongation. (b) Reduction of area.

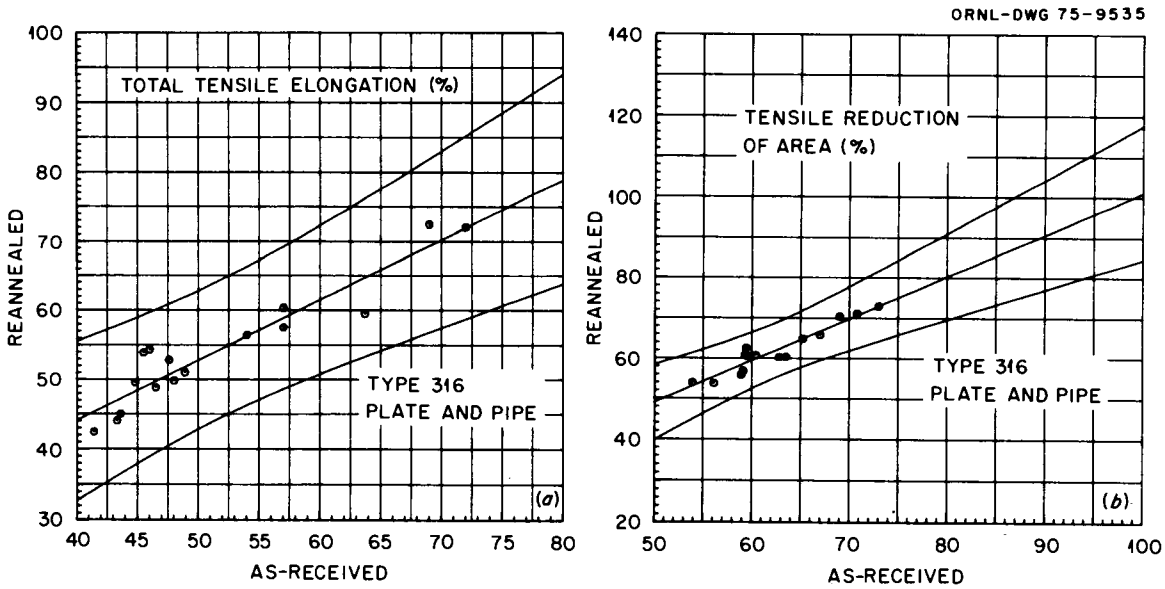

Fig. 3.16. Relation Between Tensile Properties of Plate and Pipe of Four Heats of Type 316 Stainless Steel in the As-Received (Mill-Annealed) and Reannealed (Laboratory-Annealed) Conditions. (a) Total elongation. (b) Reduction of Area.

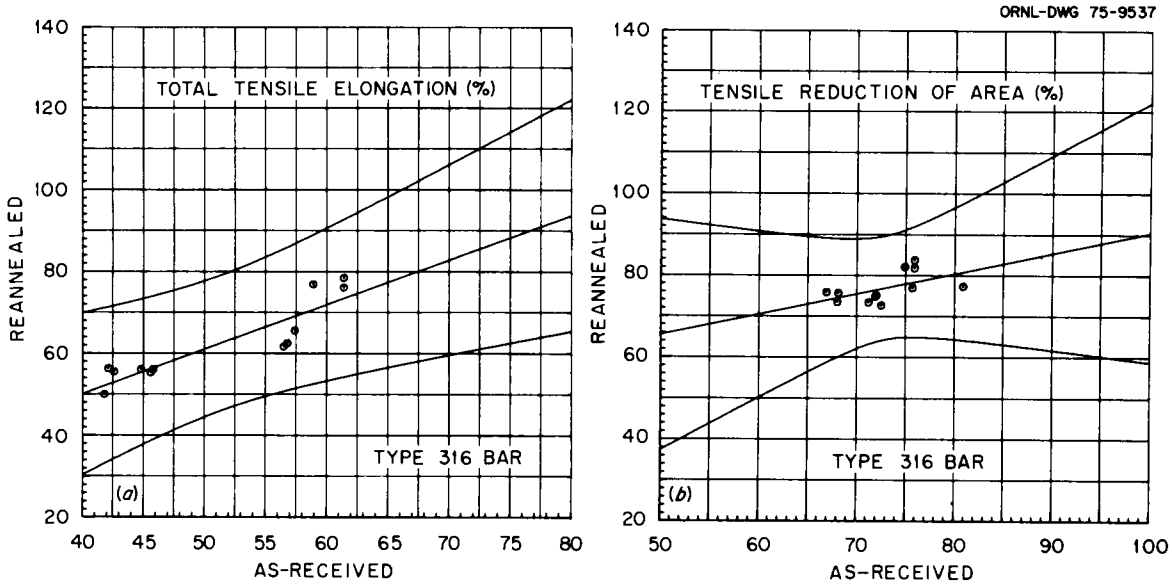

Fig. 3.17. Relation Between Tensile Properties of Three Heats of Type 316 Stainless Steel Bar in the As-Received (Mill-Annealed) and Reannealed (Laboratory-Annealed) Conditions. (a) Total elongation. (b) Reduction of area.

creep rate and time to rupture were fitted to the following equation:

$$\log_{10} P_{RA} = A + B \log_{10} P_{AR} , \tag{5}$$

where P represents the creep property, such as minimum creep rate or time to rupture.

The values of constants A and B from Eqs. (4) and (5) are summarized in Table 3.9. Note that the loading strain data on plate and pipe of type 304 stainless steel show a residual cold work equivalent to approximately 3%, in excellent agreement with results obtained from total elongation data for tensile tests. The creep strain (rupture strain excluding loading strain) and rupture strain data show that these quantities are larger in the reannealed condition for small values of strain but show a reverse effect for higher values of strain. Reduction of area showed a 1.5% greater value for the reannealed condition for the whole range of temperatures and stresses investigated. The time to rupture and minimum creep rate for various products of types 304 and 316 stainless steel can be expressed by an alternate form of Eq. (5):

Table 3.8 Summary of Constants for the Relation Between Tensile Properties in the Reannealed[a] and As-Received Conditions for Types 304 and 316 Stainless Steel

Property	Material	Constants[b] and Standard Error Limits	
		A	*B*
Yield strength	20 heats of type 304 plate and pipe		
ksi		−3.30 ± 0.44	0.922 ± 0.018
MPa		−22.8	
Ultimate tensile strength			
ksi		2.48 ± 0.45	0.950 ± 0.007
MPa		17.1	
Uniform elongation, %		1.87 ± 1.06	1.014 ± 0.021
Total elongation, %		2.92 ± 1.3	1.00 ± 0.02
Reduction of area, %		4.66 ± 2.4	0.954 ± 0.034
Yield strength	4 heats of type 316 plate and pipe		
ksi		−3.81 ± 0.74	1.062 ± 0.026
MPa		−26.3	
Ultimate tensile strength			
ksi		−1.78 ± 2.0	1.005 ± 0.027
MPa		−12.3	
Uniform elongation, %		8.55 ± 5.03	0.87 ± 0.117
Total elongation, %		9.22 ± 4.2	0.870 ± 0.081
Reduction of area, %		−3.01 ± 6.0	1.04 ± 0.10
Yield strength	3 heats of type 316 bar		
ksi		−15.26 ± 3.11	0.939 ± 0.089
MPa		−105.2	
Ultimate tensile strength			
ksi		6.38 ± 2.16	0.840 ± 0.032
MPa		44.0	
Uniform elongation, %		−1.98 ± 3.46	1.382 ± 0.093
Total elongation, %		6.45 ± 8.4	1.09 ± 0.16
Reduction of area, %		40.5 ± 18.0	0.499 ± 0.24

[a]0.5 hr at 1065°C (1950°F).

[b]$\ln P_{RA} = A + BP_{AR}$.

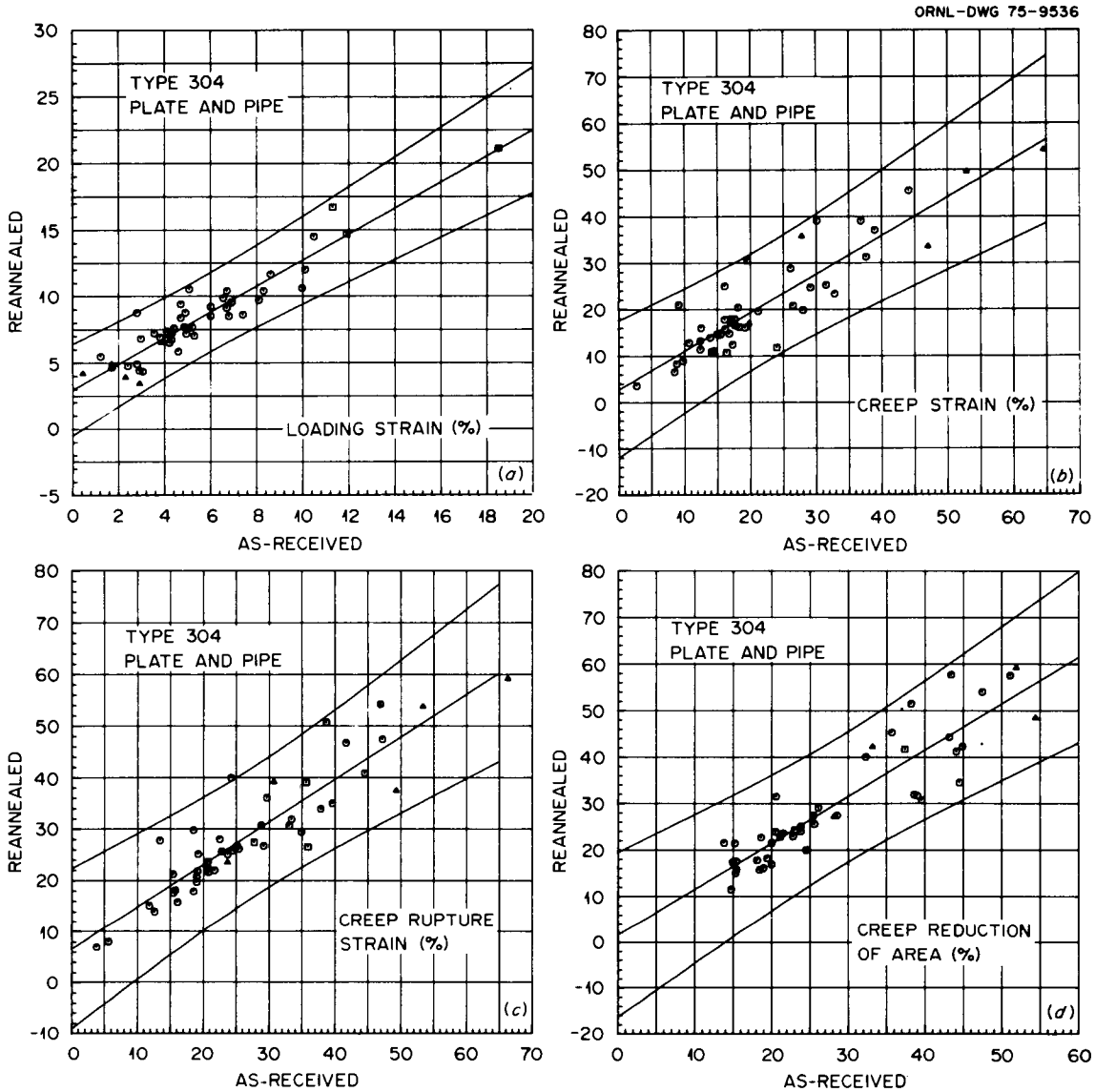

Fig. 3.18. Relation Between Creep Properties of Plate and Pipe of 20 Heats of Type 304 Stainless Steel in the As-Received (Mill-Annealed) and Reannealed (Laboratory-Annealed) Conditions. (a) Loading strain. (b) Creep strain. (c) Rupture elongation. (d) Reduction of area.

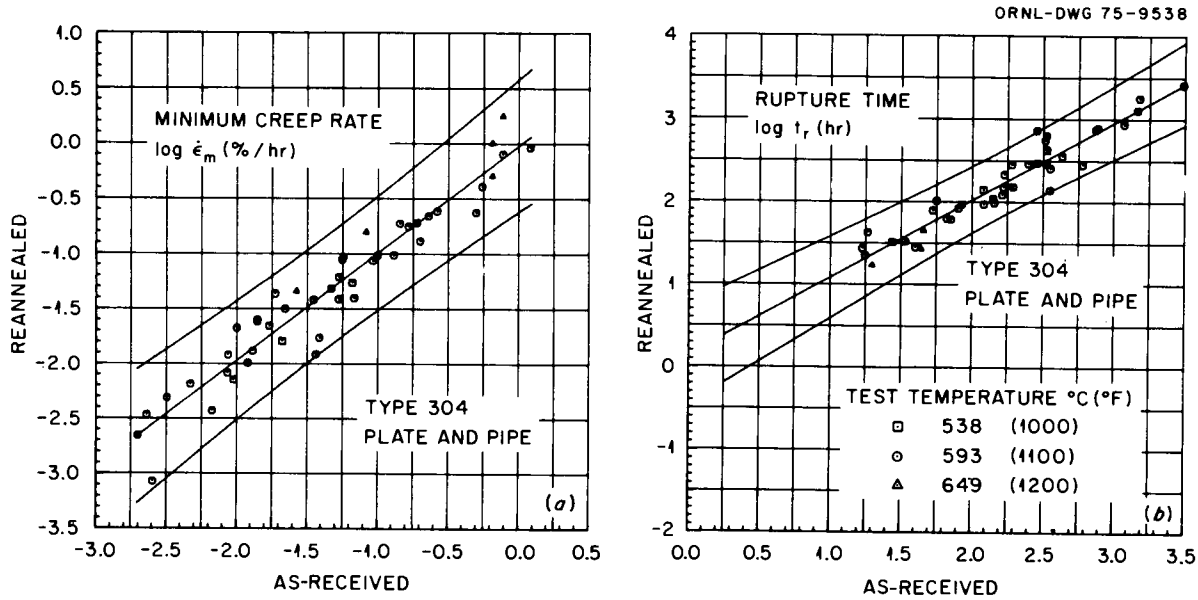

Fig. 3.19. Relation Between Creep Properties of Plate and Pipe Products of 20 Heats of Type 304 Stainless Steel in the As-Received (Mill-Annealed) and Reannealed (Laboratory-Annealed) Conditions. (a) Minimum creep rate. (b) Time to rupture.

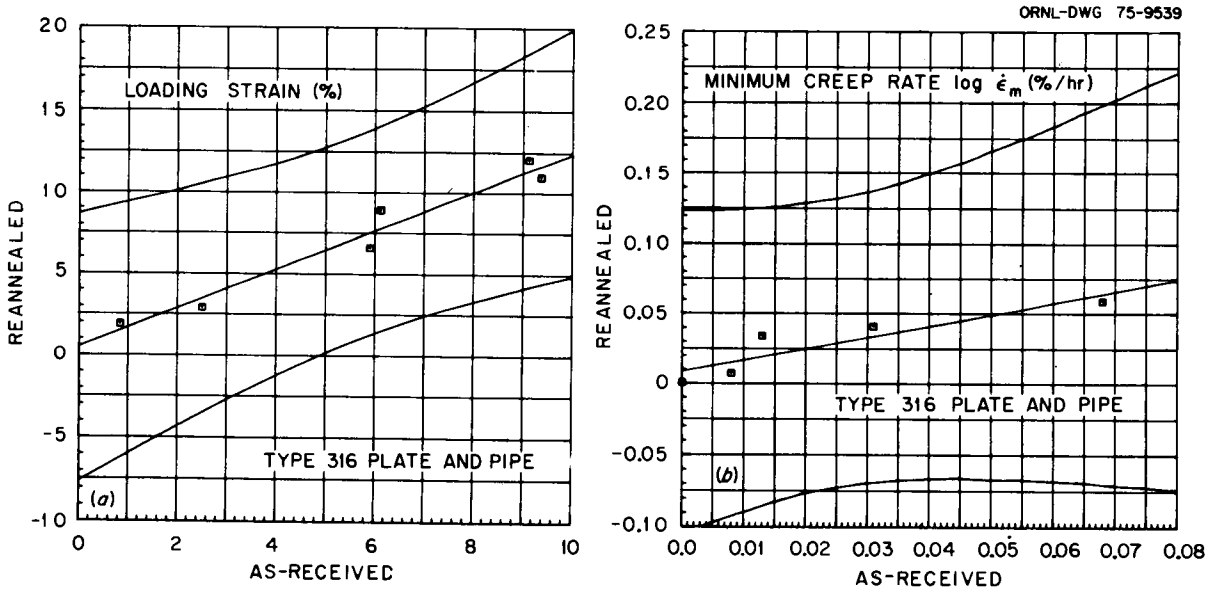

Fig. 3.20. Relation Between Creep Properties of Plate and Pipe Products of Three Heats of Type 316 Stainless Steel in the As-Received (Mill-Annealed) and Reannealed (Laboratory-Annealed) Conditions. (a) Loading strain. (b) Minimum creep rate.

Table 3.9 Summary of Constants for the Relation Between Creep Properties in the Reannealed[a] and As-Received Conditions for Types 304 and 316 Stainless Steel

Property	Material	Constants	
		A	*B*
Time to rupture,[a] hr	20 heats of type 304 plate and pipe	0.1469 ± 0.098	0.936 ± 0.043
Minimum creep rate,[b] %/hr		−0.0264 ± 0.063	0.974 ± 0.041
Loading strain, %		2.94 ± 0.34	0.978 ± 0.053
Creep strain, %		2.78 ± 1.5	0.826 ± 0.060
Rupture strain, %		6.56 ± 1.8	0.826 ± 0.060
Reduction of area, %		1.50 ± 2.2	0.999 ± 0.071
Minimum creep rate,[b] %/hr	4 heats of type 316 plate and pipe	0.00902 ± 0.0074	0.808 ± 0.022
Loading strain, %		0.495 ± 0.79	1.19 ± 0.12

[a]0.5 hr at 1065°C (1950°F).

[b]Relations for time to rupture and minimum creep rate are expressed as $\log_{10} P_{RA} = A + B \log_{10} P_{AR}$. All other quantities are expressed as the linear relation $P_{RA} = A + BP_{AR}$.

Type 304 plate and pipe $$t_r(\mathrm{RA}) = 1.40\ t_r(\mathrm{AR})^{0.936}\ , \tag{6}$$

Type 304 plate and pipe $$\dot{e}_m(\mathrm{RA}) = 0.94\ \dot{e}_m(\mathrm{AR})^{0.974}\ , \tag{7}$$

Type 316 plate and pipe $$\dot{e}_m(\mathrm{RA}) = 1.02\ \dot{e}_m(\mathrm{AR})^{0.808}\ . \tag{8}$$

Equations (6) through (8) indicate that the influence of residual cold work on time to rupture and minimum creep rate will depend on creep stress; that is, residual cold work tends to slightly increase minimum creep rate and decrease time to rupture for high stresses (rupture time 50–200 hr), but decrease minimum creep rate and increase time to rupture

for low stresses (ruptures times >200 hr). Equations (6) through (8) can be used to estimate time to rupture and minimum creep rate in one condition by knowing it the other.

In conclusion, for the test temperatures below 649°C (1200°F), where no recrystallization is expected,[12] tensile and creep properties in the reannealed (laboratory-annealed) and as-received (mill-annealed) conditions can be related by linear and logarithmic relations of the forms given in Eqs. (4) and (5). These equations with known values of constants for specified products of types 304 and 316 stainless steel can be very useful in converting data from one condition to the other.

3.2.3.2 Effect of Thermal Aging on Tensile Creep Properties of Types 304 and 316 Stainless Steels

The effects of thermal aging for periods approaching 12,000 hr on tensile and creep properties of nine heats of type 304 and four heats of type 316 stainless steel have been presented in a recent paper.[13] Some highlights of this paper are presented here.

3.2.3.2.1 Tensile Properties. Tensile properties of the reference heat of type 304 stainless steel at 593°C (1100°F) have been investigated for aging periods ranging from 1 to 10,000 hr at 593°C. Results of this investigation are summarized in Fig. 3.21. The grain boundary and matrix precipitate particle size data from the work of Etienne et al.[14] have also been included in Fig. 3.21. The yield strength remained unchanged for an aging period of approximately 1000 hr, and increased for longer periods. The ultimate tensile strength changed by only a small amount for the whole range of aging times. Ductility indices started to show a decrease after an aging time in the range of 10 to 100 hr. It can be noted from Fig. 3.21 that the yield strength started to increase after aging times necessary for matrix precipitation, whereas ductility started to drop after the nucleation of grain boundary precipitates. The influence of aging time on reduction of area is shown in Fig. 3.22 for aging periods with and without stress. Note the large decrease in reduction of area for aging under stress as compared with unstressed thermal aging.

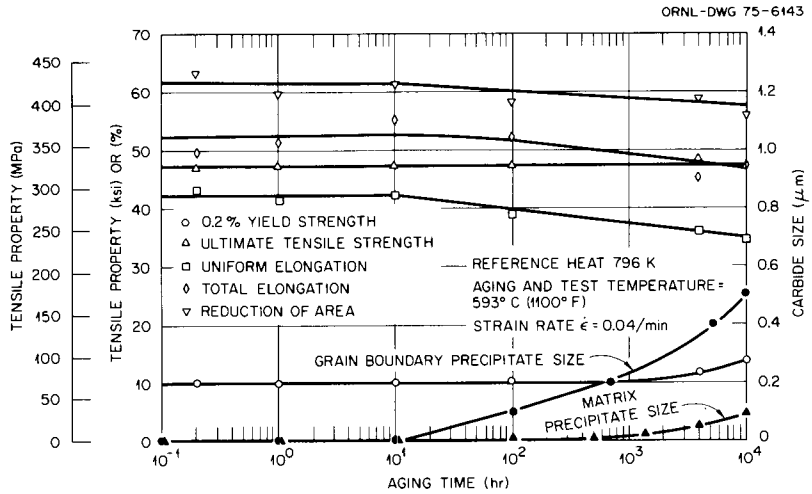

Fig. 3.21. Effect of Aging Time on Tensile Properties of Reference Heat of Type 304 Stainless Steel, Aged and Tensile Tested at 593°C (1100°F).

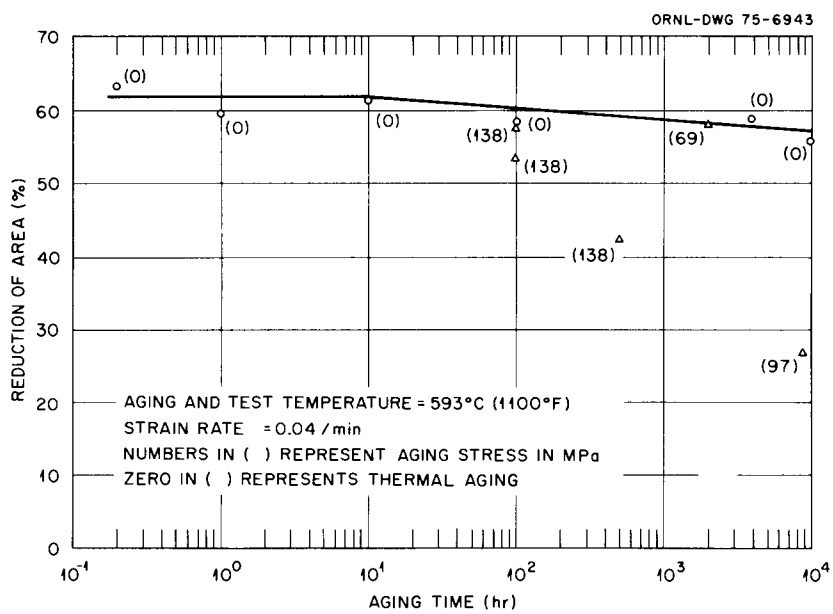

Fig. 3.22. Comparison Between Aging with and without Stress on Reduction of Area of the Reference Heat of Type 304 Stainless Steel.

The influence of aging temperature on uniform elongation at 593°C (1100°F) for an aging time of 10,000 hr is shown in Figs. 3.23 and 3.24 for types 304 and 316 stainless steel, respectively. An aging treatment of 10,000 hr at 649°C (1200°F) decreased the uniform elongation for type 304 stainless steel at 593°C (1100°F) from 31–43% to 21–27% (Fig. 3.23), and from 38–50% to 17–21% for type 316 stainless steel (Fig. 3.24). A comparison between Figs. 3.23 and 3.24 shows that the decrease in uniform elongation for type 304 stainless steel starts for aging temperatures above 482°C (900°F), whereas it starts below 482°C for type 316 stainless steel. Thus, the loss in uniform elongation is not only greater for type 316, but it even starts at a lower aging temperature. The uniform elongation of the aged types 304 and 316 stainless steel are compared with the minimum expected values[10] for types 304 and 316 stainless steel in Figs. 3.25 through 3.27. Note that the uniform elongation values, although close, are still above the minimum expected values for type 304 stainless steel, whereas they are in some cases substantially below the minimum expected values at both room temperature and 593°C (1100°F) for type 316 stainless steel.

The influence of aging temperature on total elongation at 593°C (1100°F) for a constant aging time of 10,000 hr is shown in Figs. 3.28 and 3.29 for types 304 and 316 stainless steel, respectively. Note again that the total elongation for type 316 starts dropping for an aging temperature below 482°C (900°F), whereas it happens above 482°C (900°F) for type 304 stainless steel. A comparison of total elongation and precipitate size at the grain boundaries and matrix in Fig. 3.28 shows that probably the lack of change in total elongation at 482°C (900°F) is associated with the absence of any precipitation under these conditions. In Sect. 3.2.3.2.3 we show that thermal aging at 482°C (900°F), at least to 10,000 hr, has no influence on the creep properties either. Reduction of area shows trends similar to those observed for uniform and total elongation.

3.2.3.2.2 <u>Influence of Composition on Tensile Properties of Types 304 and 316 Stainless Steel</u>. The yield strength differences observed in the

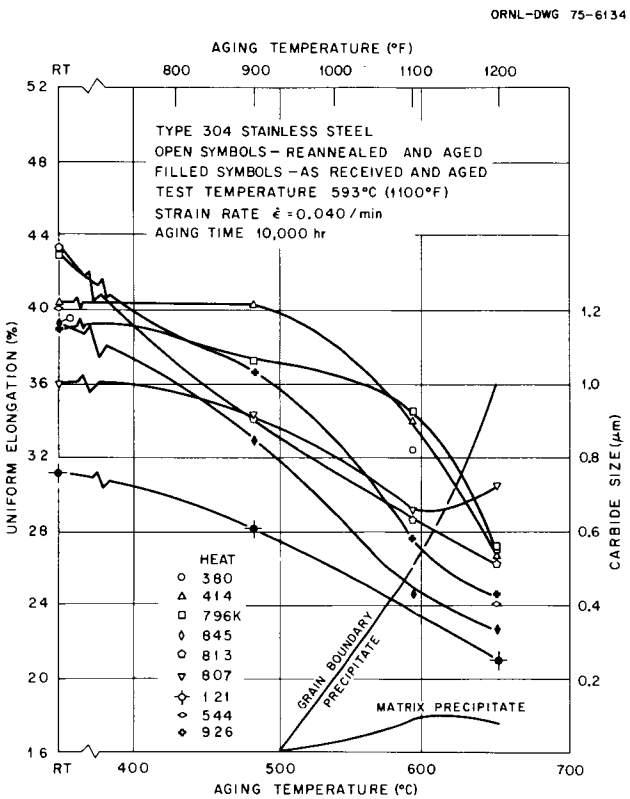

Fig. 3.23. Effect of Aging Temperature on Uniform Elongation of As-Received and Reannealed Type 304 Stainless Steel Aged for 10,000 hr and Tested at 593°C (1100°F).

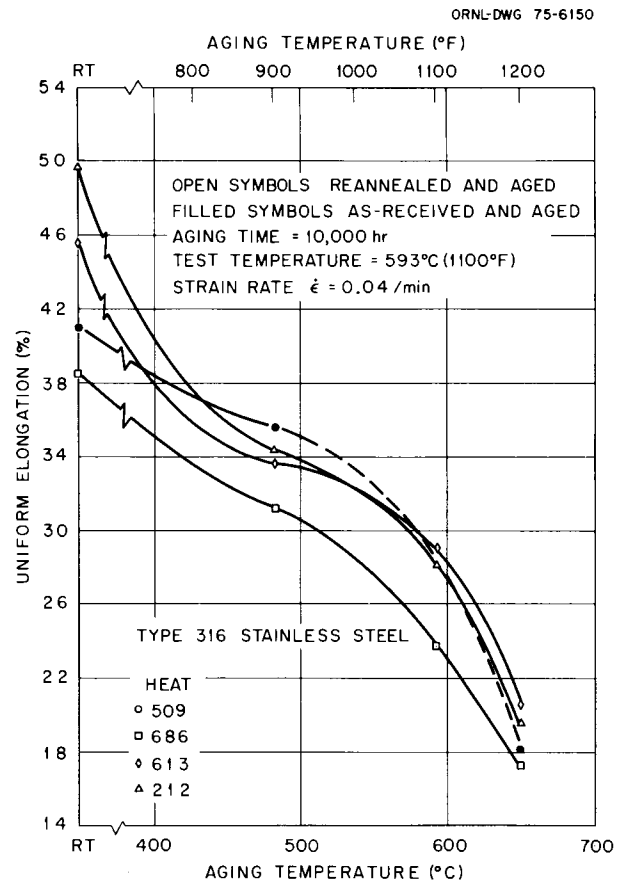

Fig. 3.24. Effect of Aging Temperature on Uniform Elongation of As-Received and Reannealed Type 316 Stainless Steel, Aged for 10,000 hr and Tested at 593°C (1100°F).

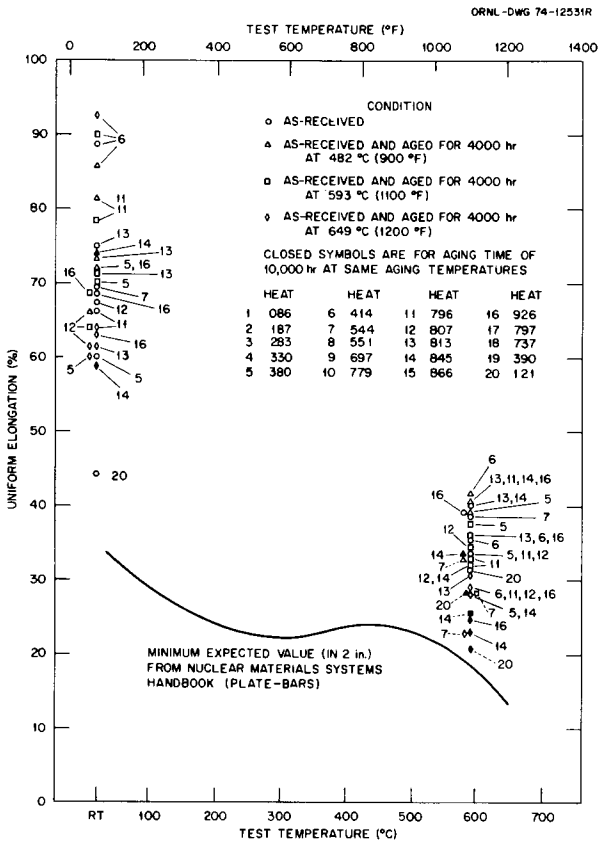

Fig. 3.25. Comparison of Uniform Elongation of As-Received Type 304 Stainless Steel for Unaged and Aged Conditions with Minimum Expected Handbook Values.

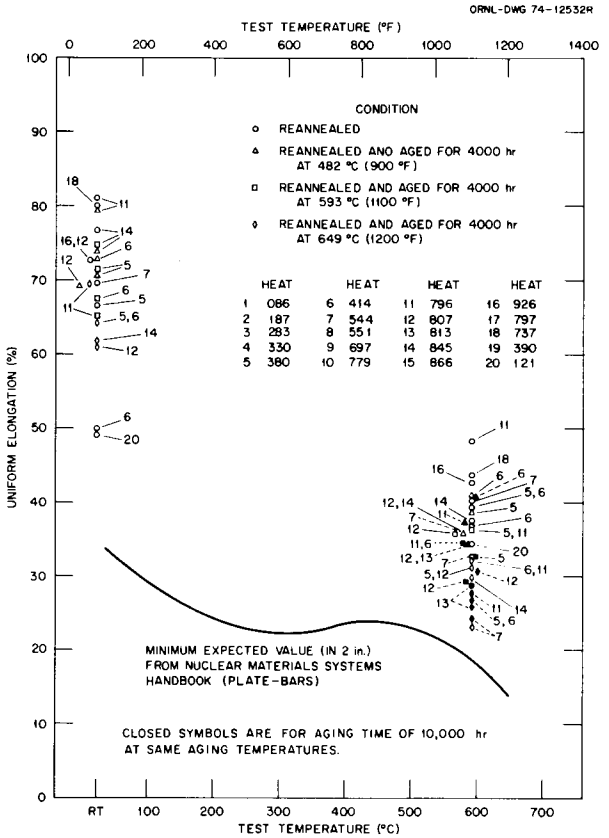

Fig. 3.26. Comparison of Uniform Elongation of Reannealed Type 304 Stainless Steel for Unaged and Aged Conditions with Minimum Expected Handbook Values.

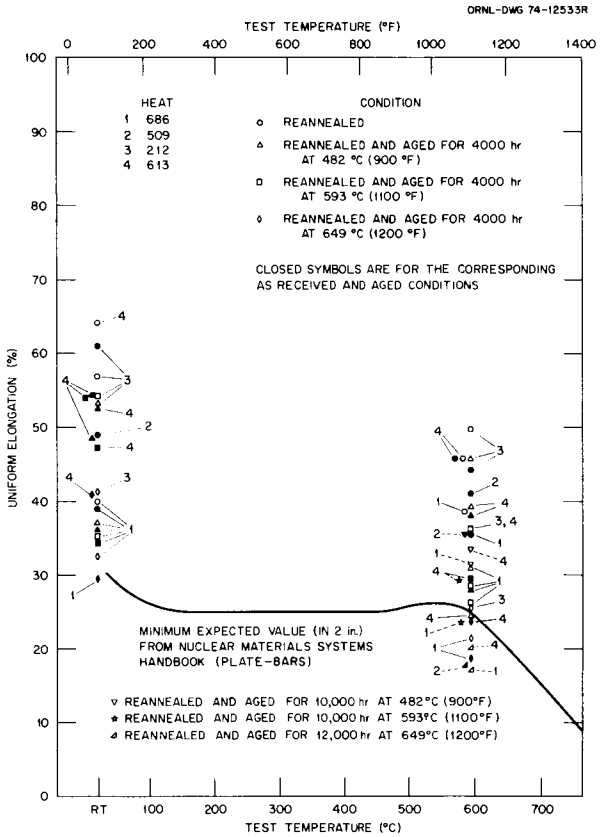

Fig. 3.27. Comparison of Uniform Elongation of As-Received and Reannealed Type 316 Stainless Steel for Unaged and Aged Conditions with Minimum Expected Handbook Values.

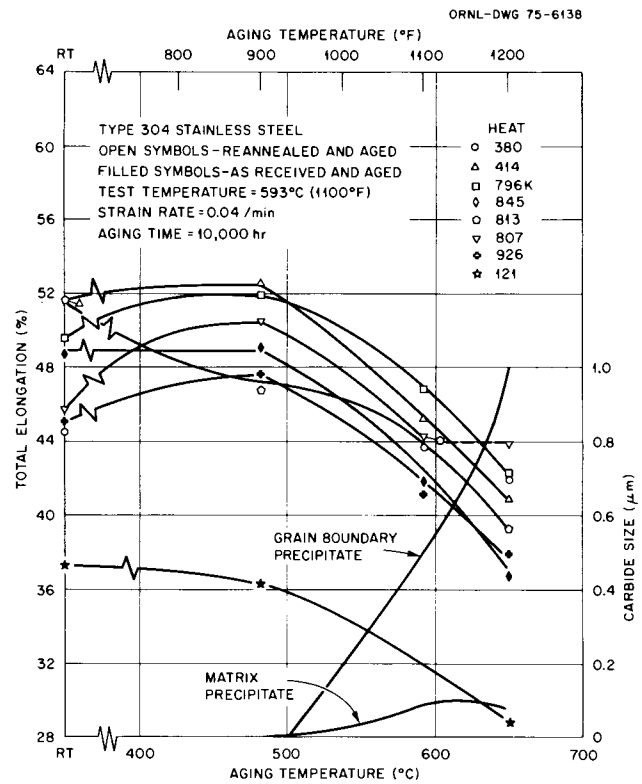

Fig. 3.28. Influence of Aging Temperature on Total Elongation of As-Received and Reannealed Type 304 Stainless Steel Aged for 10,000 hr and Tested at 593°C (1100°F).

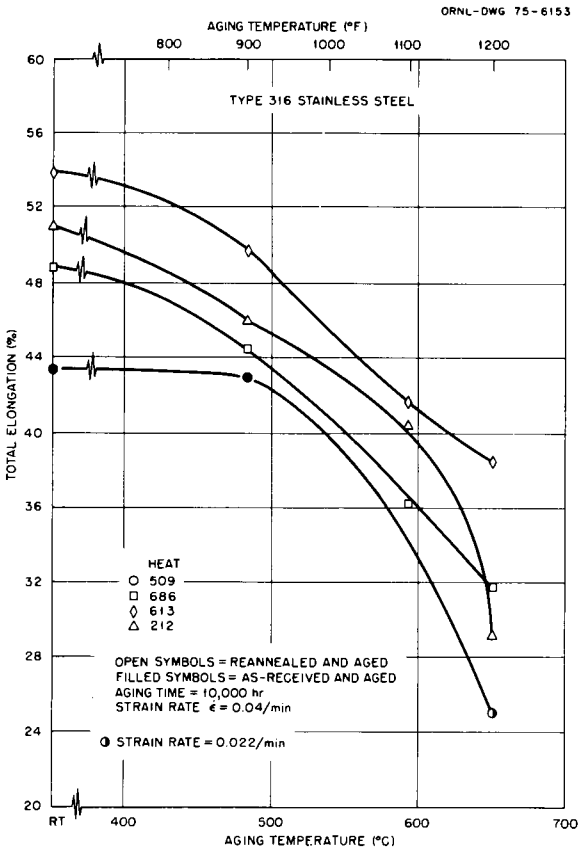

Fig. 3.29. Effect of Aging Temperature on Total Elongation of As-Received and Reannealed Type 316 Stainless Steel Aged for 10,000 hr and Tested at 593°C (1100°F).

reannealed condition of 20 heats of type 304 and seven heats of type 316 stainless steel can be related to the combination of carbon, nitrogen, and grain size variations by a relation of the form:

$$S_y = S_0 + B(C + N)D^{-1/2} , \tag{9}$$

where S_0 and B are constants, C and N are carbon and nitrogen contents in wt %, and D is the average grain intercept excluding annealing twins.

Equation (9) is quite similar to the frequently used Hall-Petch relationship:

$$\sigma_y = \sigma_0 + k_y D^{-1/2} , \tag{10}$$

where σ_0 is the fractional stress required to overcome the dislocation interaction with fine precipitates, lattice defects, and random impurity

atoms as slip proceeds within the grains, and k_y is a measure of the extent to which the dislocations are piled up at the grain boundaries. Comparison of Eqs. (9) and (10) shows that $B(C + N) = k_y$ and $S_0 = \sigma_0$. Figures 3.30 and 3.31 show the 0.2% yield strength at room temperature and 593°C (1100°F) as functions of $(C + N)D^{-1/2}$ for both the unaged and aged type 304 stainless steel. The values of S_0 and B from the least squares fits of the data for the unaged and aged materials are summarized in Table 3.10. Results from tests conducted on type 316 stainless steel are plotted in Fig. 3.32 and the constants summarized in Table 3.10.

Thermal aging, at least up to periods of 10,000 hr, did not result in any grain growth. Thus, the changes in values of B in Eq. (9) on aging should reflect the influence of intergranular precipitates. Since S_0 is a measure of frictional stress, changes in its value should reflect the influence of intragranular precipitates.

The microstructure of specimens aged for 10,000 hr at 482, 593, and 649°C (900, 1100, and 1200°F) for heat 926 of type 304 stainless steel are presented in Fig. 3.33. Note that at an aging temperature of 482°C (900°F), the precipitate has developed only at the grain boundaries. However, at 593°C (1100°F), although some precipitate is still at grain boundaries, some can be observed in the matrix. For an aging temperature for 649°C (1200°F), fine precipitate distribution is observed in the matrix and a coarser precipitate is present at the grain boundaries. Table 3.10 shows that B increases at 482°C (900°F), consistent with precipitate observed at the grain boundaries, and S_0 remains unchanged, consistent with the absence of precipitate in the matrix. For an aging temperature of 649°C (1200°F), S_0 increases by a large fraction, consistent with fine distribution of precipitate in the matrix, and B increases only by a small amount, consistent with coarser precipitates at the grain boundaries as seen in Fig. 3.33. The results at 593°C (1100°F) were in between those observed for aging temperatures of 482 and 649°C (900 and 1200°F) and are again consistent with the microstructure observed in Fig. 3.33. Results for type 316 stainless steel can also be explained by same line of argument. Note that the results presented in Table 3.10 suggest that

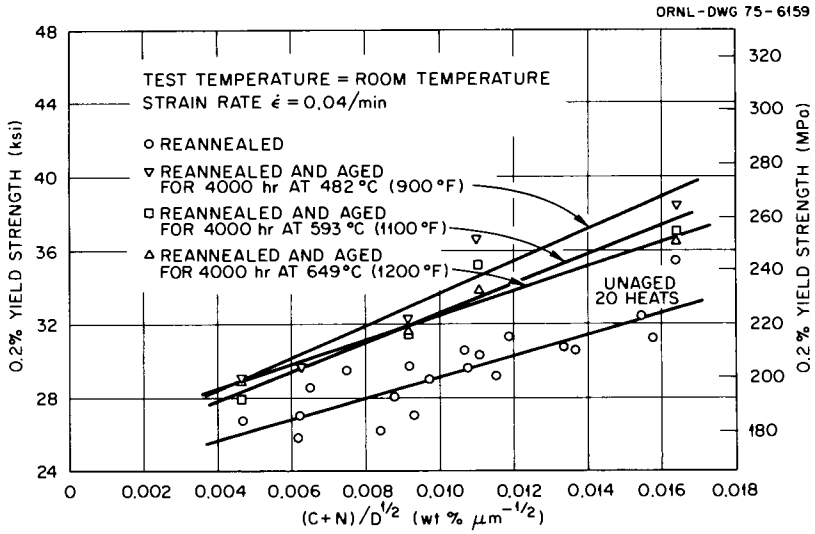

Fig. 3.30. Yield Strength (0.2%) at Room Temperature as a Function of $(C + N)D^{-1/2}$ for 20 Heats of Type 304 Stainless Steel in the Unaged Condition and for Several Heats in the Aged Condition.

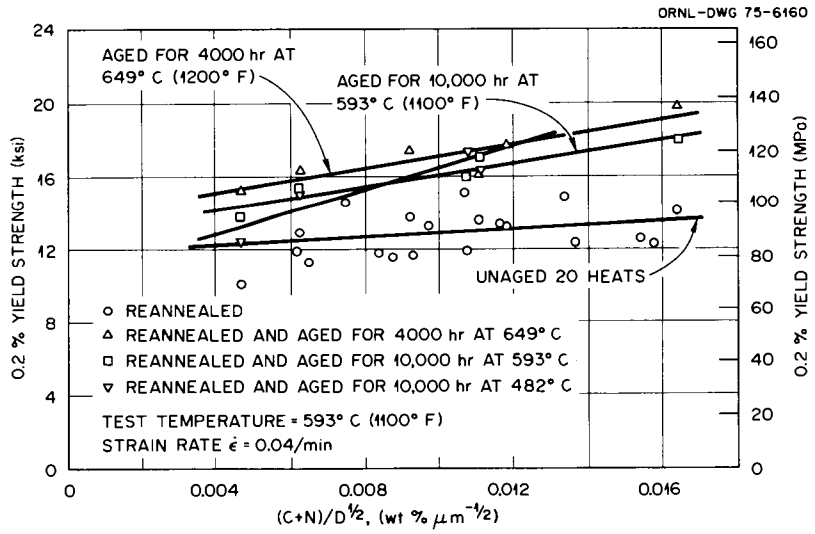

Fig. 3.31. Yield Strength (0.2%) at 593°C (1100°F) as a Function of $(C + N)D^{-1/2}$ for 20 Heats of Type 304 Stainless Steel in the Unaged Condition and for Several Heats in the Aged Condition.

Table 3.10. Effect of Interstitial Content and Grain Size on the Yield Strength of Unaged and Aged Types 304 and 316 Stainless Steel

Stainless Steel Type	Treatment			Test Temperature		Constants $S_y = S_0 + B(C + N)D^{-1/2}$				Carbide Particle Size,[a] μm	
	Time (hr)	Temperature (°C)	Temperature (°F)	(°C)	(°F)	S_0, MPa	S_0, ksi	B, MPa μm$^{1/2}$ / wt %	B, ksi μm$^{1/2}$ / wt %	Matrix	Grain Boundary
304				25	77	161	23.31	3999	579.96	0	0
304	4,000	482	900	25	77	172	24.93	6028	874.30	0	0
304	4,000	593	1100	25	77	170	24.65	5515	799.91	0.06	0.40
304	4,000	649	1200	25	77	178	25.84	4549	659.75	0.02	0.80
304				593	1100	81	11.78	770	111.71	0	0
304	10,000	482[b]	900	593	1100	72	10.42	4090	593.18	initiated	0
304	10,000	593	1100	593	1100	89	12.84	2247	325.93	0.10	0.40–0.60
304	4,000	649	1200	593	1100	95	13.71	2334	338.48	0.02	0.80
316				25	77	162	23.54	4286	621.57		
316	4,000	482	900	25	77	198	28.70	3720	539.46		
316	4,000	593	1100	25	77	198	28.73	3467	502.80		
316	4,000	649	1200	25	77	228	33.13	2080	301.63		
316				593	1100	53	7.72	3134	454.50		
316	4,000	482	900	593	1100	83	12.00	2527	366.49		
316	4,000	593	1100	593	1100	100	14.51	2173	315.09		
316	10,000	593	1100	593	1100	105	15.30	2221	322.16		
316	400	649	1200	593	1100	115	16.75	1898	275.23		

[a]Etienne, C. F., Dortland, W., and Zeedijk, H. B., "On the Capability of Austenitic Steel to Withstand Cyclic Deformation During Service at Elevated Temperature," paper presented at International Conference on Creep and Fatigue in Elevated Temperature Applications, Philadelphia, September 1973, and Sheffield, UK, April 1974.

[b]Limited data only.

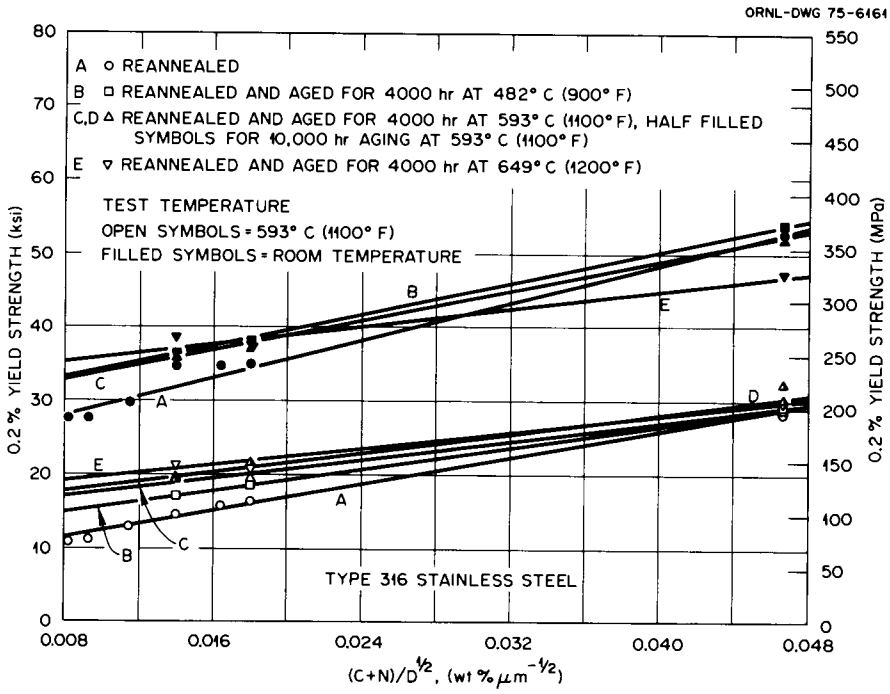

Fig. 3.32. Yield Strength (0.2%) at Room Temperature and 593°C (1100°F) for Seven Heats of Type 316 Stainless Steel in the Unaged Condition and for Several Heats in the Aged Condition.

the increase in yield strength on aging results from both the matrix and grain boundary precipitates and not simply from the intragranular precipitate alone.

3.2.3.2.3 Creep Properties. For two out of the nine heats of type 304 stainless steel, the effect of long-term low-temperature (LTLT) and short-term high-temperature (STHT) treatments on minimum creep rate and time-to-rupture data are presented in Fig. 3.34 and on ductility measures in Fig. 3.35. The LTLT consist of aging periods of 10,000 hr at temperatures in the range 482 to 649°C (900–1200°F), and STHT consists of periods up to 24 hr at temperatures above 649°C (1200°F). It should be noted that although both LTLT and STHT treatments increase minimum creep rate and decrease time to rupture, the maximum influence is observed for an aging temperature of 649°C (1200°F), as seen in Fig. 3.34. Rupture elongation and reduction of area also showed a maximum influence

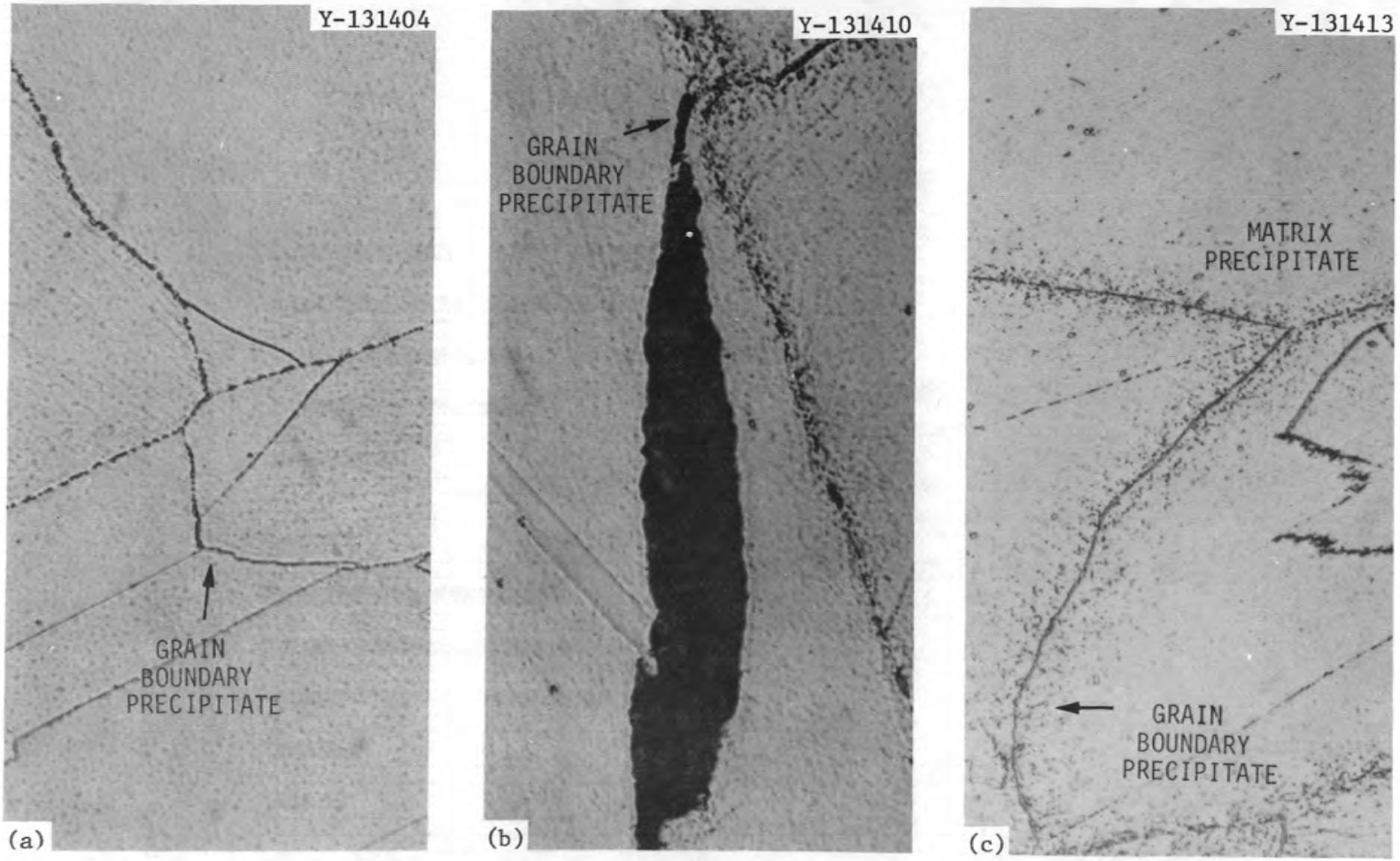

Fig. 3.33. Micrographs Showing Precipitation for Heat 926 of Type 304 Stainless Steel Aged 10,000 hr as a Function of Aging Temperature. 1500×. (a) 482°C (900°F) showing grain boundary precipitates. (b) 593°C (1100°F) showing grain boundary precipitate and some extremely small precipitate in matrix. (c) 649°C (1200°F) showing extensive precipitates at twin and grain boundaries and small fine distribution of precipitates in the matrix.

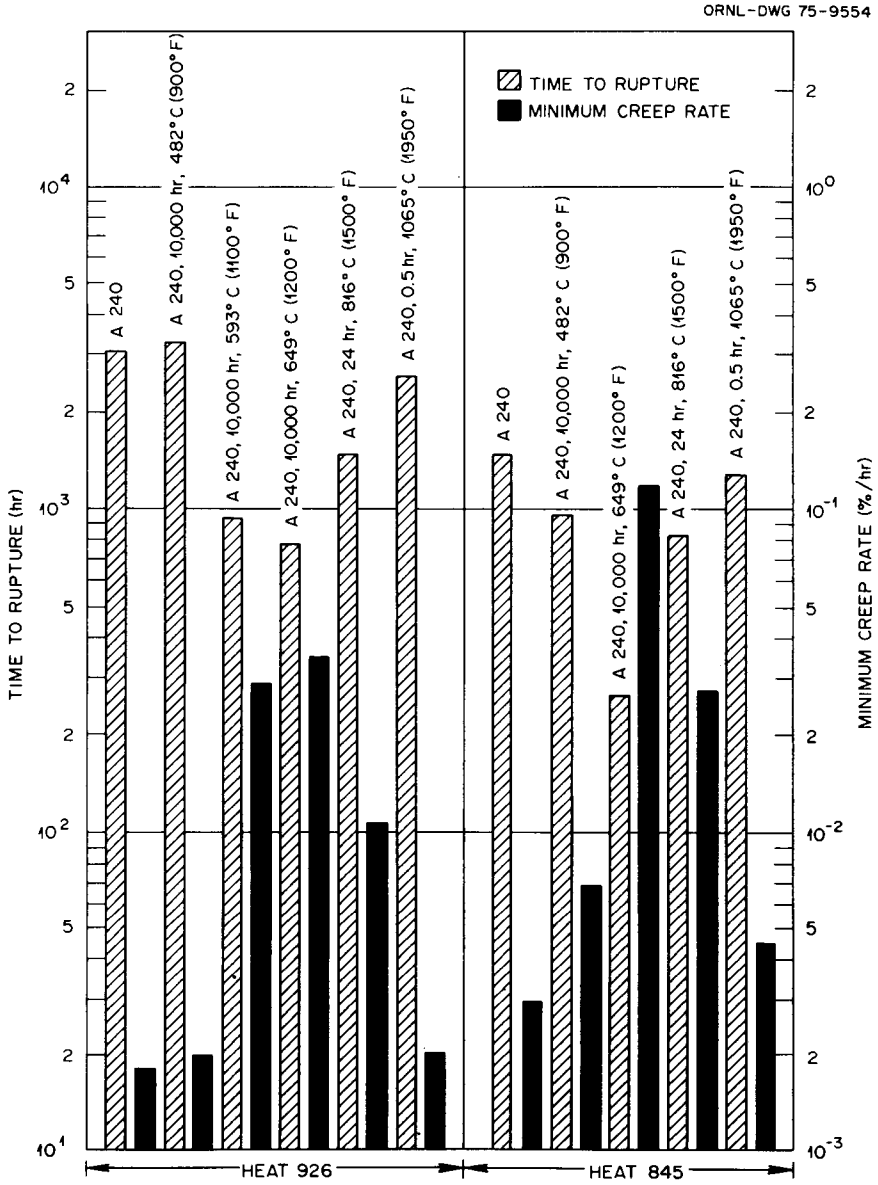

Fig. 3.34. Influence of Treatment Time and Temperature on Time to Rupture and Minimum Creep Rate of Heats 926 and 845 of Type 304 Stainless Steel Tested at 593°C (1100°F) and 30 ksi (207 MPa).

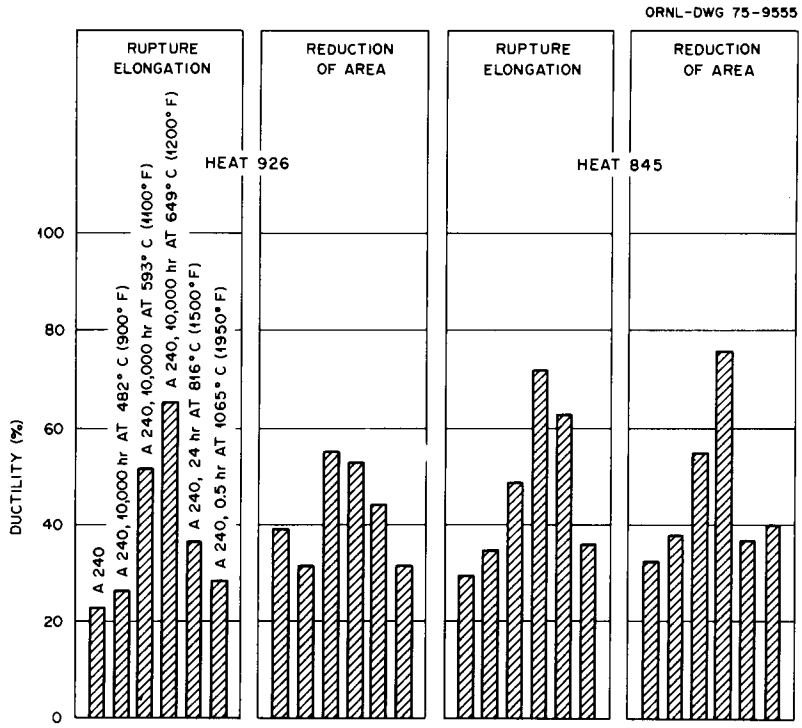

Fig. 3.35. Influence of Aging Treatment on Rupture Elongation and Reduction of Area for Heats 926 and 845 of Type 304 Stainless Steel. Creep tests were performed at 593°C (1100°F) and 30 ksi (207 MPa).

(increase) for an aging temperature of 649°C (1200°F). Furthermore, creep cavitation in aged specimens with large creep ductilities has been shown to be primarily along annealing twin boundaries, as opposed to the classical intergranular cavitation reported.[15]

The influence of LTLT on precipitation behavior of heat 926 of type 304 has already been presented in Fig. 3.33. The influence of STHT, in particular 24 hr at 816°C (1500°F), on microstructure is shown in Fig. 3.36. Note that the precipitates in STHT-treated specimens are large globules and are present only at the grain and twin boundaries. The matrix appears to be free of any precipitate. The comparison of precipitation behavior and observed creep properties reveals that in general any precipitation (at grain boundaries or matrix) on aging lowers the creep properties, but a critical combination of matrix and grain boundary precipitates is more deleterious than only grain boundary precipitate.

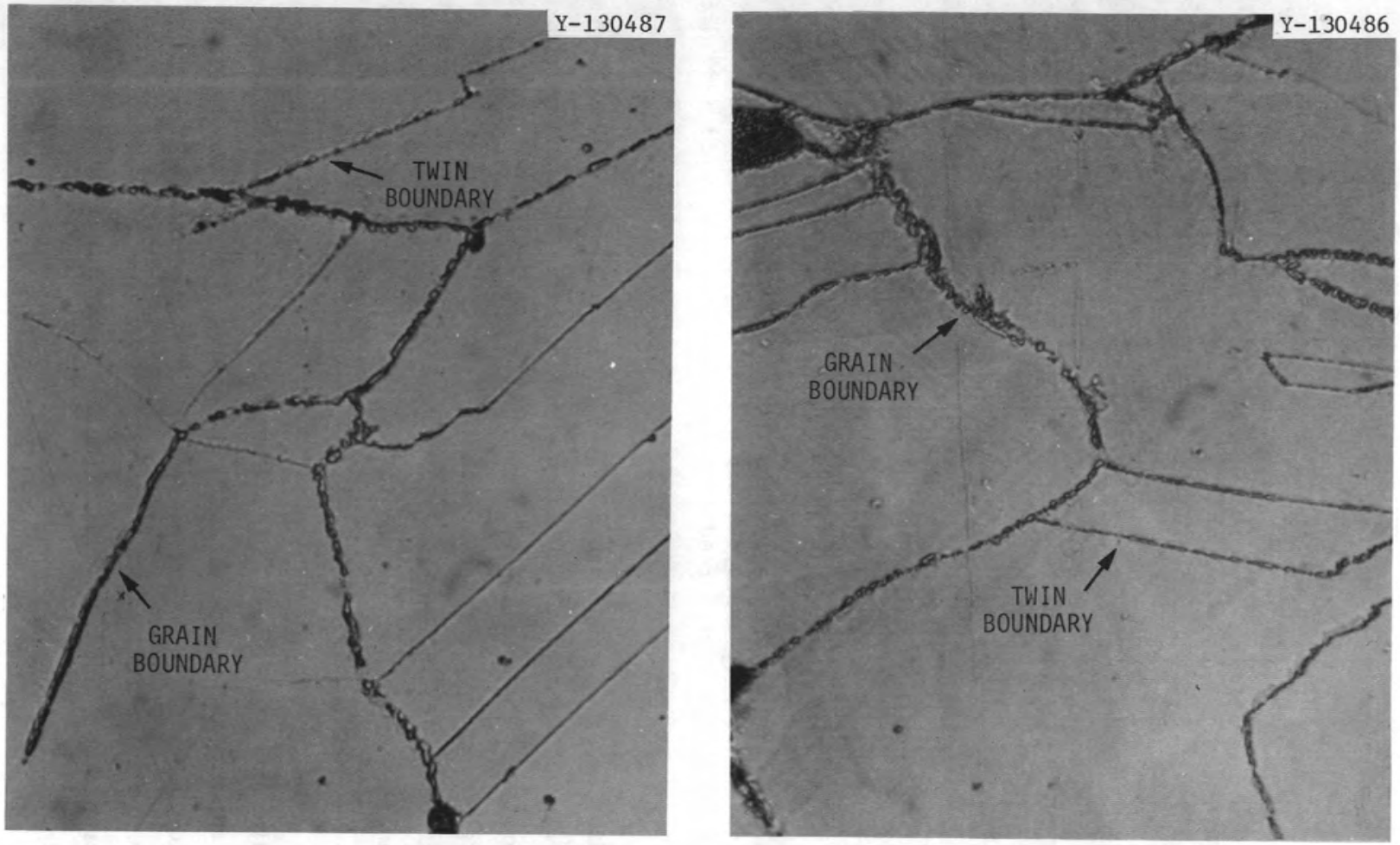

Fig. 3.36. Creep Specimens of Heat 926 of Type 304 Stainless Steel Aged 24 hr at 816°C (1500°F) and Tested at 593°C (1100°F) and 30 ksi (207 MPa). 1500×. Note the large precipitate particles at the twin and grain boundaries and their absence from the matrix.

3.2.4 Materials Behavior in Support of Development and Evaluation of Failure Criteria for Materials

3.2.4.1 Methods for Analysis of Creep and Creep-Rupture Data — M. K. Booker

Application of the previously reported[16—18] parametric method for the prediction of creep ductility has been extended to data for types 304 and 316 stainless steel, 2 1/4 Cr-1 Mo steel, and Inconel Alloy 718. In general, all results are reasonable, although trends in the data for the two stainless steels are by far the clearest. For these two materials, all ductility quantities considered exhibit increases with increases in stress and temperature. The trends for Inconel Alloy 718 are complicated but reasonably described by the parametric predictions. Unlike the other materials, which were analyzed by individual heats, the data set used to develop correlations for 2 1/4 Cr-1 Mo steel included data from several heats. In fact, the data for this ferritic steel exhibit so much scatter that no clear trends were determinable. The parametric predictions were, however, still reasonable. Table 3.11 describes the materials for the data sets used in this study.

Table 3.12 presents the results of the parametric correlations obtained for the individual quantities involved in the prediction of creep ductility.[16—18] All correlations were adequate, although those for 2 1/4 Cr-1 Mo steel were consistently poorer than the others. In any case, we can calculate from these correlations minimum values of creep ductility that provide design lower limits, even if mean trends in the data are not evident.

The method for calculation of the minimum ductility values[18] involves lower limits on each of the individual quantities in Table 3.12. The lower limit on a quanity y from Table 3.12 can be calculated[2] by

$$y_{low} = Ay_{pred} \tag{11}$$

where each A value is the "Factor for Calculation of Minimum" in Table 3.12.

Table 3.13 presents the limited results that have been obtained by the minimum commitment method (MCM),[25] while Tables 3.14 and 3.15 show

Table 3.11. Compositions and Product Forms of Materials Investigated

Heat	Reference	Product Form	Content, wt %[a]												
			C	Mn	P	S	Si	Cr	Ni	Co	Mo	Cu	N	Nb+Ta	Ti
						Type 304 Stainless Steel									
9T2796	19	25.4-mm plate	0.051	1.37	0.041	a	0.4	18.5	9.87	0.1	0.3	0.24	0.031	b	b
9T2796	20	50.8-mm plate	0.047	1.22	0.029	0.012	0.47	18.5	9.58	0.05	0.10	0.10	0.031	b	b
55697	21	7-mm rod	0.052	1.1	0.011	0.01	0.52	18.92	9.52	0.035	0.12	0.10	0.052	b	b
8043813	22	25.2-mm plate	0.062	1.87	0.04	0.0043	0.48	17.8	8.95	0.20	0.32	0.20	0.033	b	b
ASTM A 240, 479		Plate, rod	0.08[c]	2.0[c]	0.045[c]	0.03[c]	1.0[c]	17–19	8–10						
						Type 316 Stainless Steel									
332990	21	7-mm rod	0.052	1.72	0.012	0.02	0.38	17.8	13.55	0.14	2.33	0.20	0.041	b	
Garofalo et al.	15	12.7-mm bar	0.07	1.94	0.01	0.021	0.38	18.0	11.4	b	2.15	b	0.043	b	b
ASTM A 240, 479		Plate, rod	0.08[c]	2.0[c]	0.045[c]	0.03[c]	1.0[c]	16–18	10–14		2–3				
						Inconel Alloy 718									
C56445	23,24	25.4-mm pancake	0.05	0.21		0.006	0.05	18.18	52.16	0.06	3.03	b		5.31	0.76
GE Spec C50T79			0.10[c]	0.35[c]		0.03[c]	0.4[c]	17.0–21.0	50.0–55.0	0.75[c]	2.80–3.30			5.0–5.5	0.65–1.15

[a]All analyses include balance iron. No analysis available on Inconel alloy 718 heat Y8509 (ref. 24), 2 1/4 Cr-1 Mo data used included bar and pipe forms conforming to the following specifications: 2.00–2.50% Cr; 0.9–1.1% Mo; room temperature 0.2% offset yield strength ≥207 MPa (30 ksi); room-temperature ultimate tensile strength ≥414 MPa (60 ksi).

[b]Not reported.

[c]Maximum allowed.

Table 3.12. Comparison of Orr-Sherby-Dorn[a] (O-S-D) and Manson-Succop[b] (M-S) Correlations for the Quantities Involved in Creep Ductility Calculations

Heat	Data Points Used	Optimized Constants		Sum of Squared Residuals[c]		Residual Mean Square[d]		Factor for Calculation of Minimum	
		O-S-D Q	M-S D	O-S-D	M-S	O-S-D	M-S	O-S-D	M-S
				Rupture Life, t_r					
9T2796 25 mm	58	1.874×10^4	−0.02094	0.784	1.636	0.0148	0.0309	0.5767	0.4514
9T2796 51 mm	20	2.0199	−0.024694	0.17813	0.21701	0.0119	0.0145	0.5598	0.5270
55697	42	1.7236	−0.023054	0.85159	0.84874	0.0230	0.0229	0.4905	0.4912
8043813	24	2.6709	−0.029226	0.45176	1.0466	0.0238	0.0551	0.4537	0.3004
332990	39	1.9852	−0.025079	0.80472	0.79418	0.0237	0.0234	0.4818	0.4840
Garofalo et al.	132	1.8957	−0.019076	2.3442	4.5921	0.0184	0.0361	0.5630	0.4473
2 1/4 Cr-1 Mo	133	1.5290	−0.020042	10.063	10.128	0.0786	0.0791	0.3051	0.3039
Y8509	24	2.386	−0.0284	0.461	0.0570	0.0243	0.0300	0.4499	0.4117
C56445	28	2.404	−0.0301	0.142	0.131	0.0062	0.0057	0.6753	0.6864
				Time to Tertiary Creep, t_3					
9T2796 25 mm	63	1.8711×10^4	−0.020898	1.9527	3.3078	0.0337	0.0570	0.4387	0.3425
9T2796 51 mm	20	2.1089	−0.02583	0.53213	0.55371	0.0355	0.0369	0.3671	0.3600
55697	38	1.852	−0.024636	1.3005	1.4363	0.0394	0.0435	0.3888	0.3706
8043813	23	2.7752	−0.030142	0.54927	1.1491	0.0305	0.0638	0.4056	0.2711
332990	38	2.0788	−0.025914	0.96756	1.2094	0.0366	0.0366	0.4023	0.4023
Garofalo et al.	120	1.979	−0.0199	2.92	5.78	0.0254	0.0503	0.5072	0.3847
2 1/4 Cr-1 Mo	118	1.492	−0.0196	10.99	10.97	0.0972	0.0971	0.2646	0.2648
Y8509	18	2.340	−0.0272	0.314	0.345	0.0242	0.0265	0.4285	0.4119
C56445	26	2.500	−0.0319	0.413	0.307	0.0197	0.0146	0.4923	0.5433
				Minimum Creep Rate, $\dot{e}_m$					
9T2796 25 mm	58	-2.3857×10^4	0.026231	1.7795	5.4315	0.0336	0.1025	0.4363	0.2349
9T2796 51 mm	20	−2.7036	0.032933	0.48395	0.61949	0.0323	0.0413	0.3844	0.3393
55697	42	−2.3224	0.031067	0.8524	0.83727	0.0230	0.0226	0.4905	0.4935
8043813	24	−3.2695	0.035578	1.396	2.7945	0.0735	0.1471	0.2493	0.1402
332990	39	−2.5629	0.032003	0.79071	1.7551	0.0233	0.0516	0.4848	0.3404
Garofalo et al.	120	−2.1406	0.021361	3.6730	8.4604	0.0319	0.0736	0.4673	0.3148
2 1/4 Cr-1 Mo	127	−1.4234	0.018028	48.367	49.642	0.3964	0.4069	0.0690	0.0666
Y8509	19	−2.6217	0.029703	2.4781	2.7521	0.1770	0.1966	0.1039	0.0920
C56445	27	−2.8160	0.035923	1.2814	1.1287	0.0582	0.0513	0.2982	0.3211
				Average Engineering Creep Rate to Tertiary Creep, $\dot{e}_3$					
9T2796 25 mm	63	-2.3203×10^4	0.025716	1.256	4.6047	0.0217	0.0794	0.5166	0.2827
9T2796 51 mm	20	−2.8333	0.034506	0.32481	0.47696	0.0217	0.0318	0.4568	0.3873
55697	38	−2.2075	0.029408	0.72616	0.79615	0.0220	0.0241	0.4936	0.4776
8043813	23	−3.1262	0.033763	1.14	2.347	0.0633	0.1304	0.2725	0.1548
332990	38	−2.5398	0.031442	0.91896	1.8133	0.0278	0.0549	0.4522	0.3278
Garofalo et al.	120	−2.0710	0.020743	2.895	6.6122	0.0252	0.0575	0.5085	0.3601
2 1/4 Cr-1 Mo	118	−1.2391	0.01588	35.690	36.308	0.3158	0.3213	0.0913	0.0894
Y8509	18	−2.5132	0.029329	0.36249	0.32602	0.0279	0.0251	0.4025	0.4218
C56445	26	−2.7393	0.034879	1.2426	1.1772	0.0592	0.0561	0.2927	0.3024
				Average True Strain Rate to Rupture, $\dot{\varepsilon}_r$					
9T2796 25 mm	52	-2.121×10^4	0.023383	1.0034	2.4818	0.0214	0.0528	0.5126	0.3500
9T2796 51 mm	20	−2.4606	0.030088	0.46103	0.51561	0.0307	0.0344	0.3938	0.3729
8043813	24	−2.9813	0.032503	0.83046	1.8504	0.0437	0.0974	0.3427	0.2021
2 1/4 Cr-1 Mo	132	−1.5917	0.021705	35.746	18.565	0.2815	0.1462	0.1051	0.1972
Y8509	24	−2.5819	0.030738	1.1665	1.2535	0.0614	0.0660	0.2810	0.2682
C56445	27	−2.4271	0.030325	0.50206	0.39132	0.0228	0.0178	0.4690	0.5122
				Average Engineering Creep Rate to Rupture, $\dot{e}_r$					
9T2796 25 mm	58	-2.1968×10^4	0.024275	0.76324	2.697	0.0144	0.0509	0.5810	0.3603
9T2796 51 mm	20	−2.721	0.033248	0.36576	0.44576	0.0244	0.0297	0.4357	0.3998
55697	41	−2.222	0.029744	1.6613	1.5635	0.0461	0.0434	0.3637	0.3748
8043813	24	−3.0723	0.033483	0.75182	1.8646	0.0400	0.0981	0.3589	0.2010
332990	37	−2.4753	0.031204	1.7053	2.2016	0.0533	0.0688	0.3318	0.2856
Garofalo et al.	132	−2.1681	0.021616	5.2431	10.291	0.0413	0.0810	0.4229	0.2996
2 1/4 Cr-1 Mo	133	−1.6139	0.021260	21.707	21.537	0.1696	0.1682	0.1748	0.1761
Y8509	24	−2.7508	0.032688	1.3051	1.4563	0.0687	0.0766	0.2611	0.2422
C56445	28	−2.5637	0.032425	0.70233	0.63167	0.0305	0.0275	0.4187	0.4375

[a] O-S-D: $p(\sigma) = \log y - Q/T$ (K)

[b] M-S: $p(\sigma) = \log y - DT$ (K)

[c] $\Sigma R^2 = \Sigma(\log y_{pred} - \log y_{experimental})^2$

[d] RMS $= \Sigma R^2/(n - \nu)$, when n = number of data points and ν = number of coefficients in the model; here $\nu = 5$.

Table 3.13. Results of Calculations Using the Minimum Committment Method

Heat	Data Points Used	A	Sum of Squared Residuals
	Rupture Life		
9T2796 (25.4 mm)	58	−0.05	1.013
9T2796 (50.8 mm)	20	0.15	0.064
55697	45	−0.10	0.591
8043813	24	0.10	0.359
332990	39	−0.05	0.548
Y8509	24	−0.10	0.661
C56445	27	0.00	0.260
	Time to Tertiary Creep		
9T2796 (25.4 mm)	60	0.05	1.447
9T2796 (50.8 mm)	20	0.15	0.280
55697	40	0.00	1.213
8043813	23	0.05	0.435
332990	38	0.00	0.818
Y8509	18	−0.10	0.370
C56445	26	−0.05	0.386
	Minimum Creep Rate[a]		
9T2796 (25.4 mm)	60	0.00	0.975
9T2796 (50.8 mm)	20	0.10	0.094
55697	42	0.00	0.804
8043813	24	0.05	0.846
332990	39	−0.05	0.536
Y8509	19	−0.15	3.075
C56445	27	0.05	1.579

[a]Actually analyzed as $t_m = 1/\dot{e}_m$. Values in the table refer to t_m.

the predictions obtained for strain to tertiary creep, e_3, and plasticity resource, e_s (the product of rupture life and minimum creep rate). In general, ductility tends to decrease with rupture time, although trends with time are more complicated than trends with stress and temperature. Reference (2) presents a detailed summary of these results, including predictions of engineering and true strain to rupture as well as e_3 and e_s.

Table 3.14. Parametric Predictions for Engineering Creep Strain to Tertiary Creep

Temperature (°C)	Temperature (°F)	Prediction Method[a]	Predicted Strain, %, for Time to Tertiary Creep[b] 10^2 hr	10^3 hr	10^4 hr	10^5 hr
			Heat 9T2796 25-mm Plate Type 304			
538	1000	O-S-D	2.68 (0.61)	2.26 (0.51)	1.79 (0.41)	1.37 (0.31)
		M-S	2.71 (0.26)	2.54 (0.25)	2.10 (0.20)	1.66 (0.16)
593	1100	O-S-D	4.59 (1.04)	3.56 (0.81)	2.74 (0.62)	2.30 (0.52)
		M-S	4.57 (0.44)	3.74 (0.36)	2.95 (0.29)	2.48 (0.24)
649	1200	O-S-D	6.75 (1.53)	5.28 (1.20)	4.65 (1.06)	4.90 (1.11)
		M-S	6.68 (0.65)	5.30 (0.51)	4.54 (0.44)	4.45 (0.43)
704	1300	O-S-D	9.67 (2.20)	8.71 (1.98)	9.41 (2.14)	12.04 (2.73)
		M-S	9.47 (0.92)	8.26 (0.80)	8.28 (0.80)	9.70 (0.94)
			Heat 9T2796 51-mm Plate Type 304			
538	1000	O-S-D	1.08 (0.18)	1.37 (0.23)	1.17 (0.20)	0.59 (0.099)
		M-S	1.25 (0.17)	1.64 (0.23)	1.30 (0.18)	0.60 (0.083)
593	1100	O-S-D	4.82 (0.81)	2.92 (0.49)	1.27 (0.21)	0.92 (0.15)
		M-S	4.80 (0.67)	2.94 (0.41)	1.30 (0.18)	0.92 (0.13)
649	1200	O-S-D	6.27 (1.05)	3.17 (0.53)	3.28 (0.55)	5.96 (1.00)
		M-S	6.20 (0.86)	3.12 (0.43)	3.01 (0.42)	5.02 (0.70)
704	1300	O-S-D	8.22 (1.38)	10.30 (1.73)	20.98 (3.52)	56.67 (9.52)
		M-S	8.49 (1.18)	10.63 (1.48)	20.87 (2.90)	54.24 (7.54)
			Heat 55697 7.0-mm Rod Type 304			
538	1000	O-S-D	3.20 (0.61)	4.52 (0.87)	3.81 (0.73)	1.46 (0.28)
		M-S	3.26 (0.58)	4.59 (0.81)	3.77 (0.67)	1.44 (0.25)
593	1100	O-S-D	8.60 (1.65)	5.25 (1.01)	1.46 (0.28)	0.57 (0.11)
		M-S	8.45 (1.50)	5.37 (0.95)	1.62 (0.29)	0.55 (0.097)
649	1200	O-S-D	6.80 (1.30)	1.73 (1.03)	0.97 (0.19)	1.60 (0.31)
		M-S	6.77 (1.20)	1.82 (0.32)	0.87 (0.15)	1.02 (0.18)
			Heat 8043413 25-mm Plate Type 304			
538	1000	O-S-D	7.03 (0.77)	6.16 (0.68)	5.29 (0.58)	4.39 (0.48)
		M-S	7.12 (0.30)	6.56 (0.28)	5.82 (0.24)	4.78 (0.20)
593	1100	O-S-D	9.68 (1.06)	7.95 (0.87)	6.10 (0.67)	4.16 (0.46)
		M-S	9.65 (0.40)	8.17 (0.34)	6.25 (0.26)	4.24 (0.18)
649	1200	O-S-D	10.92 (1.20)	7.51 (0.83)	4.33 (0.48)	1.98 (0.22)
		M-S	10.98 (0.46)	7.72 (0.32)	4.87 (0.20)	2.85 (0.12)
704	1300	O-S-D	8.58 (0.94)	4.23 (0.46)	1.63 (0.18)	0.51 (0.056)
		M-S	9.11 (0.38)	5.45 (0.23)	3.08 (0.13)	1.69 (0.07)
			Heat 332990 7.0-mm Rod Type 316			
538	1000	O-S-D	2.60 (0.47)	2.78 (0.50)	2.34 (0.42)	1.65 (0.30)
		M-S	3.26 (0.43)	4.59 (0.60)	3.77 (0.50)	1.44 (0.19)
593	1100	O-S-D	5.86 (1.07)	4.38 (0.80)	2.92 (0.53)	2.09 (0.38)
		M-S	8.45 (1.11)	5.37 (0.71)	1.62 (0.21)	0.55 (0.07)
649	1200	O-S-D	7.71 (1.40)	5.12 (0.93)	3.82 (0.70)	4.16 (0.76)
		M-S	6.77 (0.89)	1.82 (0.24)	0.87 (0.11)	1.02 (0.13)
704	1300	O-S-D	8.86 (1.61)	7.11 (1.29)	9.09 (1.65)	27.92 (5.08)
		M-S	2.29 (0.30)	1.55 (0.20)	2.29 (0.30)	5.43 (0.72)
			Garafalo et al. 12.7-mm Bar Type 316			
593	1100	O-S-D	15.39 (3.97)	13.85 (3.57)	12.59 (3.25)	11.29 (2.91)
		M-S	15.46 (2.13)	14.03 (1.94)	12.84 (1.77)	11.37 (1.57)
649	1200	O-S-D	15.48 (4.00)	14.06 (3.63)	12.35 (3.19)	9.57 (2.47)
		M-S	15.54 (2.14)	14.20 (1.96)	12.47 (1.72)	9.70 (1.34)
704	1300	O-S-D	15.66 (4.04)	13.52 (3.49)	10.07 (2.60)	6.08 (1.57)
		M-S	15.70 (2.17)	13.69 (1.89)	10.48 (1.45)	6.72 (0.93)
			2 1/4 Cr-1 Mo Various Heats			
482	900	O-S-D	0.76 (0.02)	2.63 (0.06)	5.64 (0.14)	7.90 (0.19)
		M-S	0.63 (0.02)	2.89 (0.07)	6.10 (0.15)	7.97 (0.19)
538	1000	O-S-D	2.15 (0.05)	3.92 (0.09)	4.79 (0.11)	4.38 (0.10)
		M-S	1.97 (0.05)	3.93 (0.09)	4.95 (0.12)	4.76 (0.11)
593	1100	O-S-D	2.64 (0.06)	3.04 (0.07)	2.70 (0.06)	4.16 (0.10)
		M-S	2.53 (0.06)	3.10 (0.07)	2.93 (0.07)	3.39 (0.09)
649	1200	O-S-D	c	c	c	c
		M-S	1.91 (0.04)	1.79 (0.09)	c	c
			Inconel Alloy 718 Heat C56445 25.4-mm Pancake			
538	1000	O-S-D	2.18 (0.31)	0.94 (0.14)	0.45 (0.06)	0.25 (0.04)
		M-S	3.14 (0.51)	1.13 (0.18)	0.52 (0.08)	0.31 (0.05)
593	1100	O-S-D	1.06 (0.15)	0.58 (0.08)	0.38 (0.05)	0.32 (0.05)
		M-S	0.90 (0.15)	0.50 (0.08)	0.38 (0.06)	0.40 (0.06)
649	1200	O-S-D	0.84 (0.12)	0.65 (0.09)	0.65 (0.09)	0.47 (0.07)
		M-S	0.58 (0.10)	0.57 (0.09)	0.74 (0.12)	0.72 (0.12)
704	1300	O-S-D	1.14 (0.16)	1.19 (0.17)	0.35 (0.05)	0.01 (0.00)
		M-S	1.00 (0.16)	1.21 (0.20)	0.15 (0.02)	0.00 (0.00)
			Inconel Alloy 718 Heat Y8509 15.9-mm Bar			
538	1000	O-S-D	2.61 (0.45)	1.37 (0.24)	0.76 (0.13)	0.44 (0.08)
		M-S	2.65 (0.46)	1.28 (0.22)	0.67 (0.12)	0.39 (0.07)
593	1100	O-S-D	1.14 (0.20)	0.66 (0.11)	0.42 (0.07)	0.30 (0.05)
		M-S	1.21 (0.21)	0.66 (0.11)	0.40 (0.07)	0.29 (0.05)
649	1200	O-S-D	0.65 (0.11)	0.44 (0.08)	0.35 (0.06)	0.31 (0.05)
		M-S	0.67 (0.12)	0.44 (0.08)	0.35 (0.06)	0.32 (0.06)
704	1300	O-S-D	0.50 (0.09)	0.44 (0.08)	0.15 (0.02)	0.01 (0.01)
		M-S	0.50 (0.09)	0.44 (0.08)	0.26 (0.04)	0.00 (0.00)

[a]O-S-D = Orr-Sherby-Dorn; M-S = Manson-Succop.

[b]Expected value is followed in parentheses by lower limit.

[c]Not available.

Table 3.15. Parametric Predictions for Plasticity Resource

Temperature (°C)	Temperature (°F)	Prediction Method[a]	Predicted Plasticity Resource, %, for Rupture Time[b] 10^2 hr	10^3 hr	10^4 hr	10^5 hr
			Heat 9T2796 25-mm Plate Type 304			
538	1000	O-S-D	2.58 (0.65)	2.43 (0.61)	2.21 (0.57)	1.90 (0.48)
		M-S	2.65 (0.28)	2.97 (0.31)	2.95 (0.31)	2.62 (0.28)
593	1100	O-S-D	5.88 (1.48)	5.21 (1.31)	4.36 (1.10)	3.41 (0.86)
		M-S	5.85 (0.62)	5.71 (0.60)	4.98 (0.53)	3.96 (0.42)
649	1200	O-S-D	11.34 (2.86)	9.29 (2.34)	7.13 (1.80)	5.20 (1.31)
		M-S	11.12 (1.18)	9.54 (1.01)	7.47 (0.79)	5.50 (0.58)
704	1300	O-S-D	18.44 (4.65)	14.02 (3.53)	10.18 (2.56)	7.29 (1.84)
		M-S	18.06 (1.91)	13.99 (1.48)	10.24 (1.08)	7.34 (0.78)
			Heat 9T2796 51-mm Plate Type 304			
538	1000	O-S-D	1.50 (0.32)	1.48 (0.32)	1.26 (0.27)	0.92 (0.20)
		M-S	1.63 (0.29)	1.70 (0.30)	1.46 (0.26)	1.05 (0.19)
593	1100	O-S-D	4.70 (1.01)	3.66 (0.79)	2.55 (0.55)	1.84 (0.40)
		M-S	4.67 (0.84)	3.73 (0.67)	2.60 (0.46)	1.85 (0.33)
649	1200	O-S-D	9.57 (2.06)	6.61 (1.42)	5.08 (1.09)	4.81 (1.03)
		M-S	9.48 (1.70)	6.52 (1.17)	4.89 (0.88)	4.43 (0.79)
704	1300	O-S-D	16.01 (3.44)	12.86 (2.76)	12.80 (2.75)	15.37 (3.30)
		M-S	16.41 (2.94)	13.08 (2.34)	12.76 (2.28)	15.00 (2.68)
			Heat 55697 7.0-mm Rod Type 304			
538	1000	O-S-D	4.04 (0.97)	2.91 (0.70)	2.38 (0.57)	2.00 (0.48)
		M-S	4.07 (0.98)	2.96 (0.72)	2.44 (0.59)	2.01 (0.49)
593	1100	O-S-D	7.89 (1.89)	6.64 (1.59)	5.37 (1.29)	3.05 (0.73)
		M-S	7.69 (1.86)	6.43 (1.56)	5.14 (1.24)	3.06 (0.74)
649	1200	O-S-D	16.89 (4.05)	13.11 (3.15)	6.52 (1.56)	1.29 (0.31)
		M-S	17.18 (4.16)	12.95 (3.13)	6.74 (1.63)	2.00 (0.48)
			Heat 8043813 25-mm Plate Type 304			
538	1000	O-S-D	8.85 (1.00)	6.41 (0.77)	4.41 (0.50)	2.87 (0.32)
		M-S	8.93 (0.38)	6.84 (0.29)	4.80 (0.20)	3.09 (0.13)
593	1100	O-S-D	12.51 (1.41)	8.10 (0.92)	4.96 (0.56)	2.94 (0.33)
		M-S	12.47 (0.52)	8.30 (0.35)	5.13 (0.22)	3.09 (0.13)
649	1200	O-S-D	13.92 (1.57)	8.25 (0.93)	4.93 (0.56)	3.18 (0.36)
		M-S	13.93 (0.58)	8.42 (0.35)	5.13 (0.22)	3.27 (0.14)
704	1300	O-S-D	13.76 (1.55)	8.56 (0.97)	5.96 (0.67)	4.54 (0.37)
		M-S	13.87 (0.58)	8.67 (0.36)	5.72 (0.24)	3.98 (0.17)
			Heat 332990 7.0-mm Rod Type 316			
538	1000	O-S-D	3.24 (0.76)	3.25 (0.76)	2.90 (0.68)	2.35 (0.55)
		M-S	3.28 (0.54)	3.73 (0.62)	3.39 (0.56)	2.70 (0.44)
593	1100	O-S-D	8.77 (2.05)	7.40 (1.73)	5.71 (1.34)	4.09 (0.96)
		M-S	8.81 (1.45)	7.57 (1.25)	5.82 (0.96)	4.16 (0.69)
649	1200	O-S-D	17.16 (4.02)	12.83 (3.00)	8.97 (2.10)	6.04 (1.41)
		M-S	16.80 (2.77)	12.50 (2.06)	8.72 (1.44)	5.85 (0.96)
704	1300	O-S-D	26.93 (6.30)	18.62 (4.36)	12.53 (2.93)	c
		M-S	26.38 (4.35)	18.08 (2.98)	12.05 (1.99)	c
			Garofalo et al. 12.7-mm Bar Type 316			
593	1100	O-S-D	7.68 (2.02)	9.72 (2.56)	11.42 (3.00)	11.71 (3.08)
		M-S	8.20 (1.16)	11.13 (1.57)	13.43 (1.89)	13.31 (1.88)
649	1200	O-S-D	15.33 (4.03)	17.36 (4.56)	16.67 (4.38)	12.15 (3.20)
		M-S	15.14 (2.13)	18.07 (2.55)	17.59 (2.48)	12.86 (1.81)
704	1300	O-S-D	24.60 (6.47)	22.77 (5.99)	15.79 (4.15)	8.51 (2.24)
		M-S	24.12 (3.40)	23.17 (3.27)	16.69 (2.35)	9.50 (1.34)
			2 1/4 Cr-1 Mo Various Heats			
482	900	O-S-D	0.84 (0.02)	2.45 (0.05)	4.42 (0.09)	5.52 (0.12)
		M-S	0.47 (0.01)	2.55 (0.05)	4.94 (0.10)	6.06 (0.12)
538	1000	O-S-D	2.66 (0.06)	4.13 (0.09)	4.57 (0.10)	3.85 (0.08)
		M-S	2.24 (0.04)	4.07 (0.08)	4.80 (0.10)	4.29 (0.08)
593	1100	O-S-D	3.66 (0.08)	3.83 (0.08)	3.08 (0.06)	2.08 (0.04)
		M-S	3.33 (0.07)	3.81 (0.08)	3.33 (0.07)	2.37 (0.05)
649	1200	O-S-D	3.28 (0.07)	2.61 (0.05)	1.75 (0.04)	c
		M-S	3.00 (0.06)	2.56 (0.05)	1.78 (0.04)	c
			Inconel Alloy 718 Heat C56445 25.4-mm Pancake			
538	1000	O-S-D	2.18 (0.44)	0.94 (0.19)	0.45 (0.09)	0.25 (0.05)
		M-S	2.18 (0.48)	0.91 (0.20)	0.44 (0.10)	0.25 (0.06)
593	1100	O-S-D	1.06 (0.21)	0.58 (0.12)	0.38 (0.08)	0.32 (0.06)
		M-S	1.08 (0.24)	0.58 (0.13)	0.38 (0.08)	0.31 (0.07)
649	1200	O-S-D	0.84 (0.17)	0.65 (0.13)	0.65 (0.13)	0.47 (0.09)
		M-S	0.84 (0.18)	0.64 (0.14)	0.62 (0.14)	0.53 (0.12)
704	1300	O-S-D	1.14 (0.23)	1.19 (0.24)	0.35 (0.07)	0.01 (0.00)
		M-S	1.22 (0.27)	1.20 (0.26)	0.33 (0.07)	0.00 (0.00)
			Inconel Alloy 718 Heat Y8509 15.9-mm Bar			
538	1000	O-S-D	2.20 (0.10)	1.06 (0.05)	0.53 (0.02)	0.28 (0.01)
		M-S	2.20 (0.08)	1.04 (0.04)	0.51 (0.02)	0.27 (0.01)
593	1100	O-S-D	1.18 (0.06)	0.61 (0.03)	0.33 (0.02)	0.20 (0.01)
		M-S	1.20 (0.04)	0.61 (0.02)	0.34 (0.01)	0.21 (0.01)
649	1200	O-S-D	0.75 (0.04)	0.43 (0.02)	0.29 (0.01)	0.25 (0.01)
		M-S	0.73 (0.03)	0.43 (0.02)	0.29 (0.01)	0.26 (0.01)
704	1300	O-S-D	0.60 (0.03)	0.44 (0.02)	0.36 (0.02)	0.15 (0.01)
		M-S	0.56 (0.02)	0.43 (0.02)	0.38 (0.01)	0.19 (0.01)

[a]O-S-D = Orr-Sherby-Dorn; M-S = Manson-Succop.

[b]Expected value is followed in parentheses by lower limit.

[c]Not available.

Table 3.16 summarizes the results of correlations between rupture life, t_r, and time to tertiary creep, t_3, using a model of the form

$$t_3 = A t_r^{\beta} . \tag{12}$$

Predictions using this approach yielded good results for the data sets in Table 3.11 (plus additional data on similar material). Moreover, these results compare well with the parametric predictions shown in Table 3.12. This comparison was made by obtaining parametric predictions for both t_3 and t_r at a given stress and temperature and then plotting these predictions according to Eq. (12) with the appropriate constants from Table 3.16. Figures 3.37 and 3.38 illustrate this comparison.

Table 3.16. Results of Correlation Between Rupture Life and Time to Tertiary Creep[a] by $t_3 = A t_r^{\beta}$

Data Set	Number of Points	A	β	RMS[b]	Temperature Range of Data (°C)
304 Stainless, t_{ss}	277	0.752	0.977	0.090	482–816
304 Stainless, t_2	233	0.685	0.968	0.117	538–649
316 Stainless, t_2	183	0.526	1.004	0.071	538–816
2 1/4 Cr-1 Mo, t_{ss}	126	0.334	1.046	0.067	482–677
Inconel 718, t_{ss}	63	0.424	1.045	0.080	538–704
Inconel 718, t_2	52	0.285	1.049	0.142	538–704

[a]The time to tertiary creep, t_3, may be either the value t_{ss} determined by the 0.2% offset method or the value t_2 determined as the first deviation from linear creep.

[b]RMS = $\Sigma R^2/(n-\nu)$ where n = number of data points and ν = number of coefficients in the model; here $\nu = 2$. $\Sigma R^2 = [\ln t_3(\text{pred}) - \ln t_3(\text{exptl})]^2$.

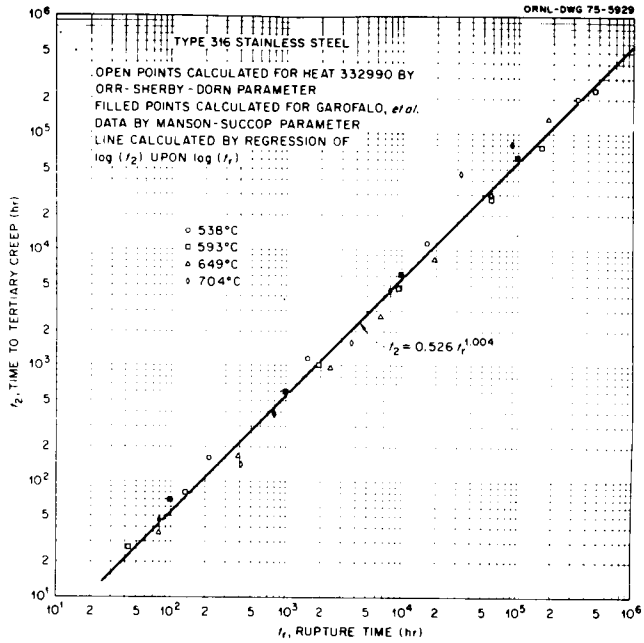

Fig. 3.37. Comparison Between Parametric Results for Single Heats and Relationship Between Rupture Time and Time to Tertiary Creep for Type 316 Stainless Steel (Annealed).

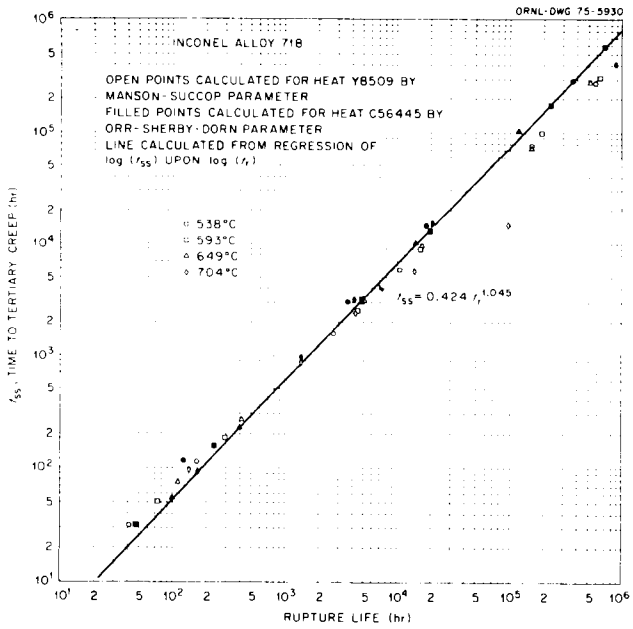

Fig. 3.38. Comparison Between Parametric Results for Single Heats and Relationship Between Rupture Time and Time to Tertiary Creep (0.2% offset) for Inconel Alloy 718 (Aged and Duplex Aged).

The close comparison between Eq. (12) and the parametric predictions indicates that Eq. (12) might be extrapolable to time levels beyond the data base used. Moreover, data for thermally aged (up to 10,000 hr) type 304 stainless steel show good agreement with that for unaged material, indicating that the relationship in Eq. (12) is relatively unaffected by long-term thermal exposure. Figure 3.39 shows data for aged and for annealed (unaged) type 304 stainless steel at 593°C. The mean line shown in Fig. 3.39 was obtained by a fit to the data in the figure, while the upper and lower tolerance limits shown were calculated from the full data base (277 points) for annealed type 304 stainless steel. Clearly, the two data sets exhibit similar behavior. Reference (26) contains a detailed summary of these investigations.

Current work involves prediction of creep ductility from empirical relationships among rupture life, minimum creep rate, time to tertiary creep, and other properties. Results in this area will be reported next quarter.

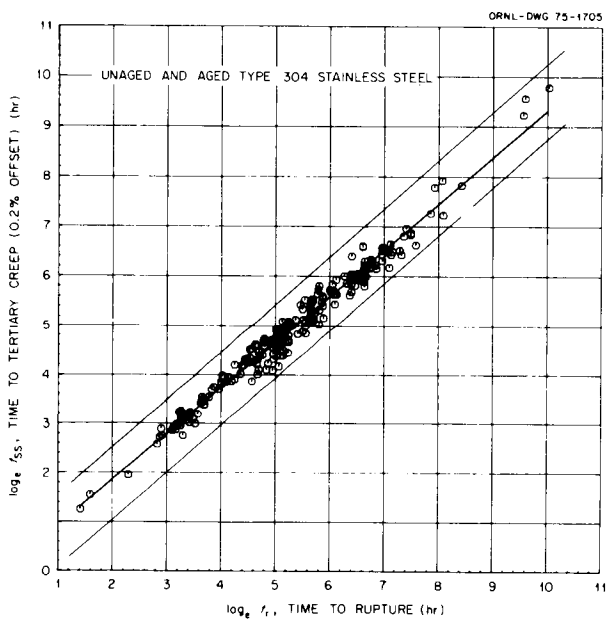

Fig. 3.39. Relationship Between Rupture Time and Time to Tertiary Creep (0.2% Offset) for Type 304 Stainless Steel at 593°C (Annealed and Thermally Aged).

3.2.4.2 Complex Loading Behavior of LMFBR Structural and Component Materials — J. P. Strizak and C. R. Brinkman

The effort to develop and strengthen engineering mechanical properties data for LMFBR structural and component materials calls for material behavior studies under complex loading in addition to basic creep properties presently under investigation. Data to be obtained will provide information on time-dependent material behavior under other than constant uniaxial tensile loading for three materials (types 304 and 316 stainless steel and 2 1/4 Cr-1 Mo steel) over stress and temperature ranges representative of LMFBR design conditions. Tests will include (1) compressive creep, (2) tensile and compressive relaxation, (3) constant-stress tensile and compressive creep, (4) creep with stress oscillations superimposed on sustained stress, (5) creep tests with stress oscillations, and (6) creep tests interrupted by strain cycles; Fig. 3.40 shows representative loading history curves for these various tests.

To date, testing facility requirements have been reviewed and specifications written. Our dual-channel complex-loading testing machine is presently being fabricated by Monterey Dynamics of Monterey, California, while design of test specimen grips, axial and diametral extensometers, and heating systems is continuing at ORNL. The testing system consists of two load frames, an electronic control console, and a hydraulic power supply. The system employs (1) closed-loop electro-pneumatic (plant air) control for the long-term static portions of the tests shown in Fig. 3.40 [includes the mean stress or mean load in (e)], and (2) closed-loop electro-hydraulic control for dynamic portions of tests as shown in Fig. 3.40(e), (f), and (g). [Because of long hold periods in tension and compression, the stress oscillations in (f) could be applied manually employing the static control loop mentioned above; the static control loop will maintain the constant load or stress intervals in (g), and the dynamic loop will be employed for the strain cycling.] Figs. 3.41 and 3.42 show a drawing of a load frame and a diagram of the electro-pneumatic and electro-hydraulic closed-loop circuits, respectively. As a trade-off of cost versus convenience the dynamic control loop of the testing system is switchable to one channel (one load frame) at a time; however, creep tests interrupted by strain cycles [Fig. 3.40(g)] can be

ORNL-DWG 75-9522

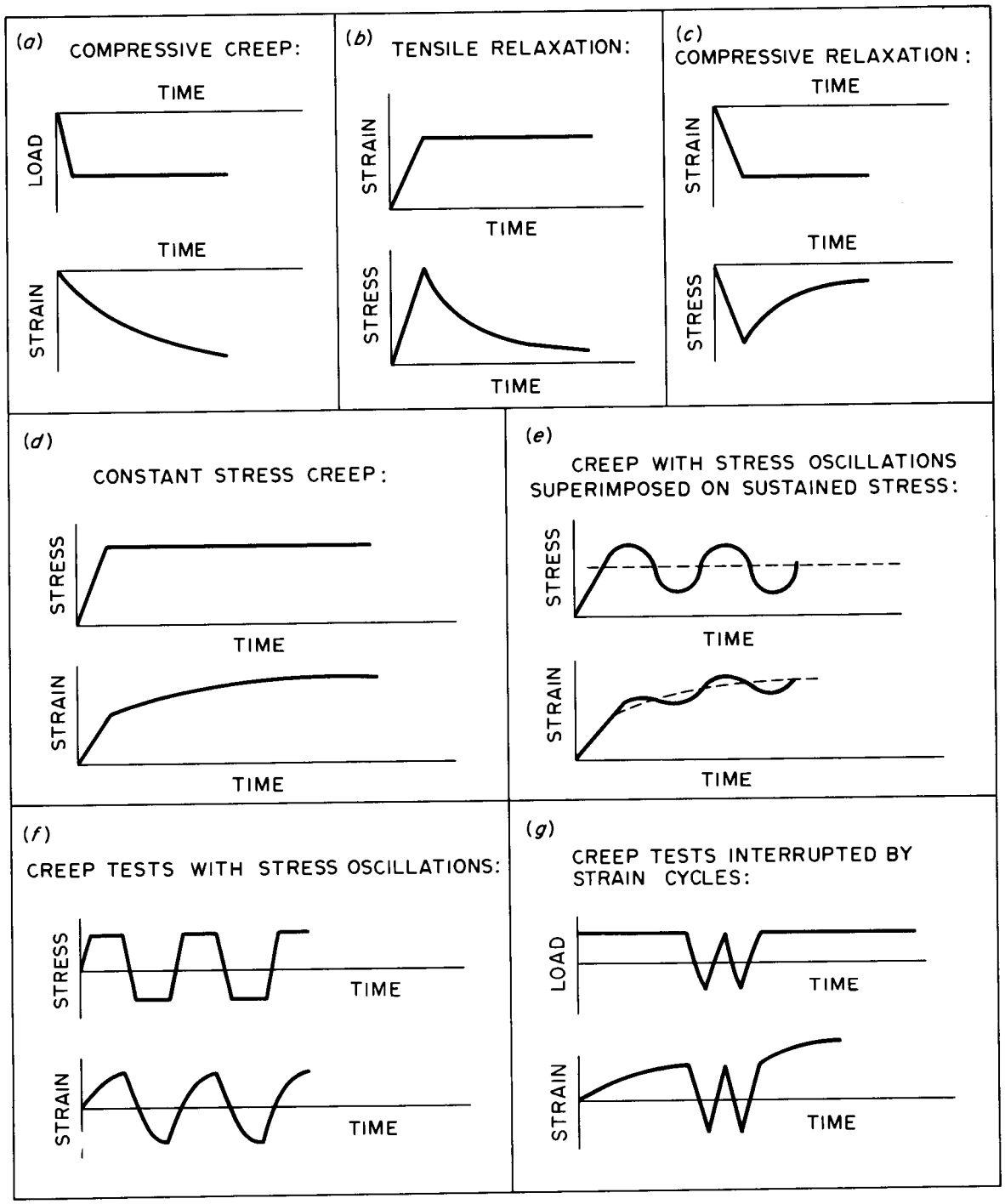

Fig. 3.40. Complex Loading Tests. Upper curve for each test depicts the controlled test parameter (independent variable) as a Function of Time, while the lower curve for each test is representative of the dependent variable.

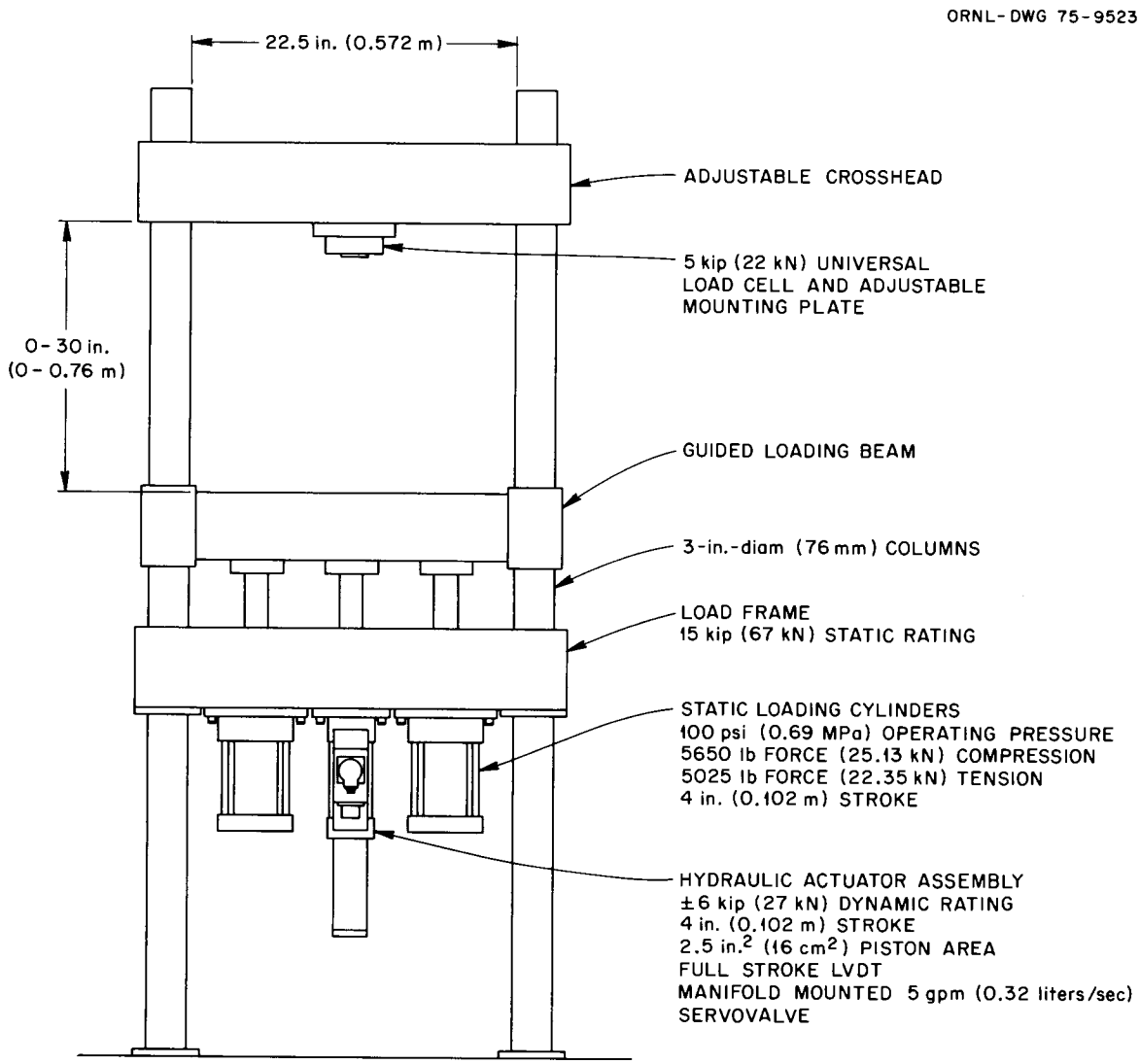

Fig. 3.41. Schematic Drawing of Load Frame for the Complex Loading Testing Machine.

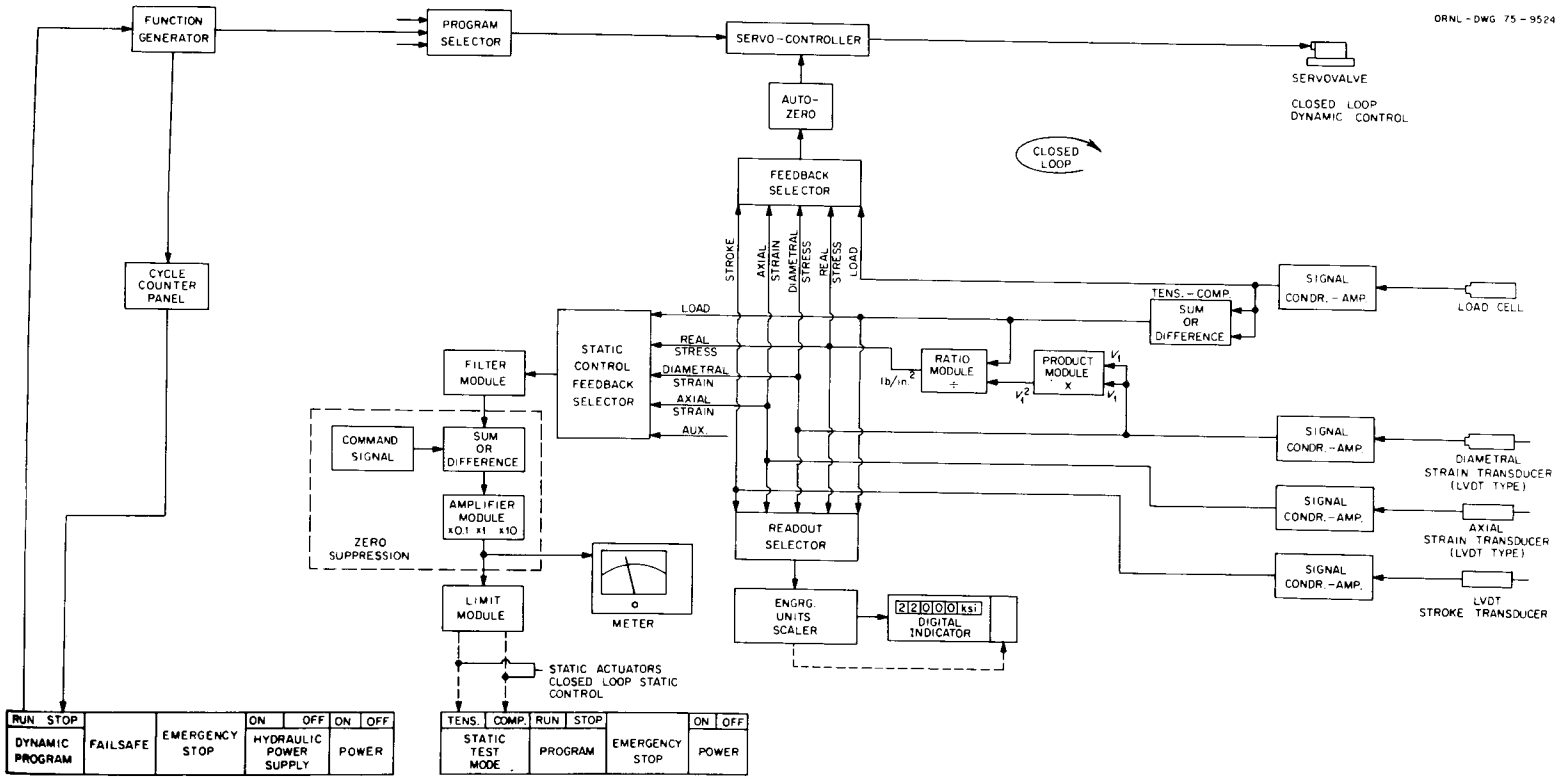

Fig. 3.42. Closed Loop Control Diagram for the Complex Loading Testing Machine.

performed simultaneously on both channels of the testing system provided that the strain cycling periods are alternated between system channels.

Delivery of the testing machine and completed fabrication of specimen grips, extensometry, and heating systems are projected for September 30, 1975. Assembly and checkout of the testing system should begin in early October.

3.2.5 Material Data Processing — M. K. Booker, B.L.P. Booker,* and C.O. Stevens

The computerized system for the in-house acquisition, analysis, storage, and retrieval of mechanical properties data is continuing to function, expand, and develop. Efforts during this past quarter have been concentrated on expanding the data base for the Mechanical Properties Data Storage and Retrieval System (DSRS), with emphasis on the input of fatigue and creep-fatigue data for nuclear structural materials. Also, the capabilities of the system are being expanded to allow the processing of weld metal data, including all the background information needed to characterize the welds. Tables 3.17 and 3.18 present a breakdown of the current data stored on the system.

In addition to data input, the capabilities of the TENSIS[27,28] and FATIGUE[28] computer programs have been expanded. Figure 3.43 shows a plot output from TENSIS in its present form, showing test temperature, strain rate, etc. in contrast with the old version,[28] which labelled plots with test number only. The FATIGUE program has been modified to allow processing of data from strain-controlled tests involving no hold time, tensile holds, compressive holds, or tensile and compressive holds. Figure 3.44 shows a typical plot output from the FATIGUE program.

3.2.6 Elastic Properties of Engineering Construction Materials — J. P. Hammond

Precise measurements show that for metals the "elastic" stress-strain relationships are not perfectly linear, even at low stresses and strain levels, and they become progressively more nonlinear as

---

*Consultant.

Table 3.17. Mechanical Properties ORNL Data Base — Data Summary July 1, 1975

Material	Number of Individual Tests								
	Tensile	Creep	Fatigue	Impact	Slow Bend	Relaxation	Total	Total Last Quarter	New Tests
304 SS	830	489				11	1330	1198	132
316 SS	164	48					212	206	6
2 1/4 Cr-1 Mo	393	74	23	73	18		581	540	41
Incoloy 800	102						102	102	
308 SS	80	14					94	89	5
Hastelloy X	34						34	34	
9 Cr-1 Mo	18						18	18	
INOR-8		246					246	122	124
Other	230	41		83	38		392	337	55
Total	1851	912	23	156	56	11	2969	2646	363
Total Last Quarter	1762	661		156	56	11			
New Tests	89	251	23				363		

Table 3.18. Mechanical Properties Supplemental Data Base — Data Summary July 1, 1975

Material	Number of Individual Tests					
	Tensile	Creep	Fatigue	Total	Total Last Quarter	New Tests
2 1/4 Cr-1 Mo	41	134	278	453	380	73
316 SS	9	171	237	417	283	134
304 SS		45	77	122	45	77
Inconel 718	157	187	209	553	540	13
Incoloy 800	253	168	34	455	402	53
Incoloy 800H	390	451	219	1060	825	235
A 533-B	77			77	77	
1 Cr-1 Mo 1/4 V	1		4	5	5	
Total	928	1156	1058	3142	2557	585
Total Last Quarter	895	1133	529	2557		
New Tests	33	23	529	585		

stress increases. Discrepancies thus often occur between elastic constants determined at different strain levels and rates of strain (for example, constants determined by dynamic and static techniques).

The purpose of this program is to correlate the two separate categories of elastic constants (dynamic and static) for reactor materials of interest, giving specific attention to temperature and other significant test variables. In addition to proportionality constants (Young's modulus, E; shear modulus, G; and Poisson's ratio, ν), elastic and proportional limits (E.L. and P.L.) will be determined. This information is needed to enable more exact and enlightened use of this class of information in engineering design and structural verification work.

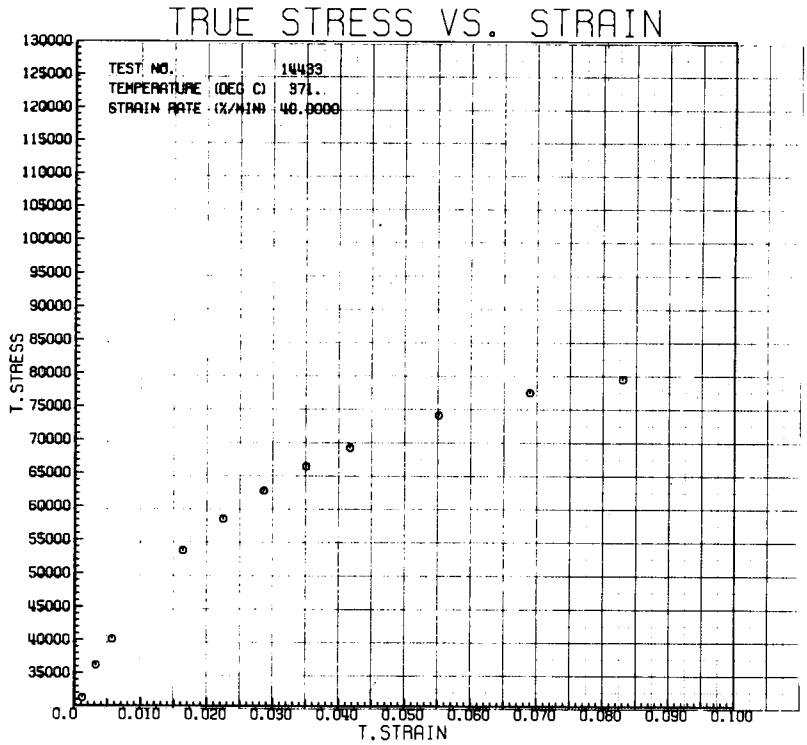

Fig. 3.43. Sample TENSIS True Stress-True Strain Plot.

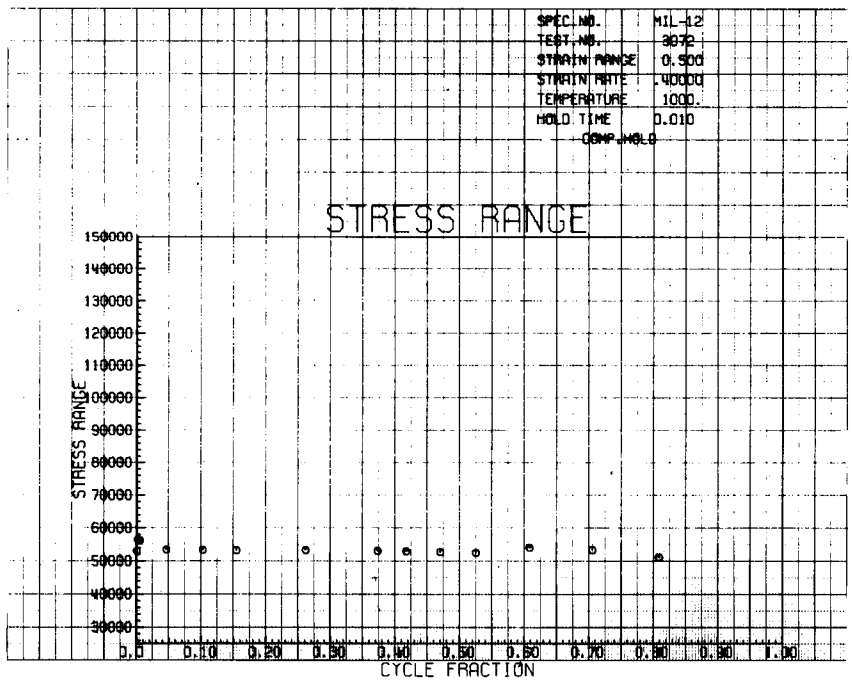

Fig. 3.44. Sample FATIGUE Stress Range Plot.

3.2.6.1 Elastic Properties Determined by Dynamic Tests — J. P. Hammond and M. W. Moyer*

Dynamic (sonic) elastic constants (E, G, and ν) are being established at room temperature on bulk samples by the pulse-echo method (5 MHz) and at elevated temperatures on wires by the remote magnetostrictive technique (0.2 MHz). The methods of determining elastic constants from sound velocities were previously reported.[29] The modulus data, which consist of sets of 52 or more points from room temperature to 650°C (1200°F) or higher, are fitted with cubic polynomials by regression analysis. The equations are of a form that normalizes the high-resolution but less accurate elevated-temperature data to the accurate (0.2–0.6% error) room-temperature values. Results are obtained as computer readout graphs that give best estimates of the elastic property as a function of temperature.

The dynamic elastic constants of 2 1/4 Cr-1 Mo steel (0.135% C, isothermally annealed) were reported earlier[30] for the range 27 to 788°C (80–1450°F). However, the wire specimen on which the elevated-temperature data were taken was cold swaged from a diameter of 1/4 in. (6.4 mm) to 1/16 in. (1.6 mm), and a crystallographic texture introduced by the swaging might have influenced the results. During the last quarter the dynamic elastic constants of 2 1/4 Cr-1 Mo steel were reestablished with a more appropriate wire specimen machined directly from the central region of the 1-in. (25-mm) plate, to preclude introduction of preferred orientation during specimen fabrication, and ground to final size.

Cubic polynomials of the following form were established for E, G, and ν:

$$X = X_0 \; [1 + A_x(T - T_0) + B_x(T - T_0)^2 + C_x(T - T_0)^3] \; ,$$

where

X = the property (E, G, or ν)

X_0 = same at 80°F

---

*Laboratory Development, Oak Ridge Y-12 Plant.

T = temperature in °F

T_0 = 80°F, and

A_x, B_x, and C_x = constants.

The coefficients for the respective properties and standard deviations are given in Table 3.19. Graphical displays of the equations with the data points superimposed are given in Figs. 3.45 through 3.47.

The room-temperature elastic constants of 2 1/4 Cr-1 Mo steel with standard deviations, to which the elevated-temperature properties were normalized, were:

$$E = 31.11 \times 10^6 \pm 0.12 \times 10^5 \text{ psi} = 214.5 \pm 0.08 \text{ GPa},$$

$$G = 12.13 \times 10^6 \pm 0.53 \times 10^4 \text{ psi} = 83.63 \pm 0.037 \text{ GPa},$$

$$\nu = 0.282 \pm 0.0001.$$

Estimates of the elastic properties established with the polynomials at 26.7°C (80°F) and at 28°C (50°F) intervals from 38 to 649°C (100—1200°F) are given in Table 3.20.

The graphs of the dynamic Young's and shear moduli for 2 1/4 Cr-1 Mo are nearly linear with temperature (Figs. 3.45 and 3.46), and the Poisson's ratio shows a mild sinusoidal shape, as before.[30] The elastic constants established for the completely machined specimen did not differ substantially from those determined earlier on the swaged wire, even though we suspect that the latter had a strong crystallographic texture but the former did not. The underlying reasons for the surprisingly similar results are being investigated. The specimen conditions being examined were reported previously.[31]

As a result of much effort, improved precedures that we believe are reliable were developed for determining static elastic constants by use of linear voltage differential transformers (LVDT) and resistance strain gages. A major difficulty in both approaches is assuring that loads are applied axially. In the case of the strain gage method, a specimen of square cross section designed for mounting six gages has been substituted for the former rectangular bar with four gages. The extra set of two gages (mounted vertically) will enable correction for bending due to nonaxial loading and any other causes and will be applicable to all three elastic constants.

Table 3.19. Coefficients for Polynomial Fit to Elastic Constants[a]

Constant	x_0	A_x, °F^{-1}	B_x, °F^{-2}	C_x, °F^{-3}	Std Dev of Fit
E	3.11×10^7 psi	-3.05×10^{-4}	-6.22×10^{-9}	-1.71×10^{-10}	6.87×10^4 psi
G	1.21×10^7 psi	-2.10×10^{-4}	-4.54×10^{-7}	2.73×10^{-10}	9.35×10^4 psi
ν	0.282	-4.67×10^{-4}	2.19×10^{-6}	-2.14×10^{-6}	2.79×10^{-4}

[a]For moduli (E, G) in pascals and T in °C, x_0 should be multiplied by 6895, A_x by 9/5, B_x by $(9/5)^2$, and C_x by $(9/5)^3$. T_0 would be 26.7°C.

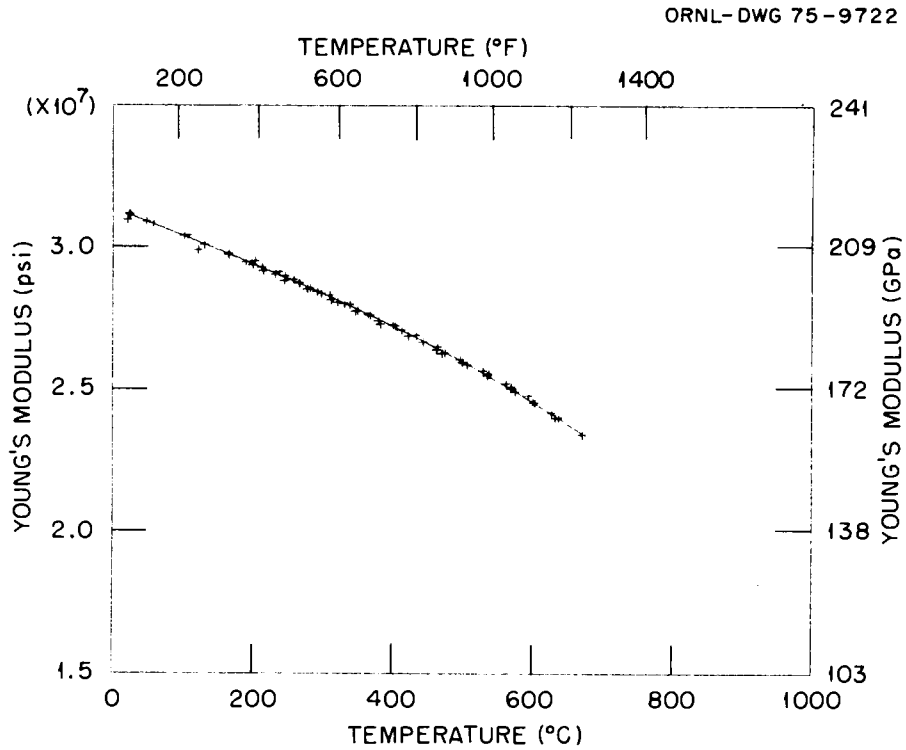

Fig. 3.45. Young's Modulus (E) of 2 1/4 Cr-1 Mo Steel, Heat 20017.

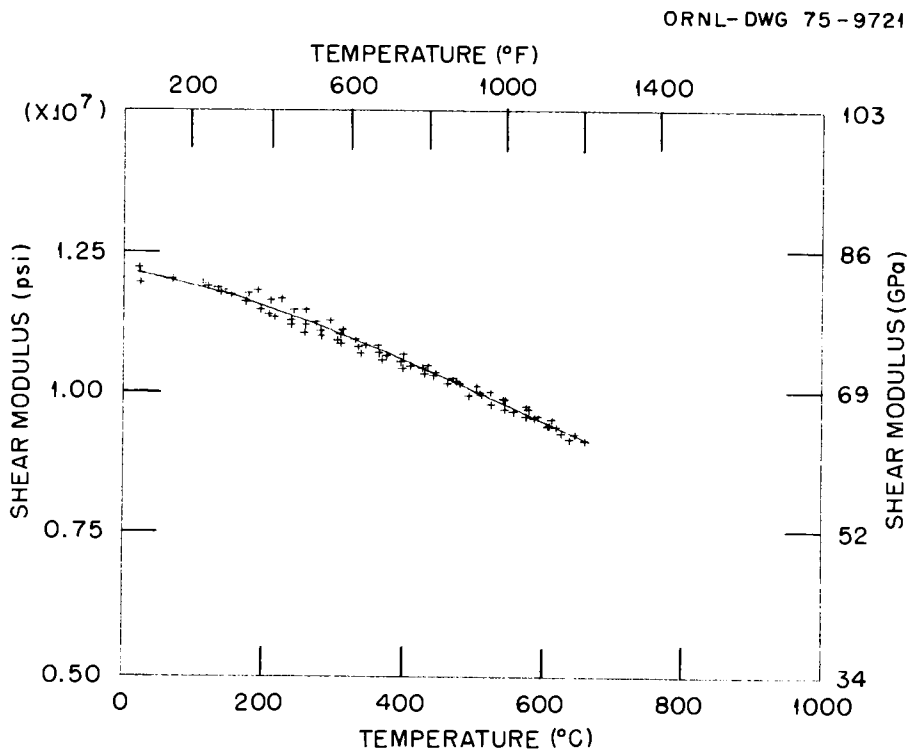

Fig. 3.46. Shear Modulus (G) of 2 1/4 Cr-1 Mo Steel, Heat 20017.

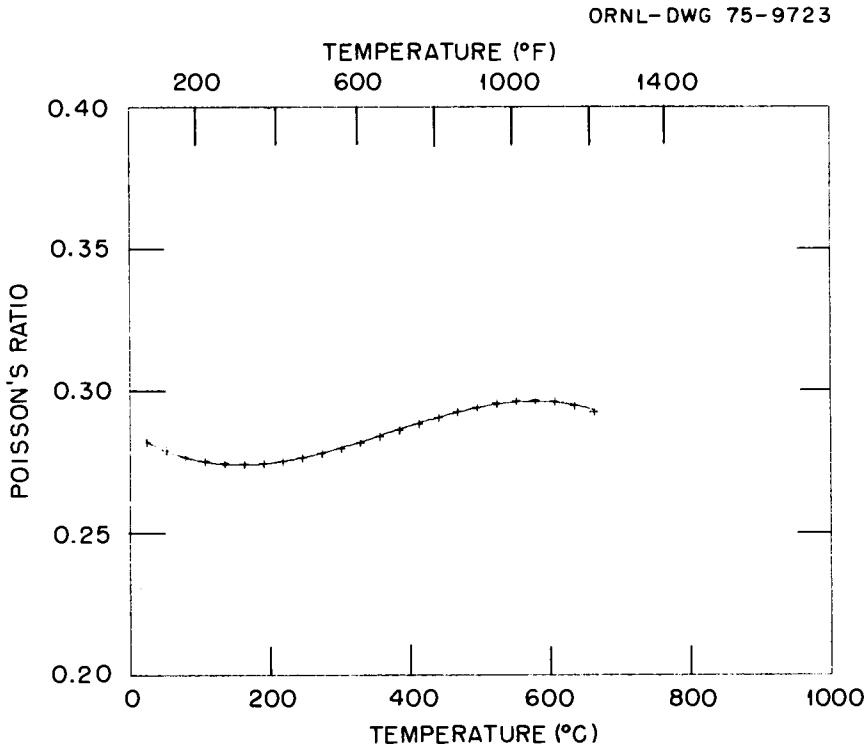

Fig. 3.47. Poisson's Ratio (ν) of 2 1/4 Cr-1 Mo Steel, Heat 20017.

Static Young's moduli were determined on 2 1/4 Cr-1 Mo steel (0.135% C, isothermally annealed) from 27 to 732°C (80–1350°F) with the LVDT equipment employing the improved technique. Determinations were made in quadruplicate at gage strain rates of 0.1, 0.01, and 0.001/hr. Strains in the range of 100 to 150 × 10^{-6} appeared to be recoverable to 732°C (1350°F). To permit repeated testing on the same sample measurements were made for strains to 100 × 10^{-6} by the chord modulus method (ASTM E 231-69).

The following cubic polynomial was determined from the resulting data by regression analysis and used to estimate the static modulus at room temperature and at 28°C (50°F) intervals from 38 to 649°C (100–1200°F):

$$E = 30.487 - 3.83584 \times 10^{-3}T - 2.66228 \times 10^{-9}T^3 ,$$

where E is the Young's modulus (in millions of psi) and T the temperature in °F. The contribution of the quadratic term to the cubic model proved negligible, so the term was omitted. Estimates of the static Young's

Table 3.20. Dynamic Elastic Constants of 2 1/4 Cr-1 Mo Steel, Ht 20017

Temperature		Modulus, psi (GPa)				
(°C)	(°F)	*E*		*G*		ν
25	80	31.12×10^6	(214.6)	12.14×10^6	(83.7)	0.282
38	100	30.99	(213.7)	12.10	(83.4)	0.280
66	150	30.72	(211.8)	12.02	(82.9)	0.278
93	200	30.46	(210.0)	11.94	(82.3)	0.275
121	250	30.19	(208.2)	11.84	(81.6)	0.275
149	300	29.92	(206.3)	11.74	(80.9)	0.274
177	350	29.65	(203.8)	11.63	(80.2)	0.274
204	400	29.37	(202.5)	11.52	(79.4)	0.275
232	450	29.09	(200.6)	11.40	(78.6)	0.276
260	500	28.80	(198.6)	11.27	(77.7)	0.277
288	550	28.50	(196.5)	11.14	(76.8)	0.279
316	600	28.20	(194.4)	11.01	(75.9)	0.281
343	650	27.90	(192.4)	10.87	(74.9)	0.283
371	700	27.58	(190.2)	10.73	(74.0)	0.285
399	750	27.26	(188.0)	10.59	(73.0)	0.287
427	800	26.92	(185.6)	10.44	(72.0)	0.290
454	850	26.58	(183.2)	10.29	(70.9)	0.292
482	900	26.22	(180.8)	10.14	(69.9)	0.294
510	950	25.85	(178.2)	9.98	(68.8)	0.295
538	1000	25.47	(175.6)	9.83	(67.8)	0.296
566	1050	25.08	(172.9)	9.67	(66.7)	0.297
593	1100	24.68	(170.2)	9.52	(65.6)	0.297
621	1150	24.26	(167.3)	9.36	(64.5)	0.296
649	1200	23.82	(164.2)	9.21	(63.5)	0.294

modulus from room temperature to 649°C (1200°F) appear in Table 3.21. The standard deviation was 0.0926.

Table 3.21. Static Young's Modulus of 2 1/4 Cr-1 Mo Steel, Heat 20017

Temperature		*E*	
(°C)	(°F)	(psi)	(GPa)
25	80	30.18×10^6	208.1
38	100	30.10	207.5
66	150	29.90	206.2
93	200	29.70	204.8
121	250	29.49	203.3
149	300	29.26	201.7
177	350	29.03	200.2
204	400	28.78	198.4
232	450	28.52	196.6
260	500	28.24	194.7
288	550	27.93	192.8
316	600	27.61	190.4
343	650	27.26	188.0
371	700	26.89	185.4
399	750	26.49	182.6
427	800	26.06	179.7
454	850	25.59	176.4
482	900	25.09	173.0
510	950	24.56	169.3
538	1000	23.99	165.4
566	1050	23.38	161.2
593	1100	22.72	156.6
621	1150	22.03	151.9
649	1200	21.28	146.7

The static Young's modulus for 2 1/4 Cr-1 Mo steel is presented graphically in Fig. 3.48 together with the curve for our recent dynamic data and the *ASME Pressure Vessel Code* values for comparisons. The temperature-dependent curve for our static Young's moduli lies between the dynamic curve and code values. Whereas the difference between static modulus and the code values is less than 10^6 psi (7 GPa) at the lower temperatures, the difference reaches 2 to 3 × 10^6 psi (15–20 GPa) above about 483°C (900°F). The code does not specify the method of modulus determination, the carbon level, or the heat treatment of the steel.

Our static moduli exhibit strain-rate sensitivity (increasing E with $\dot{\varepsilon}$) that began at 538°C (1000°F) and become more pronounced at 704 and 732°C (1300 and 1350°F). Our early data[30] on dynamic moduli determined on swaged wire are included in Fig. 3.48 for the temperature range 649 to 760°C (1200–1400°F) and appear to constitute a reasonable extrapolation of the present results.

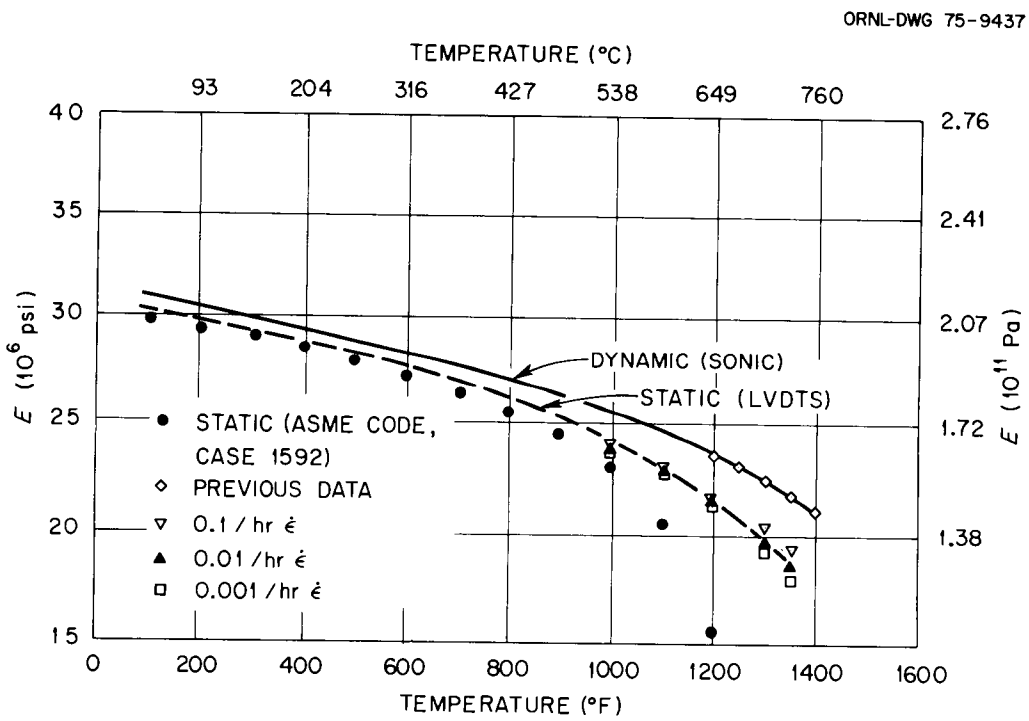

Fig. 3.48. Comparison of Young's Moduli on 2 1/4 Cr-1 Mo Steel.

3.3 MECHANICAL AND METALLURGICAL BEHAVIOR OF WELDMENTS FOR LMFBR — P. Patriarca, G. M. Slaughter, W. R. Martin, and C. R. Brinkman

3.3.1 Studies of Strain Distribution in Weldments and Room-Temperature Elastic Constants — B. R. Dewey* and R. T. King

We have previously described the methods of preparing whole weld cross sections of the FFTF vessel test welds for tensile testing at room temperature.[32] The test welds are made with type 308 CRE weld metal in 2.4-in.-thick (60-mm) type 304 stainless steel plate. The tests are performed on rectangular bar gage specimens 0.25 × 2.37 in. (6.3 × 60 mm) in cross section, with a simple tensile load applied parallel to the 6.0-in. (152-mm) gage length and transverse to the welding direction. Room-temperature tests were first performed on specimens with a photoelastic coating on the gage section to identify critical areas of high strain, and later tests were performed on specimens whose deformation was monitored with strain gage rosettes.[33] Data analyses presented below are for a specimen that was tested in the as-welded condition.

Plots of principal stress against principal strain for the data at each point where a strain gage rosette is installed have been constructed by means of a computer program. These plots in turn furnish a means for partially determining elastic compliances of the weld metal. We have found some considerable variations in these compliances, which gives further evidence that the elastic nonhomogeneity as well as the anisotropy are important factors in the mechanical analysis of weldments.

3.3.1.1 Elastic Compliances

In mechanical properties testing, the measurement of compliance data is more direct than the measurement of stiffness data because the former requires the input of known loads while the latter required the input of known strains. For the weldment under consideration, the

---

*Subcontractor from Department of Engineering Science and Mechanics, University of Tennessee, Knoxville.

stress can be considered to be in the direction of the applied load. (This is still true when a suitable correction for bending is made.)

If it is assummed that weld metal has orthotropic symmetry, the compliance tensor can be written with nine independent elastic constants as

$$[S] = \begin{bmatrix} S_{11} & S_{12} & S_{13} & 0 & 0 & 0 \\ & S_{22} & S_{23} & 0 & 0 & 0 \\ & & S_{33} & 0 & 0 & 0 \\ & & & S_{44} & 0 & 0 \\ & & & & S_{55} & 0 \\ (\text{sym}) & & & & & S_{66} \end{bmatrix}, \tag{13}$$

where the strain $\{\varepsilon\}$ is the following function of stress $\{\sigma\}$

$$\{\varepsilon\} = [S]\{\sigma\}. \tag{14}$$

In the present test, only surface strains can be measured, and we assume that only σ_1 is nonzero.* Hence if Eq. (14) is written out we have, typically

$$\begin{aligned} \varepsilon_1 &= S_{11}\sigma_1 \quad , \\ \varepsilon_2 &= S_{12}\sigma_1 \quad , \end{aligned} \tag{15}$$

where subscripts 1 and 2 are principal directions. Thus, the elastic compliances S_{11} and S_{12} can be determined from the slope of the principal-stress principal-strain curves. The compliances can be expressed in the familiar engineering constants as

$$\begin{aligned} S_{11} &= 1/E_1 \ , \\ S_{12} &= \nu_{21}/E_2 \ , \end{aligned} \tag{16}$$

where, we note, additional tests would be required to determine a Poisson's ratio for weld metal.

---

*For simplicity we assume that the 1-direction is within a few degrees of the direction of loading, and consequently $\sigma_1 >> \sigma_2$.

The results for the engineering constants as given in Eq. (16) are in Table 3.22, where the assumption is made for the apparent Poisson's ratio that $E_1 = E_2$. We feel that this assumption is valid in the base metal and heat-affected zone but not in the weld metal.

3.3.1.2 Interpretation of Results

The elastic constant data in Table 3.22, while showing considerable scatter, do show a trend toward E_1 being lower in weld metal than in base metal. Since the 1-direction is generally perpendicular to the equiaxed grain structure in the weld, this finding agrees with other studies,[34,35] which showed that the masimum value of E was obtained at some angle to the columnar crystal axis.

The uncertainty of the Poisson's ratio for weld metal remains. If weld testing and analysis of behavior of weldments are to progress, it is important that the elastic properties of weld metal be determined in a form similar to Eq. (13). Furthermore, if fracture mechanics specimens, hourglass fatigue specimens, etc. contain welds, the uncertainty of the elastic properties will continue to make the results reported from such tests difficult to interpret.

3.3.2 Task Force on Alternate Structural Materials for Liquid Metal Fast Breeder Reactors — R. T. King, J. H. DeVan, G. M. Goodwin, R. L. Heestand, and H. C. McCurdy*

A Task Force was operative within the Metals and Ceramics Division of ORNL from May 1974 to May 1975 to investigate alternate structural materials for LMFBR applications. Three preliminary reports have been drafted to deal separately with the following problems:

Phase I. identify existing and potential problems with types 304 and 316 stainless steel as LMFBR structural alloys for vessels, piping, and components;

Phase II. assess available commercial alloys and their properties that may solve problems identified in Phase I;

Phase III. identify specific objectives of a program plan to develop alternate structural alloy(s) to the point where an LMFBR system based thereon may be designed by 1985.

---

*Reactor Division

Table 3.22. Variation of Elastic Constants in Type 304-308 Stainless Steel Weldment

Gage	Location	E_1, Modulus of Elasticity (psi)	(GPa)	ν_{21}, Poisson's Ratio
1	Weld, final pass region	23.8×10^6	164	0.40[a]
2	HAZ, quarter thickness region	25.0	172	0.34
4	Weld, quarter thickness region	26.0	179	0.43[a]
5	Weld, root pass region	23.1	159	0.31[a]
7	HAZ, root pass region	28.0	193	0.33
8	Weld, quarter thickness region	21.3	147	0.24[a]
9	Weld, final pass region	29.1	201	0.41[a]
10	Base Metal	27.0	186	0.29
11	Weld, reverse side of gage 1	22.2	153	0.33[a]
12	Weld, reverse side of gage 5	22.2	153	0.27[a]
13	Base Metal	26.0	179	0.30

[a]Uncertain because of incomplete experimental data.

The summaries of the technical findings for Phase I and Phase II are given below without extensive references; a final report is in an advanced stage of preparation.

3.3.2.1 Summary of Phase I Findings

There are sound technical justifications for selecting unstabilized austenitic stainless steels for primary pressure boundaries and major components in sodium-cooled reactors. These reasons, not necessarily listed in the order of relative importance, include the following:

1. Present ASME code rules allow the use of these materials for high-temperature nuclear systems.

2. The nuclear experience and data base for types 304 and 316 stainless steel are relatively large and growing rapidly from numerous experimental programs, component tests, and reactor systems. Nonnuclear applications at elevated temperature are also adding rapidly to the experience and data base.

3. Many product forms and shapes are readily available.

4. Austenitic stainless steels tend to have better strength than most ferritics above about 540°C (1000°F), and type 304 stainless steel is a relatively low-cost austenitic stainless steel.

5. Irradiation effects are *relatively* well-understood and characterized.

6. The material is widely used, and, consequently, there are numerous competing suppliers of materials who are capable of meeting or upgrading to meet standards for nuclear materials.

7. Corrosion and mass-transfer resistance are adequate for at least thick sections for sodium service to 650°C (1200°F), if the carbon and oxygen potentials of the sodium are maintained at the low levels that are now feasible in principle. Air-side corrosion resistance is also acceptable.

8. Long-time strength characteristics appear adequate for many applications, and the materials have relatively good metallurgical stability. They are not as subject to ambient temperature embrittlement as ferritic materials, and do not exhibit ductile-to-brittle transitions.

9. The technology of welding types 304 and 316 stainless steel is relatively well-developed.

10. Improvements are possible in existing unstabilized austenitic stainless steels to optimize the materials for elevated-temperature service by specifying certain composition ranges.

However, these statements are judgments that are subject to change with time. They are influenced by changing plant requirements, design and operating conditions, characteristics of available materials, fabrication and inspection technology, and environmental concerns. For example, current U.S. LMFBR designs (Clinch River Plant) are limited to about 480°C steam temperatures. While core materials are important in this thermal stress limitation, there are problems with structural and pressure boundary materials that also affect this limit. Improved materials may hasten the use of higher steam temperatures, placing the LMFBR in a more competitive position. There are also persisting problems with the use of unstabilized austenitic steels that have been known and "lived with" for years. An example of prime importance is stress-corrosion cracking and intergranular attack, which recur in types 304 and 316 stainless steel despite measures taken to prevent their occurrence. Certain of both classes of problems are summarized below:

1. Types 304 and 316 stainless steel are susceptible to stress-corrosion cracking (SCC) and intergranular attack (IGA), particularly when they are in the sensitized condition and exposed to certain environmental conditions. Many components will become sensitized in service at current LMFBR operating temperatures. Experience has shown that incidents of SCC and IGA failures recur despite countermeasures.

2. The future availability of chromium and nickel is not controlled within this country. Alternate materials that would improve this nation's self-sufficiency in the energy field are desirable.

3. Several unresolved problems exist in the welding of austenitic alloys, including both present fabrication and potential operational problems: (a) the wide range of compositions and properties permitted for weld metal, (b) determining proper ferrite contents to prevent hot cracking and yet avoid embrittlement problems, (c) measurement of ferrite

content, (d) distortion or shrinkage, (e) formation of sensitized heat-affected zones, and selection of stress relief treatments to avoid sensitization, (f) difficulties in ultrasonic inspection of austenitic steel weld joints, (g) difficulties with weld transition joints if austenitic and ferritic materials are included in the same pressure boundary.

4. Although considerable data exist on the properties of austenitic stainless steels, many of these data are not relevant to high-temperature sodium service. It is clear that many additional data, including behavior under complex loadings that vary with time, are needed for types 304 and 316 stainless steel, and future needs may be *nearly* as great as those for other materials that are not presently as well developed.

5. Pressure boundaries and major components made of types 304 and 316 stainless steel in current LMFBR designs will account for approximately 20% of the total cost of power generation. If alternate materials having lower basic materials costs or fabrication costs can be found, substantial savings might be realized.

6. Recent conservative calculations indicate that decarburization of thin sections (for example, intermediate heat exchanger tubing) may reduce the carbon level below the specification range for the materials, thus requiring lowering of the allowable stresses and possible reduction of efficiency and economy. Future design to higher temperatures than those that occur in FFTF and CRBRP with types 304 and 316 stainless steel tubes in intermediate heat exchangers will require new data to establish design feasibility.

7. Wide ranges of composition allowed for types 304 and 316 stainless steel lead to wide variability in properties, posing problems for the designer. This is not peculiar to austenitic stainless steels, but the effect is that the technical safety factors of a design can be less than well-known, and require expensive overdesign to assure safety and reliability.

8. The relatively high coefficient of thermal expansion and low thermal diffusivity and conductivity cause relatively high stresses to develop in austenitic stainless steels during thermal transients. These

cyclic stresses increase the probability of excessive deformation by ratchetting and creep-fatigue mechanisms. A stronger material that is more resistant to time-dependent deformation at LMFBR temperatures, including ratchetting and creep-fatigue, would permit more of the design analysis to be done by conservative simplified methods, and thus reduce the amount of costly and time-consuming inelastic analysis.

3.3.2.2 Summary of Phase II Findings

The Phase II activities involved discussions with industrial nonnuclear and nuclear users of pertinent materials, and rough screening of all alloys to yield selected alloy classes; the screening of alloys by class; and the final selection of alloys within the most promising classes to yield a list of specific commercial alloys for further consideration or development. The criteria used in these processes involve consideration of corrosion and compatibility, welding, fabrication, mechanical properties, engineering codes, and overall design (including strategic material conservation). The specific classes of alloys and the alloys within these classes that are recommended for further investigation are summarized in Table 3.23. No single alloy was found that should be considered a universal panacea; the candidates selected for further investigation and development should be considered for various applications on a component-by-component and part-by-part basis, as designers will undoubtedly do.

The ferritic steels are recommended because they may solve or alleviate virtually all the difficulties mentioned for types 304 and 316 stainless steel in the Phase I Task Force Report; however, they introduce other problems in fabrication, particularly in welding. The 15 Cr-15 Ni austenitic alloys are included because their high-temperature strength may be useful to designers who might wish to continue with austenitic systems; they may have application in thin sections where additional strength is needed immediately, and later in other parts and components. The partially stabilized types 304 and 316 stainless steels are austenitic alternates under development that may reduce sensitization and subsequent attack traceable to contamination during fabrication and

Table 3.23. Summary of Recommendations from Phase II Study by Task Force on Alternate LMFBR Structural Alloys

Alloy Class	Alloy Subclass	Specific Alloys Selected for Further Investigation and Development	
		High Priority	Low Priority
Ferritic Steels	Medium Cr-Mo (8% < Cr < 14%), Stabilized	Jethete M154 Timken 9 Cr-1 Mo, Modified	Sandvik HT9 CRBN R-8 EM-12
Austenitic Steels	15Cr-15Ni	B&W 15-15N Sandvik 12R72	
	Partially Stabilized Types 304 and 316 Stainless Steel	Types 304 and 316[a]	
Nickel-Bearing Solid Solution Alloys	Intermediate Nickel (32Ni-20Cr)	Alloy 800H Alloy 800	
	High Nickel (45-77Ni, 25-5Cr)		Alloy 600

[a]Purchased to specifications with tighter limits on stabilizing elements. As these alloys are presently conceived, their mechanical properties and chemical compositions would satisfy the specifications and standards for types 304 and 316 stainless steels (thus ruling out types 304L and 316L).

erection operations, but that will probably be accepted as types 304 and 316 stainless steels for code purposes. The intermediate nickel alloys, Alloy 800H and Alloy 800, have strength advantages over types 304 and 316 stainless steel, while the high-nickel Alloy 600 has strength advantages in certain temperature ranges. Nickel-bearing alloys are envisioned for parts having special water corrosion requirements, but their use is likely to be limited by cost and sodium corrosion considerations.

The Task Force recognizes the utility of all the existing materials in the elevated-temperature design codes. If the system temperatures drop far below present CRBR design levels, the engineering code-accepted 2 1/4 Cr-1 Mo alloy, or 2 1/4 Cr-1 Mo overlaid with corrosion-resistant austenitic material on the inner surface, could probably be used in more of the plant, particularly the heat transport system.

3.4 MECHANICAL PROPERTIES OF STEAM GENERATOR AND HEAT EXCHANGER MATERIALS — C. R. Brinkman

3.4.1 High-Strain-Rate Tensile Properties of 2 1/4 Cr-1 Mo Steel — R. L. Klueh

Last quarter[36] we reported on the high-strain-rate tensile properties of annealed 2 1/4 Cr-1 Mo steel and then discussed the effects of strain rate on the properties over the range 2.67×10^{-6} to 144/sec and from 25 to 566°C (75 to 1050°F). We have now completed similar tests on the same heat of material, but for the normalized-and-tempered condition. Although the steel to be used in the CRBRP steam generator will be in the annealed condition, the normalized-and-tempered data to be presented here should have relevance for welds.

Given a normalized-and-tempered heat treatment (air cooled from the austenitizing temperature, then tempered at a lower temperature), the microstructure of a 2 1/4 Cr-1 Mo steel can range from entirely bainite to one with bainite and large amounts of proeutectoid ferrite, depending on the section size heat-treated: the smaller the section size, the larger the amount of bainite present. Since the weld metal for a given weld pass will usually be quite small and will be air cooled, the microstructure is expected to be primarily bainite.[37] Thus, studies on a bainitic microstructure should have relevance for weld metal.

In the present studies, a 1-in.-thick (25-mm) plate (heat 20017) was normalized and tempered; the microstructure after heat treatment was completely bainitic. As part of the safety analysis for the steam generator, high-strain-rate elevated-temperature tensile properties are required. Such data have not been previously obtained.

Pieces of the plate were normalized and tempered by heating for 1 hr at 927°C (1700°F), then air cooling, and finally tempering for 1 hr at 704°C (1300°F). The microstructure after this heat treatment is shown in Fig. 3.49 and was entirely bainite. Information on the heat of steel used and the test procedure were previously reported.[36]

The test results are given in Table 3.24. For the four highest strain rates, tests were made at six temperatures between 25 and 566°C (77 and 1050°F), while tests at the lower strain rates were made at

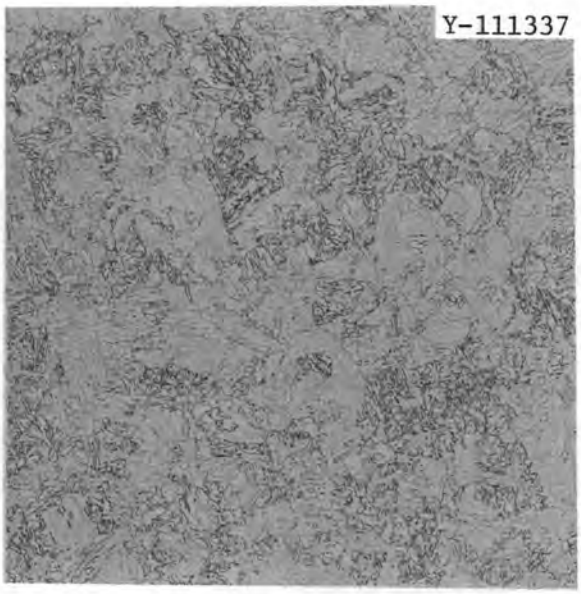

Fig. 3.49. Microstructure of the Normalized-and-Tempered 2 1/4 Cr-1 Mo Steel. 100×.

eight temperatures between 25 and 593°C (77 and 1100°F). Although all results are given in Table 3.24, in the graphical presentation of the results, the 25 to 566°C (77–1050°F) temperature range will be used. In Figs. 3.50 through 3.53 the three-dimensional representations of the 0.2% yield stress, ultimate tensile strength, total elongation, and reduction of area are given over the entire strain rate range of 2.67×10^{-6} to 144/sec and from 25 to 566°C (77–1050°F).

At 25°C (77°F) the yield stress increased with increasing strain rate, the largest effect occurring at the two highest strain rates. At 204°C (400°F), there is relatively little change across the eight orders of magnitude in strain rate, while at 371 and 454°C (700 and 850°F) there is a rather gradual decrease in yield strength with increasing strain rate. Just the opposite occurs at 566°C (1050°F): the yield stress increases with increasing strain rate. At the intermediate temperature of 510°C (950°F), the effect of strain rate on yield strength is relatively minor. In general, the topography of the three-dimensional representation (Fig. 3.50) shows a shallow "valley" of decreasing slope from about 6.67×10^{-5}/sec and 204°C (400°F) toward 144/sec and 454°C (850°F) followed by a slight "ridge" at higher temperatures. Near the high-temperature low-strain-rate corner the yield stress drops off precipitously.

Table 3.24. Tensile Properties of Normalized-and-Tempered 2 1/4 Cr-1 Mo Steel

Strain Rate (sec^{-1})	Temperature (°C)	Temperature (°F)	Strength, MPa (ksi) 0.2% Yield	Ultimate Tensile	Fracture	Elongation, % Uniform	Total	Reduction of Area (%)
144	25	75	668 (96.9)	730 (106.0)	358 (52.0)	12.7	26.6	75
	25	75	730 (106.0)	822 (119.0)	429 (62.2)	11.7	25.7	73
	204	400	548 (79.6)	655 (95.1)	358 (52.0)	12.4	22.4	74
	371	700	478 (69.4)	576 (83.6)	358 (52.0)	11.5	17.4	70
	454	850	469 (68.1)	561 (81.4)	316 (45.9)	5.9	16.3	70
	454	850	471 (68.3)	595 (86.3)	345 (50.0)	6.0	16.2	70
	510	950	468 (67.9)	548 (79.6)	351 (51.0)	6.2	15.5	68
	510	950	465 (67.5)	593 (86.1)	351 (51.0)	5.8	17.0	70
	566	1050	460 (66.7)	582 (84.5)	351 (51.0)	6.0	16.8	67
	566	1050	443 (64.0)	568 (82.4)	323 (46.9)	5.4	15.8	69
16	25	75	635 (92.2)	731 (106.0)	394 (57.1)	9.4	23.5	73
	25	75	710 (103.0)	815 (118.0)	443 (64.3)	10.2	23.9	70
	204	400	531 (77.1)	633 (91.8)	365 (53.0)	11.9	20.4	72
	371	700	464 (67.3)	564 (81.8)	351 (51.0)	9.4	16.7	70
	454	850	454 (65.9)	551 (80.0)	337 (49.0)	4.6	15.1	68
	454	850	453 (65.7)	555 (80.6)	337 (49.0)	6.8	17.1	69
	510	950	458 (66.5)	555 (80.6)	330 (47.9)	4.9	15.5	65
	510	950	462 (67.1)	548 (79.6)	302 (43.9)	5.4	16.2	65
	566	1050	451 (65.5)	526 (76.3)	267 (38.8)	5.3	16.6	73
	566	1050	448 (65.1)	527 (76.5)	274 (39.8)	5.1	17.2	72
1.6	25	75		689 (100.0)	365 (53.0)	8.6	23.4	73
	25	75	588 (85.3)	696 (101.0)	351 (51.0)	8.7	22.8	73
	204	400	516 (74.9)	617 (89.6)	351 (51.0)	11.5	19.5	69
	371	700	464 (67.3)	573 (83.2)	358 (52.0)	9.5	16.5	68
	454	850	471 (68.3)	558 (81.0)	330 (47.9)	5.7	15.7	69
	454	850	468 (67.9)	562 (81.6)	338 (49.0)	7.0	17.1	68
	510	950	469 (68.1)	545 (79.2)	288 (41.8)	6.1	17.3	71
	510	950	468 (67.9)	548 (79.6)	281 (40.8)	6.1	18.3	70
	566	1050	450 (65.3)	510 (74.1)	232 (33.7)	4.9	18.9	77
	566	1050	448 (65.1)	505 (73.2)	211 (30.6)	5.1	18.6	77
0.16	25	75	565 (82.0)	661 (95.9)	288 (41.8)	7.9	22.2	73
	25	75	562 (81.6)	661 (95.9)	281 (40.8)	8.2	23.6	74
	204	400	513 (74.5)	616 (89.4)	358 (52.0)	11.5	18.4	71
	371	700	471 (68.3)	590 (85.7)	365 (53.0)	8.2	16.9	68
	454	850	482 (70.0)	550 (79.8)	295 (42.8)	5.3	17.5	69
	454	850	450 (65.3)	545 (79.2)	253 (36.7)		16.3	67
	510	950	461 (66.9)	534 (77.5)	246 (35.7)	4.6	17.7	74
	510	950	453 (65.7)	540 (78.3)	260 (37.7)	5.2	17.7	75
	566	1050	443 (64.3)	479 (69.6)	211 (30.6)		17.4	79
	566	1050	417 (60.6)	482 (70.0)	211 (30.6)	4.2	17.7	80
6.67×10^{-3}	25	75	560 (81.3)	675 (97.9)	350 (50.8)	8.3	22.2	74.5
	204	400	498 (72.3)	611 (88.7)	341 (49.5)	6.6	18.7	73.4
	371	700	479 (69.5)	610 (88.6)	362 (52.6)	6.2	17.4	63.8
	454	850	458 (66.4)	566 (82.1)	288 (41.8)	5.4	18.6	69.1
	510	950	436 (63.3)	518 (75.2)	217 (31.5)	4.6	19.5	73.0
	538	1000	423 (61.4)	471 (68.4)	260 (37.7)	3.1	20.1	74.2
	566	1050	389 (56.4)	439 (63.7)	168 (24.4)	3.0	22.1	77.8
	593	1100	384 (55.7)	419 (60.8)	134 (19.4)	1.6	22.1	82.4
6.67×10^{-4}	25	75	559 (81.1)	669 (97.1)	350 (50.8)	8.1	21.5	73.9
	204	400	494 (71.7)	616 (89.4)	360 (52.3)	7.0	19.1	72.2
	371	700	480 (69.7)	619 (89.8)	360 (52.2)	6.9	18.9	66.9
	454	850	445 (64.6)	572 (83.0)	302 (43.8)	5.2	19.4	69.1
	510	950	414 (60.1)	498 (72.2)	217 (31.5)	4.2	20.3	72.2
	538	1000	425 (61.7)	464 (67.3)	168 (24.4)	2.4	19.8	79.2
	566	1050	384 (55.8)	420 (61.0)	84 (12.2)	1.9	21.2	80.7
	593	1100	369 (53.6)	385 (55.9)	99 (14.3)	0.9	27.7	87.6
6.67×10^{-5}	25	75	531 (77.1)	643 (93.3)	351 (50.9)	8.5	21.2	73.4
	204	400	485 (70.4)	609 (88.4)	358 (51.9)	6.9	19.3	70.5
	371	700	493 (71.6)	620 (90.0)	354 (51.4)	6.1	18.2	66.8
	454	850	452 (65.6)	544 (79.0)	252 (36.6)	4.6	19.3	70.5
	510	950	442 (64.2)	487 (70.7)	168 (24.4)	2.2	20.9	79.2
	538	1000	411 (59.7)	436 (63.3)	84 (12.2)	1.6	27.4	83.7
	566	1050	361 (52.4)	379 (55.0)	32 (4.7)	0.8	29.2	86.2
	593	1100	319 (46.3)	336 (48.8)	14 (2.0)	0.7	36.2	88.7
2.67×10^{-6}	25	75	535 (77.6)	634 (92.0)	287 (41.9)	7.4	20.9	68.6
	204	400	507 (73.6)	645 (93.6)	415 (60.2)	8.3	19.9	64.4
	371	700	469 (68.1)	623 (90.4)	352 (51.1)	6.0	19.0	68.1
	454	850	449 (65.2)	536 (77.8)	250 (36.3)	3.2	19.8	75.0
	510	950	405 (58.8)	431 (62.5)	49 (7.1)	1.1	21.3	83.4
	538	1000	362 (52.5)	384 (55.8)	21 (3.1)	0.4	24.9	87.2
	566	1050	289 (42.0)	302 (43.9)	14 (2.0)	0.6	27.4	85.6
	593	1100	223 (32.3)	248 (36.0)	14 (2.0)	0.5	33.6	76.7

ORNL-DWG 75-5747

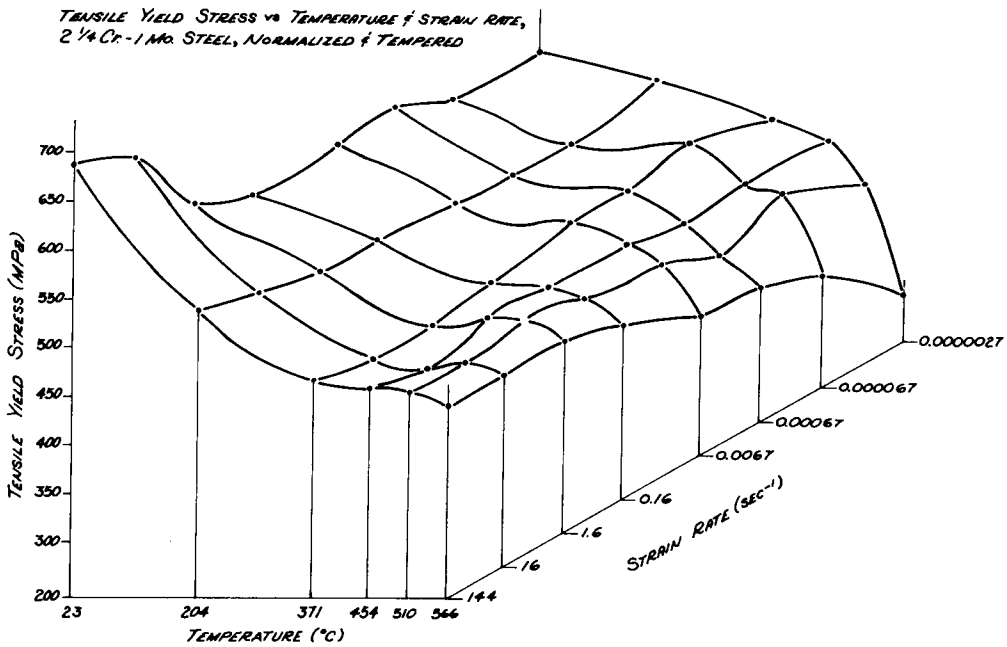

Fig. 3.50. Yield Strength as a Function of Temperature and Strain Rate.

ORNL-DWG 75-5746

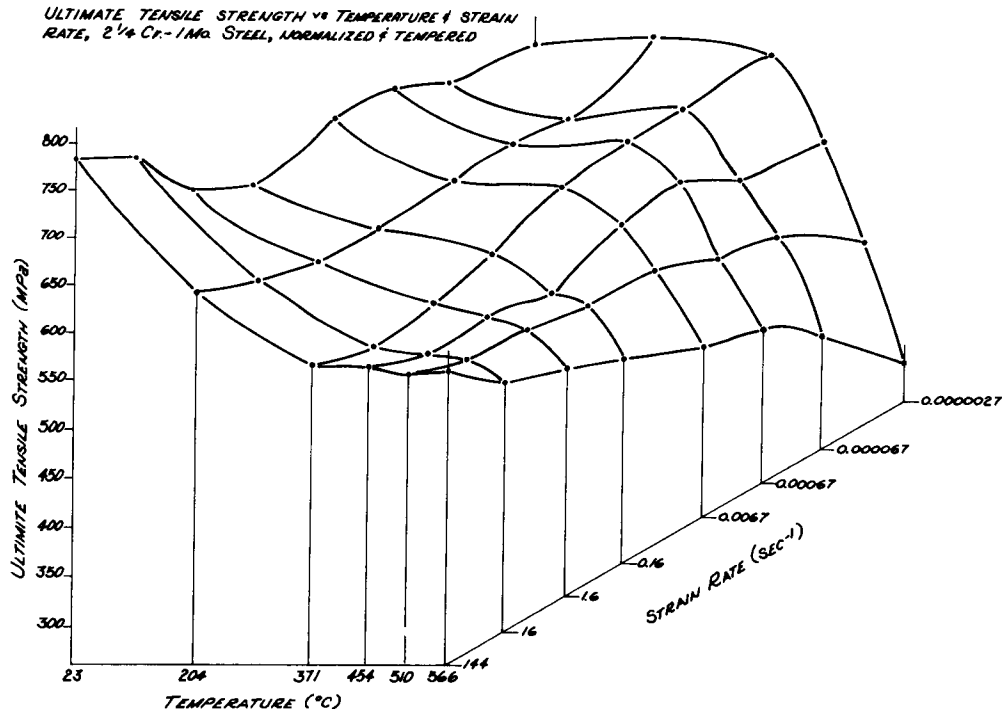

Fig. 3.51. Ultimate Tensile Strength as a Function of Temperature and Strain Rate.

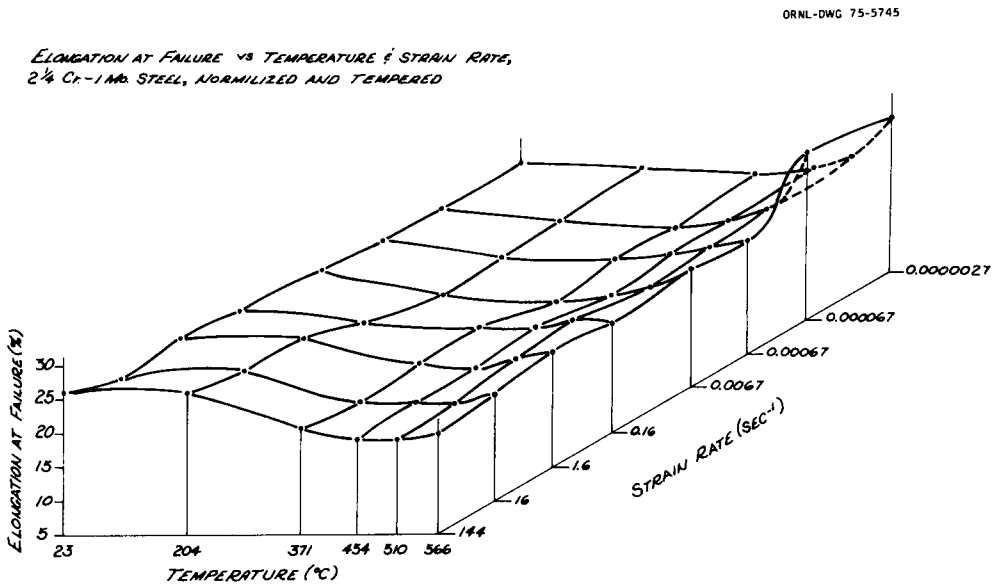

Fig. 3.52. Total Elongation as a Function of Temperature and Strain Rate.

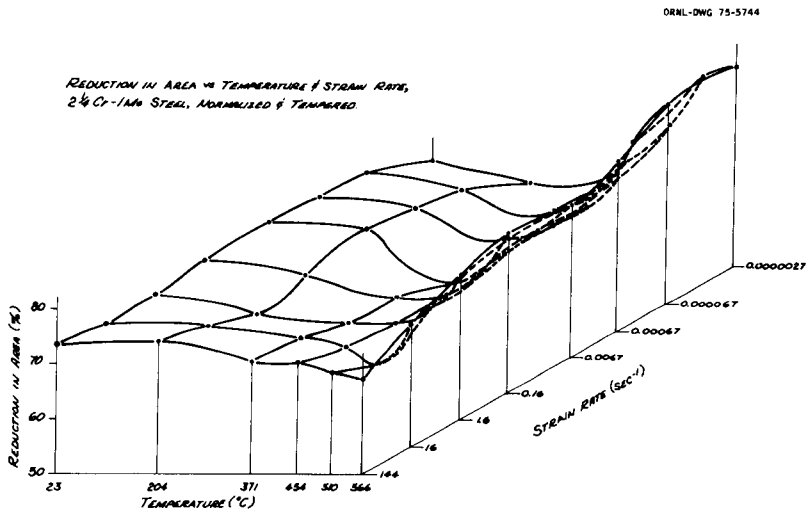

Fig. 3.53. The Reduction of Area as a Function of Temperature and Strain Rate.

In many respects, the ultimate tensile strength behavior is similar to that of the yield stress. There is again a gradual "downhill" slope toward the high-strain-rate high-temperature corner of Fig. 3.51 and a rapid drop in ultimate tensile strength at the high-temperature low-strain-rate corner. However, the deterioration in strength in the latter region occupies a much larger portion of the high-temperature low-strain-rate corner. If the planes of constant strain rate are examined, the hint of a strain aging peak is observed, at least at the lowest strain rates. This is illustrated in Fig. 3.54, where selected curves of ultimate tensile strength versus temperature are given. At 2.67×10^{-6}/sec, there is a plateau between 25 and 371°C (77 and 700°F), followed by a rapid drop in strength at the higher temperatures. At 6.67×10^{-5} and 6.67×10^{-4}/sec (curves not shown), there is a slight peak at 371°C (700°F), but it is again so slight that describing it as a plateau between 25 and 371°C (77 and 700°F) is probably more appropriate. At 6.67×10^{-3}/sec, the plateau is found between 204 and 371°C (400 and 700°F), though at the higher temperatures the strength does not deteriorate as rapidly as it did at the lower strain rates. As the strain rate is increased, the plateau is shifted to higher temperatures. At 144/sec, Fig. 3.54 shows that the plateau is between 371 and 566°C (700 and 1050°F). In Fig. 3.51 the plateaus and peaks give rise to a ridge of decreasing slope that runs diagonally from the low-temperature low-strain-rate corner to the high-temperature high-strain-rate corner of the diagram.

Total elongation and reduction of area, as seen in Figs. 3.52 and 3.53, are only slightly affected by strain rate and temperature. Only at the highest temperatures and the lowest strain rates was an effect observed. At 510 and 566°C (950 and 1050°F), the total elongation and reduction of area showed a large increase as the strain rate was decreased.

Strain rate and temperature effects on fracture stress (not shown graphically) were qualitatively similar to the effect on the ultimate tensile strength. Uniform elongation (also not shown graphically) was little affected by strain rate below 454°C (850°F). However, as the strain rate was decreased at 454°C (850°F), the uniform elongation decreased by 50%: from 6% at 144/sec to 3% at 2.67×10^{-6}/sec. Though

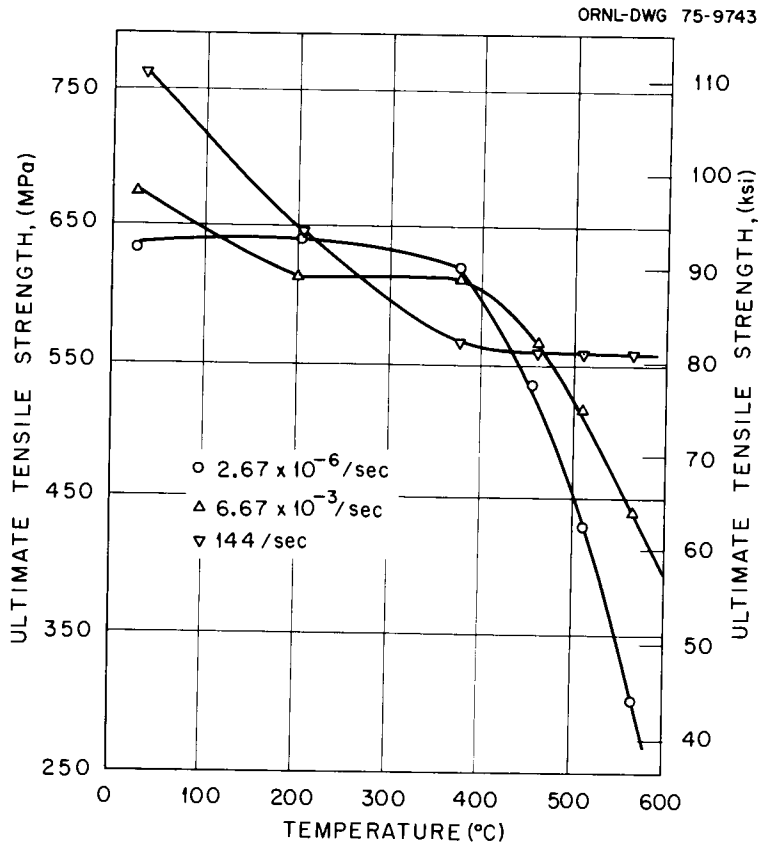

Fig. 3.54. The Ultimate Tensile Strength as a Function of Temperature at 2.67×10^{-6}, 6.67×10^{-3}, and 144/sec.

the uniform elongation at 144/sec was again about 6% at 510 and 566°C (950 and 1050°F), the decrease with decreasing strain rate was somewhat greater: at 2.67×10^{-6}/sec, the uniform elongation was about 1% at 510°C (950°F) and 0.6% at 566°C (1050°F).

The general trends in properties discussed above are well illustrated by examining the engineering stress-strain curves shown in Fig. 3.55. Curves are shown for strain rates of 2.67×10^{-6}, 6.67×10^{-3}, 0.16, and 144/sec at (a) 25, (b) 371, and (c) 566°C (77, 700, and 1050°F). The large increase in strength at 25°C (77°F) at the highest strain rate is seen in Fig. 3.55(a), where the 144/sec curve is displaced upward relative to the two lower strain rate tests also shown. At 371°C (700°F) [Fig. 3.55(b)], a reversal of properties is noted and is a reflection of the moderate dynamic strain aging ridge that appears in Figs. 3.50 and 3.51. Here

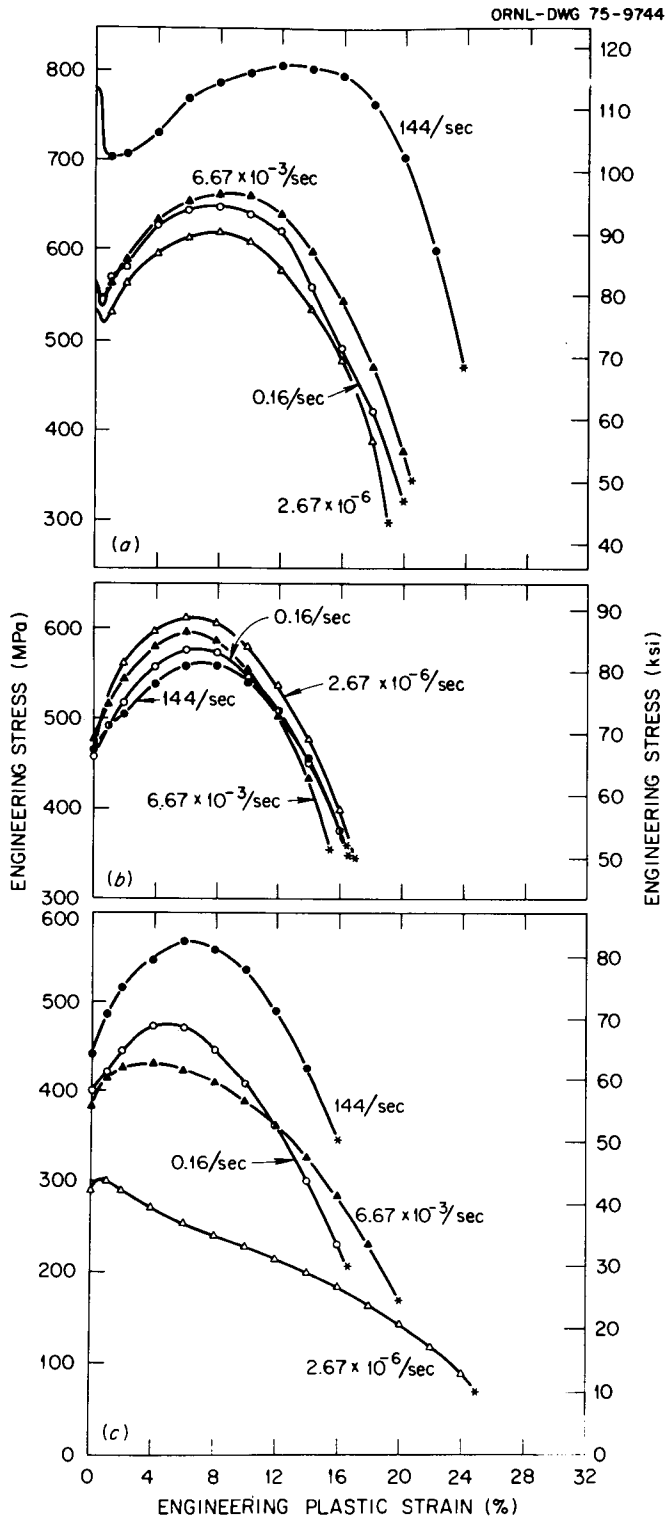

Fig. 3.55. Engineering Stress-Strain Curves for Plastic Deformation for Strain Rates of 2.67×10^{-6}, 6.67×10^{-3}, 0.16, and 144/sec at (a) 25°C. (b) 371°C. (c) 566°C.

the strength is highest for tests at the lowest strain rate, though the differences in the four curves are relatively slight. Finally, at 566°C (1050°F) [Fig. 3.55(c)], the trend again reverses, and the test with the highest strain rate has the highest strength. Additionally, Fig. 3.55(c) shows the large drop in uniform elongation and fracture strength and the large increase in total elongation that occur as the strain rate is decreased at elevated temperatures.

Yield points, with their accompanying Luder's strain, were observed for all strain rates at 25°C (77°F). All tests at strain rates of 6.67×10^{-3}/sec and above exhibited yield points at 204°C (400°F), while at 371°C (700°F) slight yield points were observed at strain rates of 1.6/sec and above. Stress-strain curves with large-amplitude serrations were noted at 2.67×10^{-6} and 2.67×10^{-5}/sec at 204°C (400°F) and 6.67×10^{-4} and 6.67×10^{-3}/sec at 371°C (700°F). For the three lowest strain rates at 25°C (77°F) and temperatures above 371°C (700°F), slight serrations were often noted. Above 6.67×10^{-3}/sec we were unable to detect serrations because of "noise" in the high-speed equipment. All specimen failures were ductile cup-cone fractures, and metallography indicated that the failures were of a transgranular mode with no evidence of any intergranular separation.

Large quantities of normalized-and-tempered 2 1/4 Cr-1 Mo steel — especially plates and forgings — are used by the electric utility industries. As a result, this material has been tested considerably, although apparently not over an extended strain rate range. Because of the variations in microstructure that result when different section sizes are heat-treated, a range of strengths is found when "normalized-and-tempered" steel tested by different investigators is compared.

Smith[38] collected and published all available tensile properties data for 2 1/4 Cr-1 Mo steel. When the strength properties obtained in this study are compared with those given by Smith, we find that for strain rates between 6.67×10^{-3} and 6.67×10^{-5}/sec the properties fall near the upper part of the scatter band of data given by Smith. Likewise, at 2.67×10^{-6}/sec the low-temperature tests fall in this region, while the high-temperature tests tend toward the lower half of the scatter

band. For the high-strain-rate tests, from 0.16 to 144/sec, most of the data fall above or just inside Smith's scatter band for normalized-and-tempered steel.

It turns out that the data of this study fall quite nicely in Smith's scatter band for quenched-and-tempered material. For the strain rate range of 6.67×10^{-5} to 6.67×10^{-3}/sec, these data tend toward the center of the scatter band. Considering the microstructure, the good agreement with quenched-and-tempered steel is not surprising. Since the steel of this study was entirely bainite, it would be expected to have properties as strong as or stronger than most of the normalized-and-tempered values given by Smith, where the material tested was of various product forms in various thicknesses. Likewise, one would expect the properties of the present study to compare favorably with those of a quenched-and-tempered steel, since the faster cooling rate during quenching would result in larger amounts of bainite in the microstructure. Although the strain rates for the tests compiled by Smith were not given, we would expect then to be around 6.67×10^{-5} to 6.67×10^{-3}/sec [ASTM specifications for tensile testing (E 151) recommend a strain rate of 0.005/min (8.33×10^{-5}/sec) to the 0.6% offset strain and 0.1/min (1.67×10^{-3}/sec) to failure]. Thus, the good agreement at these strain rates is not unexpected. Smith gives only a small amount of data on weld metal. Again, however, the agreement of the data of this study and Smith's compilation is excellent.

We previously reported[36] on the behavior of this same heat of steel in the annealed condition, where the microstructure consisted of proeutectoid ferrite, small amounts of bainite, and fine pearlite; the proeutectoid ferrite contained small carbide particles throughout the matrix. Since bainite is also a ferrite but contains a very fine carbide precipitate, it does not appear unreasonable to compare the qualitative behavior of the two heat-treated conditions.

In the annealed condition, the ultimate tensile strength exhibited the most change with strain rate and temperature. The effect on yield strength was relatively minor: at 25°C (77°F), there was a large increase with increasing strain rate above 0.16/sec, and there was a minor

peak in the topography of the relationship of yield strength, temperature, and strain rate at intermediate temperatures and strain rates. Qualitatively, the total elongation and reduction of area of the annealed steel behaved similarly to those for the normalized-and-tempered steel shown in Figs. 3.52 and 3.53.

At 25°C (77°F) the ultimate tensile strength for the annealed steel increased quite rapidly with increasing strain rate. For a constant strain rate the relationships of ultimate tensile strength with temperature exhibited a dynamic strain aging peak [i.e., as the temperature was increased above 25°C (77°F), the strength first decreased, then increased, went through a peak, then decreased]. The maximum peak height occurred at about 350°C (662°F) and the lowest strain rate tested (2.67×10^{-6}/sec). As the strain rate was increased the peak height decreased and occurred at progressively higher temperatures. For the highest strain rate tested (144/sec) the peak occurred near 566°C (1050°F). In three dimensions, this gave rise to a diagonal "ridge" that crossed from about 350°C (662°F) and 2.67×10^{-6}/sec to about 566°C (1050°F) and 144/sec and a diagonal "valley" between the peak and room temperature.

Although there are similarities in the ultimate tensile strength behavior of the two heat-treated conditions, the primary difference is the pronounced dynamic strain aging "peaks" (for a constant strain rate) for the annealed steel as opposed to the more subdued "plateaus" of the normalized-and-tempered steel. Since the matrix material in each heat-treated condition is ferrite, the decreased peak height for the bainitic ferrite must be due to the nature of the carbon and carbides. Transmission electron microscopy shows that the tempered bainite of the normalized-and-tempered steel contains much more precipitate than the proeutectoid ferrite of the annealed steel. This may mean that most of the carbon is removed from solution during the tempering treatment, thus making less available for subsequent dynamic strain aging.

3.4.2 Heat-to-Heat Variations of 2 1/4 Cr-1 Mo Steel — R. L. Klueh

In austenitic stainless steels, heat-to-heat variations in mechanical properties are generally attributed to differences in chemical composition. For a ferritic material, such as 2 1/4 Cr-1 Mo steel, where

a phase transformation can occur during heat treatment, differences in the heat treatment process could give rise to mechanical property differences. Furthermore, several different methods are used to heat-treat ferritic steels. As a result, we are conducting a series of tests designed to determine the effect of heat treatment on mechanical properties.

At present, isothermally annealed 2 1/4 Cr-1 Mo steel is being considered for use in the steam generator of the CRBRP. Since the decision to use isothermally annealed material was made after a considerable amount of mechanical properties data had been collected on fully annealed material (furnace cooled from the austenitizing temperature), it was of interest to determine the kinds of differences that can result from different annealing treatments. Also, much of the data available in the literature is on fully annealed material.[38]

Before the decision was made to use annealed material for the steam generator, a limited amount of data on normalized-and-tempered steel was obtained and is presented in Sect. 3.4.1 of this report. For comparative purposes some of those data will be presented here.

The 2 1/4 Cr-1 Mo steel tested was from a heat of commercial material obtained from Babcock and Wilcox (B&W heat 20017); the chemical composition is given in Table 3.25. The steel was in the form of a 1-in.-thick (25-mm) plate, and sections of this plate were annealed by austenitizing for 1 hr at 927°C (1700°F) and then furnace cooling. We tested material taken from plates cooled at two different rates, hereafter referred to as AN-1 and AN-2. To obtain steel in the isothermally annealed condition, the plates were furnace cooled from 927 to 704°C at about 83°C/hr (150°F/hr), held at 704°C for 2 hr, then furnace cooled; this material will be referred to as IA. For a separate experiment, six tensile specimens taken from the plate were heat treated in a furnace where the cooling rate could be automatically controlled. Three specimens were cooled to room temperature at rates of 28, 56, and 83°C/hr (50, 100, and 150°F/hr), and three other specimens were cooled at these rates to 704°C (1300°F), held at 704°C for 2 hr, then air cooled.

Tensile tests were performed in air on a 44-kN Instron test machine according to the requirements of ASTM E 8–69 and E 151–64. The specimens

Table 3.25. Chemical Composition of 1-in. (25-mm) Plate of Annealed 2 1/4 Cr-1 Mo Steel (Heat 20017)

Analysis	Chemical Composition, wt %							
	C	Mn	Si	Cr	Mo	Ni	S	P
Vendor	0.11	0.55	0.29	2.13	0.90		0.014	0.011
ORNL	0.135	0.57	0.37	2.2	0.92	0.16	0.016	0.012

were heated in a three-zone resistance furnace with temperature controlled to ±2°C with less than a 3°C temperature variation along the specimen gage length. The test machine was operated at constant crosshead velocity, and the reported strain rates were determined from the crosshead velocity and the initial gage length. Tensile specimens having a 0.25-in.-diam × 1.25-in.-long (6.35 × 31.75-mm) reduced section were fitted with an extensometer to measure the strains below 5%. Good agreement was obtained between the extensometer charts and the load-deflection charts above the 0.2% offset stress. Total elongation was determined from gage marks on the specimen, while uniform elongation was determined from the load-deflection charts.

Figure 3.56 shows the cooling rates of the test materials. Cooling curves A, B, and C were for the specimens given a controlled furnace cool to room temperature at rates of 28, 56, and 83°C/hr (50, 100, and 150°F/hr), respectively. Curves D and E are those of AN-2 and AN-1, respectively (AN-2 was cooled faster). Finally, the dashed curves AI, BI, and CI were the controlled isothermal anneals, where the specimens were cooled to 704°C (1300°F) at rates of 28, 56, and 83°C/hr (50, 100, and 150°F/hr), respectively, then held at 704°C (1300°F) for 2 hr and air cooled. The isothermally annealed plate, IA, was cooled to 704°C (1300°F) like AI, but instead of air cooling after 2 hr at 704°C (1300°F), it was furnace cooled [from 704°C (1300°F) to about 300°C (572°F); the cooling curve would be just to the left of curve E in Fig. 3.56]. Also shown is the cooling curve (N) for the 1-in. plate when air cooled (normalized).

When specimens from each of these anneals were examined metallographically, all were found to be primarily proeutectoid ferrite with

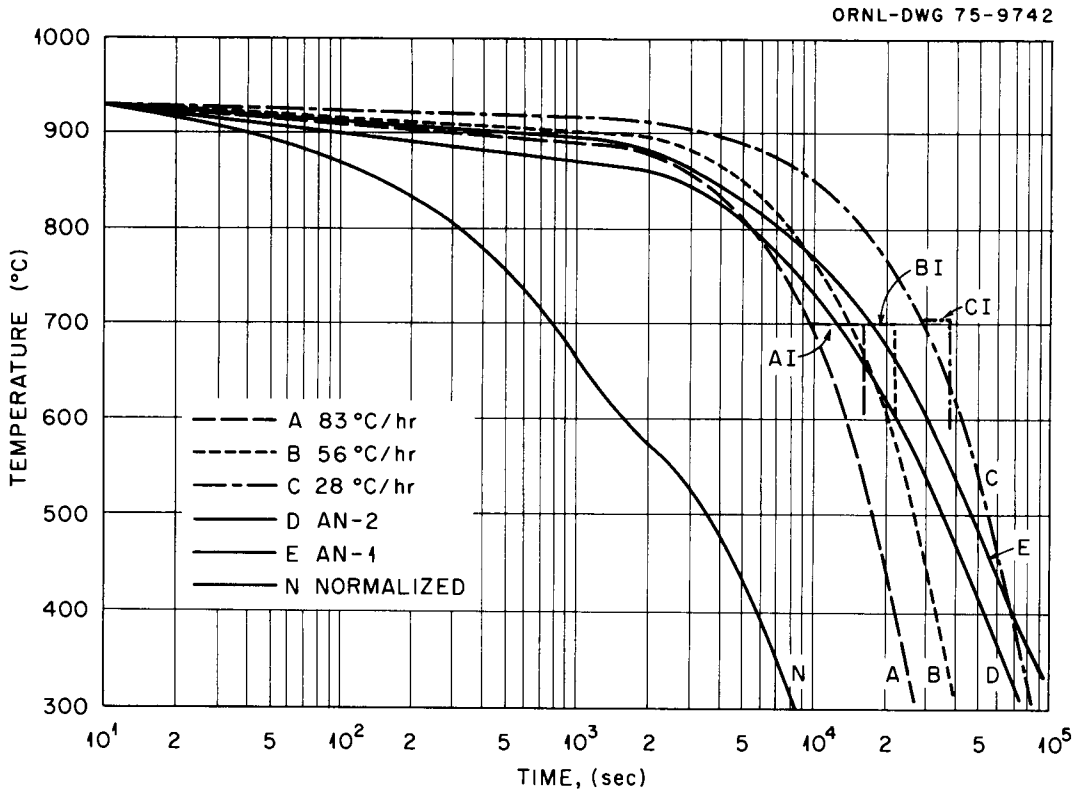

Fig. 3.56. Cooling Rate Curves for 2 1/4 Cr-1 Mo Steel Test Materials.

some pearlite and bainite, the amounts depending on the cooling rates. With the exception of the specimen cooled to room temperature at 83°C/hr (150°F/hr) (the fastest cooling rate used), the ferrite had a "salt and pepper" structure, indicating that it contained a very fine precipitate. In Table 3.26 the estimated amounts of bainite and pearlite in each specimen are given, along with estimated ferrite grain sizes. Figure 3.57 shows photomicrographs of AN-1, AN-2, and IA, the most extensively tested plate materials.

3.4.2.1 Tensile Properties

Table 3.27 shows the room-temperature tensile properties for the six specimens given the different full anneals or isothermal anneals. Obviously, the three specimens given a full anneal show the largest variation in room-temperature tensile properties: an increase in the cooling rate from 927°C (1700°F) to room temperature led to increased

Table 3.26. Estimated Amounts of Austenite Decomposition Products in the Microstructure

Cooling Rate (°C/hr)	Microstructural Constituents, %[a]		Ferrite Grain Size (ASTM)
	Bainite	Pearlite	
28 to 25°C	10–15	5–10	6
55 to 25°C	20	1–2	5
83 to 25°C	30	Little	5
28 to 704°C[b]	3–5	5–8	5
55 to 704°C[b]	5–10	3–5	5
83 to 704°C[b]	10–15	1–2	5
Furnace Cool AN-1	5	5–6	6
Furnace Cool AN-2	25	Little	5
83 to 704°C[c]	15	1–2	5

[a]Balance = Ferrite

[b]Held for 2 hr at 704°C, then air cooled.

[c]Held for 2 hr at 704°C, then furnace cooled to 250°C.

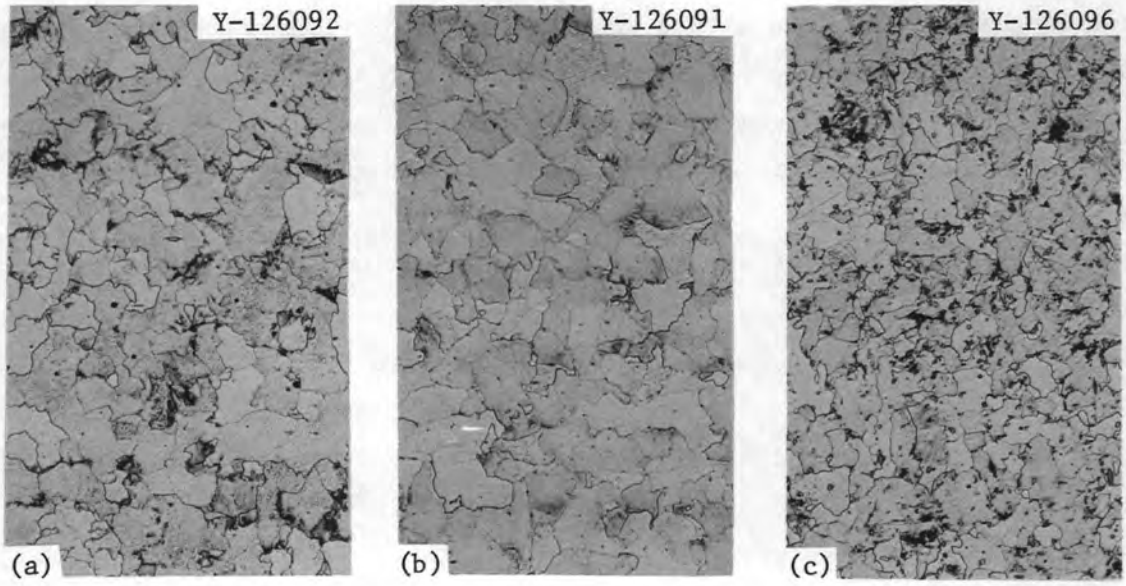

Fig. 3.57. Microstructures of 2 1/4 Cr-1 Mo Steel Test Materials Taken from Plates Given Three Different Annealing Treatments. (a) AN-1; full anneal (furnace cooled) at slow rate. (b) AN-2; full anneal, but cooled faster than AN-1. (c) IA, isothermal anneal.

Table 3.27. Effect of Heat Treatment on Room-Temperature Tensile Properties of 2 1/4 Cr-1 Mo Steel at a Strain Rate of 6.67×10^{-4}/sec

Cooling Rate[a] (°C/hr)	Strength, MPa (ksi)			Elongation, %		Reduction of Area (%)
	Yield	Ultimate	Fracture	Uniform	Total	
28 to RT	249 (36.1)	500 (72.5)	312 (45.3)	12.9	28.0	70.9
55 to RT	274 (39.7)	546 (79.3)	375 (54.4)	12.7	27.0	62.6
83 to RT	298 (43.2)	583 (84.6)	452 (65.6)	13.2	25.8	53.5
28 to 704°C[b]	272 (39.5)	475 (68.9)	277 (40.2)	15.1	31.1	73.4
55 to 704°C[b]	280 (40.7)	508 (73.7)	288 (41.8)	12.6	28.2	72.1
83 to 704°C[b]	277 (40.2)	483 (70.1)	300 (43.6)	13.8	29.3	71.0

[a]All specimens were cooled from 927°C, where they had been held for 1 hr before cooling.

[b]These specimens were held for 2 hr at 704°C, then air cooled.

strength and decreased total elongation and reduction of area, though the uniform elongation was only slightly affected. On the other hand, the different cooling rates to 704°C (1300°F) for the isothermally annealed specimens had much less effect on the properties. Thus, it appears that the cooling rate to 704°C (1300°F) for the isothermal anneal has relatively little effect on the room-temperature tensile properties, while the cooling rate from the austenitizing temperature to room temperature can considerably affect the properties.

The effect of heat treatment was examined in greater detail for a series of specimens taken from heat-treated plates, namely AN-1 [cooled to 704°C (1300°F) in about 3.5 hr], AN-2 [cooled to 704°C (1300°F) in about 4.8 hr], and IA (isothermally annealed). Specimens taken from these plates were tensile tested between 25 and 593°C (77 and 1100°F) at strain rates of 2.67×10^{-6}, 6.67×10^{-5}, 6.67×10^{-4}, and 6.67×10^{-3}/sec. The results are given in Tables 3.28 through 3.30. Over this range of test variables, there were significant differences in properties, which must be attributed to the heat treatment.

Table 3.28. Tensile Properties of Annealed 2 1/4 Cr-1 Mo Steel — Slower Cool (AN-1)

Temperature		Strength, MPa (ksi)			Elongation, %		Reduction of Area
(°C)	(°F)	Yield	Ultimate	Fracture	Uniform	Total	(%)
			Strain Rate — 6.67×10^{-3}/sec				
25	75	260 (37.7)	527 (76.4)	309 (44.8)	12.0	28.2	69.9
204	400	219 (31.7)	443 (64.2)	282 (40.9)	11.8	24.6	70.9
260	500	232 (36.9)	492 (71.3)	342 (49.6)	9.1	20.2	62.8
316	600	239 (36.1)	494 (71.6)	367 (53.3)	9.3	19.1	57.7
371	700	228 (33.0)	499 (72.4)	359 (52.0)	9.0	19.0	57.4
454	850	216 (31.3)	468 (67.9)	287 (41.6)	10.2	22.9	64.2
510	950	208 (30.2)	428 (62.1)	218 (31.6)	8.5	24.7	70.9
538	1000	211 (30.6)	424 (61.5)	204 (29.6)	8.5	23.3	72.5
566	1050	196 (28.4)	367 (53.2)	148 (21.4)	9.1	28.3	80.3
593	1100	201 (29.1)	354 (51.3)	138 (20.0)	7.6	27.8	81.7
			Strain Rate — 6.67×10^{-4}/sec				
25	75	258 (37.4)	525 (76.1)	316 (45.8)	12.8	28.3	67.3
204	400	221 (32.0)	450 (65.2)	294 (42.6)	11.0	23.7	66.2
260	500	244 (35.4)	489 (70.9)	352 (51.1)	9.0	20.0	62.4
316	600	239 (34.6)	516 (74.9)	395 (57.3)	9.2	19.0	57.8
371	700	227 (32.9)	514 (74.5)	352 (51.0)	9.5	20.1	56.9
454	850	230 (33.3)	499 (72.4)	310 (44.9)	8.7	21.0	61.5
510	950	224 (32.5)	459 (66.5)	231 (33.5)	8.9	23.6	69.2
538	1000	217 (31.5)	423 (61.3)	119 (17.3)	8.4	26.3	73.9
566	1050	208 (30.2)	374 (54.3)	63 (9.1)	7.7	25.9	79.3
593	1100	203 (29.5)	328 (47.5)	35 (5.1)	6.8	36.5	84.7
			Strain Rate — 6.67×10^{-5}/sec				
25	75	254 (36.8)	514 (74.6)	309 (44.8)	13.3	28.7	69.5
204	400	236 (34.3)	474 (68.8)	315 (45.7)	10.9	22.9	66.0
260	500	247 (35.8)	525 (76.2)	396 (57.5)	9.3	19.4	57.1
316	600	239 (34.6)	554 (80.3)	432 (62.6)	9.1	18.6	51.2
371	700	229 (33.2)	516 (74.8)	343 (49.8)	10.4	21.3	58.6
454	850	221 (32.1)	494 (71.7)	281 (40.7)	8.7	21.8	64.5
510	950	215 (31.2)	416 (60.3)	210 (30.5)	7.4	29.4	76.2
538	1000	203 (29.5)	354 (51.3)	212 (30.8)	7.4	36.4	82.6
566	1050	203 (29.5)	333 (48.3)	49 (7.1)	6.8	37.0	84.0
593	1100	185 (26.8)	250 (36.2)	17 (2.5)	5.8	37.2	89.0
			Strain Rate — 2.67×10^{-6}/sec				
25	75	243 (35.2)	489 (71.0)	295 (42.8)	12.7	28.0	68.6
204	400	233 (32.8)	491 (71.2)	341 (49.6)	9.7	21.0	63.9
260	500	247 (35.9)	566 (82.2)	450 (65.3)	10.2	19.1	54.2
316	600	244 (35.4)	593 (86.1)	436 (63.3)	10.3	20.2	56.2
371	700	229 (33.3)	563 (81.7)	356 (51.7)	10.1	20.6	66.5
454	850	226 (32.8)	500 (72.6)	210 (30.5)	9.5	23.8	67.2
510	950	206 (29.9)	351 (50.9)	99 (14.4)	6.2	35.8	83.8
538	1000	189 (27.5)	268 (38.9)	64 (9.3)	4.6	30.6	86.6
566	1050	174 (25.3)	209 (30.3)	41 (5.9)	3.7	56.7	88.4
593	1100	145 (21.0)	165 (24.0)	33 (4.9)	3.6	59.0	86.2

Table 3.29. Tensile Properties of Annealed 2 1/4 Cr-1 Mo Steel — Faster Cool (AN-2)

Temperature		Strength, MPa (ksi)			Elongation, %		Reduction of Area
(°C)	(°F)	Yield	Ultimate	Fracture	Uniform	Total	(%)
			Strain Rate — 6.67×10^{-3}/sec				
25	75	273 (39.6)	566 (82.1)	365 (53.0)	12.3	26.4	64.5
93	200	243 (35.3)	509 (73.9)	331 (48.0)	11.3	26.0	66.2
204	400	237 (34.4)	475 (69.0)	331 (48.0)	9.6	22.0	61.9
316	600	247 (35.8)	498 (72.3)	380 (55.1)	8.7	18.3	56.3
371	700	248 (36.0)	528 (76.6)	408 (59.2)	7.9	17.5	53.7
454	850	232 (33.7)	525 (76.2)	352 (51.1)	8.5	19.8	56.8
510	950	240 (34.8)	489 (71.0)	280 (40.7)	8.3	20.2	63.1
538	1000	239 (34.7)	466 (67.7)	260 (37.7)	8.1	20.8	64.9
566	1050	248 (36.0)	420 (61.0)	210 (30.5)	7.3	21.7	70.1
593	1100	220 (32.0)	388 (56.3)	176 (25.5)	7.1	26.0	72.9
			Strain Rate — 6.67×10^{-4}/sec				
25	75	274 (39.7)	555 (80.6)	358 (52.0)	11.3	27.5	65.8
93	200	264 (38.3)	506 (73.5)	335 (48.6)	10.1	24.9	65.4
204	400	245 (35.5)	491 (71.3)	345 (50.1)	10.0	21.7	60.9
316	600	251 (36.4)	546 (79.3)	426 (61.9)	9.3	18.3	50.9
371	700	247 (35.8)	542 (78.7)	422 (61.2)	9.0	18.7	49.8
454	850	254 (36.8)	531 (77.1)	365 (53.0)	8.6	19.4	54.3
510	950	245 (35.6)	500 (72.6)	289 (41.9)	8.9	20.7	62.5
538	1000	242 (35.1)	489 (71.0)	288 (41.8)	8.6	22.2	60.6
566	1050	243 (35.2)	430 (62.4)	204 (29.6)	9.2	24.7	69.1
593	1100	234 (34.0)	371 (53.8)	127 (18.4)	8.4	30.4	74.1
			Strain Rate — 6.67×10^{-5}/sec				
25	75	268 (38.9)	538 (78.1)	358 (51.9)	12.1	26.9	63.1
93	200	253 (36.7)	500 (72.6)	338 (49.1)	11.0	24.0	62.9
204	400	259 (37.6)	508 (73.7)	372 (54.0)	9.3	21.0	59.1
316	600	251 (36.4)	557 (80.8)	443 (64.3)	9.0	19.0	49.8
371	700	253 (36.7)	569 (82.6)	433 (62.8)	10.0	19.4	51.5
454	850	243 (35.2)	566 (82.2)	386 (56.0)	10.8	21.6	54.3
510	950	243 (35.2)	506 (73.5)	302 (43.9)	10.9	24.2	59.0
538	1000	237 (34.4)	464 (67.3)	246 (35.7)	8.9	25.6	64.0
566	1050	235 (34.1)	391 (56.8)	391 (22.4)	7.0	28.1	70.0
593	1100	223 (32.4)	328 (47.6)	328 (15.3)	5.8	37.6	78.4
			Strain Rate — 2.67×10^{-6}/sec				
25	75	271 (39.4)	525 (76.2)	351 (51.0)	11.9	24.6	62.0
93	200	269 (39.1)	494 (71.7)	337 (48.9)	10.8	23.0	61.6
204	400	265 (38.4)	551 (80.0)	437 (63.4)	9.7	18.8	51.4
316	600	256 (37.2)	612 (88.8)	463 (67.2)	9.7	18.9	48.8
371	700	260 (37.8)	649 (94.2)	471 (68.3)	12.5	22.0	50.4
454	850	256 (37.1)	502 (72.8)	302 (43.9)	10.7	25.0	61.9
510	950	262 (38.0)	479 (69.5)	260 (37.7)	11.1	27.2	60.1
538	1000	243 (35.3)	378 (54.9)	77 (11.2)	7.0	28.7	70.9
566	1050	236 (34.1)	307 (44.6)	14 (2.0)	4.4	32.7	79.6
593	1100	203 (28.9)	241 (35.0)	14 (2.0)	1.8	44.3	80.3

Table 3.30. Tensile Properties of Isothermally Annealed 2 1/4 Cr-1 Mo Steel (IA)

Temperature		Strength, MPa (ksi)			Elongation, %		Reduction of Area (%)
(°C)	(°F)	Yield	Tensile	Fracture	Uniform	Total	
			Strain Rate — 6.67×10^{-3}/sec				
25	75	265 (38.4)	534 (77.5)	308 (44.7)	12.0	27.5	72.2
204	400	218 (31.7)	464 (64.7)	266 (38.7)	10.3	24.2	70.0
260	500	217 (31.4)	444 (64.4)	288 (41.8)	9.4	22.4	69.5
316	600	227 (33.0)	492 (71.4)	329 (47.8)	8.5	19.8	67.8
371	700	214 (31.1)	488 (70.8)	347 (50.4)	8.8	18.7	59.2
454	850	220 (32.0)	471 (68.4)	273 (39.6)	9.0	22.6	65.1
510	950	215 (31.2)	432 (62.7)	220 (31.9)	8.4	23.3	68.3
538	1000	209 (30.4)	386 (56.0)	169 (24.5)	8.1	27.0	73.0
566	1050	199 (28.9)	364 (52.9)	114 (16.5)	8.2	28.6	80.4
593	1100	202 (29.3)	329 (47.8)	105 (15.3)	6.9	33.7	82.7
			Strain Rate — 6.67×10^{-4}/sec				
25	75	254 (36.8)	521 (75.6)	309 (44.9)	12.4	27.8	70.8
204	400	220 (31.9)	452 (65.6)	288 (41.8)	10.2	23.0	67.3
260	500	232 (33.7)	467 (67.8)	313 (45.4)	9.6	21.0	67.3
316	600	225 (32.7)	495 (71.8)	355 (51.5)	10.1	21.0	62.1
371	700	228 (33.1)	505 (73.3)	349 (50.7)	9.7	20.5	57.7
454	850	217 (31.5)	475 (68.9)	271 (39.4)	8.9	23.6	65.2
510	950	214 (31.0)	423 (61.4)	189 (27.5)	8.2	23.6	71.7
538	1000	212 (30.8)	385 (55.9)	147 (21.2)	7.7	28.2	76.7
566	1050	207 (30.1)	354 (51.4)	78 (11.3)	7.1	32.8	80.2
593	1100	195 (28.3)	288 (41.8)	42 (6.1)	5.7	40.6	85.3
			Strain Rate — 6.67×10^{-5}/sec				
25	75	249 (36.2)	513 (74.4)	301 (43.7)	12.9	28.5	73.0
204	400	225 (32.6)	462 (67.1)	299 (43.4)	10.3	22.7	68.2
260	500	236 (34.2)	500 (72.5)	355 (51.5)	9.3	20.2	61.9
316	600	226 (32.8)	520 (75.5)	376 (54.5)	9.1	19.5	57.6
371	700	225 (32.6)	512 (74.3)	344 (49.9)	9.6	20.6	60.1
454	850	218 (31.7)	469 (68.0)	253 (36.7)	8.4	22.5	67.3
510	950	214 (31.0)	404 (58.7)	175 (25.4)	7.9	27.5	74.7
538	1000	209 (30.3)	347 (50.4)	106 (15.4)	7.1	31.6	81.9
566	1050	205 (29.7)	310 (45.0)	70 (10.1)	5.7	44.1	87.1
593	1100	181 (26.2)	236 (34.2)	49 (7.1)	5.0	59.4	89.5
			Strain Rate — 2.67×10^{-6}/sec				
25	75	241 (35.0)	489 (71.0)	296 (43.0)	13.3	26.4	70.1
204	400	238 (34.6)	501 (72.7)	347 (50.4)	9.5	20.3	62.1
260	500	235 (34.1)	539 (78.2)	397 (57.6)	9.4	21.1	55.8
316	600	229 (33.2)	543 (78.8)	370 (53.7)	9.9	21.1	61.8
371	700	230 (33.3)	528 (76.6)	335 (48.7)	9.8	21.4	60.9
454	850	218 (31.7)	454 (65.9)	196 (28.4)	8.3	24.8	72.2
510	950	209 (30.4)	345 (50.1)	35 (5.1)	5.1	32.5	84.0
538	1000	203 (29.5)	265 (38.5)	35 (5.1)	3.1	44.2	87.6
566	1050	184 (26.7)	214 (31.1)	35 (5.1)	2.7	61.2	86.8
593	1100	156 (22.7)	172 (25.0)	15 (2.1)	2.9	64.0	87.3

The yield strengths of AN-1 and IA showed very little difference, while AN-2 was slightly stronger. AN-2 also showed much less of a decrease in yield strength with increasing temperature and showed essentially no effect of strain rate, whereas, the other two heat treatments showed a decrease in yield strength for the 2.67×10^{-6}/sec strain rate above about 510°C (950°F). In Fig. 3.58, the yield strength is shown as a function of temperature for AN-1, AN-2, and IA.

Smith[38] has compiled the available data for the elevated-temperature properties of commercial 2 1/4 Cr-1 Mo steel gathered from published literature and industrial laboratories. For the tensile properties of the annealed steel, Smith gave a scatter band of data. The scatter band is shown in Fig. 3.58, and all three heat treatments give yield stresses that fall near the center of the scatter band. Only at the highest test temperatures do the properties of AN-2 deviate from the center into the upper half of the scatter band; this deviation occurs for AN-2 because the yield stress for this material does not decrease as rapidly with temperature as it does for the other two heat treatments.

The ultimate tensile strength behavior was somewhat more complicated than the yield stress behavior. In Fig. 3.59 the ultimate tensile strengths for the three heat treatments are shown as functions of temperature for strain rates of 2.67×10^{-6} and 6.67×10^{-3}/sec. Again, AN-1 and IA show similarities: the ultimate tensile strengths are the same between 25 and 200°C (77 and 392°F) at both strain rates; they are also the same from 510 to 593°C (950–1100°F) at 2.67×10^{-6}/sec and from about 371 to 593°C (700–1100°F) at 6.67×10^{-3}/sec. At the intermediate temperatures, where the peaks occur in the curves of Fig. 3.59, significant differences occur between the IA and AN-1 heat treatments and AN-2.

In the regions of the peaks in Fig. 3.59 dynamic strain aging occurs,[36] and it is in the range of these strain aging peaks that the largest deviations for the three heat treatments occur. At 2.67×10^{-6}/sec the strain aging peaks for AN-1 and IA occur at about the same temperature — near 315°C (600°F) — while the peak for AN-2 is shifted to a somewhat higher temperature — about 371°C (700°F). This shift to higher temperatures for AN-2 is also obvious at 6.67×10^{-3}/sec.

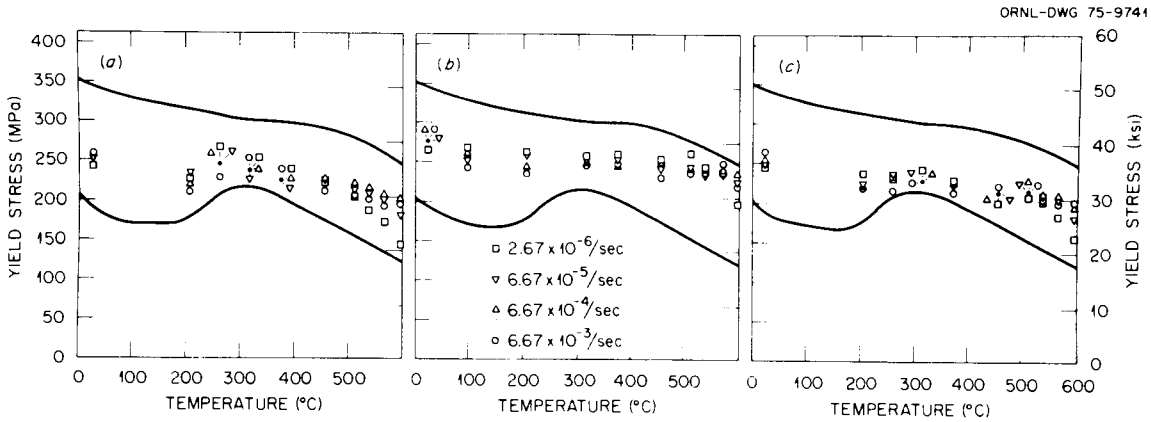

Fig. 3.58. Yield Strength as a Function of Temperature for (a) AN-1, (b) AN-2, and (c) IA. Also shown is the scatter band for the data on annealed 2 1/4 Cr-1 Mo steel compiled by Smith.

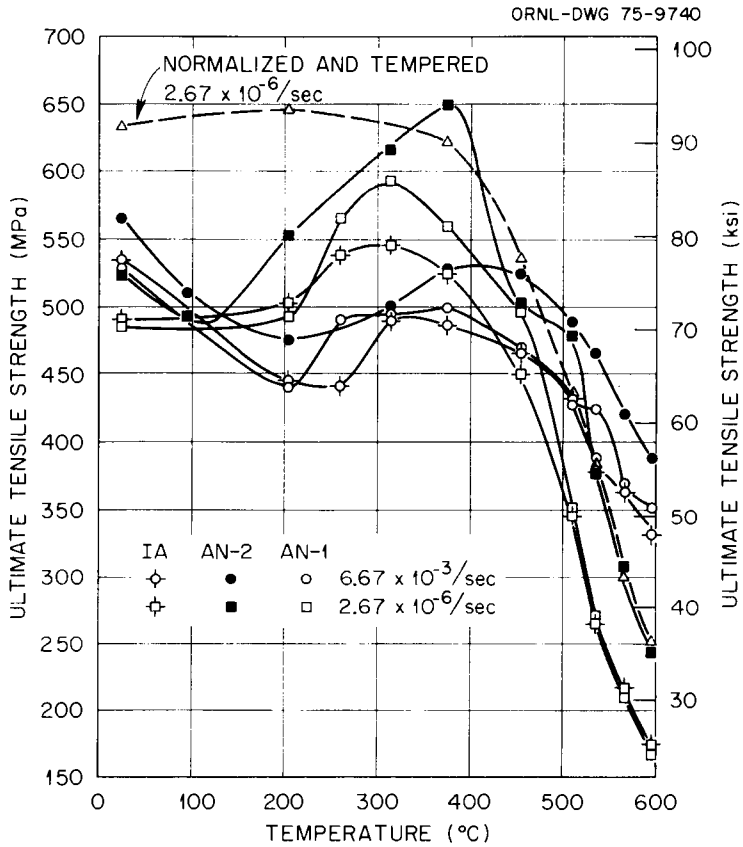

Fig. 3.59. The Ultimate Tensile Strength for the Three Different Heat Treatments AN-1, AN-2, and IA as Functions of Temperature at Strain Rates of 6.67×10^{-3} and 2.67×10^{-6}/sec. Also shown is the curve for this same steel in the normalized-and-tempered condition at a strain rate of 2.67×10^{-6}/sec.

To get an idea of how much dynamic strain aging has increased the ultimate tensile strength in the neighborhood of the peak, Fig. 3.59 also shows data for normalized-and-tempered material taken from this same heat of steel and also tested at a strain rate of 2.67×10^{-6}/sec (Sect. 3.4.1). The microstructure for the steel in that heat-treated condition was completely bainitic. As seen from the figure, AN-2 in the region of the strain aging peak exceeds the strength of the bainitic material.

When the results of Fig. 3.59 are compared with the scatter band from Smith's compilation[38] for the annealed steel, the curves for all three heat treatments at a strain rate of 6.67×10^{-3}/sec are found to fall within the scatter band. Smith gives no details on the strain rates of the tests in his compilation. However, if most of the tests conformed to the ASTM specification E 151, the ultimate tensile strength in most of those tests would probably be reached at a strain rate of about 6.67×10^{-3}/sec or greater [E 151 recommends a strain rate of 0.005/min (8.33×10^{-5}/sec) to the 0.6% offset strain and 0.1/min (1.67×10^{-3}/sec) to failure]. Thus, under test conditions similar to those in Smith's compilation the data for all three heat treatments would appear to fall within his scatter band.

3.4.2.2 Discussion

Kunitake[39] has determined a continuous cooling transformation diagram for 2 1/4 Cr-1 Mo steel. Except for carbon content, Kunitake's steel had a chemical composition similar to the heat of steel used in the present study. Whereas the steel of this investigation contained about 0.135% C, Kunitake's contained 0.09% C. When the microstructural analysis given in Table 3.26 is compared with that given by Kunitake, however, it becomes obvious that the continuous cooling diagrams differ for the two steels. According to Kunitake's diagram, the cooling rates used in the present study should pass well into the pearlite region. However, the microstructures analyzed in Table 3.26 indicated that this did not occur. One possible reason for this difference is the higher hardenability that results from increased carbon content (i.e., the start of the ferrite transformation is moved to longer times).

Although our studies do not enable us to determine the start of the ferrite transformation curve, our microstructural analysis indicates that the start of the pearlite transformation has been shifted to longer times by several hours. In Fig. 3.60, the estimated curves for the formation of a trace of pearlite and for pearlite formation for the heat of steel used in these studies are shown as dashed lines, along with the curves given by Kunitake. The estimated curves were drawn by use of the shapes and lower temperatures determined by Kunitake and are only meant to be schematic. Note that although chemical composition is probably the most important determinant of hardenability, it is not the only one. Previous work with this steel[40] indicated that it may have a larger austenitic grain size, which would also increase hardenability.

As a result of the cooling rate studies and room-temperature tensile tests, it appears that for an isothermal anneal, the rate at which the steel is cooled to 704°C (1300°F) has little effect on the strength and ductility. However, for a continuous furnace cool the effect of cooling rate is quite important, even at the relative low cooling rates employed for these studies. This is especially true when the cooling rates for the two continuously cooled plates are compared (curves D and E of Fig. 3.56). If we assume that essentially all the ferrite that forms has formed by the time the steel reaches 700°C (1292°F), only about an hour difference is involved for the two steels.

Although the different cooling rates to 700°C (1292°F) resulted in different amounts of proeutectoid ferrite, and thus more bainite for AN-2 than AN-1, this difference in bainite content cannot be used to account for the strength differences, especially in the region of the dynamic strain aging peaks. If the amount of bainite were accounting for the differences, then one would expect a larger dynamic strain aging peak for the normalized-and-tempered steel, which is entirely bainite. On the contrary, however, no peak was observed for this completely bainitic steel. Hence, the explanation must involve the proeutectoid ferrite, which makes up the bulk of the microstructure for both AN-1 and AN-2.

To continue these studies, we have tempered specimens from AN-1 and AN-2 for 1 hr at 704°C (1300°F) to determine whether the differences

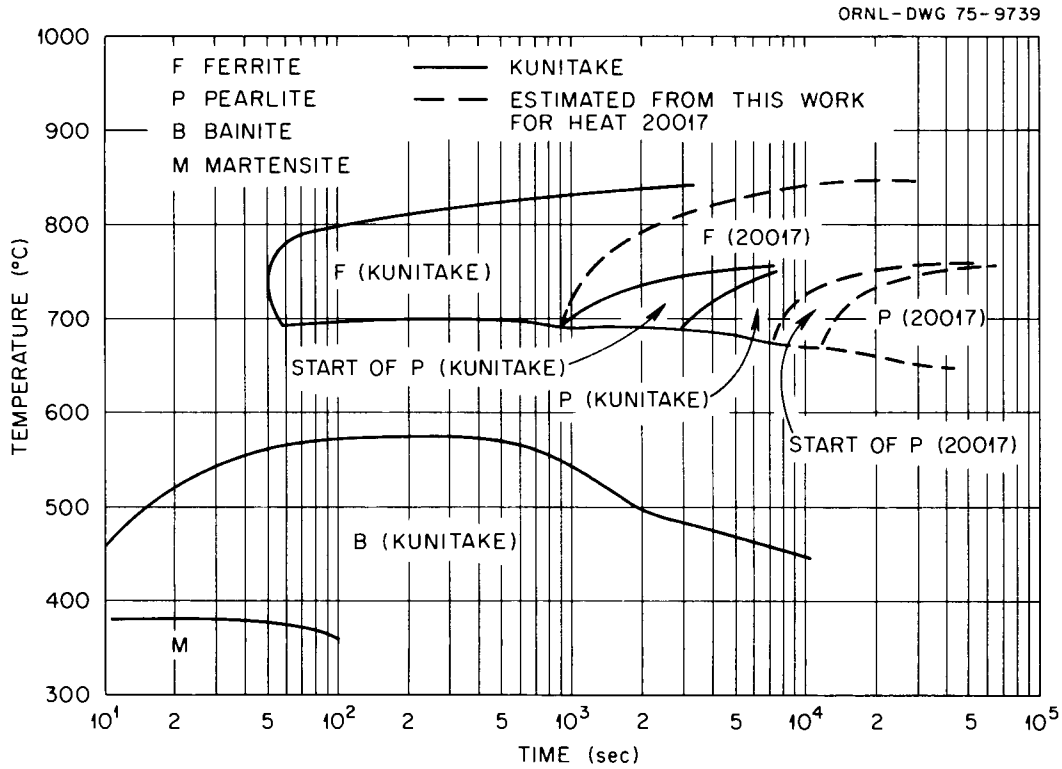

Fig. 3.60. Estimated Continuous Cooling Diagram for Heat 20017 as Determined from Microstructural Studies and Kunitake's Diagram.

between these two heat treatments can be minimized. Next quarter the results for the creep-rupture studies on these steels will be reported. We are also examining the materials by transmission electron microscopy.

3.4.3 Fatigue Behavior of 2 1/4 Cr-1 Mo Steel — C. R. Brinkman

3.4.3.1 Creep-Fatigue Data Analysis — M. K. Booker

Analysis of creep-fatigue data for 2 1/4 Cr-1 Mo steel is continuing. Unfortunately, many methods of analysis require a larger range of data than are currently available,[41] although data are continually being obtained, and analysis by various techniques will eventually be attempted. At present, analysis has been performed by the methods of strain range partitioning[42] and linear summation of damage,[43] since these methods can be performed on the available data. Preliminary results were reported previously.[41]

The previous linear summation results have been recalculated by use of a revised equation for rupture life as a function of stress and temperature, given in Sect. 3.4.4 of this report. This method involves numerical integration of a typical relaxation curve during a hold period to calculate the creep damage per cycle as

$$D_c(1) = \int_0^{t_h} dt/t_r \ , \tag{17}$$

where t_h is the total hold time and t_r is the rupture life. The total creep damage is then

$$D_c = N_h D_c(1) \ , \tag{18}$$

where N_h is the total number of cycles to failure in the given hold-time test.

The fatigue damage is given by

$$D_F = N_h/N_f \ , \tag{19}$$

where N_f is the number of cycles to failure that would have been expected with no hold time. Then, the total damage is given by

$$D = D_c + D_F \ . \tag{20}$$

Figure 3.61 shows the results of calculations from Eq. (20) for the currently available data. The smaller data points in the figure were calculated by use of expected values of t_r and N_f. The larger symbols indicate calculations made by use of lower limit values on t_r and N_h (i.e., t_m and N_D). Thus,

$$D_c^{\,d} + D_F^{\,d} = D_d \ , \tag{21}$$

where $D_c^{\,d}$ and $D_F^{\,d}$ are the values of creep and fatigue damage calculated from t_m and N_D. The N_D values were obtained from the ORNL fatigue design

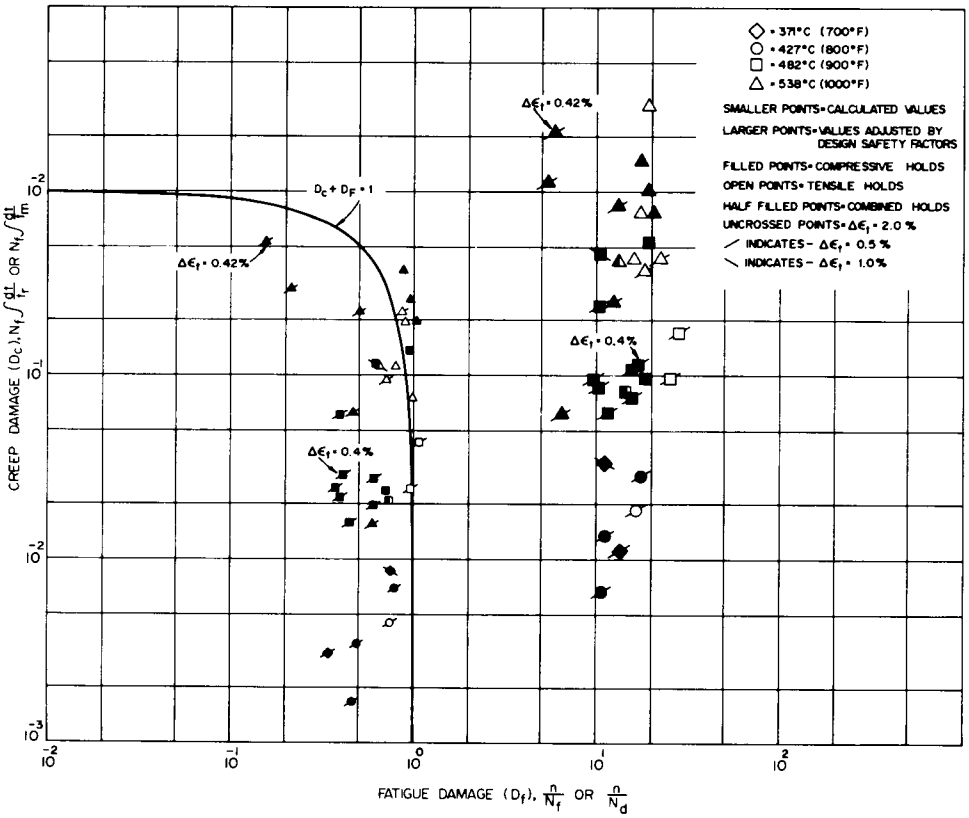

Fig. 3.61. Results of Linear Summation of Damage Calculations for Hold-Time Fatigue Data for Isothermally Annealed 2 1/4 Cr-1 Mo Steel.

curves[41] for this material, while the t_m values were obtained by

$$t_m = t_r/(1.728\varepsilon) \ , \tag{22}$$

where 1.728 is a statistical adjustment factor and ε is the residual standard error of the equation for rupture life in Sect. 3.4.4. Equation (22) defines t_m such that the probability is 0.95 that 90% of the measured values of log (rupture life) fall within 1.728ε of log t_r. Thus, approximately 95% of the values of rupture life will fall above t_m.

Clearly, from Fig. 3.61 the design damage values always exceed 1, being about 10 or greater in general.

Current creep fatigue design rules[44] specify that

$$\sum_{j=1}^{P} (n/N_D)_j + \sum_{k=1}^{9} (t/T_d)_k \leq D^* , \tag{23}$$

where

D^* = some specified "damage factor" (currently undefined for 2 1/4 Cr-1 Mo steel),

n = the number of cycles applied under loading condition j,

N_D = the number of design allowable cycles under loading condition j,

t = time duration of loading condition k,

T_D = allowable time under loading condition k.

T_D is calculated[44] as the lower limit time to rupture at the temperature of interest under a stress given by the stress from load k divided by a factor K', which is defined as 0.9 for austenitic stainless steels and for Incoloy Alloy 800H.

Work is under way to determine appropriate values of D^* and K' for 2 1/4 Cr-1 Mo steel by analysis of the current data. Results of such investigations will be reported later.

3.4.3.2 Subcritical Crack Growth of 2 1/4 Cr-1 Mo Steel — W. R. Corwin

Studies are continuing on the effects of temperature, mean stress level, frequency, and environment on the subcritical fatigue crack growth of 2 1/4 Cr-1 Mo steel. All specimens that have been used in this study to date are from heat 20017 in the isothermally annealed condition. Its mechanical properties have been reported in previous quarterlies.

3.4.3.2.1 Limits of Data Analyses. The crack growth rates are analyzed and presented as one or more functions of the stress intensity factor, K. Therefore a question that must be addressed is the upper limit of crack length beyond which the ΔK expressions used for linear elastic fracture mechanics (LEFM) are no longer valid because of the limitations of LEFM. Determining exact departure from LEFM conditions during testing is still unclear, although several approximations can

be made. The basic problem for load-controlled tests is to determine at what crack length the macroscopic stress state is such that near the crack tip gross yielding or inelastic deformation occurs. One method is to use a simple strength of materials approach and calculate the net section stress in the vicinity of the crack tip without including the stress concentration effects of the crack.

For a WOL-type specimen this includes both a tension component and a bending component, whereas for a center-notch specimen only a tension component is required. This approach gives a net section tensile stress, S_n for the center-notch specimen of

$$S_n = P/(w - 2a)T \ , \tag{24}$$

where P is the applied load, w is the specimen width, $2a$ is the total tip to tip crack length, and T is the specimen thickness.

A similar expression for the WOL-type specimen, which assumes a bending moment equal to the crack length plus one-half the remaining ligament width, is

$$S_n = \frac{P}{(w - a)T} \left[1 + \frac{3(a + w)}{w - a}\right] . \tag{25}$$

This expression has been applied to the data using a yield criterion of $0.9\sigma_{ys}$, where σ_{ys} is either the monotonic or cyclic yield strength. The results were indicated on Figs. 3.108 through 3.111 in the last quarterly[41] and are tabulated in Table 3.31. The limits thus defined, however, appear to be somewhat overconservative, and therefore we also investigated other approaches, which are based primarily on observation of the specimen itself. As gross plastic flow begins the specimen naturally thins locally at the crack tip, and a shear lip is formed.

The crack length at which a shear lip forms has been measured on several specimens at the three testing temperatures investigated, from room temperature to 593°C (1100°F). The results contain enough scatter that drawing conclusions based on such measurements is difficult. The major source of inaccuracy is determining exactly where the shear lip

Table 3.31. Apparent Limits of LEFM for Several Specimens as Computed by Eq. (25) — Average Values of a/w and Associated Stress Intensity Factors Producing Local Section Stresses Near the Crack Tip Equal to 90% of Monotonic or Cyclic Yield

Test Temperature		R[a]	Monotonic Yield Limits[b]			Cyclic Yield Limits[b]		
(°F)	(°C)		a/w	K_{max} ksi (in.)$^{1/2}$	ΔK ksi (in.)$^{1/2}$	a/w	K_{max} ksi (in.)$^{1/2}$	ΔK ksi (in.)$^{1/2}$
Room		0.05	0.5550	21.53	20.46	0.5825	23.51	22.35
950	510	0.033	0.5120	19.98	19.32	0.5593	23.40	22.63
950	510	0.05	0.5120	19.98	18.98	0.5593	23.40	22.23
950	510	0.2	0.5120	19.98	15.98	0.5593	23.40	18.72
950	510	0.5	0.5120	19.98	9.99	0.5593	23.40	11.70
1100	593	0.05	0.4735	18.63	17.70	0.5380	22.07	20.91

[a] R is the ratio of the minimum tensile load to the peak tensile load.

[b] To convert K_{max} and ΔK to MPa m$^{1/2}$, multiply by 1.099.

begins. Minute perturbations on the edge of the crack face begin almost at the onset of testing and very gradually increase and coalesce with increasing crack length. At specimen failure of course a shear lip has become prominent; however, choosing the point where plane stress conditions clearly dominate is highly subjective and, as a result, is a poor indication of the onset of overall ligament yielding.

Post-test measurements of local specimen thickness versus crack length, however, appear to reproducibly indicate the upper limit beyond which the ΔK expressions referred to above should be considered invalid or at best questionable for correlating plane strain crack growth data. The method for determining these points is illustrated in Fig. 3.62 for three specimens at 593°C (1100°F). Local thickness measurements along the crack length taken on each specimen after the completion of its test were normalized by dividing each by the original specimen thickness (see Table 3.32). The normalized thickness measurements were then plotted versus the normalized crack length, a/w, as shown in Fig. 3.62. In this manner it is easily seen where significant thinning begins, even in specimen 17 ATL, where a small amount of thinning is apparent before necking (possibly due to creep or ratchetting effects). To consistently obtain an estimate of the upper limit value of a/w, the intersection of the curve and a line offset 0.1% below its upper linear portion was taken. This value of a/w was then used to determine the limiting K_{max} and ΔK values for each test shown in Table 3.33, along with the results from room temperature and 510°C (950°F) tests. These apparent limiting values of ΔK at each temperature are also shown on Fig. 3.63 as heavy vertical lines on the da/dn versus ΔK curves. Three conclusions may be drawn: (1) As would be expected, the maximum stress intensity factor that can be obtained without specimen yielding decreases with increasing temperature, presumably because of temperature-related material softening. (2) At 593°C (1100°F), where there is a strong frequency effect, as shown in Fig. 3.62, the limiting K_{max} decreases with decreasing frequency for similar reasons. (3) The limiting K_{max} for a given set of temperature and frequency conditions seems to decrease with decreasing maximum load. This is indicated by comparing the three tests at 510°C (950°F) or the

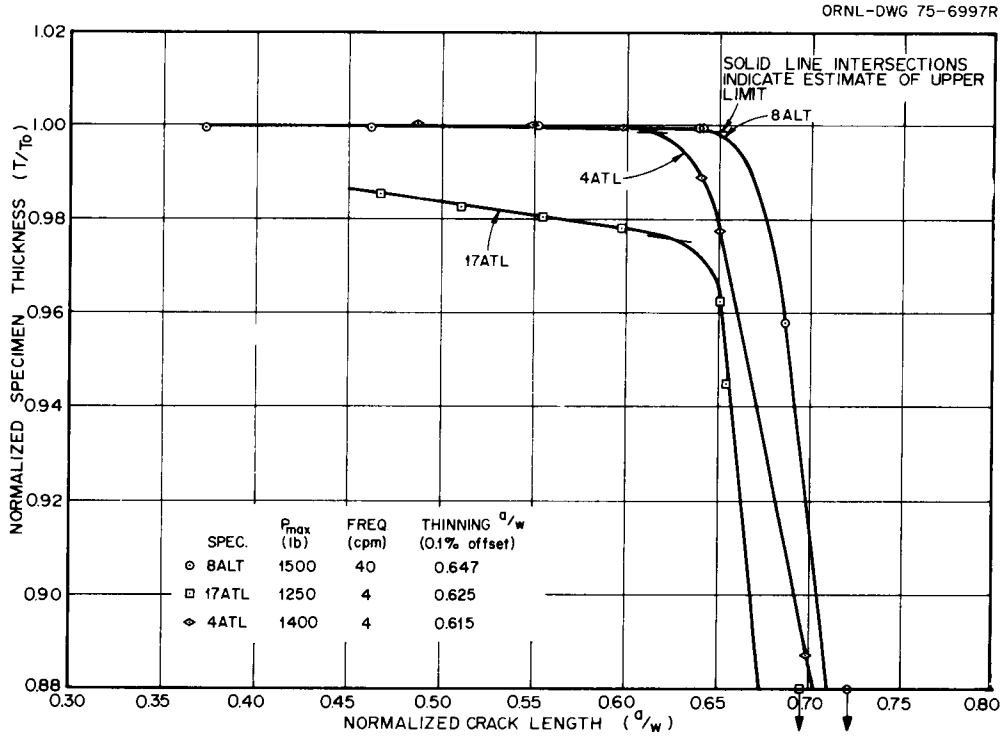

Fig. 3.62. Limits of Plane Strain Crack Propagation of 2 1/4 Cr-1 Mo Steel at 593°C (1100°F) in Air with R = 0.05.

Table 3.32. Thickness Along Crack Length of 2 1/4 Cr-1 Mo Steel Fatigue Crack Propagation Specimens Tested at 593°C (1100°F)

Specimen	Maximum Load (lb)	Maximum Load (kN)	R	Frequency (cpm)	Thickness, in. (mm) T_0, original	Thickness, in. (mm) T, local	Normalized Thickness, T/T_0	Normalized Crack Length a/w
8 ALT	1500	6.67	0.05	40	0.5042 (12.807)	0.5030 (12.776)	0.9976	0.3745
						0.5030 (12.776)	0.9976	0.4638
						0.5025 (12.764)	0.9966	0.5531
						0.5000 (12.700)	0.9917	0.6405
						0.5000 (12.700)	0.9917	0.6424
						0.4830 (12.268)	0.9580	0.6870
						0.3852 (9.784)	0.7104	0.7209
17 ATL	1250	5.56	0.05	4	0.5013 (12.733)	0.4941 (12.550)	0.9856	0.4682
						0.4925 (12.510)	0.9824	0.5113
						0.4913 (12.479)	0.9801	0.5555
						0.4902 (12.451)	0.9779	0.5988
						0.4823 (12.250)	0.9621	0.6521
						0.4733 (12.022)	0.9441	0.6540
						0.4240 (10.770)	0.8458	0.6956
						0.3234 (8.214)	0.6451	0.7239
4 ATL	1400	6.23	0.05	4	0.5040 (12.802)	0.5040 (12.802)	1.0000	0.4881
						0.5033 (12.784)	0.9986	0.5497
						0.5023 (12.758)	0.9966	0.5991
						0.4982 (12.654)	0.9885	0.6420
						0.4927 (12.515)	0.9776	0.6508
						0.4470 (11.354)	0.8869	0.6964
						0.3030 (7.696)	0.6012	0.7847

Table 3.33. Apparent Upper Limits of Plane Strain Crack Propagation for 2 1/4 Cr-1 Mo Steel as Indicated by Specimen Thinning at the Crack Tip

Specimen	Temperature (°C)	Temperature (°F)	R	Maximum Load (lb)	Maximum Load (kN)	Frequency (cpm)	Thinning, a/w (0.1% offset)	Limiting Stress Intensity Factors, ksi $\sqrt{in.}$ (K_{max})	(MPa $\sqrt{m}$)	ΔK	(MPa $\sqrt{m}$)
1 ATL	Room		0.05	1250	5.56	420	0.770	55.00	(60.44)	52.25	(57.42)
4 ALT	510	950	0.033	1512	6.72	40	0.654	35.12	(38.59)	33.96	(37.32)
1 CLT	510	950	0.05	1750	7.78	200	0.623	35.72	(39.25)	33.93	(37.28)
6 CTL	510	950	0.5	1450	6.45	50	0.650	33.35	(36.65)	16.67	(18.32)
Average	510	950						34.73	(38.16)		
17 ATL	593	1100	0.05	1250	5.56	4	0.625	25.69	(28.23)	24.40	(26.81)
4 ATL	593	1100	0.05	1400	6.23	4	0.615	27.48	(30.20)	26.11	(28.69)
Average	593	1100				4		26.58	(29.23)	25.26	(27.76)
8 ALT	593	1100	0.05	1500	6.67	40	0.647	33.67	(37.00)	31.99	(35.15)

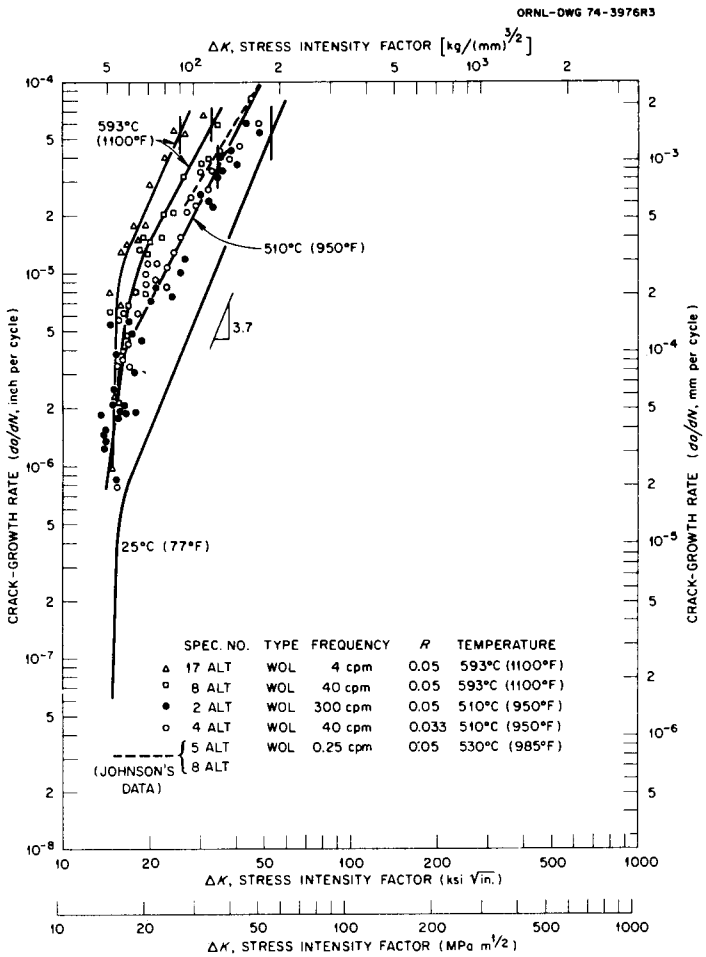

Fig. 3.63. Effect of Temperature and Frequency on Fatigue Crack Propagation of 2 1/4 Cr-1 Mo Steel.

two at 593°C (1100°F) at 4 cpm. This conclusion is also supported by comparing the functional forms of S_n and K_{max} for the WOL specimen. Within the region of interest S_n increases faster with increasing crack length than does K_{max}. Therefore, to cover a larger region of stress intensity, tests with low P_{max} may be required physically to obtain low da/dn values, and tests with high P_{max} and short crack length may be required to obtain high da/dn values yet still be within the LEFM regime.

3.4.3.2.2 Mean Stress Studies. Mean stress studies at 510°C (950°F) have been completed, with the last test at R = 0.75 finished. The results of this test are shown in Fig. 3.64(a), along with a summary of results for lower R ratio from the previous quarterly.[41] We tried to

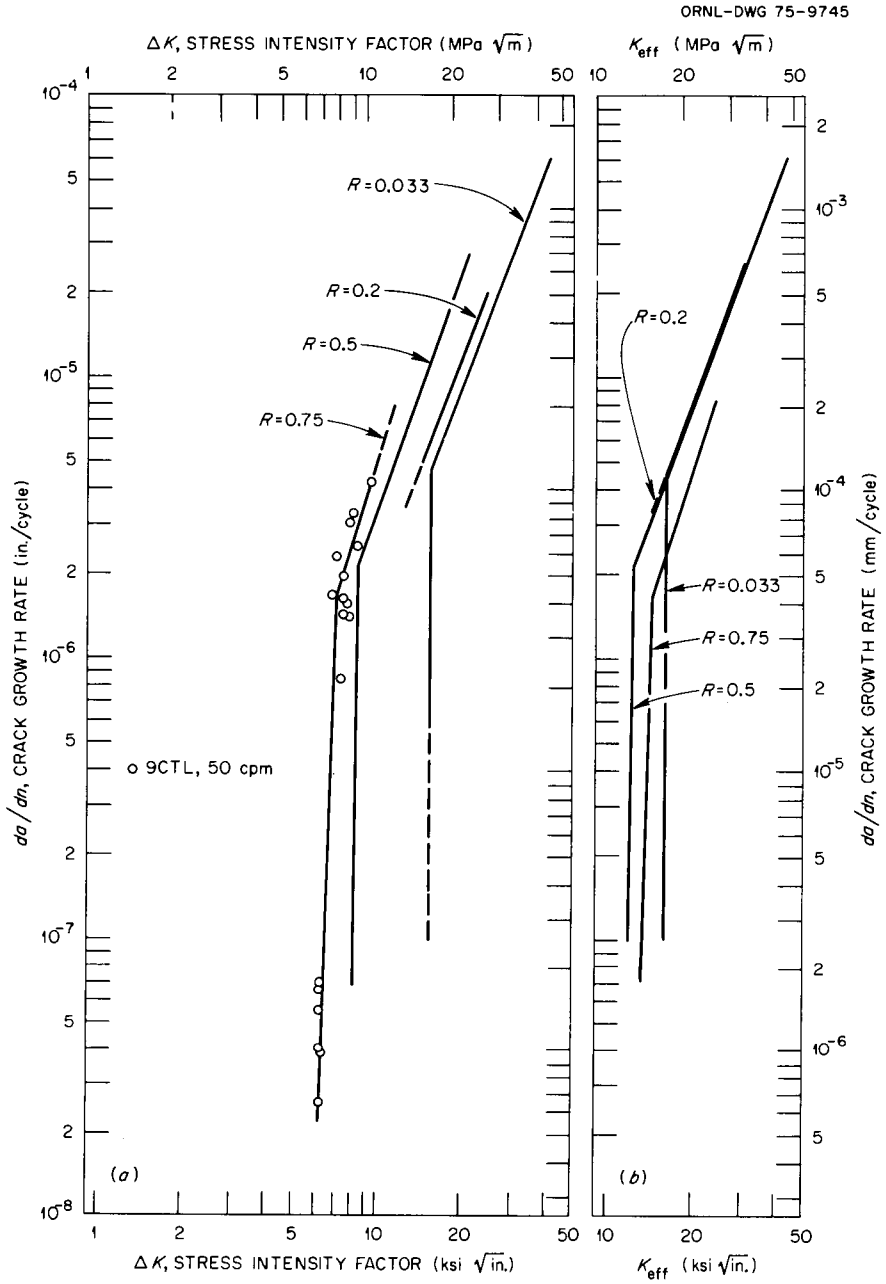

Fig. 3.64. Effect of Stress Ratio on Fatigue-Crack Propagation of 2 1/4 Cr-1 Mo Steel at 510°C (950°F) in Air at 40–50 cpm. (a) da/dn vs ΔK. (b) da/dn vs K_{eff} $[K_{max}(1 - R)^{0.5}]$.

normalize the crack growth data for R using the concept of K_{eff} as described last quarter.[41] However, as seen in Fig. 3.64(b), the portion of the data above the knee of the curve was not normalized, whereas that for lower R ratios was. The crack growth rate appears lower than would be expected on the basis of the previous tests. This may be due to crack tip blunting by the sustained high stresses in the creep temperature range.

Tests varying R ratio at room temperature have been undertaken. Testing at $R = 0.75$ has been completed, and testing at $R = 0.5$ has begun. Results for $R = 0.75$ are shown in Fig. 3.65. Room-temperature R ratio data will be normalized this quarter.

3.4.3.2.3 Environmental Effects. Testing in steam at 510°C (950°F) at 200 cpm and comparative tests in air have been completed. As shown in Fig. 3.66, there is little or no effect on the fatigue-crack propagation behavior of this material at a frequency of 200 cpm. If anything there is a very slight retardation of growth rates at the higher ΔK levels. The apparent variation is, however, within the experimental band, and certainly no substantial effects were noted.

Tests are currently in progress at 4 cpm in both air and steam at 510°C (950°F) to investigate the effects of steam at lower frequencies.

3.4.4 Mechanical Property Correlations of 2 1/4 Cr-1 Mo Steel for LMFBR Steam Generators — T. L. Hebble*

3.4.4.1 Rupture Life

A new mathematical model for rupture life of annealed 2 1/4 Cr-1 Mo steel has been developed and is based on an augmented data set, which included information from creep tests at 427, 454, and 510°C (800, 850, and 950°F). This model has the form

$$\widehat{\log_{10} t_r} = b_0 + b_1 T + b_2 T \log_{10} \sigma + b_3 \sigma \ , \qquad (26)$$

*Mathematics and Statistics Research Department.

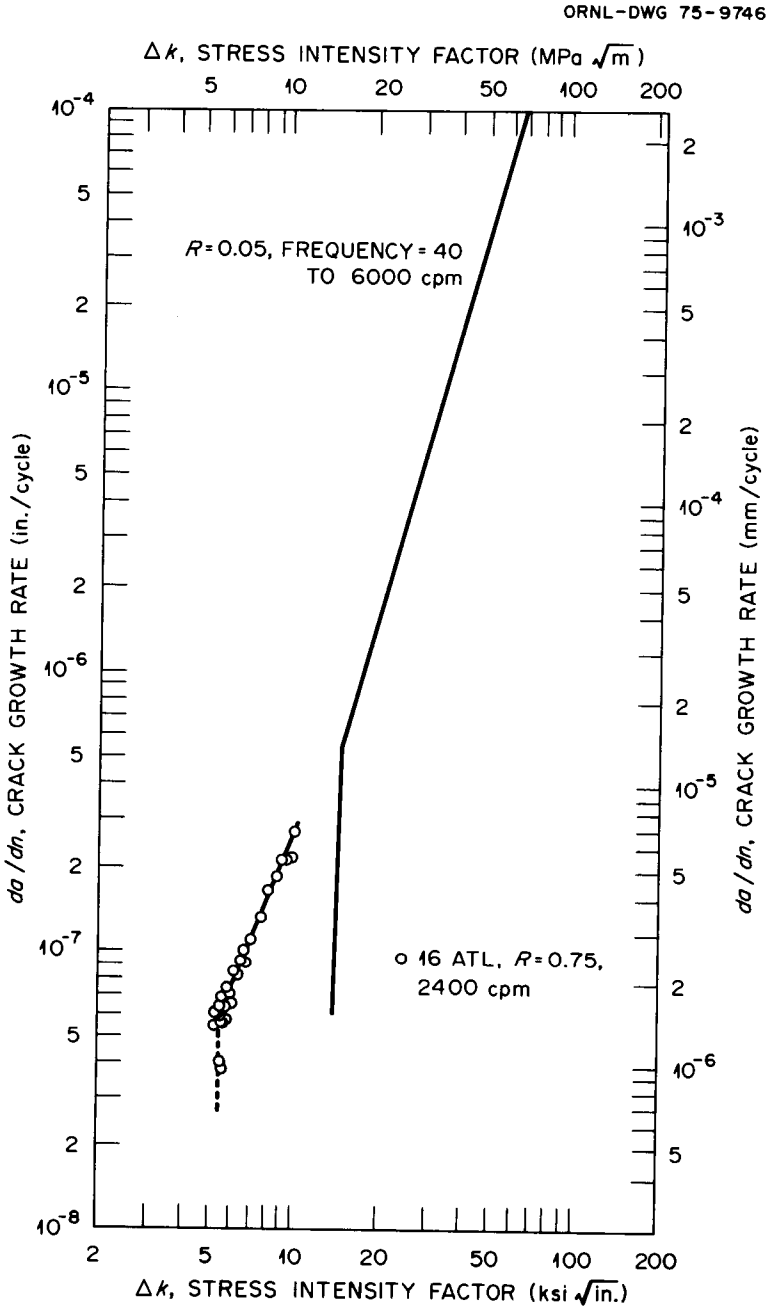

Fig. 3.65. Effect of Stress Ratio on Fatigue-Crack Propagation of 2 1/4 Cr-1 Mo Steel at Room Temperature in Air.

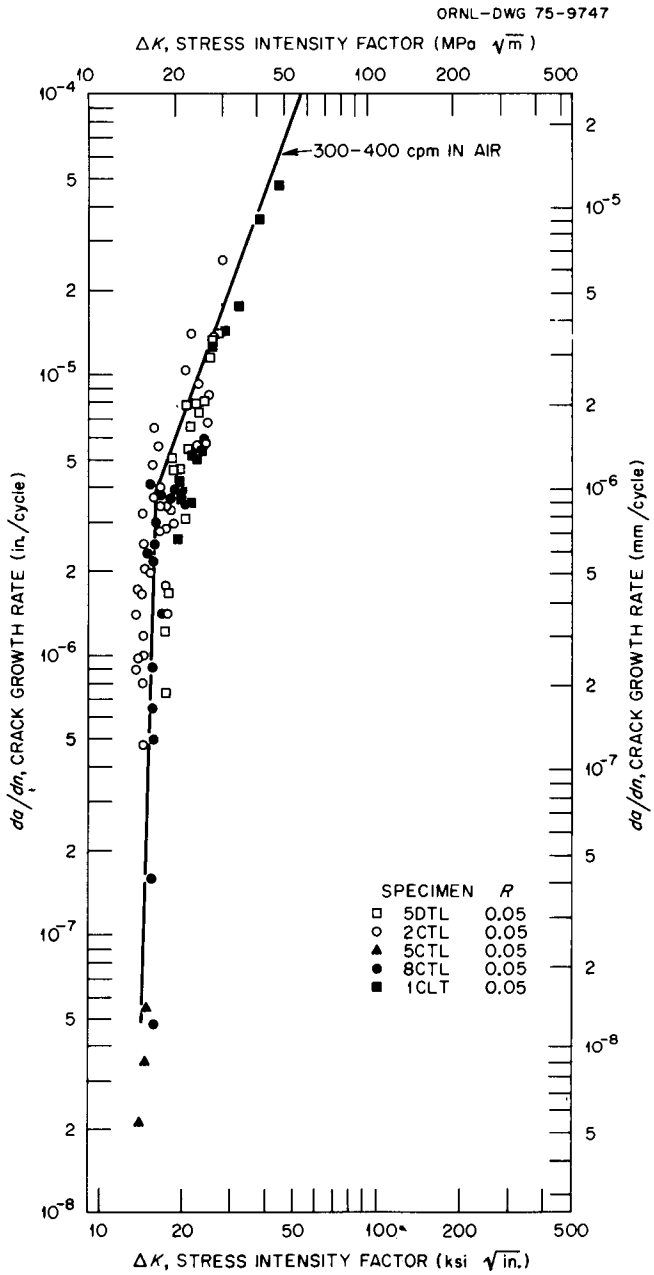

Fig. 3.66. Fatigue-Crack Propagation of 2 1/4 Cr-1 Mo Steel in Air and Steam at 510°C (950°F) and 200 cpm. Summary line for 300–400 cpm tests shown for comparison.

where

$\widehat{\log_{10} t_r}$ = expected value of the common logarithm of rupture life, t_r (hr),

T = temperature (°C),

σ = stress (MPa), and

b_0, b_1, b_2, b_3 = unknown constants estimated from the data.

The unknown constants were estimated from 617 observations by the method of least squares. The estimated constants with standard errors given in brackets are

$$b_0 = 16.76\ [\pm 0.36];$$
$$b_1 = -0.00762\ [\pm 0.00104];$$
$$b_2 = -0.00731\ [\pm 0.00042];$$
$$b_3 = -0.00688\ [\pm 0.00068].$$

Table 3.34 lists the values of rupture life determined from Eq. (26), with lower limits given in parenthesis at several levels of temperature and stress. Graphical examples of Eq. (26) with data and (P = 0.90, λ = 0.95) central tolerance limits are given in Figs. 3.67, 3.68, and 3.69 for 510, 538, and 566°C (950, 1000, and 1050°F), respectively.

The lower limit of rupture life, denoted L (hr), is defined to be

$$L = 10^M , \tag{27}$$

where

M = lower (P = 0.90, λ = 0.95) central tolerance limit about $\log_{10} t_r$,

$= \log_{10} t_r - [3.347\ \sqrt{Z'VZ} + 1.743s]$,

$\log_{10} t_r$ = expected value of common logarithm of rupture life, t_r(hr), and is determined from Eq. (26),

s = residual standard error with 613 degrees of freedom

= 0.3452,

V = variance-covariance matrix

Table 3.34. Expected Rupture Life and Lower Limit for 2 1/4 Cr-1 Mo Steel

Test Temperature (°C)	Test Temperature (°F)	Rupture Life,[a] hr, for Each Creep Stress in MPa (ksi)									
		34 (5)	69 (10)	103 (15)	138 (20)	172 (25)	207 (30)	241 (35)	276 (40)	310 (45)	345 (50)
371	700						(200,000)	(77,000)	260,000 (31,000)	110,000 (13,000)	47,000 (5,400)
399	750					(130,000)	(46,000)	130,000 (17,000)	51,000 (6,900)	21,000 (2,800)	8,900 (1,100)
427	800				(100,000)	220,000 (31,000)	73,000 (11,000)	26,000 (4,000)	10,000 (1,500)	4,000 (590)	1,700 (230)
454	850			(110,000)	170,000 (26,000)	48,000 (7,600)	15,000 (2,500)	5,300 (900)	2,000 (330)	770 (120)	310 (47)
482	900		(200,000)	190,000 (30,000)	39,000 (6,700)	10,000 (1,900)	3,200 (590)	1,100 (200)	380 (70)	150 (25)	59 (9.2)
510	950		(58,000)	45,000 (8,100)	8,900 (1,700)	2,200 (440)	660 (130)	210 (43)	75 (14)	28 (5.0)	11 (1.8)
538	1000		91,000 (17,000)	11,000 (2,200)	2,000 (420)	480 (100)	140 (29)	43 (8.8)	15 (2.8)	5.4 (0.9)	2.1 (0.3)
566	1050	(97,000)	24,000 (4,600)	2,600 (560)	450 (99)	100 (22)	28 (5.8)	8.7 (1.7)	2.9 (0.5)	1.0 (0.2)	0.4 (0.1)
593	1100	220,000 (29,000)	6,200 (1,200)	620 (130)	100 (21)	22 (4.4)	5.9 (1.1)	1.8 (0.3)	0.6 (0.1)	0.2 (0.0)	b b

[a]Lower limit given in parentheses. Rupture lives exceeding 300,000 hr are omitted.

[b]Stress exceeds ultimate tensile strength at 593°C (1100°F).

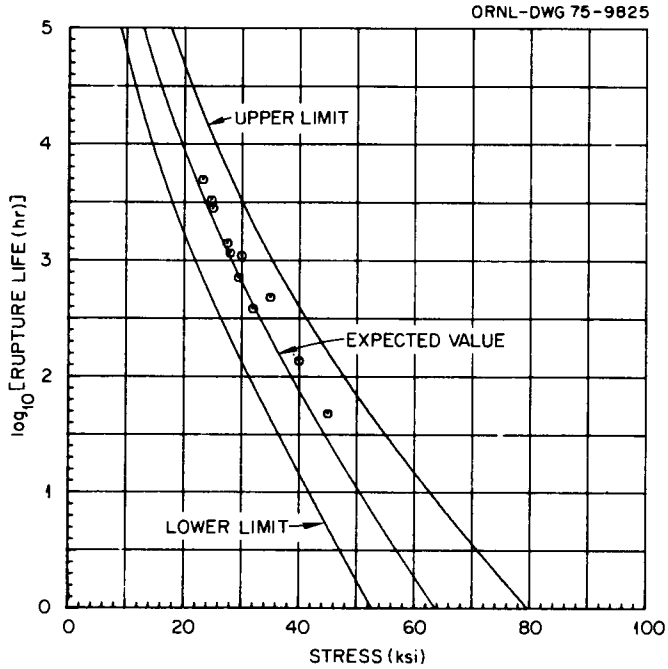

Fig. 3.67. Rupture Life of 2 1/4 Cr-1 Mo Steel at 510°C (950°F) — Expected Values with (P = 0.90, λ = 0.95) Tolerance Limits.

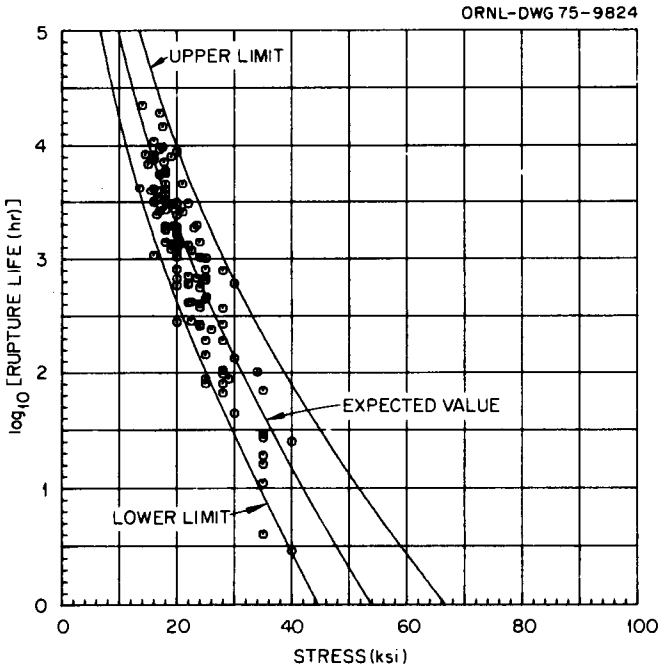

Fig. 3.68. Rupture Life of 2 1/4 Cr-1 Mo Steel at 538°C (1000°F) — Expected Values with (P = 0.90, λ = 0.95) Tolerance Limits.

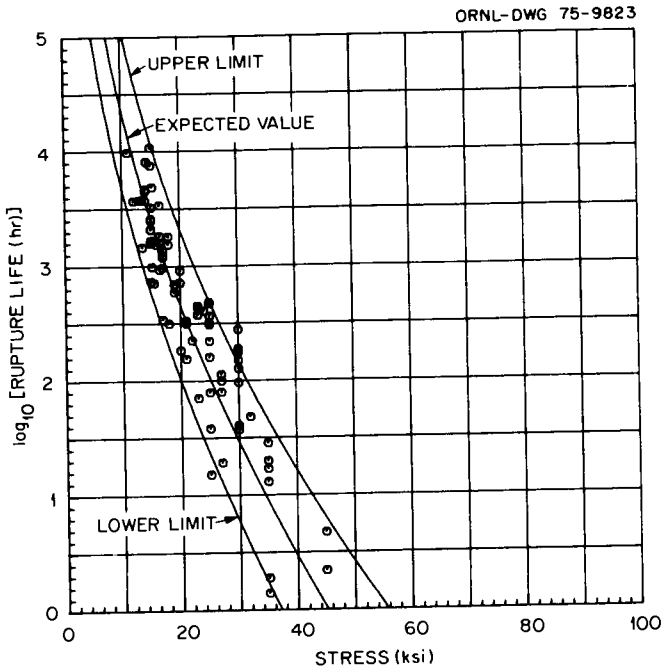

Fig. 3.69. Rupture Life of 2 1/4 Cr-1 Mo Steel at 566°C (1050°F) — Expected Values with (P = 0.90, λ = 0.95) Tolerance Limits.

$$V = \begin{bmatrix} 1.3211 \times 10^{-1} & -2.6252 \times 10^{-4} & 2.8573 \times 10^{-5} & -1.2522 \times 10^{-4} \\ -2.6252 \times 10^{-4} & 1.0716 \times 10^{-6} & -3.6521 \times 10^{-7} & 6.4848 \times 10^{-7} \\ 2.8573 \times 10^{-5} & -3.6521 \times 10^{-7} & 1.8012 \times 10^{-7} & -2.5798 \times 10^{-7} \\ -1.2522 \times 10^{-4} & 6.4848 \times 10^{-7} & -2.5798 \times 10^{-7} & 4.6517 \times 10^{-7} \end{bmatrix},$$

Z' = transpose of vector Z representing point at which tolerance limit is sought

= $[1, T, T \log_{10}\sigma, \sigma]$,

T = test temperature (°C).

The (P = 0.90, λ = 0.95) tolerance limits specify the bounds within which a proportion P of the observations fall at a confidence level of λ. Thus, at a confidence level of 0.95, 95% of the observations are expected to fall above the lower limit or below the upper limit. These limits are simultaneous in all levels of temperature and stress (i.e., the limits may be calculated repeatedly without affecting the level of confidence).

3.4.4.2 Comparison of Lower Stress Limits with Code Case 1592

Minimum stress levels derived from Eqs. (26) and (27) are higher at shorter times and lower at longer times than the corresponding stress

levels published[44] in ASME Code Case 1592. In Table 3.35, minimum stresses to cause rupture from Code Case 1592 are compared with calculated stresses to cause rupture in a time equal to the lower (P = 0.90, λ = 0.95) tolerance limit. The entry at each temperature-stress combination contains three numbers. The stress calculated from Eqs. (26) and (27), the stress from Code Case 1592, and the difference, a negative sign indicating that the proposed value is less than the Code value.

Figures 3.70, 3.71, and 3.72 graphically compare some Code Case values from Table 3.35 with results generated by Eqs. (26) and (27). Code values are plotted as line segments, which intersect the lower tolerance limit. With the exception of code values, these three graphs display the same information as that shown in Figs. 3.67, 3.68, and 3.69.

3.4.4.3 Time to Start of Tertiary Creep

The mathematical model for time to start of tertiary creep is being revised; reevaluation of certain tests has delayed selection of a suitable equation. Although a final decision has not been made, a competing model having the same form as Eq. (26) is given here:

$$\widehat{\log_{10} t_3} = a_0 + a_1 T + a_2 T \log_{10} \sigma + a_3 \sigma \quad , \tag{28}$$

where

t_3 = time (hr) to start of tertiary creep (0.2% offset),

$\widehat{\log_{10} t_3}$ = expected value of common logarithm of t_3,

T = temperature (°C),

σ = stress (MPa), and

a_0, a_1, a_2, a_3 = unknown constants.

The unknown constants, estimated from 137 observations by method of least squares, with standard errors given in brackets, are

Table 3.35. Minimum Stress to Rupture — A Comparison of Code Case 1592 and Values Calculated from Eqs. (26) and (27)

Time (hr)		Minimum Stress, ksi (MPa), at Each Temperature							
		399°C 750°F	427°C 800°F	454°C 850°F	482°C 900°F	510°C 950°F	538°C 1000°F	566°C 1050°F	593°C 1100°F
10	Calculated	76.7(529)	67.2(463)	58.1(401)	49.6(342)	41.7(288)	34.5(238)	27.9(192)	22.3(154)
	Code Case	58.0(400)	56.0(386)	52.0(359)	46.0(317)	40.0(276)	31.5(217)	26.0(179)	21.0(145)
	Difference	18.7(129)	11.2(77)	6.1(42)	3.6(25)	1.7(12)	3.0(21)	1.9(13)	1.3(9)
30	Calculated	70.4(485)	61.1(421)	52.3(361)	44.2(305)	36.7(253)	29.9(206)	23.9(165)	19.0(131)
	Code Case	57.0(393)	56.5(390)	50.5(348)	41.0(283)	35.0(241)	27.5(190)	22.5(155)	18.0(124)
	Difference	13.4(92)	4.6(32)	1.8(12)	3.2(22)	1.7(12)	2.4(17)	1.4(10)	1.0(7)
100	Calculated	63.5(438)	54.5(376)	46.1(318)	38.3(264)	31.3(216)	25.1(173)	20.0(138)	15.7(108)
	Code Case	56.0(386)	55.0(379)	46.0(317)	36.0(248)	30.0(207)	24.0(165)	19.0(131)	15.1(104)
	Difference	7.5(52)	−0.5(−3)	0.1(1)	2.3(16)	1.3(9)	1.1(8)	1.0(7)	0.6(4)
300	Calculated	57.4(396)	48.6(335)	40.5(279)	33.1(228)	26.6(183)	21.1(145)	16.7(115)	13.0(90)
	Code Case	54.6(376)	48.5(334)	40.5(279)	32.0(221)	26.0(179)	21.0(145)	16.5(114)	13.0(90)
	Difference	2.8(19)	0.1(1)	0.0(0)	1.1(8)	0.6(4)	0.1(1)	0.2(1)	0.0(0)
10^3	Calculated	50.6(349)	42.2(291)	34.5(238)	27.6(190)	21.9(151)	17.2(119)	13.5(93)	10.4(72)
	Code Case	53.0(365)	43.0(296)	35.0(241)	28.0(193)	22.2(153)	17.9(123)	14.0(97)	10.8(74)
	Difference	−2.4(−17)	−0.8(−6)	−0.5(−3)	−0.4(−3)	−0.3(−2)	−0.7(−5)	−0.5(−3)	−0.4(−3)
3×10^3	Calculated	44.6(308)	36.4(251)	29.2(201)	23.0(159)	18.0(124)	14.1(97)	10.9(75)	8.3(57)
	Code Case	51.2(353)	37.5(259)	31.0(214)	25.0(172)	19.5(134)	15.2(105)	12.0(83)	9.1(63)
	Difference	−6.6(−46)	−1.1(−8)	−1.8(−12)	−2.0(−14)	−1.5(−10)	−1.1(−8)	−1.1(−8)	−0.8(−6)
10^4	Calculated	38.0(262)	30.4(210)	23.9(165)	18.6(128)	14.4(99)	11.1(77)	8.5(59)	6.4(44)
	Code Case	48.0(331)	34.5(238)	27.5(190)	21.6(149)	17.0(117)	13.1(90)	10.0(69)	7.5(52)
	Difference	−10.0(−69)	−4.1(−28)	−3.6(−25)	−3.0(−21)	−2.6(−18)	−2.0(−14)	−1.5(−10)	−1.1(−8)
3×10^4	Calculated	32.2(222)	25.2(174)	19.5(134)	15.0(103)	11.5(79)	8.8(61)	6.6(46)	4.9(34)
	Code Case	43.3(299)	30.5(210)	24.0(165)	19.0(131)	14.6(101)	11.0(76)	8.3(57)	6.2(43)
	Difference	−11.1(−77)	−5.3(−37)	−4.5(−31)	−4.0(−28)	−3.1(−21)	−2.2(−15)	−1.7(−12)	−1.3(−9)
10^5	Calculated	26.2(181)	20.1(139)	15.3(105)	11.7(81)	8.9(61)	6.7(46)	5.0(34)	3.7(26)
	Code Case	37.5(259)	27.0(186)	21.0(145)	16.4(113)	12.6(87)	9.4(65)	7.0(48)	5.0(35)
	Difference	−11.3(−78)	−6.9(−48)	−5.7(−39)	−4.7(−32)	−3.7(−26)	−2.7(−19)	−2.0(−14)	−1.3(−9)
3×10^5	Calculated	21.2(146)	16.1(111)	12.1(83)	9.1(63)	6.8(47)	5.1(35)	3.8(26)	2.8(19)
	Code Case	34.1(235)	24.0(165)	18.5(128)	14.1(97)	11.0(76)	7.9(54)	5.8(40)	4.1(28)
	Difference	−12.9(89)	−7.9(−54)	−6.4(−44)	−5.0(−34)	−4.2(−29)	−2.8(−19)	−2.0(−14)	−1.3(−9)

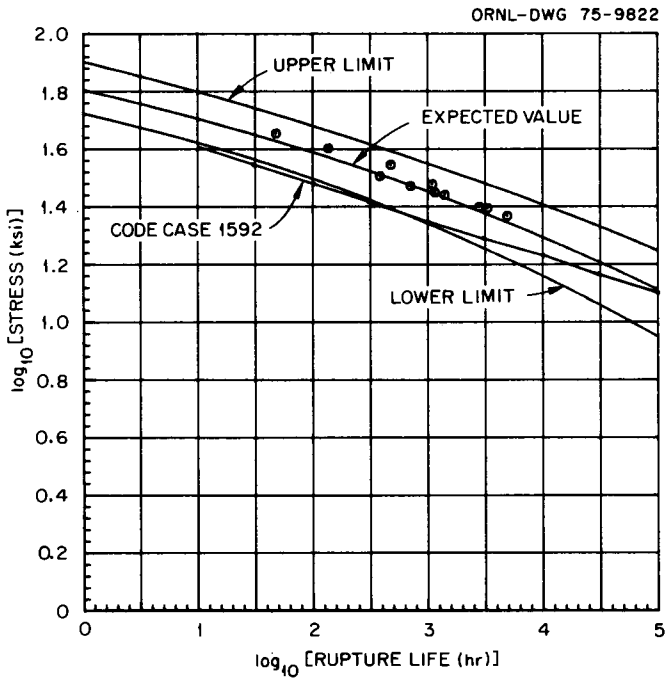

Fig. 3.70. Rupture Life of 2 1/4 Cr-1 Mo Steel at 510°C (950°F) — Expected Values with (P = 0.90, λ = 0.95) Tolerance Limits and Code Case 1592 Minimum Stress Values.

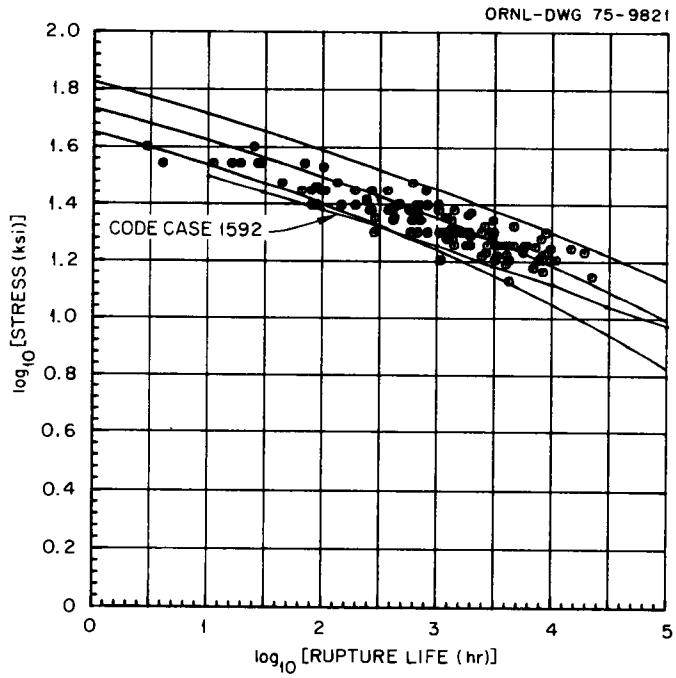

Fig. 3.71. Rupture Life of 2 1/4 Cr-1 Mo Steel at 538°C (950°F) — Expected Values with (P = 0.90, λ = 0.95) Tolerance Limits and Code Case 1592 Minimum Stress Values.

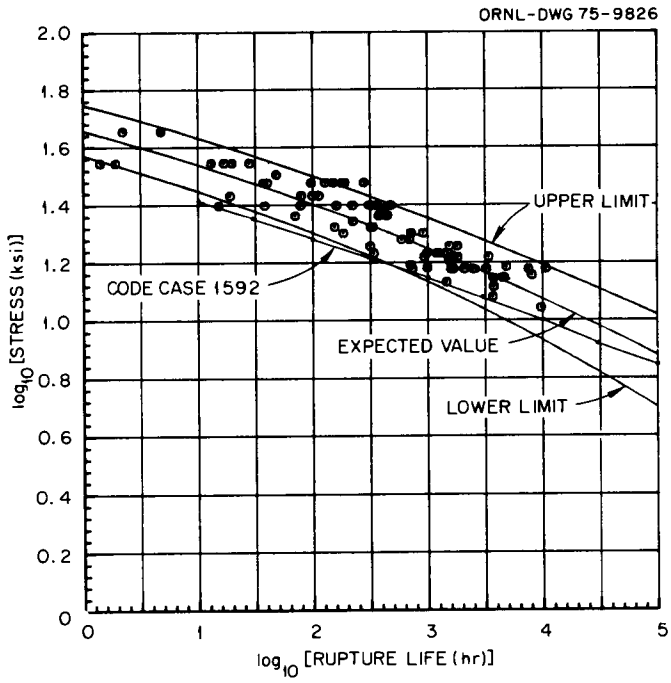

Fig. 3.72. Rupture Life of 2 1/4 Cr-1 Mo Steel at 566°C (950°F) — Expected Values with (P = 0.90, λ = 0.95) Tolerance Limits and Code Case 1592 Minimum Stress Values.

$$a_0 = 14.46\ [\pm 0.83],$$
$$a_1 = -0.00750\ [\pm 0.00111],$$
$$a_2 = -0.00589\ [\pm 0.00055],$$
$$a_3 = -0.00502\ [\pm 0.00087].$$

The residual mean square, a measure of variability, generated from Eq. (28) above (= 0.1247) compares favorably with that generated from Eq. (26) (= 0.1192). This is reassuring, since each response is similar in character.

3.4.5 Mechanical Properties of a Weld-Overlaid Stainless Steel Forging — R. L. Klueh

With the exception of one long-time test still in progress, the experimental portion of our creep-rupture studies[45] on the type 304 stainless steel forging overlaid with type 308 stainless steel are complete. Tests were made at 482, 538, and 593°C (900, 1000, and 1100°F) on the as-forged type 308 stainless steel, type 304 stainless steel forging immediately adjacent to the fusion line, and type 308 stainless

steel weld metal. Axial, radial, and tangential (relative to the cylindrical forging) specimens were tested. During this quarter, our metallographic studies were completed and the results of these studies are discussed below.

Visual inspection of the specimens from as-forged type 304 stainless steel indicated that, with one exception, failure occurred without neck formation (i.e., uniform deformation in the gage section). The only exception was the 65-ksi (448-MPa) test at 482°C, and this was not truly a creep test, since it ruptured on load. Cracks were observed on the external surfaces of the gage length of all specimens tested at 593°C. At 538°C, only the tests below 48 ksi (331 MPa) had cracks on the external surface. No external cracks were noted at 482°C.

When examined metallographically, the fractures of the as-forged material at 593°C were a mixture of grain boundary cracks and ductile tearing, with the number of wedge-type cracks increasing as stress was decreased. An example of these cracks is shown in Fig. 3.73. In the test that was discontinued after 2600 hr at 593°C and 30 ksi (207 MPa) with 5.5% elongation, grain boundary cracks were beginning to form at the external surface.

Metallographic examination of as-forged specimens ruptured at 538°C revealed fractures similar to those observed at 593°C; a large number of grain boundary cracks were observed all along the gage length. At the highest stresses, there was considerable grain distortion near the fracture, indicating that although grain boundary cracking probably played a role in the failure, the fracture was primarily transgranular. However, as the stress was lowered, the fracture mode became progressively more intergranular.

Axial specimens tested at 482°C (900°F) and 64 and 60 ksi (441 and 414 MPa) were examined metallographically. Surprisingly, in both specimens grain boundaries were beginning to open. As noted at the higher temperatures, the fracture at the lower stress displayed more intergranular aspects.

The type 304 stainless steel specimens taken from immediately adjacent to the fusion line also ruptured with essentially no neck formation at 538 and 593°C. At 593°C cracks were visible on the external

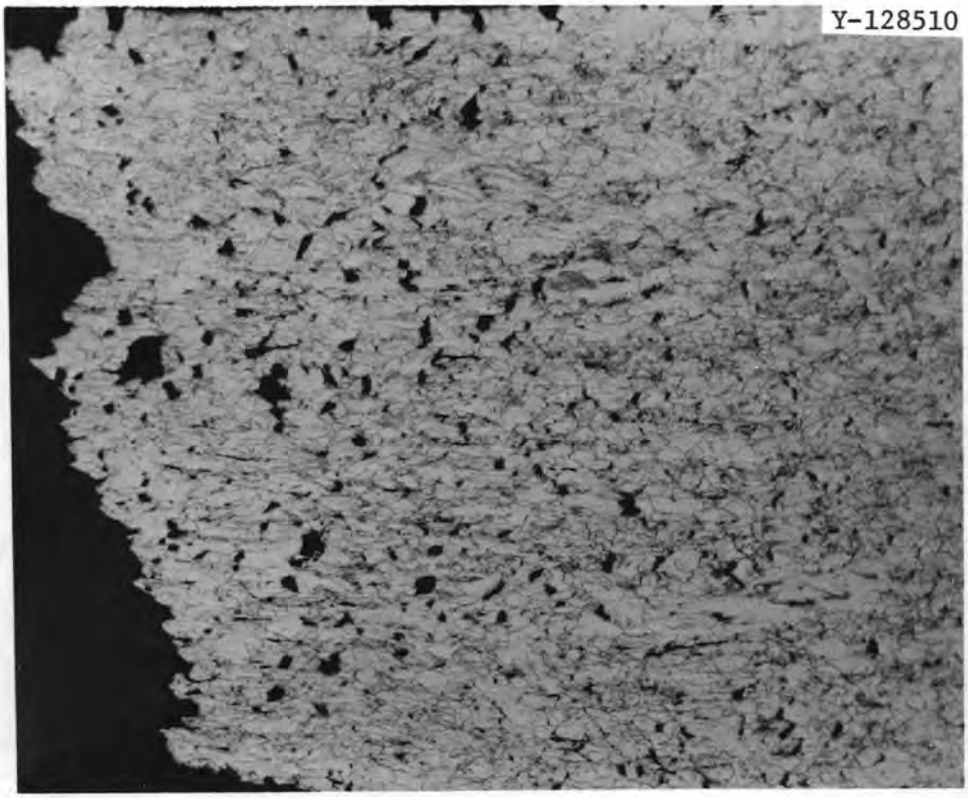

Fig. 3.73. An Example of the Cracks Formed in the Type 304 Stainless Steel Forging at 593°C. Fracture was from a specimen tested at 35 ksi (241 MPa). 20×.

surface of all specimens. Only on specimens tested below 55 ksi (379 MPa) at 538°C were any external cracks visible. The three specimens tested at 482°C appeared to form a slight neck, and no external cracks were visible.

Metallographically, the observations were also similar to those made on the as-forged material. At 593 and 538°C, all the failed specimens had many wedge-type cracks back from the actual fracture surface, similar to those shown in Fig. 3.73. Again, the number and size of these cracks increased as the creep stress decreased; likewise, the fractures became progressively more intergranular as the stress decreased. Only one specimen tested at 482°C was examined, a radial specimen: it had numerous grain boundary cracks in the gage length, but the fracture appeared to be mostly transgranular.

For the type 308 stainless steel, the elongation and reduction of area values for all specimens decreased with decreasing rupture stress[45] (increasing rupture life). Visual inspection of the ruptured specimens indicated that the specimens necked when tested at high stresses. These failures appeared to be of a shear type. Additionally, two types of anisotropic deformation behavior were noted. The cross section of both the radial and the tangential specimens often deformed to an ellipse, rather than a circle. Furthermore, certain specimens had a "knobby" appearance after test. That is, usually one or more points on the specimen gage section, in addition to the region that necked to failure, appeared to be in the process of forming a neck. "Knobby" deformation was much more prevalent and pronounced in the radial specimens. We previously explained this type of anisotropic deformation for the tensile tests[46] in terms of the circumferential passes made in the overlay process. The radial specimens were taken from material that spans several passes, while the tangential specimens were taken almost parallel to a pass. The observed deformational behavior reflects the property differences across a pass.

For the 30-ksi (207-MPa) test at 593°C pronounced neck formation was no longer observed, though the deformation appeared quite ductile. Instead of forming a neck, the specimen "tapered down" gradually toward the failed region over a longer portion of the gage length. At 27.5 and 25 ksi (190 and 172 MPa), the fractures were quite flat and the amount of tapered deformation decreased as the stress decreased. At 482 and 538°C, the failed specimens formed necks and appeared to fail by a ductile shear type of fracture mode. The amount of necking decreased as the rupture stress decreased.

Metallographic examination of the specimens tested at 593°C showed progressively more interphase crack formation as the stress was decreased below 40 ksi (276 MPa). Even at 45 ksi (310 MPa), where there was considerable neck formation, there were indications that crack formation had started at the external surfaces. An example of the types of cracks that appeared at the lower stresses are shown in Fig. 3.74.

For the highest stresses at 538°C, there was no indication of interphase crack formation. As the stress was lowered, however, progressively

Fig. 3.74. An Example of the Cracks Formed in the Type 308 Stainless Steel Overlay at the Lower Stresses at 593°C. Fracture was from a specimen tested at 30 ksi (207 MPa). As polished. 20×.

more cracks became evident in the gage section. Similar observations were made at 482°C. No interphase cracks were observed on the specimen tested at 62.5 ksi (431 MPa), while the gage length of the specimen tested at 60 ksi (414 MPa) did contain cracks. The fractures for both specimens were primarily transgranular.

We also tested axial specimens taken across the fusion line and containing both type 304 stainless steel forging and type 308 stainless steel weld metal in the gage section. Visual inspection of the failed specimens tested at 593°C indicated some neck formation, with the amount decreasing as the stress decreased. At 538 and 482°C, the specimens exhibited more neck formation at the highest stresses, but the amount again decreased with decreasing stress. With the exception of the first 30-ksi (207-MPa) test (a duplicate test was run) at 593°C and the 60-ksi (414-MPa) test at 482°C, failures were judged to be in the weld metal. For the two exceptions, the failure appeared to be very near the fusion line.

Observations concerning the position of the failures were verified by metallography. The two specimens that were judged to have failed very near the fusion line showed partial separations at the fusion line. Indications were that failure was initiated at the fusion line in the specimen interior, then propagated toward the surface. Failure propagation immediately near the surface was through weld metal, leaving an upraised "ring" of weld metal around the outer edge of the type 304 stainless steel piece of the failed specimen. This is shown in Fig. 3.75. The fusion-line failure at 482°C showed a similar fracture.

As seen in Fig. 3.75, parts of the microstructure of the type 304 stainless steel shown are not typical of the microstructure of most of the forging. A few other specimens examined metallographically displayed areas similar to that shown in Fig. 3.75. Since such regions were not

Fig. 3.75. Photomicrograph of Composite Specimen That Failed at the Fusion Line Between Type 304 and 308 Stainless Steel Weld Metal. Test was at 593°C and 30 ksi (207 MPa). Note the unusual grain structure of the type 304 stainless steel near the fusion line separation. Also note the start of fusion-line separation at the external surface. 100×.

confined to the region adjacent to the fusion line, they must be a result of the forging process and not the overlay process. We were unable to determine if these are regions of unrecrystallized material or large grains caused by unnatural grain growth. Metallographic examination of the other specimens (those that failed in the weld metal) indicated that as the stress was decreased both the amount of interphase crack formation in the weld metal and the amount of grain boundary separation in the base metal increased.

We are presently preparing a report on the creep-rupture studies.

3.5 HIGH-TEMPERATURE DESIGN — W. L. Greenstreet,* J. M. Corum,* and C. E. Pugh*

3.5.1 Exploratory Studies in Support of Structural Design Methods

3.5.1.1 Characterization of the Product Forms of the Reference Heat of Type 304 Stainless Steel — R. W. Swindeman and V. K. Sikka

Tensile testing of the product forms of the reference heat of type 304 stainless steel (heat 9T2796) has been completed, and a final tabulation of data is provided in Table 3.36. Efforts are being made to develop a method whereby the tensile curves for different products can be linked to a set of reference curves. Pursuing this, we have taken extensometer data at 593°C (1100°F) and processed them according to the relation that was developed for the 25-mm (1-in.) plate product.[47] For inelastic strain, e_p, between 0.1 and 5% this relation shows that the engineering stress, S, can be represented by a Ludwik-type[48] equation:

$$S = Ke_p^{3/4} + S_0$$

where K is a constant independent of temperature (below 649°C) and strain rate (in the range 10^{-5} to 10^{-1}/sec) and S_0 is a constant for a given temperature and strain rate. The values for K and S_0 for each product at 593°C are provided, along with plots for stress vs strain in Fig. 3.76.

---

*Reactor Division.

Table 3.36. Summary of Tensile Data for Different Product Forms of the Reference Heat of Type 304 Stainless Steel (Heat 9T2796)

Item, Designation	Product Form	Size		Temperature		Yield Strength		Tensile Strength		Elongation, %		Reduction of Area
		(in.)	(mm)	(°C)	(°F)	(ksi)	(MPa)	(ksi)	(MPa)	Uniform	Total	(%)
4, L	Plate	3/8	9.5	25	77	25.0	172.0	82.6	569	80	86	85
				593	1100	10.4	71.7	48.9	336	44	50	69
5, J	Plate	1/2	12.7	25	77	25.8	178.0	84.6	583	77	83	80
				593	1100	11.1	76.0	49.5	341	41	48	65
6, H	Plate	3/4	19	25	77	25.8	178.0	82.9	571	72	83	81
				593	1100	10.5	72.4	49.5	341	41	50	63
7, M	Plate	1	25	25	77	25.5	176.0	83.4	575	71	88	84
				93	200	20.6	142.0					
				204	400	16.0	110.0					
				316	600	15.1	104.0					
				427	800	12.7	87.6	60.1	414	39	48	74
				482	900	11.8	81.1					
				538	1000	11.05	76.1	54.5	375	39	48	70
				593	1100	10.5	72.3	49.3	339	34	46	66
				649	1200	10.9	74.8	41.5	286	30	48	46
				704	1300	10.9	74.8	27.0	186	23	49	44
				760	1400	9.8	67.7	25.3	174	16	48	40
8, K	Plate	2	50	25	77	26.6	183.0	78.4	540	79	85	78
				100	212			64.0	440	60	66	83
				200	392			57.7	398	47	62	79
				260	500	15.8	109.0	57.2	394	47	51	73
				350	662			56.6	390	44	44	69
				427	800	12.7	87.5	57.2	394	46	45	60
				482	900	11.8	81.3	55.8	384	46	52	71
				538	1000	11.1	76.5	49.6	342	43	52	67
				593	1100	10.85	74.8	46.55	321	46	47	61
				649	1200	10.2	70.3	40.2	277	36	48	49
				704	1300	11.1	76.8	31.2	215	29	43	41
10, B	Pipe	4 sched 160	102	25	77	26.6	183.0	82.9	571	70	86	83
				593	1100	11.7	80.6	49.5	341	44	55	69
11, A	Pipe	8 sched 80	203	25	77	26.3	181.0	83.0	572	70	84	82
				427	800	13.0	89.6	59.3	409	46	49	73
				538	1000	12.0	82.7	54.3	374	46	50	69
				593	1100	11.2	77.2	49.2	339	44	54	69
15, D	Pipe	2 1/2 CD	64	25	77	25.4	175.0	84.0	579	74	81	84
				593	1100	10.9	75.3	50.7	349	40	46	69
23, S	Bar	5/8 CD	16	25	77	24.3	167.0					
				593	1100	11.85	81.7	50.0	346	38	51	
18, R	Bar	5/8 HR	16	25	77	28.0	193.0	86.9	599	71	85	84
				93	200	23.0	578.0					
				204	400	18.8	129.0					
				316	650	17.0	117.0					
				427	800	16.2	112.0					
				482	900	14.3	98.1					
				538	1000	14.6	100.6					
				593	1100	{13.8	95.1	50.1	344	38	49	66
						9.6	66.0	53.1	365	34	50	
				649	1200	13.9	95.8					
				704	1300	10.7	73.7					
				760	1400	10.55	72.7					
19, T	Bar	1 HR	25	25	77	25.2	173.6	85.6	588	76	90	
				593	1100	10.3	71.0					
20, G	Bar	1 3/4 HR	44	25	77	26.8	185	82.9	571	79	87	85
				593	1100	13.0	89.6	48.7	336	42	49	67
21, F	Bar	1 7/8 HR	48	25	77	24.7	170.0	82.9	571	77	84	84
				593	1100	9.52	65.6	48.8	336	44	48	68
22, E	Bar	4 1/2 HR	114	25	77	26.3	181.0	85.2	587	70	85	84
				593	1100	10.7	73.7	47.2	325	42	48	65
51, C	Gun-drilled bar	2 1/2 OD	64	25	77	23.5	162.0	81.4	560	80	88	85
				593	1100	9.5	65.4	48.9	337	44	51	68

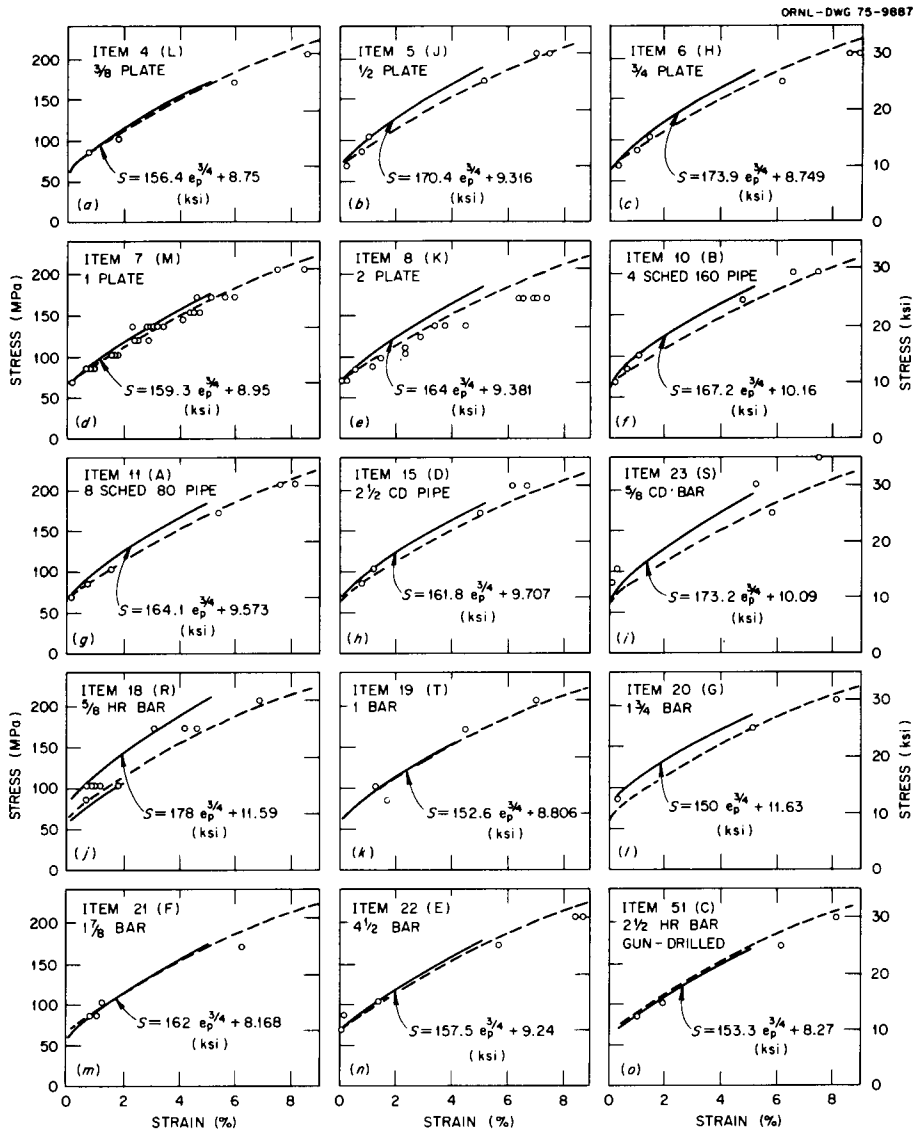

Fig. 3.76. Tensile Yield Curves at 593°C (1100°F) for Type 304 Stainless Steel (Heat 9T2796). Solid lines represent the fit of the Ludwik equation to extensometer data. Broken lines represent a model describing the tensile behavior of 25-mm (1-in.) plate. Open symbols represent loading strain data from creep tests on the different product forms.

Also included in the figures is the "reference" yield curve, which is based on a model applicable to a broad range of temperatures and strain rates.[47] Generally, the K and S_0 values used to calculate the reference curves differ from the K and S_0 values for the various products; hence we will need to develop a method for "normalizing" the yield curves for

the different product forms in order to make use of the reference curves, which cover a broader range of testing variables. Inelastic loading strain data, obtained from creep tests, are also provided in Fig. 3.76. At high stress levels the loading strains generally exceed the strain produced in tensile testing. This difference is probably due to differences in the "hardness" of a creep machine compared with a tensile machine, especially when step loading is used to apply the creep stress.

3.5.1.2 Exploratory Testing to Identify Behavioral Features — R. W. Swindeman

Previously, the exploratory testing program has emphasized studies concerned with the behavior of a reference heat of type 304 stainless steel [25-mm (1-in.) plate of heat 9T2796] under monotonic and cyclic straining conditions. During this last reporting period exploratory testing of this material was somewhat reduced in order to allocate equipment and resources to complete the product form characterization of the type 304 stainless steel reference heat (tensile and creep testing) and to begin exploratory tests on 2 1/4 Cr-1 Mo steel. Actually, exploratory tensile testing of the reference heat of type 304 stainless steel has been completed, and a final report is being prepared.[49] Rupture testing under constant load has also been completed, and we are preparing a report that is concerned with the representation of the rupture behavior.[19]

Some studies directed toward the understanding of the creep deformation behavior of type 304 stainless steel are still under way, however, since such an understanding is helpful in the development of constitutive equations. Extensive studies of the substructure produced by tensile and creep testing have been completed by Bhargava and Moteff,[50] and we are using their information, along with data obtained from light microscopy, to assist in these deformation studies. Generally, the secondary creep rate observed for the 25-mm (1-in.) plate follows a well-defined pattern as the temperature and stress are varied, and several correlations for secondary creep rate data are available.[2,50,51]

What is more difficult is the understanding and treatment of the transient creep components. As reported elsewhere,[19,51] an abrupt discontinuity is observed in the primary creep behavior as the stress is changed

through a critical stress region. If we assume that the transient strain for any time, $e_1(t)$, can be represented by the exponential form:

$$e_1(t) = e_t[1 - \exp(-rt)] ,$$

where t is time, e_t is the transient component, and r is the rate constant, then the change is reflected in the trend of both the stress dependency of the transient creep exponent, e_t, and the rate constant, r.

The stress and temperature dependences for e_t and r are provided in Figs. 3.77 and 3.78. To establish that the discontinuity exists in other product forms of the reference heat, data for the 16-mm (0.63-in.) bar are also included. Unfortunately, the irregularity occurs in the range of stresses and temperatures of greatest interest to the exploratory testing program. For example, we would like to examine creep and rupture behavior under time-varying loads around 593°C (1100°F) for stresses in the range 103 to 172 MPa (15–25 ksi) and times from 100 to 10,000 hr. The discontinuity appears to exist around 138 MPa (20 ksi) and also 1000 hr, which is in the middle of this range of interest.

Also, an adequate description of the creep behavior of heat 9T2796 appears to require at least two terms involving the primary creep. If we chose to use the transient type formulation, then two transient creep terms plus a secondary creep rate term are required. One formulation of this type, of course, is the double-exponential creep equation, as developed by Blackburn[52] and Pugh.[53] If one is concerned only with curve fitting, then the rational polynomial, again developed by Pugh[53] could be used. In Fig. 3.77, where the transient component, e_t, has been plotted, we have observed that the e_t values for stresses above the discontinuity tend to increase with increasing stress and then decrease. If we assume that the high-stress transient component is associated with a short-term transient and that the values for e_t "peak out" near 189 MPa (27.5 ksi), then one can draw through the data a bell-shaped curve that is centered at 189 MPa (27.5 ksi). (The dependent variable, e_t, has been drawn on the absissa for convenience of comparison with loading strains.) The dashed lines sketched in Fig. 3.77 represent the visual fit of an empirical equation to the data:

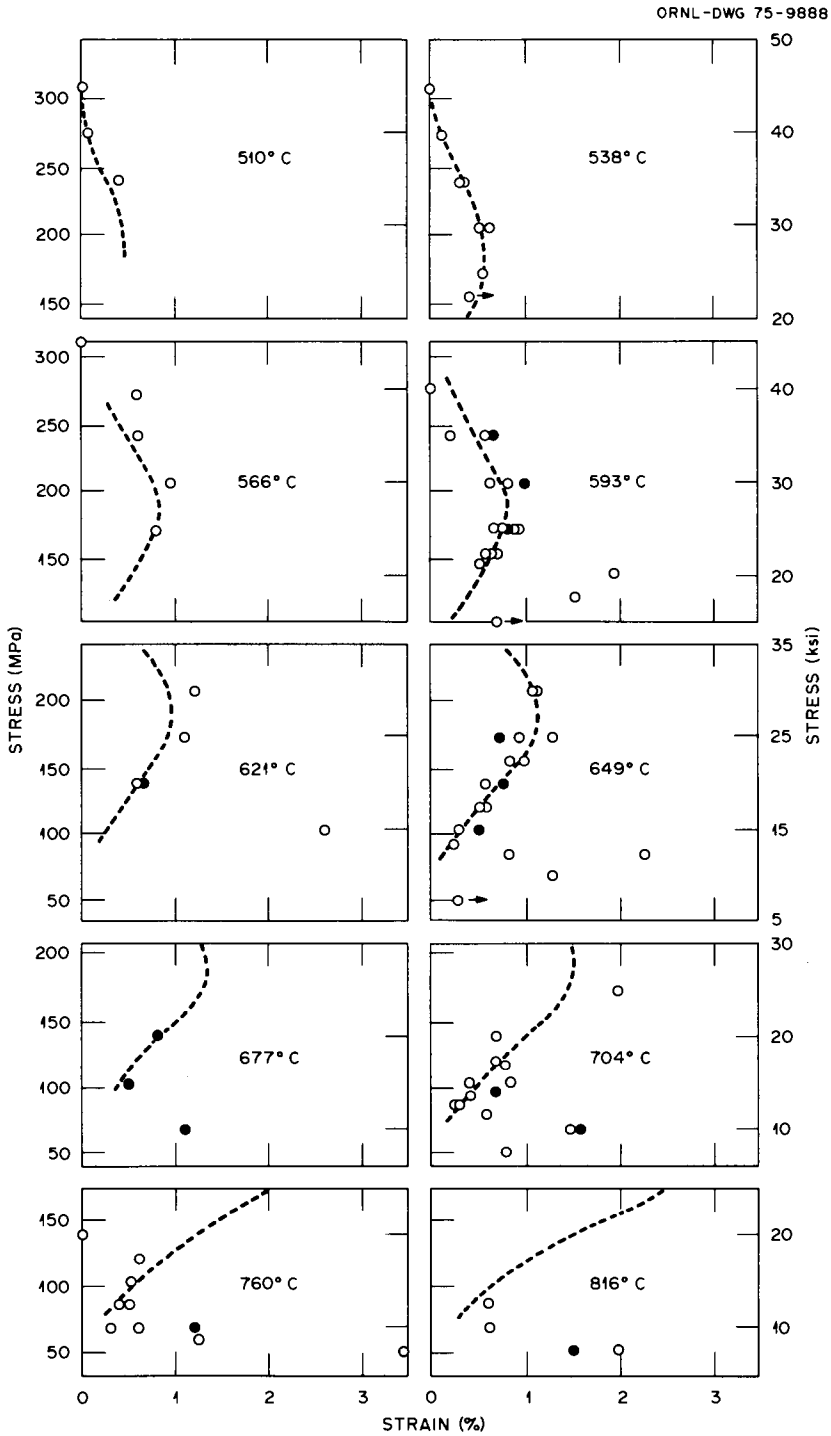

Fig. 3.77. Variation in the Transient Creep Component, e_t, with Stress and Temperature for Type 304 Stainless Steel (Heat 9T2796). Open symbols are for 25-mm plate and solid symbols for 16-mm bar. Dashed lines represent the fit of an equation to the short-time data.

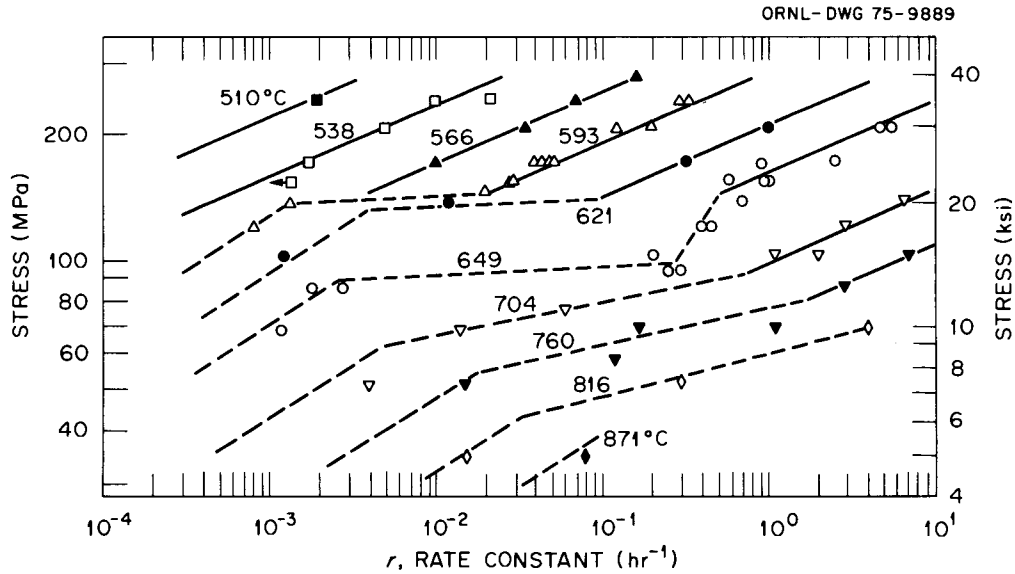

Fig. 3.78. Variation in the Rate Constant, r, with Stress and Temperature for Type 304 Stainless Steel (Heat 9T2796 25-mm Plate).

$$e_t = K \exp(-Q/RT) \exp[-B(S - S_b)^2] \ ,$$

where K, Q, R, B, and S_b are all constants, independent of temperature and stress. The above equation does not appear to have any physical significance, however, and data for stresses below the discontinuity are insufficient to establish any meaningful trend.

Several investigators[54-56] have tried to develop or justify the use of the exponential-type expression for transient creep, and in some cases the rate constant has been found to relate to the secondary creep rate. We have not been able to establish such a correlation. However, the rate constant, r, for the short-time transient can apparently be related to the absolute temperature, T, by an activation energy and to the stress, S, by a simple power law:

$$r = KS^n \exp(Q/RT) \ ,$$

where K, n, and Q are constants and R is the universal gas constant. The applicability of this relation is in the range defined by the solid lines in Fig. 3.78. Examination of the long-term transient creep behavior is still under way and a great deal more study appears necessary before any

meaningful relation between the transient rate constant, r, and the testing variables can be developed in this region. As mentioned elsewhere, this rate constant could be associated with expressions other than the expontential. An example might be the Li[57] equation.

Testing has been under way to collect more data concerning creep behavior under varying stresses for type 304 stainless steel. Typical curves for a series of tests at 593°C (1100°F) are shown in Fig. 3.79. Five creep curves are plotted representing one constant-load test at 138 MPa (20 ksi) and four variable-load tests. All variable-load tests spent about half their time at 138 MPa (20 ksi) and the remainder at lower stresses. For ease of comparison, therefore, the time scale of the constant-load test was doubled. Three of the variable-load tests produced

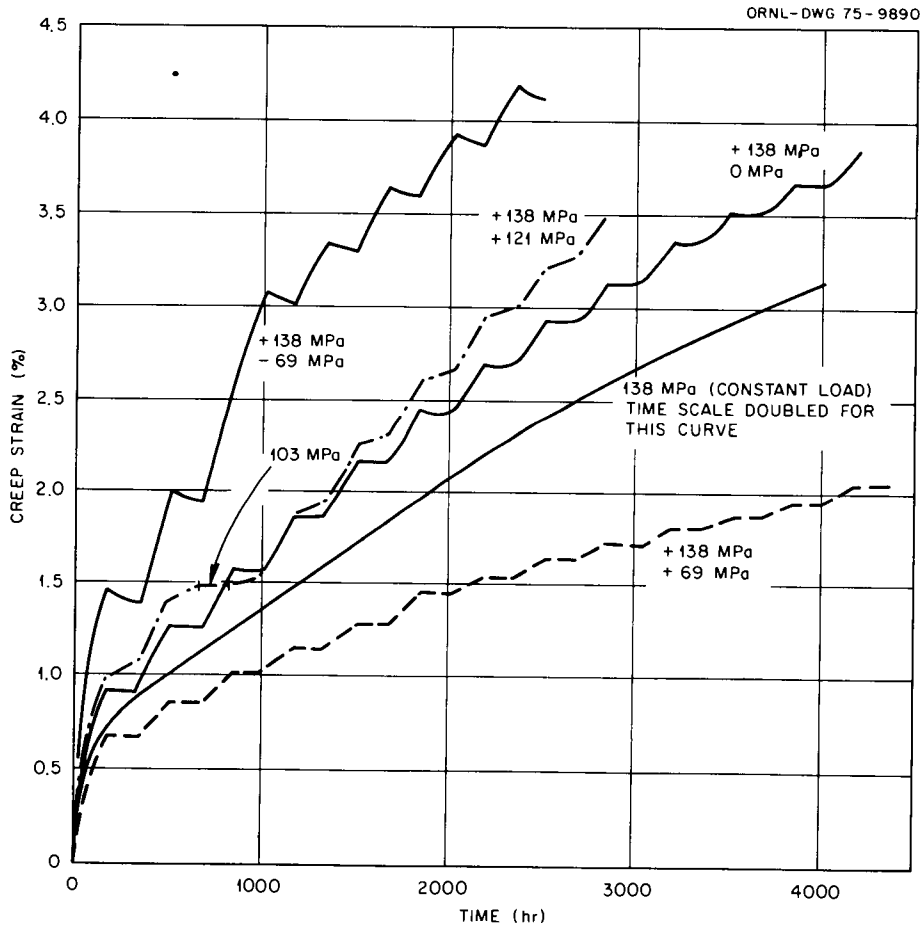

Fig. 3.79. Creep Curves for Type 304 Stainless Steel (Heat 9T2796) Under Varying Stresses at 593°C (1100°F).

average creep rates that exceeded the constant-load test. Only the test with the ratio +138/—121 MPa (+20/—17.5 ksi) was expected to produce higher average creep rates if any assumes the auxiliary hardening rules[58] proposed for type 304 stainless steel apply. One test, at the stress ratio +138/+69 MPa (+20/+10 ksi), exhibited a lower average creep rate. The results obtained to date suggest that additional *and very careful* testing is needed in the area of creep under variable loads before any meaningful improvements can be made in advancing the status of the hardening rules based on uniaxial data.

3.5.1.3 Exploratory Testing of 2 1/4 Cr-1 Mo Steel — R. W. Swindeman and R. L. Klueh

Exploratory testing of 2 1/4 Cr-1 Mo steel is of limited scope. Uniaxial tensile and creep data are being obtained as part of the Steam Generator Program, and our work is supplemental. Primarily, we are examining creep-plasticity interactions and relaxation behavior. We have completed a series of relaxation tests that involved multiple loadings at 510 and 566°C (950 and 1050°F). Some results for 510°C are shown in Fig. 3.80. Specimen SA211A was tested for 1000 hr and then reloaded to

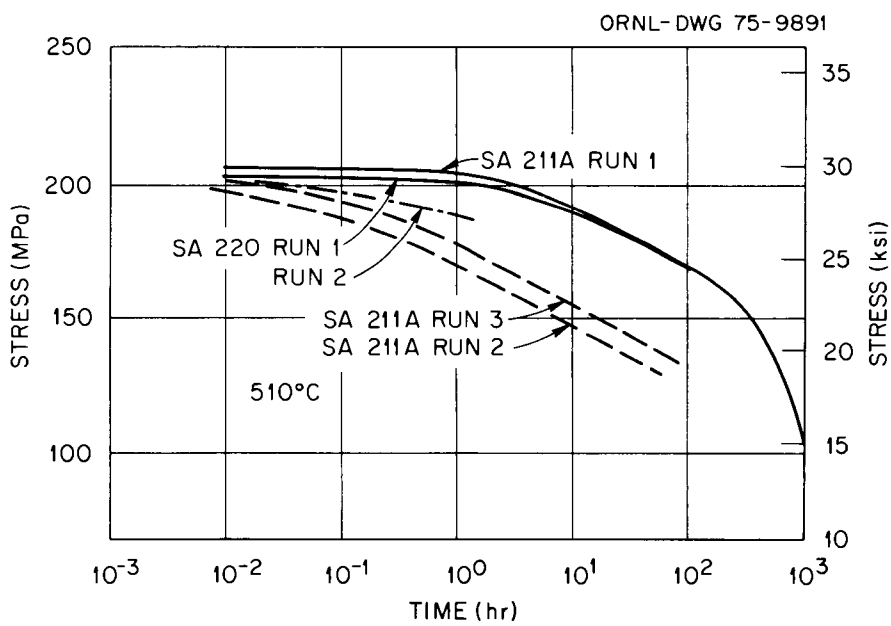

Fig. 3.80. Effect of Reloading on the Relaxation Curve for 2 1/4 Cr-1 Mo Steel at 510°C (950°F).

207 MPa (30 ksi). On the second run the relaxation rates were greater than for the virgin material, at least for times extending to 100 hr. A third loading agreed fairly well with the second loading. This, of course, implies that time- or strain-dependent weakening occurred during the initial 1000 hr testing period at 510°C. We tested another specimen, SA220, holding the virgin specimen for only 100 hr. The relaxation curve agreed with the first loading of specimen SA211A. On the second loading of specimen SA220, we observed a smaller increase in relaxation rates than for the longer time exposure. However, the results again suggest that a time- or strain-dependent weakening process is occurring for this material when the starting stresses are high. Currently, reloadings at lower starting stresses, less than 138 MPa (20 ksi), are being performed to see if the effect exists for stresses more closely approximating service conditions.

At 566°C (1050°F) time or strain weakening is very evident. In Fig. 3.81 results for two tests are shown. The curves correspond to relaxation for virgin material starting near 138 and 207 MPa (20 and 30 ksi). The curves show the same general features as the curve for the virgin specimen tested at 510°C (SA211A). The results obtained after reloading are shown in Fig. 3.82. For both specimens the starting stresses were increased by approximately 34 MPa (5 ksi). Comparison of Figs. 3.81 and 3.82 shows that the relaxation rates for short times are much higher after the second loading. Third loadings were also performed and tests exhibited similar trends as shown in Fig. 3.83. Data for the strain rate are plotted against stress in Fig. 3.84 for specimens SA221 and 223. The strain rate at 566°C (1050°F) for the virgin material exhibits a sigmoidal behavior, while the rate for subsequent reloadings exhibits a trend similar to that expected from constant-load creep experiments. Indeed, calculation of the relaxation curve based on secondary creep rate data agrees quite well with experimental data.

One creep-plasticity interaction test was performed on 2 1/4 Cr-1 Mo steel during this reporting period, and the results are summarized below. Figure 3.85 shows how the accumulated creep strain influences the cyclic hardening behavior. For example, after the first week of creep at 566°C

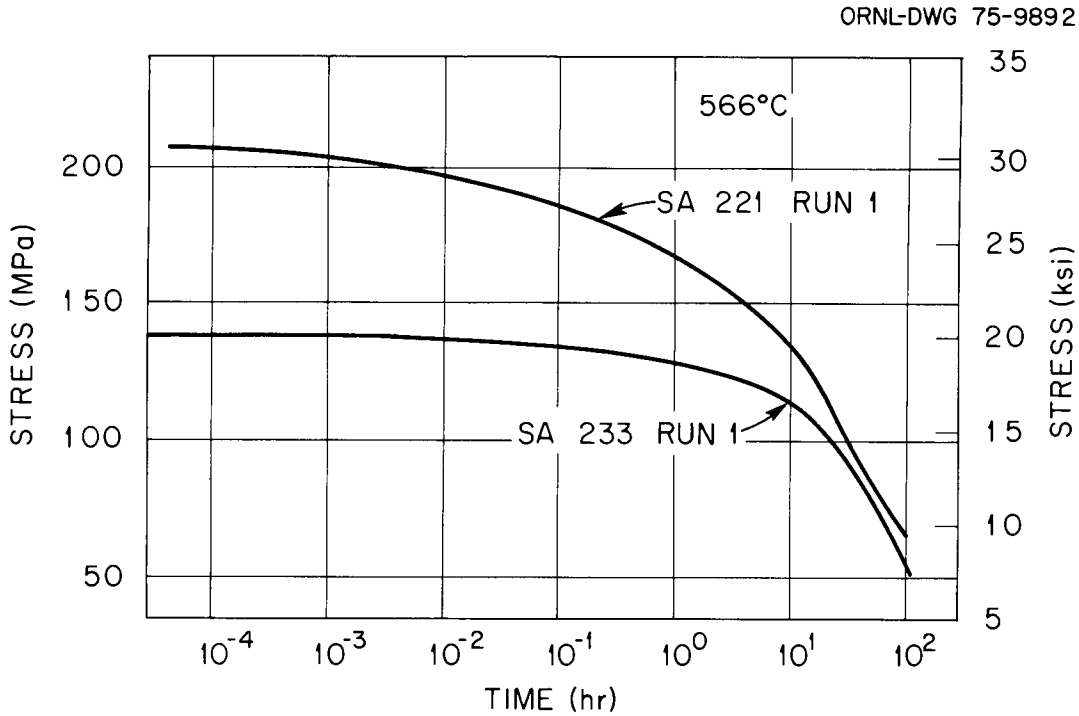

Fig. 3.81. Relaxation Curves for 2 1/4 Cr-1 Mo Steel in the Annealed Condition at 566°C (1050°F).

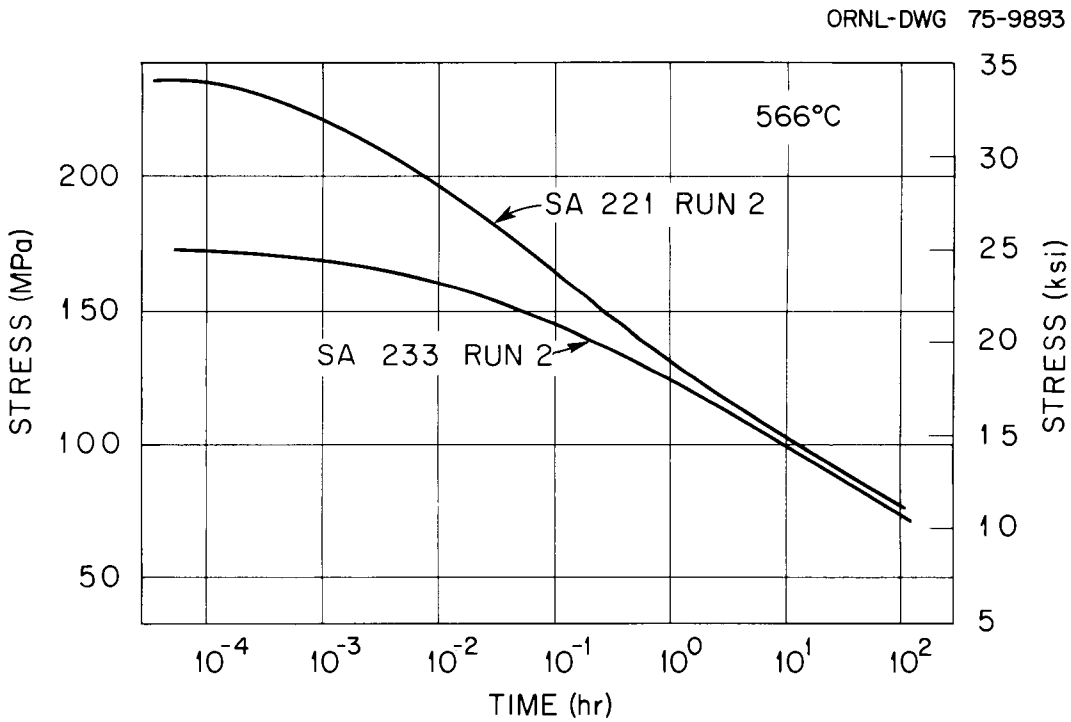

Fig. 3.82. Relaxation Curves for 2 1/4 Cr-1 Mo Steel Reloaded After 100 hr Prior Exposure at 566°C (1050°F).

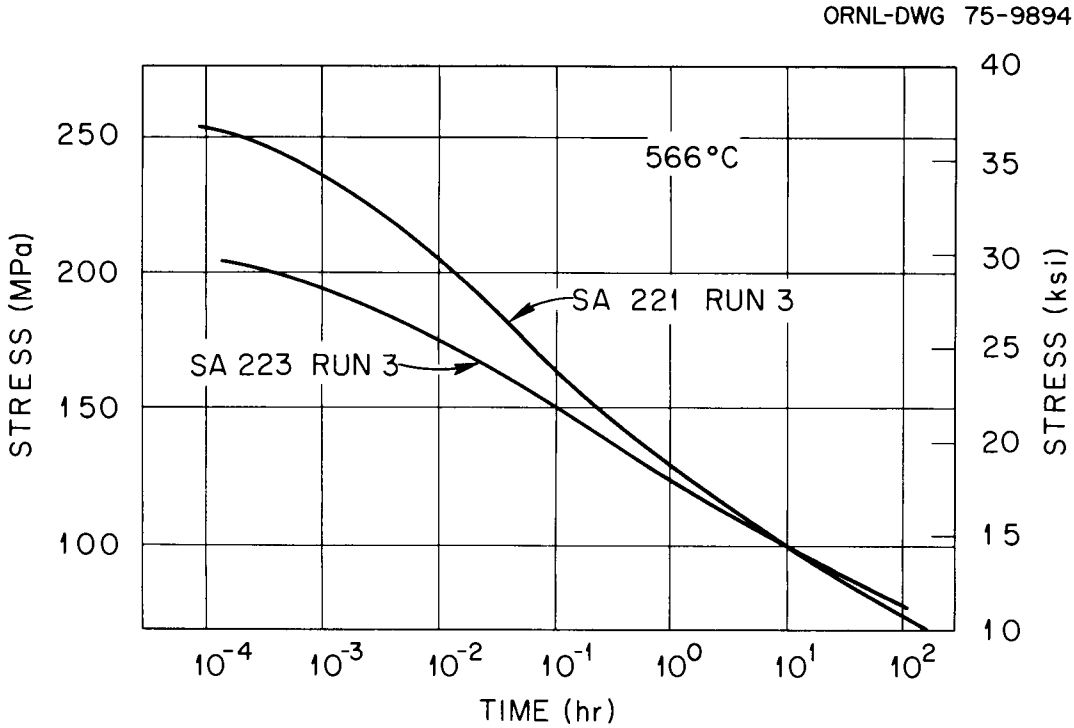

Fig. 3.83. Relaxation Curves for 2 1/4 Cr-1 Mo Steel Reloaded after 200 hr Prior Exposure at 566°C (1050°F).

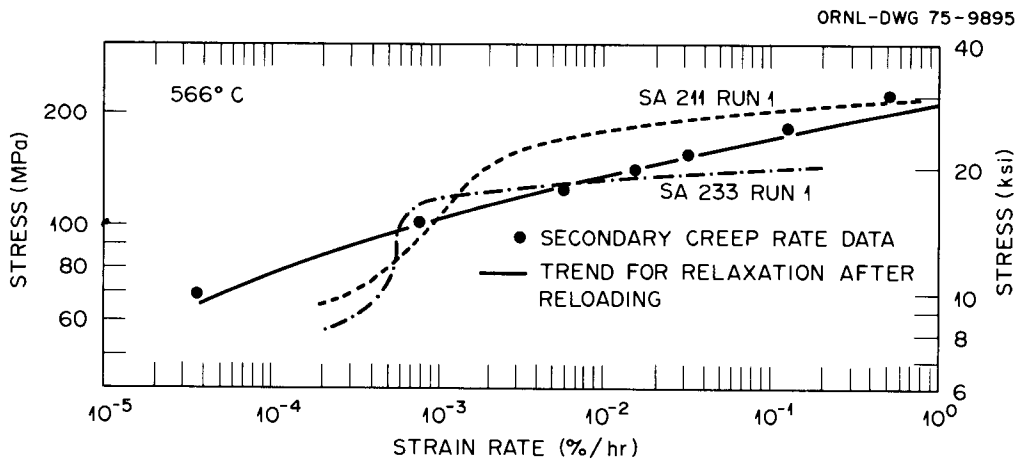

Fig. 3.84. Stress vs Strain Rate Obtained from Relaxation Tests on 2 1/4 Cr-1 Mo Steel at 566°C (1050°F).

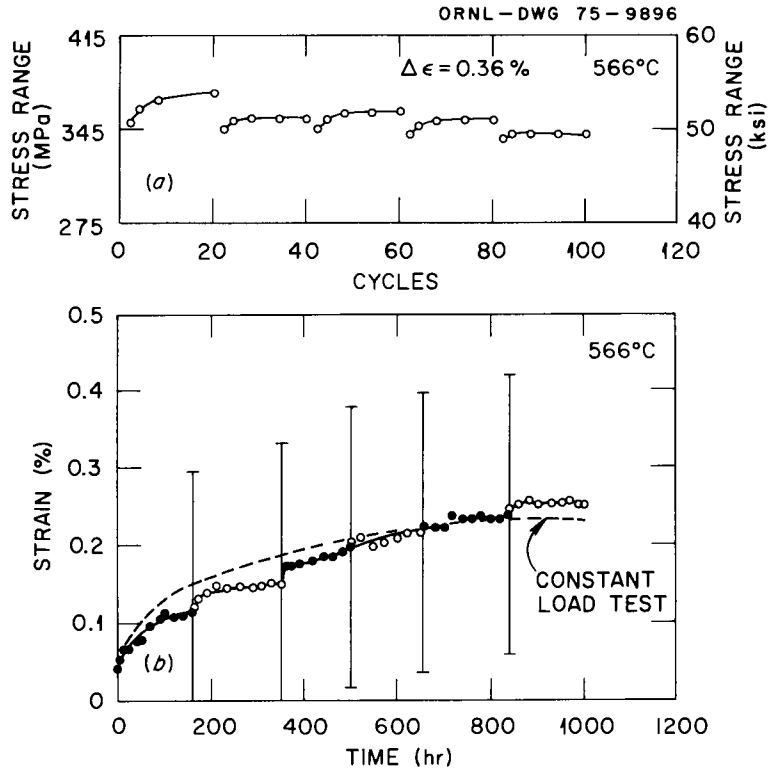

Fig. 3.85. Results of a Creep Plasticity Test on Annealed 2 1/4 Cr-1 Mo Steel at 566°C (1050°F). Specimen was creep tested at 69 MPa (10 ksi) with 20 strain cycles at one-week intervals.

20 cycles at 0.36% strain range were introduced. The stress range was initially near 344 MPa (50 ksi) and after 20 cycles was near 372 MPa (54 ksi). A subsequent period of creep produced softening when cycling was resumed, as shown by the value for the stress range at 21, 41, 61, and 81 cycles. However, the amount of softening was quite small, and one could approximate the cyclic strength fairly well by using the first-cycle hysteresis loop. Figure 3.85(b) shows how the cyclic strain influenced the creep curve at 69 MPa (10 ksi). Again the influence is quite small, as may be seen by comparing the dashed curve for a constant load creep test with the symbols that show the trend for the interspersed creep and plasticity test. After 1000-hr exposure, the specimen was cycled at 0.72% strain range, and the short-time creep curve investigated by loading to different locations with the hysteresis loop. Tests of this sort have been recommended by Manson, Halford, and Nactigall[59]

for determining strain components within a hysteresis loop. A typical loop is shown in Fig. 3.86 and the symbols locate points on the loop at which creep tests were performed. For example, the loop might be repeated several times to assure stability; then strain control might be stopped at point B and the stress held constant for some arbitrary time, say several hours. After creep to point B1 cycling might be resumed and then stopped at some new point. Some typical creep curves are shown in Fig. 3.87. As might be expected, the amount of creep depends on the actual stress level, say 69, 103, or 138 MPa, and also on whether or not the prior plastic straining was in the same direction as the creep. For example, the creep at point b is much less than the creep at point B. In either case, we find that the creep rates are usually higher than the secondary creep rates based on constant-load data when the creep load periods are short, say less than 100 hr.

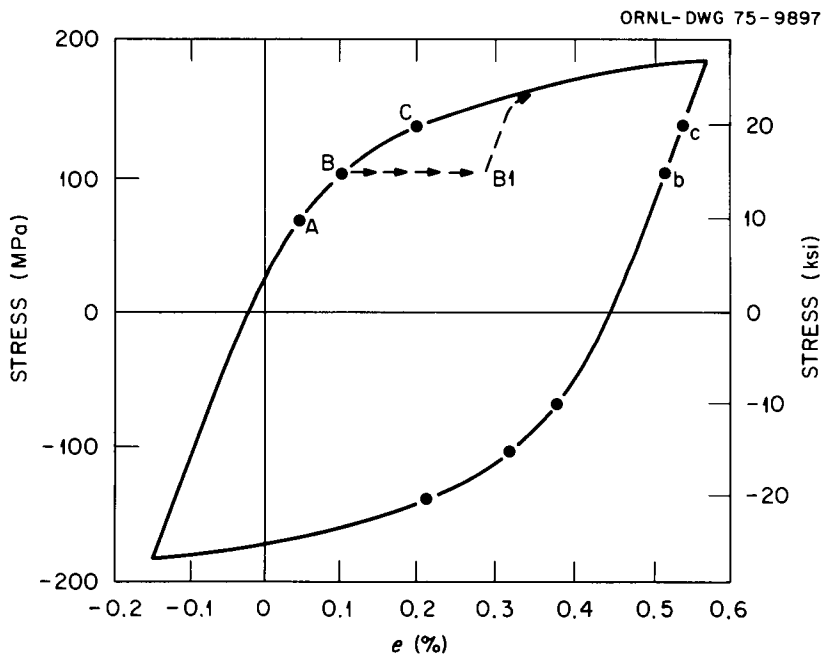

Fig. 3.86. Hysteresis Loop for 2 1/4 Cr-1 Mo at 566°C (1050°F) at 0.72% Strain Range. Symbols designate stresses at which short-time creep tests were performed. Specimen had been exposed to 1000 hr creep at 69 MPa (10 ksi) and cycling at 0.36% strain range.

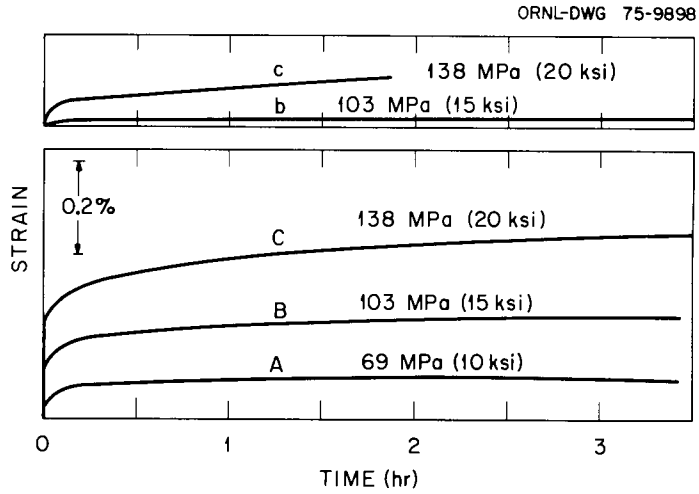

Fig. 3.87. Creep Curves Obtained after Holding the Stress at Different Locations Within the Hysteresis Loop for the 2 1/4 Cr-1 Mo Steel at 566°C (1050°F).

3.5.2 Investigations of Creep Failure under Uniaxial and Multiaxial Conditions — C. C. Shultz, Babcock and Wilcox

(No report)

3.6 MECHANICAL PROPERTIES OF HTGR STEAM GENERATOR AND PRIMARY CIRCUIT MATERIALS — P. L. Rittenhouse

The principal aims of this program are to (1) determine the long-term compatibility of HTGR steam-cycle plant alloys with their environment and (2) determine, compile, and analyze materials design data for the commercial HTGR. Achievement of these goals requires mechanical property determinations (tensile, creep, low-cycle fatigure, and crack growth) on HTGR alloys at temperatures and in environments (helium and steam) appropriate to their service in the reactor system.

3.6.1 Tensile Testing — P. L. Rittenhouse

Tensile tests of 1/2-in. (13-mm) Hastelloy S plate (heat 8635T) have been completed over the temperature range 22 to 871°C (72–1600°F). The results of these tests, conducted at a strain rate of 0.4%/min, are shown in Table 3.37. Testing of plate from an Inconel 617 heat (XX01A3US) is now in progress.

Table 3.37. Tensile Properties of Hastelloy S

Test	Temperature (°C)	Temperature (°F)	Strength, MPa (ksi) 0.2% Yield	Strength, MPa (ksi) Ultimate Tensile	Elongation (%)	Reduction of Area (%)
15324	22	72	457 (66.3)	934 (135.5)	50.8	69.2
15325	22	72	466 (67.6)	931 (135.0)	52.8	68.1
15326	22	72	455 (66.0)	924 (134.0)	51.6	60.1
15355	22	72	465 (67.4)	929 (134.8)		61.6
15327	149	300	425 (61.6)	879 (127.5)	52.4	61.7
15328	149	300	417 (60.5)	880 (127.6)	51.2	53.3
15329	288	550	376 (54.6)	852 (123.6)	53.7	60.4
15330	288	550	363 (52.7)	850 (123.2)	52.2	43.4
15331	288	550	368 (53.4)	858 (124.4)	48.4	54.8
15332	427	800	350 (50.7)	836 (121.2)	50.4	54.5
15333	438	820	366 (53.1)	852 (123.5)	52.6	41.7
15334	482	900	348 (50.5)	829 (120.2)	51.6	38.9
15335	482	900	361 (52.3)	835 (121.1)	47.1	50.9
15336	482	900	359 (52.0)	837 (121.4)	50.9	41.2
15337	538	1000	359 (52.0)	818 (118.6)	49.2	45.4
15338	538	1000	333 (48.3)	805 (116.8)	52.8	35.2
15339	593	1100	330 (47.8)	789 (114.4)	45.6	39.0
15340	593	1100	363 (52.6)	793 (115.0)	45.3	36.3
15341	593	1100	367 (53.3)	786 (114.0)	62.6	43.7
15342	649	1200	358 (51.9)	654 (94.9)	94.4	74.1
15343	649	1200	363 (52.7)	655 (95.0)	96.0	76.5
15344	649	1200	365 (52.9)	652 (94.5)	96.2	75.6
15345	704	1300	345 (50.0)	496 (71.9)	83.7	82.1
15346	704	1300	349 (50.6)	494 (71.7)	93.1	83.0
15354	704	1300	355 (51.5)	501 (72.7)	81.9	80.2
15347	760	1400	314 (45.6)	365 (52.9)	79.6	85.0
15348	760	1400	345 (50.0)	362 (52.5)	81.7	86.0
15349	816	1500	276 (40.0)	278 (40.3)	93.9	86.6
15350	816	1500	259 (37.5)	262 (38.0)	71.0	86.0
15351	816	1500	276 (40.0)	282 (40.9)		93.7
15352	871	1600	173 (25.1)	175 (25.4)	78.2	90.6
15353	871	1600	175 (25.4)	178 (25.8)	78.7	85.6

3.6.2 Environmental Creep Testing — P. L. Rittenhouse

Environmental creep tests continue, employing a premixed gas supply in a once-through loop at a pressure of 1.1 to 1.5 atm (0.11–0.15 MPa). The nominal composition of the gas is 250–325 μatm (2.5–3.3 Pa) H_2, 25–35 μatm (2.5–3.5 Pa) CH_4, 12–20 μatm (1.2–2.0 Pa) CO, 8–30 μatm (0.8–3.0 Pa) H_2O, and balance helium. An oxygen potential meter recently installed in the system indicates an oxygen partial pressure of about 10^{-19} μatm (10^{-20} Pa). This level is consistent with those expected in operating gas-cooled reactors.

Details of the ten environmental creep tests operated during the quarter are shown in Table 3.38. Tests 15045 [2 1/4 Cr-1 Mo, 593°C (1100°F), 69 MPa (10 ksi)] and 15377 [9 Cr-1 Mo, 482°C (900°F), 172 MPa 25 ksi)] were discontinued during the last week of June. Test 15045 was terminated after 3200 hr at a total strain of about 1% to make testing space available for other materials. (Two other tests, 15023 and 15047, identical to 15045, are continuing.) Test 15377 was shut down because of extremely erratic strain readings of presently unknown cause. Both the specimens will be examined closely for any evidence of reaction with the impurities (i.e., H_2, CO, CH_4, and H_2O) in the simulated HTGR primary coolant environment.

Table 3.38. Current Environmental Creep Tests

Test	Test Frame	Material	Heat	Temperature		Stress		Comments
				(°C)	(°F)	(MPa)	(ksi)	
15023	I-168	2 1/4 Cr-1 Mo	X-6216	593	1100	69	10	
15045	I-160	2 1/4 Cr-1 Mo	X-6216	593	1100	69	10	Discontinued
15046	I-161	2 1/4 Cr-1 Mo	X-6216	593	1100	103	15	
15047	I-169	2 1/4 Cr-1 Mo	X-6216	593	1100	69	10	
15058	I-162	Hastelloy X	2600-3-4936	704	1300	138	20	In tertiary creep at 1600 hr
15363	I-163	9 Cr-1 Mo	316381-1A	538	1000	103	15	
15369	I-164	2 1/4 Cr-1 Mo	36202	538	1000	103	15	
15373	I-166	2 1/4 Cr-1 Mo	36202	482	900	207	30	In tertiary creep at 500 hr
15374	I-165	2 1/4 Cr-1 Mo	36202	482	900	172	25	In tertiary creep at 800 hr
15377	I-167	9 Cr-1 Mo	316381-1A	482	900	172	25	Discontinued

Strain data for times up to 3000 hr are shown for all tests in Table 3.39. Readings from 15058 [Hastelloy X, 704°C (1300°F), 138 MPa (20 ksi)], 15373 [2 1/4 Cr-1 Mo, 482°C (900°F), 207 MPa (30 ksi)], and 15374 [2 1/4 Cr-1 Mo, 482°C (900°F), 172 MPa (25 ksi)] indicate that they entered tertiary creep at about 1600, 500, and 800 hr, respectively. All other tests are in second-stage creep. Two new tests, Hastelloy X at 649 and 704°C (1200 and 1300°F), and 172 MPa (25 ksi), are being initiated.

3.6.3 Subcritical Crack Growth Studies — W. R. Corwin and J. L. Frazier*

Comparative testing at 510°C (950°F) in steam and air at 200 cpm have been completed on 2 1/4 Cr-1 Mo steel. As shown in Fig. 3.66 (p. 157) the steam atmosphere causes little or no effect under those conditions. Similar comparative tests are currently under way at 4 cpm.

*Oak Ridge Y-12 Plant.

Table 3.39. Strain-Time Data From Environmental Creep Tests[a]

Time (hr)	Total Strain (%) for Each Test									
	15023	15045	15046	15047	15058	15363	15369	15373	15374	15377
200	0.22	0.17	0.20	0.14	1.56	0.14	0.35	1.70	0.64	0.35
400	0.29	0.23	0.38	0.17	2.23	0.18	0.59	2.07	0.72	0.39
600	0.34	0.27	0.55	0.22	2.67	0.23	0.83	2.43	0.80	0.42
800	0.39	0.32	0.73	0.28	3.03	0.28	1.04	2.92	0.90	0.46
1000	0.44	0.36	0.87	0.34	3.31	0.33	1.22	3.45	1.01	0.49
1200	0.49	0.41	0.99	0.40	3.65	0.37	1.39	4.17	1.16	
1400	0.54	0.45	1.11	0.45	3.97	0.42	1.56	4.96	1.36	
1600	0.59	0.50	1.22	0.52	4.34					
1800	0.64	0.54	1.34	0.58	4.78					
2000	0.69	0.59	1.46	0.64	5.23					
2200	0.74	0.64	1.57	0.70	5.81					
2400	0.79	0.69	1.69	0.76	6.37					
2600	0.84	0.75	1.80	0.82	7.04					
2800	0.89	0.81	1.92	0.88	7.86					
3000	0.94	0.87	2.03	0.94	8.82					

[a]Materials and conditions are given in Table 3.38.

Testing has begun in simulated HTGR primary coolant helium on 2 1/4 Cr-1 Mo steel. Test conditions are 510°C (950°F), R = 0.05 with a frequency of 40 cpm. Testing equipment has been modified to allow remote crack monitoring via the electrical potential technique. This reduces both equipment downtime and specimen exposure to air necessitated by optical crack measurements. Although the test is not yet complete, it appears that fatigue cracking resistance is less in the HTGR coolant than in air. There are insufficient data for presentation at this time.

Specimen preparation of Hastelloy X has begun. Upon completion, this material will be incorporated into the subcritical crack growth studies.

3.6.4 Fatigue Life Testing — J. P. Strizak

Strain-controlled fatigue tests in air at 371°C (700°F) on 2 1/4 Cr-1 Mo steel continued on the MTS system. Design of an environmental chamber to permit use of the system for strain-controlled tests in simulated HTGR primary coolant helium has been completed. Assembly and check-out of the chamber on the MTS system will begin in July. Design of a backup environmental chamber that will also permit strain-controlled fatigue testing in vacuum to 10^{-8} to 10^{-7} torr (1.3–13 μPa) is presently under way. Fatigue specimens from 1/2-in. (13-mm) Hastelloy X plate (2600-3-4936) are being prepared.

3.7 REFERENCES

1. W. F. Simmons and J. A. Van Echo, "Report on the Elevated-Temperature Properties of Stainless Steels," *ASTM Data Ser.* DS 5 S1, American Society for Testing and Materials, Philadelphia, 1965.
2. M. K. Booker, C. R. Brinkman, and V. K. Sikka, "Correlation and Extrapolation of Creep Ductility Data for Four Elevated-Temperature Structural Materials," to be presented at Symposium on Structural Materials for Elevated-Temperature Nuclear Power Generation Service, ASME Winter Meeting, Houston, Texas, Nov. 30–Dec. 4, 1975.
3. F. Garofalo, *Fundamentals of Creep and Creep-Rupture in Metals*, Macmillan, New York, 1965.

4. R. N. Stevens, "Grain Boundary Sliding in Metals," *Met. Rev.* 11: 129–42 (1966).

5. F. Garofalo, *Ductility*, American Society for Metals, Metals Park, Ohio, 1968, pp. 87–129.

6. ASTM Designation: A 240-71, "Standard Specification for Stainless and Heat-Resisting Chromium and Chromium-Nickel Steel Plate, Sheet and Strip for Fusion Welded Unfired Pressure Vessels," *Annual Book of ASTM Standards, Part 3*, American Society for Testing and Materials, Philadelphia, April 1972.

7. ASTM Designation: A 312-71, "Standard Specification for Seamless and Welded Austenitic Stainless Steel Pipe, *Annual Book of ASTM Standards, Part 1*, American Society for Testing and Materials, Philadelphia, April 1972.

8. ASTM Designation: A 479-71, "Standard Specification for Stainless Steel and Heat-Resisting Steel Bars and Shapes for Use in Boilers and Other Pressure Vessels," *Annual Book of ASTM Standards, Part 3*, American Society for Testing and Materials, Philadelphia, April 1972.

9. "Heat Treating of Stainless Steel and Heat-Resisting Alloys," *Metals Handbook*, Vol. 2, American Society for Metals, Metals Park, Ohio, 1971, pp. 243–54.

10. Hanford Engineering Development Laboratory, *Nuclear Systems Materials Handbook*, TID-26666 (continually revised).

11. V. K. Sikka, R. W. Swindeman, and T. L. Hebble, "Relation Between Tensile Properties in the As-Received (Mill-Annealed) and Reannealed (Laboratory-Annealed) Conditions for Types 304 and 316 Stainless Steel," *Mechanical Properties Test Data for Structural Materials Quart. Progr. Rep. Apr. 30, 1975*, ORNL-5105, pp. 102–13.

12. R. A. Moen and G. V. Smith, "A Consideration on Limits of Cold Working in Nuclear Construction," *J. Eng. Mater. Technol.* 97: 162–71 (April 1975).

13. V. K. Sikka, C. R. Brinkman, and H. E. McCoy, "Effect of Thermal Aging on Tensile and Creep Properties of Types 304 and 316 Stainless Steel," to be presented at Symposium on Structural Materials for Elevated-Temperature Nuclear Power Generation Service, ASME Winter Meeting, Houston, Texas, Nov. 30–Dec. 4, 1975.

14. C. F. Etienne, W. Dortland, and H. B. Zeedijk, "On the Capability of Austenitic Steel to Withstand Cyclic Deformation During Service at Elevated Temperature," paper presented at International Conference on Creep and Fatigue in Elevated Temperature Applications, Philadelphia, 1973, and Sheffield, UK, April 1974.

15. F. Garofalo, R. W. Whitmore, and F. Von Gemmingen, "Creep and Creep-Rupture Relationships in an Austenitic Stainless Steel," *Trans. Metall. Soc. AIME* 221: 310–19 (1961).

16. M. K. Booker, "Materials Behavior in Support of Development and Evaluation of Failure Criteria for Materials," *Mechanical Properties Test Data for Structural Materials Quart. Progr. Rep. Oct. 31, 1974,* ORNL-5103, pp. 148–57.

17. Ibid., *Jan. 31, 1975,* ORNL-5104, pp. 166–81.

18. Ibid., *Apr. 30, 1975,* ORNL-5105, pp. 141–64.

19. R. W. Swindeman, "Creep-Rupture Correlations for Type 304 Stainless Steel (Heat 9T2796)," to be presented at Symposium on Structural Materials for Elevated-Temperature Nuclear Power Generation Service, ASME Winter Meeting, Houston, Texas, Nov. 30–Dec. 4, 1975.

20. V. K. Sikka, H. E. McCoy, M. K. Booker, and C. R. Brinkman, "Heat-to-Heat Variation in Creep Properties of Types 304 and 316 Stainless Steels," presented at the 2nd National Congress on Pressure Vessels and Piping, 1975 ASME Summer Meeting, June 23–27, 1975.

21. L. D. Blackburn, Hanford Engineering Development Laboratory, private communication, November 1973.

22. R. W. Swindeman and C. E. Pugh, *Creep Studies on Type 304 Stainless Steel (Heat 8043813) Under Constant and Varying Loads,* ORNL-TM-4427 (June 1974).

23. J. R. Barker, E. W. Ross, and J. F. Radavich, "Long Time Stability of Inconel 718," *J. Met.* 20(1): 31–41 (January 1970).

24. C. E. Korth, Aerojet Nuclear Company, private communication, January 1975.

25. S. S. Manson and C. R. Ensign, *A Specialized Model for Analysis of Creep-Rupture Data by the Minimum Commitment, Station Function Approach,* NASA-TM-X-52999 (1970).

26. M. K. Booker and V. K. Sikka, "Interrelationships Between Creep Life Criteria for Four Nuclear Structural Materials," presented at 1975 Annual Meeting, American Nuclear Society, New Orleans (June 1975); submitted for publication.

27. M. K. Booker and C. O. Stevens, "Structural Materials Information Center," *Mechanical Properties Test Data for Structural Materials Quart. Progr. Rep. Jan. 31, 1975,* ORNL-5104, pp. 182–85.

28. M. K. Booker and C. O. Stevens, "Material Data Processing," *Mechanical Properties Test Data for Structural Materials Quart. Progr. Rep. Apr. 30, 1975,* ORNL-5105, pp. 164–72.

29. H. E. McCoy, M. W. Moyer, and T. W. Dews, "Measurements of Elastic Constants of Type 304 Stainless Steel," *Fuels and Materials Development Program Quart. Progr. Rep Dec. 31, 1973,* ORNL-TM-4524, pp. 75–82.

30. J. P. Hammond and M. W. Moyer, "Measurement of Elastic Constants of 2 1/4 Cr-1 Mo Steel by the Dynamic Method," *Mechanical Properties Test Data for Structural Materials Quart. Progr. Rep. Apr. 30, 1974,* ORNL-4963, pp. 126–33.

31. J. P. Hammond, "Specimens for Dynamic Elastic Properties Study," *Fuels and Materials Development Program Quart. Progr. Rep. Sept. 30, 1974,* ORNL-TM-4726, Table 3.15, p. 138.

32. R. G. Berggren and R. T. King, "Deformation Characteristics of Whole Weldment Cross Sections," *Mechanical Properties Test Data for Structural Materials Quart. Progr. Rep. Apr. 30, 1974,* ORNL-4963, pp. 143–51.

33. B. R. Dewey, R. T. King, and R. G. Berggren, "Studies of Strain Distribution in Weldments," *Mechanical Properties Test Data for Structural Materials Quart. Progr. Rep. Jan. 31, 1975,* ORNL-5104, pp. 191–95.

34. C. R. Brinkman and G. E. Korth, *Heat-to-Heat Variations in the Fatigue and Creep-Fatigue Behavior of AISI Type 304 Stainless Steel and the Fatigue Behavior of Type 308 Stainless Steel Weld Metal,* ANCR-1097 (May 1973).

35. V. M. Zemzin and E. A. Chekhover, "The Modulus of Elasticity of Welds in Alloy Steels," *Weld. Res. Abroad* 10(6): 68–73 (1964).

36. R. L. Klueh, "Strain Rate Effects on the Tensile Properties of Annealed 2 1/4 Cr-1 Mo Steel," *Mechanical Properties Test Data for Structural Materials Quart. Progr. Rep. Apr. 30, 1975*, ORNL-5105, pp. 187–96.

37. R. L. Klueh and D. A. Canonico, *Carbon Effects on the Mechanical Properties of 2 1/4 Cr-1 Mo Steel Weldments*, ORNL-5033 (June 1975).

38. G. V. Smith, *Supplemental Report on the Elevated-Temperature Properties of Chromium-Molybdenum Steels (An Evaluation of 2 1/4 Cr-1 Mo Steel), ASTM Data Ser.* DS 6 S2, American Society for Testing and Materials, Philadelphia, March 1971.

39. T. Kunitake, *Sumitomo Met.* 12:17 (1960).

40. R. L. Klueh, "The Effect of Carbon on 2 1/4 Cr-1 Mo Steel (I). Microstructure and Tensile Properties," *J. Nucl. Mater.* 54(1): 41–54 (November 1974).

41. C. R. Brinkman, M. K. Booker, J. P. Strizak, W. R. Corwin, J. M. Leitnaker, and J. L. Frazier, "Fatigue Behavior of 2 1/4 Cr-1 Mo Steel, *Mechanical Properties Test Data for Structural Materials Quart. Progr. Rep. Apr. 30, 1975*, ORNL-5105, pp. 200–30.

42. S. S. Manson, G. R. Halford, and M. H. Hirschberg, *Creep-Fatigue Analysis by Strain-Range Partitioning*, NASA-TM-67838 (1971).

43. R. D. Campbell, "Creep Fatigue Interaction Correlation for 304 Stainless Steel Subjected to Strain-Controlled Cycling with Hold Times at Peak Strain," *J. Eng. Ind.* 887–92 (1971).

44. *Interpretations of the ASME Boiler and Pressure Vessel Code, "Case 1592,"* American Society of Mechanical Engineers, New York, 1974.

45. R. L. Klueh, "Mechanical Properties of Weld-Overlaid Stainless Steel Forging," *Mechanical Properties Test Data for Structural Materials Quart. Progr. Rep. Apr. 30, 1975*, ORNL-5105, pp. 232–41.

46. R. L. Klueh and D. A. Canonico, "Elevated-Temperature Tensile Strength and Microstructure of a Weld-Overlaid Type 304 Stainless Steel Forging," pp. 113–40 in *Symposium on Elevated-Temperature Properties of Austenitic Stainless Steel*, (June 24–28, 1974, Miami Beach, Florida), American Society for Mechanical Engineers, New York, 1974.

47. R. W. Swindeman, "Representation of the Tensile Behavior of Reannealed Type 304 Stainless Steel by the Voce Equation," *J. Eng. Mater. Technol.* 97: 98–106 (April 1975).

48. P. Ludwik, *Elemente der Technologischen Mechanik*, Springer, Berlin, 1909.

49. R. W. Swindeman, *Low-Strain Tensile Behavior of Type 304 Stainless Steel*, ORNL report in preparation.

50. R. K. Bhargava, R. W. Swindeman, and J. Moteff, "Correlation of the Microstructure with the Creep and Tensile Properties of AISI 304 Stainless Steel," paper to be presented at the ASME Winter Annual Meeting, Houston, Texas, Nov. 30–Dec. 4, 1975.

51. R. W. Swindeman and C. E. Pugh, "Isochronous Stress-Strain Behavior of Laboratory Reannealed Type 304 Stainless Steel (Heat 9T2796) to 5000 Hr," pp. 31–47 in Symp. Elevated Temperature Properties of Austenitic Stainless Steel (June 24–28, 1974, Miami Beach, Florida), American Society of Mechanical Engineers, New York, 1974.

52. L. D. Blackburn, "Isochronous Stress-Strain Curves for Austenitic Stainless Steels," pp. 15–48 in *The Generation of Isochronous Stress-Strain Curves*, ed. by A. O. Schaefer, American Society of Mechanical Engineers, New York, 1972.

53. C. E. Pugh, "Constitutive Equations for Creep Analysis of LMFBR Components," pp. 1–15 in *Advances in Design for Elevated-Temperature Environment*, American Society of Mechanical Engineers, New York, 1975.

54. F. Garofalo et al., "Strain-Time, Rate-Stress, and Rate-Temperature Relations During Large Deformations in Creep," pp. 1–31 in *Joint International Conference on Creep*, Institution of Mechanical Engineers, London, 1963.

55. P. W. Davies et al., "An Equation to Represent Strain/Time Relationships During High Temperature Creep," *Scr. Metall.* 3: 671–74 (1969).

56. J. Gittus, "Strain, Recovery, and Work-Hardening During Creep Due to Dislocations," *Philos. Mag.* 23: 1281 (1971).

57. J.C.M. Li, "A Dislocation Mechanism of Transient Creep," *Acta Metall.* 11: 11 (1963).

58. C. E. Pugh et al., *Currently Recommended Constitutive Equations for Inelastic Design Analysis of FFTF Components*, ORNL-TM-3602 (Sept. 1972).

59. S. S. Manson, G. R. Halford, and A. J. Nachtigall, *Separation of the Strain Components for Use in Strain Range Partitioning*, NASA-TMX-71737 (1975).

4. NAVAL RESEARCH LABORATORY

L. E. Steele

4.1 INTRODUCTION - L. E. Steele

The research program of the NRL Engineering Materials Division, Thermostructural Materials Branch, includes the study of the behavior of structural materials useful in reactor construction. Within the scope of the title above much unirradiated data are developed. This report is developed using such data to support the USERDA and USNRC objective of compiling structural materials properties data for use in national reactor development programs. The NRL program is sponsored by the Office of Naval Research, the U. S. Energy Research and Development Administration, the U. S. Nuclear Regulatory Commission, and the U. S. Army Engineer Power Group. The unirradiated materials properties data contributed here include that developed in the course of research in the areas of high temperature materials, radiation damage, and fracture mechanics.

4.2 ELASTIC PLASTIC TOUGHNESS OF TYPE 316 STAINLESS STEEL FORGING - F. J. Loss and R. A. Gray, Jr.

4.2.1 Introduction

The J-Integral method is being used to characterize the fracture toughness of austenitic stainless steel (SS) and nickel-base alloys for advanced reactor structural applications. These alloys generally exhibit elastic plastic behavior that precludes analysis by conventional linear elastic methods. The J Integral provides a means to investigate the short term crack extension in the elastic plastic regime. Since experimental application of this approach is still in the definitive stage, the present research fulfills the dual roles of (a) material characterization and (b) development of experimental techniques for J-Integral measurement. The current research explores the toughness of Type 316 SS forging material taken from the Army's MH-1A reactor pressure vessel. The J-Integral values are defined using a multi-specimen R-curve technique that is being evaluated as a measurement method.

4.2.2 Experimental Procedure

Notched bend specimens of three different sizes (Table 4.1) were prepared from a 3-1/8-in. (80 mm) thick ring forging nozzle cutout from the MH-1A vessel. Chemical and tensile properties are given in reference 1.

The specimens were fatigue precracked at a ΔK maximum of 25 ksi$\sqrt{in.}$ (27.5 MPa$\sqrt{in.}$) to a depth between 0.3 and 0.5 of the specimen width. Testing was conducted statically in three-point bend at a temperature of 500 F (260 C). The specimen load and midspan deflection were monitored on an x-y recorder.

Table 4.1. Specimen Dimensions

Thickness (B)		Width (W)		Span (S)	
in.	mm	in.	mm	in.	mm
0.197	5	0.394	10	1.76	45
0.394	10	0.788	20	3.57	91
1.00	25.4	2.0	51	8.0	203

To compute the applied J-Integral value at a given specimen deflection it is necessary to measure the crack extension which occurred with rising load up to that point. This was accomplished by two procedures, namely: heat tinting and sectioning. With the heat tinting procedure the tip of the fatigue precrack was marked with ink while the specimen was partially loaded. The specimen then was loaded to a predetermined deflection whereupon the temperature was increased to 900 F (482 C) for several minutes to oxidize the crack surface. After cooling to room temperature the specimen was broken apart to reveal the crack extension that extended beyond the region of ink stain. Several identical specimens were tested to different values of load to characterize the crack extension behavior. With the sectioning method, the fatigue crack was marked with ink as before and the specimen loaded at 500 F (260 C) to the desired value. The load was removed and the thickness of the unbroken specimen was reduced to reveal the crack extension at the 1/4 and 1/2 thickness locations.

4.2.3 Fracture Morphology

Two examples of the fracture surface of Type 316 forging specimens are shown in Fig. 4.1. The specimen in Fig. 4.1a was loaded to the maximum (limit load) value; the one in Fig. 4.1b was loaded to the minimum value commensurate with measurable stable crack extension. It is important to note that the crack extension is preceded by a "stretching" of the material at the crack tip, and that these two regions must be distinguished from one another since the J-Integral value is concerned only with the initiation of crack extension. The fatigue crack, stable crack extension, and ultimate specimen separation are identified in the two fractographs. The zone of fatigue precrack does not exhibit a marked difference in macrographic morphology from the zones of stretch and plastic deformation, contrary to the observations with austenitic SS plate. Therefore, it was necessary to develop an experimental technique to distinguish the various regions. This was accomplished by ink staining and heat tinting as previously described. The fatigue crack, as revealed by ink staining, appears here as a darkened, faceted region. The stretch zone and crack extension surface, delineated by the post-test heat tint, appear as the single dark band beneath the fatigue crack. Though not discernible here there are color differences between the various surfaces that permit a measurement of the regions of (a) fatigue precrack and (b) crack extension plus stretch zone. Specimens tested to loads less than maximum have shown the formation of "islands" in the heat-tinted, crack extension region. These "islands" result from crazing of the metal oxide film which is caused by the metal stretching as a result of additional strain in the vicinity of the crack tip when the specimens are broken open at room temperature. As can be seen in Fig. 4.1, specimens tested to maximum load do not show islands probably because the maximum strain has already been developed (neglecting the slight difference in plasticity between test temperature and room temperature).

The combination of pre-test ink stain and post-test heat tint permits a distinction to be made between the fatigue surface and the region of ductile tearing. However, the method does not readily permit discrimination between the stretch zone and the region of stable (rising

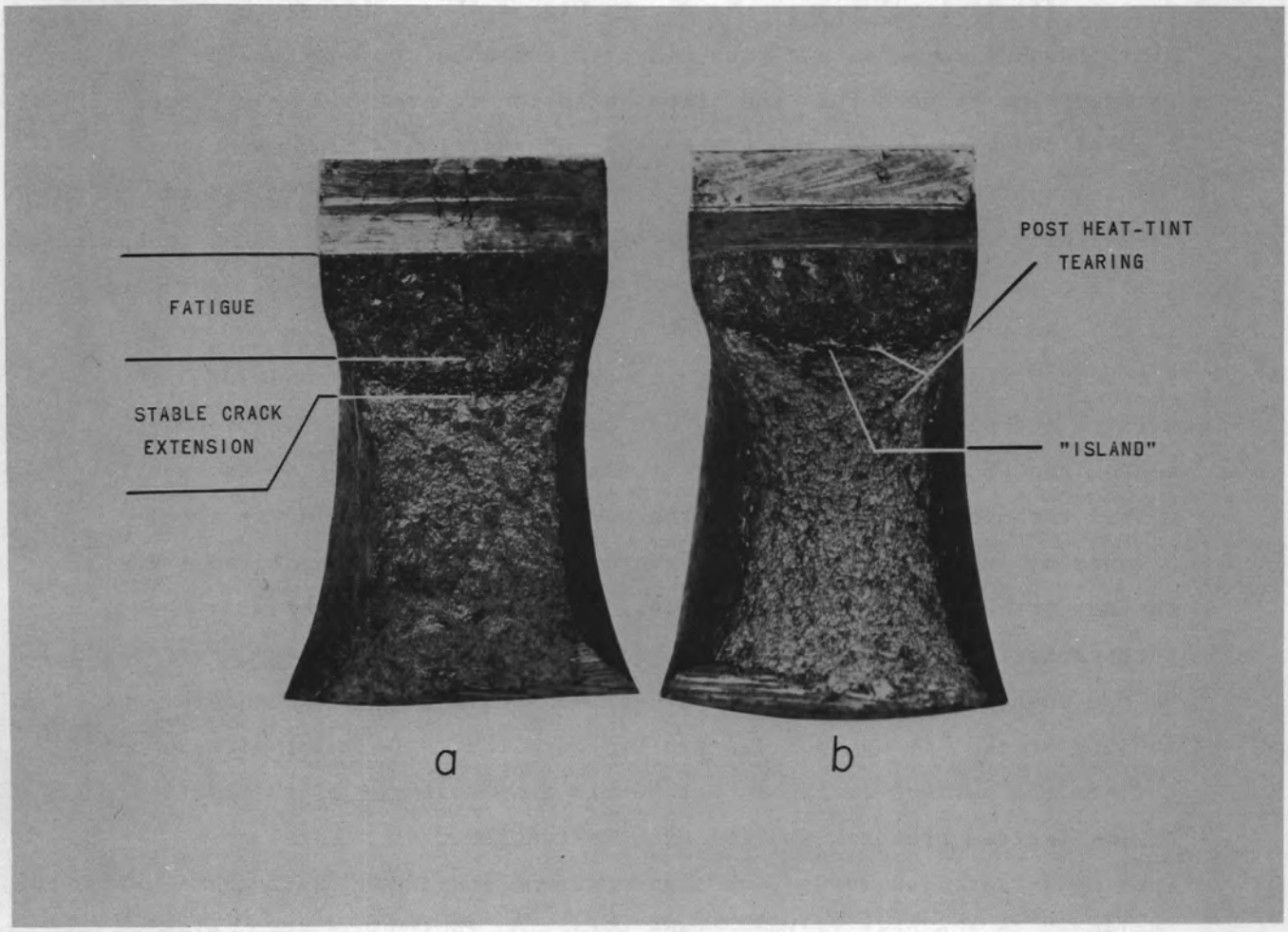

Fig. 4.1. Typical crack length determination from fracture surfaces of a 0.4-in. (10 mm) specimen of 316 SS forging tested to maximum (limit) load (7a) and to a nominally lower load (7b) at 500 F (260 C), using the pre-test ink stain, post-test heat tinting, and subsequent room temperature separation.

load) crack extension. The total crack extension measurements are further complicated by the island formation which resulted in an overestimation of the size of the heat tinted metal by perhaps 0.01 in. (0.25 mm) on 0.2 and 0.4 in. specimens.

To enable a better delineation of the stretch zone from the region of crack extension, a few specimens were sectioned, after having attained the desired load, so as to reveal the crack profile at the 1/4 and 1/2 T locations.

The crack profiles of two 0.4 in. thick specimens are shown in Fig. 4.2. The first dark-field lighted macrograph illustrates a specimen loaded sufficiently to define the crack tip stretch without crack extension. The second macrograph is of a specimen tested at near limit load. The total crack length can be easily measured in the absence of the distortion caused by post-test separation that was inherent to the heat tinting procedure. One normally expects stretch to exhibit itself as a 45 degree convex surface between the fatigue and crack extention regions. It is evident from the photomicrograph of the crack tip of the latter specimen that the contour of the parted stretch zone can be projected on a vertical plane and the stable crack extension measured. By viewing the fracture profile obliquely the fatigue crack can also be accurately determined from the ink stain. This sectioning procedure was carried out at the 1/2 and 1/4 T locations to determine a mean average crack front.

The transmission electron micrographs in Fig. 4.3 are typical representations of the failure modes encountered in the regions of fatigue crack, stretch, and stable crack extension. The fracture mode in the fatigue crack region is predominately transgranular cleavage as seen in the upper inset. While some traces of fatigue striation may be seen, it is probable that the heat tinting has obliterated their signature. The middle inset is located at the tip of the fatigue crack, where the termination of the fatigue striations at the stretch zone is readily seen. The small elongated dimples present in the stretch zone are indicative of shear failure in the presence of a small plastic zone field-size and point toward the direction of crack initiation. The lower inset displays the effects of a large plastic zone size. The highly

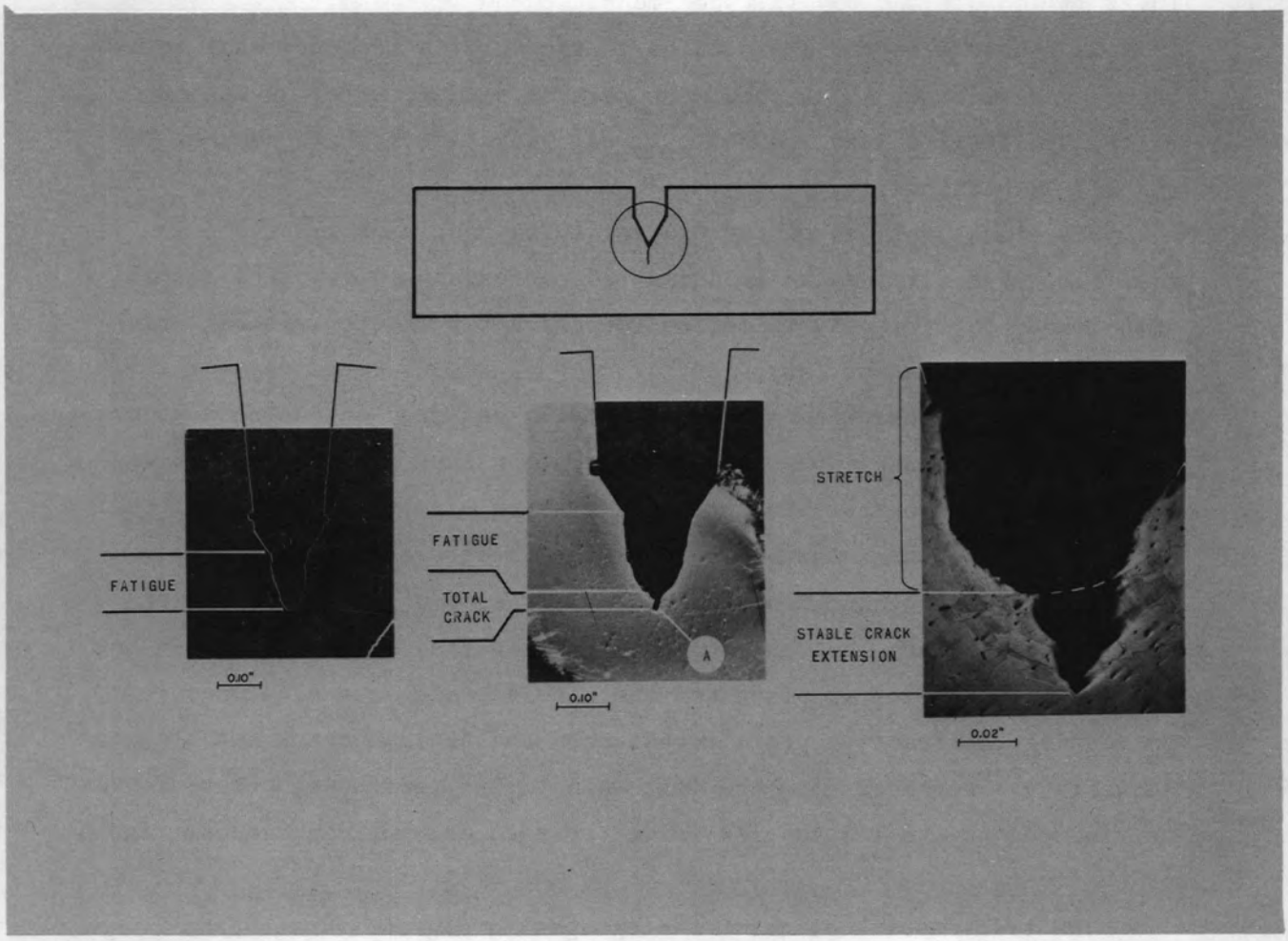

Fig. 4.2. Crack length determination from the fracture profile of a 0.4-in. (10 mm) specimen of 316 SS forging tested to a low load (left) and to maximum load (center) points at 500 F (260 C). The micrograph on the right is a higher magnification of the crack tip region (A) seen in the center macrograph.

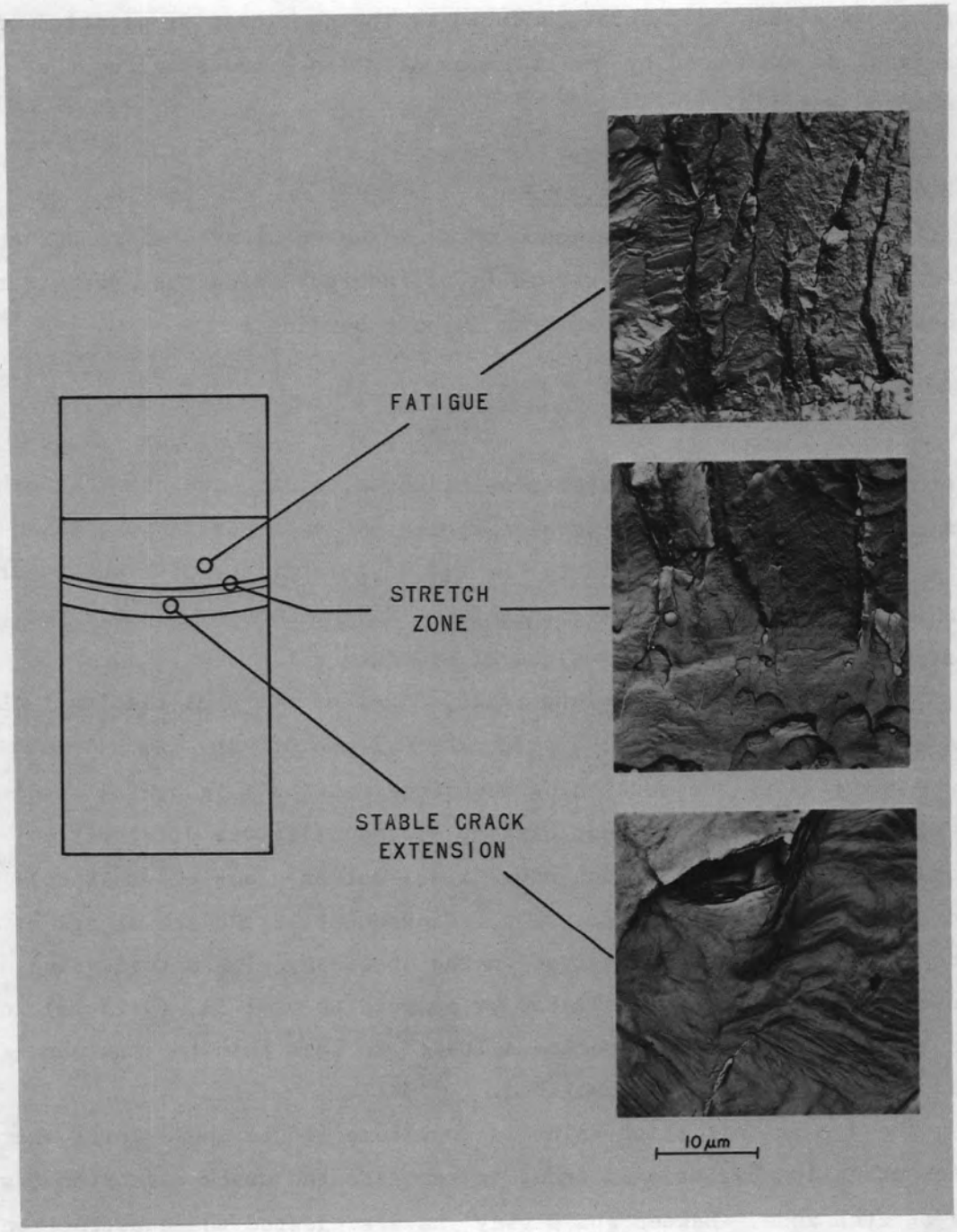

Fig. 4.3. Transmission electron micrographs of the fractured surface of a 0.2-in. (5 mm) specimen of 316 SS forging tested to maximum (limit) load at 500 F (260 C) showing the various modes of metal failure in the regions of fatigue, stretch, and stable crack extension.

elongated dimple that predominated over the many others which were present when the material began to plasticize has "cleared" the surface of other features. In this zone, the gross distortion of the fracture surface as a result of strain induced by the continued propagation of the crack is evidenced by the numerous slip lines transversing the fractured surface.

4.2.4 J-Integral Determinations

J-Integral values were computed from the total area (A) under the load vs midspan deflection record (i.e., energy) using the approximate equation for a deeply notched beam in pure bending[2]:

$$J = \frac{2A}{B(W-a)}$$

Where B, W, and a are the specimen thickness, width, and crack length, respectively. For computational purposes the value of "a" was taken as the original crack length to the tip of the fatigue precrack. Care was taken to insure that the deflections of the loading jig did not contribute to the measured values of specimen deflection.

The R-curve determinations based on use of the heat tinting technique are illustrated in Fig. 4.4 for the 0.2 and 0.4 in. thick specimens. The R curve using the sectioning technique for the 1 in. thick specimen is also shown. With the heat tinting procedure it was difficult to visually separate the stretch zone (i.e., out-of-plane deformation) from the region of crack extension. Consequently, the sum of crack extension and stretch is plotted on the abscissa. The actual value of the abscissa may be overestimated by as much as 0.01 in. (0.25 mm) for the heat tinted data for specimens loaded to less than the maximum load point as previously described.

The J_{Ic} or initiation value is considered to be the J level where crack extension begins. In order to separate the crack extension from the stretch zone, Landes and Begley[3] have suggested the construction of a stretch zone line on the R-curve plot given by $J/2\sigma_{flow}{}^*$; the $\sigma_{flow}{}^*$ is taken as 1/2 $(\sigma_{YS} + \sigma_{TS})$ where σ_{YS} and σ_{TS} are the yield and tensile strengths respectively.

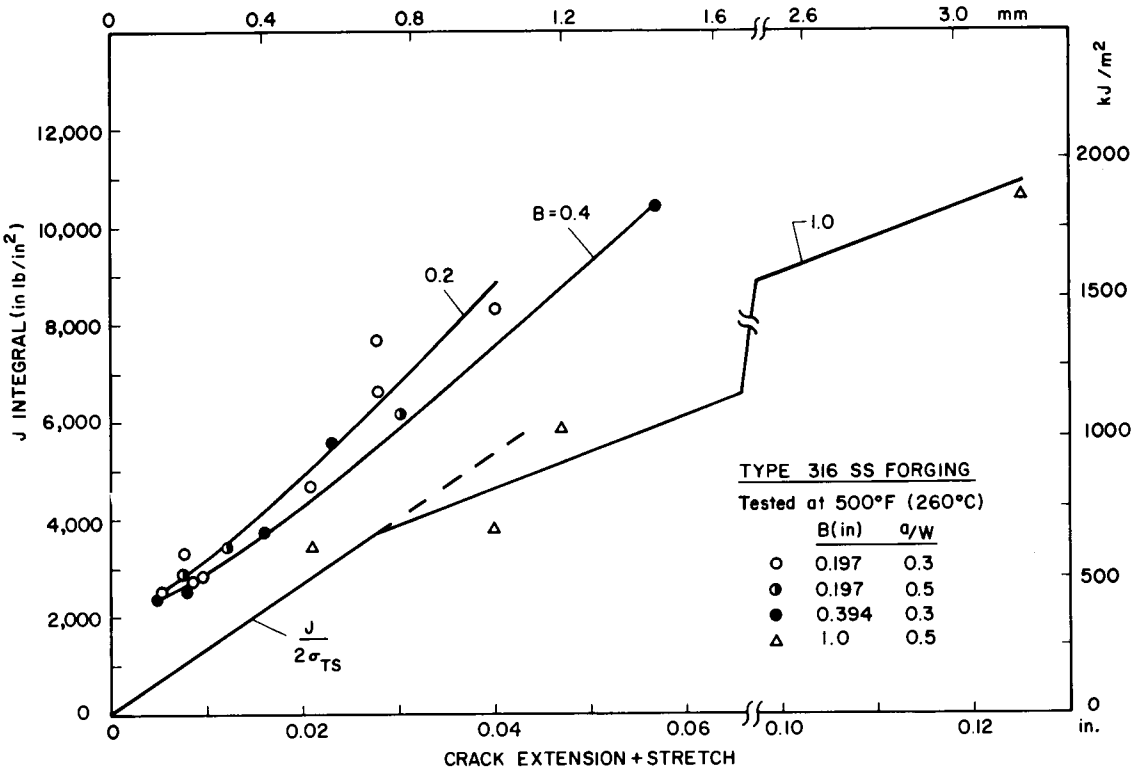

Fig. 4.4. R-curve trends for Type 316 SS forging material for different thickness specimens. The value of the abscissa for the 0.2 and 0.4-in. (5 and 10 mm) specimens was determined from measurements of the heat tinted region of the fractured specimens while the value for the 1-in. (25 mm) specimens was measured at the 1/4 and 1/2 T thickness location on specimens that were sectioned but not broken apart.

intersection of this line with the R-curve would then provide an estimate of J_{Ic}. Such a construction was attempted in Fig. 4.4. The resulting line did not intersect either the 0.2 in. (5 mm) or the 0.4 in. (10 mm) specimen data. The line did intersect the 1 in. specimen data but at a value of 0.08 in. (2 mm) on the abscissa at which point it was apparent that considerable crack extension had already occurred. Consequently, a stretch zone line was plotted on the basis of $J/2\sigma_{TS}$*. This value intersects the 1 in. specimen data at a point where crack extension was first observed by the sectioning technique and suggests a value of J_{Ic} equal to 3700 in.lb/in.^{2} (647 kJ/m^2). It is not possible to determine a J_{Ic} value from the smaller specimens without first separating the stretch zone from the crack extension as discussed later.

It is apparent from Fig. 4.4 that there is a size effect in J_{Ic} for the range of thicknesses investigated. Landes and Begley[3] have proposed a minimum thickness requirement based on experiments conducted with A216 steel. Applying this criterion it is seen that approximately a 2 in. (51 mm) thick specimen would be required to measure the indicated J_{Ic} of 3700 in.lb/in.^{2}. Using σ_{TS} in place of σ_{flow} reduces the thickness requirement to 1.4 in. (36 mm). If the latter procedure is acceptable, it is considered that the 1 in. data provide a reasonable estimate for the J_{Ic} value that would be obtained from thicker specimens but that the 0.2 and 0.4 in. specimens are too thin to permit thickness-independent J_{Ic} determinations at this high level of J_{Ic}.

Fortunately, the indicated J_{Ic} value is sufficiently high that fracture is not considered likely with structural thicknesses of 0.2 to 0.4 in. For example, in the case of plane strain, it is assumed that $J_{Ic} = \mathcal{G}_{Ic}$ and that the K_{Ic} may be calculated from the expression

$$\mathcal{G}_{Ic} = \frac{(1-\nu^2)\ K_{Ic}^2}{E}$$

where ν and E are Poisson's ratio and Young's modulus, respectively. For a J_{Ic} = 3700 in.lb/in.^{2}, the equivalent K_{Ic} exceeds 300 ksi/in. (328 MPa/in).

*σ_{flow} is taken as 1/2 ($\sigma_{YS} + \sigma_{TS}$) where σ_{YS} and σ_{TS} are the yield and tensile strengths respectively.

An attempt to apply this value of K to a structural member of 0.4 in. thickness would probably first result in failure by tensile overload. For alloys of lower toughness, as can result from neutron irradiation, small specimens, such as those investigated, are suitable to characterize the J_{Ic} levels.

In order to more clearly determine the crack extension behavior, a few specimens were sectioned after having obtained the desired load as previously described. This method results in a better visual indication of the stretch zone than is apparent when the specimens are heat tinted and then broken apart. Figure 4.5 illustrates the R-curve trend as a function of crack extension alone. In other words, the J_{Ic} value is taken as the intersection of the R curve with the ordinate. Again, a size effect is apparent with the 0.2 and 0.4 in. specimens exhibiting a J_{Ic} value twice as high as that for the 1 in. specimens, 6200 in.lb/in.^{2} (1085 kJ/m^2) vs 3200 in.lb/in.^{2} (560 kJ/m^2). Note that the J_{Ic} value of 3200 in.lb/in.^{2} (560 kJ/m^2) is consistent with the value of 3700 in.lb/in^2 (647 kJ/m^2) determined from Fig. 10.

Finally, a slightly increasing trend in the size of the stretch zone (as determined from the sectioning technique) was noted with increasing applied J levels, i.e., 0.016 to 0.023 in. (0.4 to 0.6 mm), for the 1 in. specimen. This behavior suggests an increasing plastic deformation in the region of the stretch zone as the specimen deflection is increased. This observation is consistent with the plastically induced "island formation" resulting from the increased plasticity when the heat tinted specimens were broken apart at room temperature.

4.3 INFLUENCE OF DELTA FERRITE CONTENT ON NOTCH TOUGHNESS OF AUSTENITIC STAINLESS STEEL WELDMENTS - J. R. Hawthorne and B. H. Menke

4.3.1 Background

Welded austenitic stainless steel has been used for selected primary system components of water-cooled nuclear power reactors and is a major design consideration for forthcoming liquid metal-cooled (fast breeder) reactors. Studies of representative thick section weldments have shown significant differences in notch toughness between parent metal (high) and weld deposit (low).[4] Moreover, significant variations

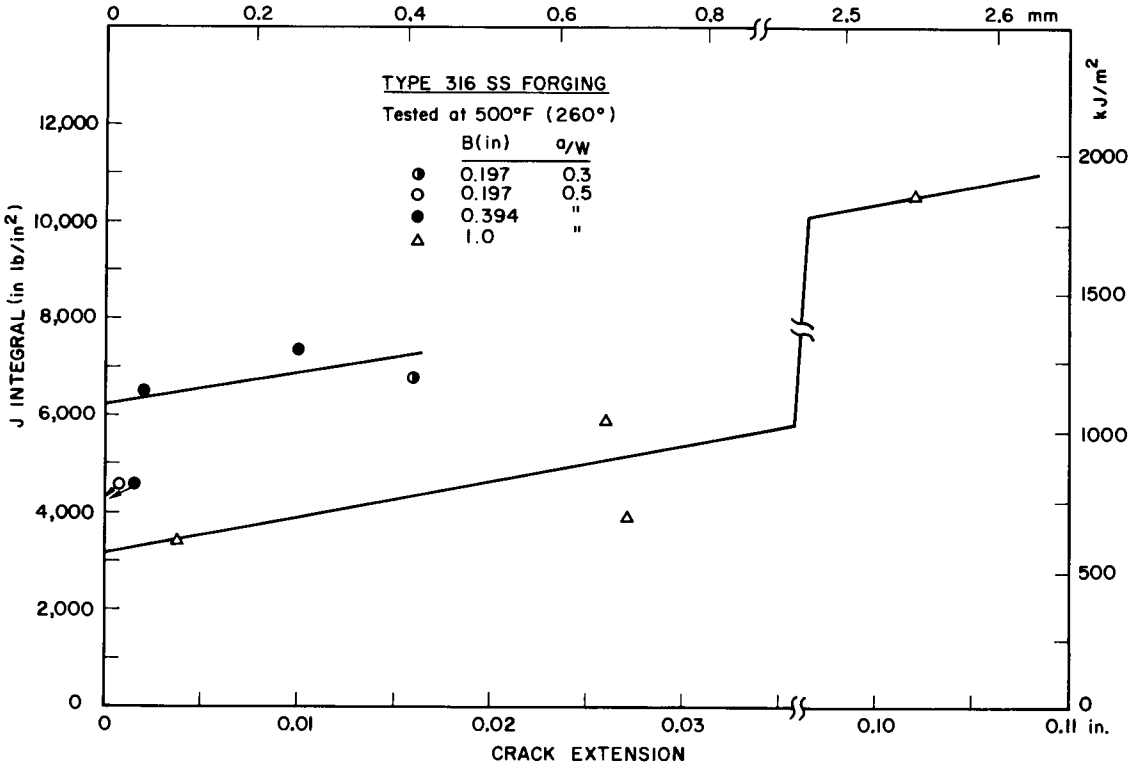

Fig. 4.5. R-curve trends for Type 316 stainless steel forging plotted on the basis of crack extension beyond the stretch zone as determined by the sectioning technique. The J_{Ic} value is represented by the intersection of the R curve with the ordinate.

in notch toughness between weld deposits also have been observed. Weld deposit notch toughness levels in the unirradiated conditions, in general, are not so low as to cause concern for fracture resistance qualities; however, neutron irradiation can cause a reduction in weld deposit toughness levels even with moderate fluence (n/cm^2) exposures.[4] Accordingly, the determination of factors contributing to variable notch toughness of austenitic stainless steels for both pre- and postirradiation conditions is of interest to reactor applications. Delta ferrite content is one of several suspect factors; the contribution of this variable to notch toughness is being qualified for Army and ERDA sponsors. Phase one studies (unirradiated condition) essentially have been conpleted; findings are reported here.

4.3.2 Materials

The range of delta ferrite content of most interest to reactor applications is 2 to 15%. To represent this range a series of four 2-1/2 in. thick shielded metal arc weldments (Type 304 base plate, Type 308 filler) were obtained from the Arcos Corporation by contract. The electrode composition and coatings used were those developed by Arcos for a prior Metal Properties Council project. A reference plate from NRL stock served as base material.

Chemical compositions of the weld deposits are listed in Table 4.2. Weld microstructures are illustrated in Fig. 4.6. Delta ferrite contents of the individual welds, as determined by Magne-Gage, were 2.9, 6.7, 9.9, and 13.7%, respectively. Delta ferrite determinations by the Welding Research Council (WRC) chart are indicated also in Table 4.2. Table 4.3 summarizes the welding parameters and conditions. Each weld was a full thickness weld. The weld root regions were arc-air back gouged and ground to all weld metal (3/4-in. min. weld width) after layer seven. Welding was accomplished under full mechanical restraint; however, opposite faces were welded alternately in a sequence designed to minimize unbalanced stresses.

Test specimens, including standard Charpy-V (C_v), Dynamic Tear (DT), and 0.226 in. gage dia. tensile specimens were taken through the thickness of the weldment and with the long dimension of the specimen

Table 4.2. Chemical Compositions of AISI Type 308 Shielded Metal Arc Weld Series with Variable Delta Ferrite Content

NRL Weld Code	Delta Ferrite Content (%)			Chemical Composition (wt-%)[a]								
	aim	Magne-Gage	WRC Chart	C	Mn	Si	P	S	Cr	Ni	Mo	N
V41 (178 AA)[b]	2-3	2.9	2.0	.056	1.88	.32	.024	.011	19.71	10.35	.05	.068
V42 (179 A)	5-7	6.7	5.5	.060	1.54	.31	.029	.009	19.90	9.25	.05	.074
V43 (180 A)	9-11	9.9	9.5	.060	1.65	.32	.029	.011	20.89	9.11	.06	.079
V44 (181 KA)	13-15	13.7	11.8	.060	1.38	.43	.028	.010	21.08	8.93	.08	.084

[a] Core wire for all electrodes from same steel melt.
[b] Arcos Corporation sample number.

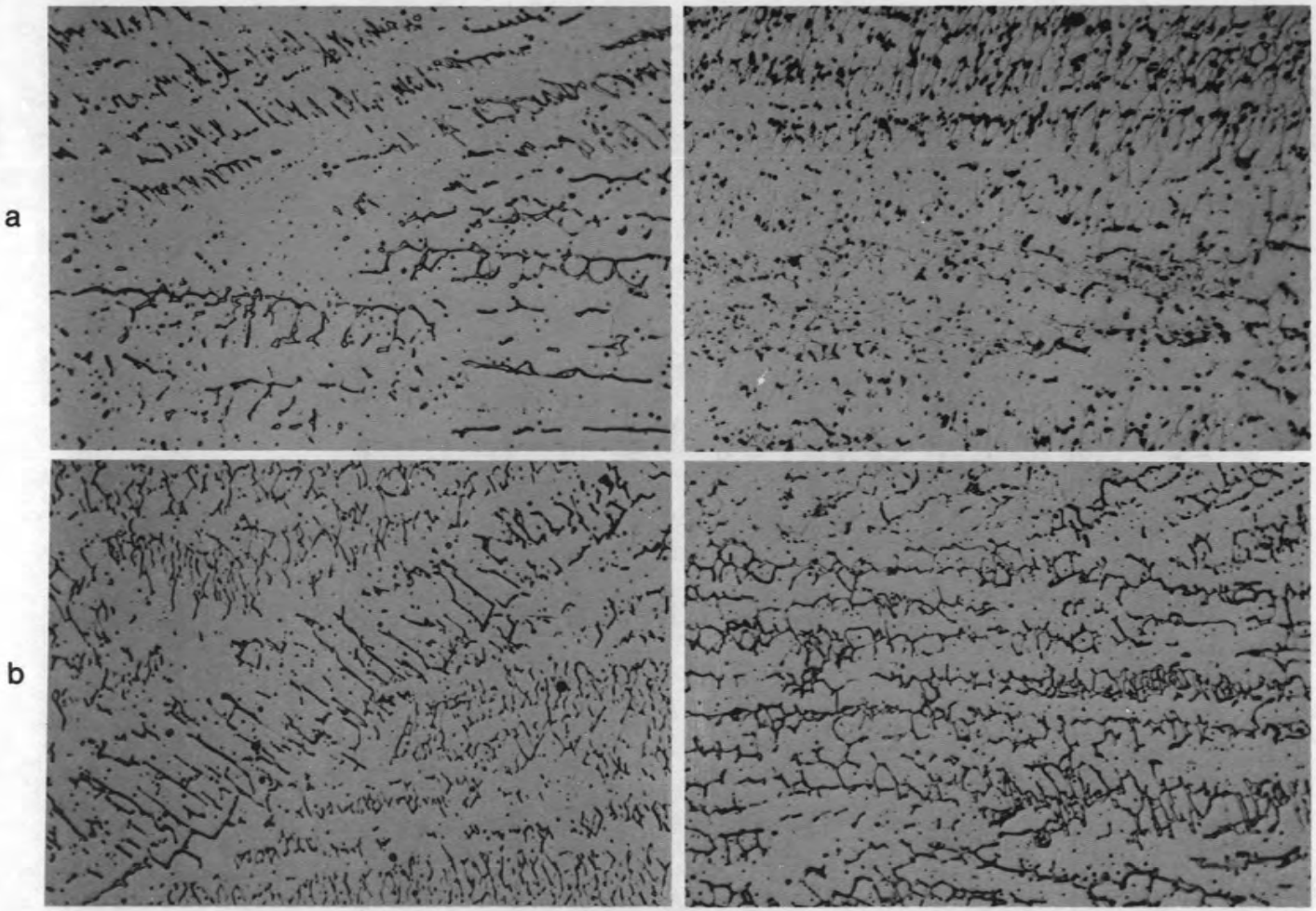

Fig. 4.6. Weld Deposit Microstructures
a - Weld Code V41 (2.9% delta ferrite)
b - Weld Code V42 (6.7% delta ferrite)
c - Weld Code V43 (9.9% delta ferrite)
d - Weld Code V44 (13.7% delta ferrite)

Table 4.3. Welding Parameters and Conditions for Variable Delta Ferrite Content Weld Series

Parameter/Condition	Specification
Base plate	AISI Type 304 (2.5 in. thick) (AL Heat No. 346779-1)
Weld process	Manual shielded metal arc
Joint	Balanced double-U (7 deg bevel)
Restraint	Full(mechanical + welded end blocks)
Current	105A, dcrp (welds V41, V42); 110-112A, dcrp (welds V43, V44)
Voltage	21V (welds V41, V42); 22-23V (welds V43, V44)
Travel speed	8 ipm
Weld sequence	Side 1 - 7 layers, side 2 - 7 layers, Side 1 - balance, side 2 - balance
Total layers (side 1)	13 (welds V41, V42); 11 (welds V43, V44)
Interpass Cleaning	Acetone, wire brush
PWHT	None

perpendicular to the welding direction to conserve test stock. The notch of the C_v and DT specimens was made perpendicular to the weldment surface. The width of the weld deposit spanning the DT specimen notch was at least 0.75 inches.

4.3.3 Experimental Results

Strength and notch ductility determinations were made at 75, 500, and 900 F (24, 260, and 482 C) and are summarized in Tables 4.4 and 4.5, respectively. The C_v tests were also made at 1100 F (593 C).

In Table 4.4, the decrease in yield and tensile strength with increasing temperature is as expected. A trend toward increasing strength with increasing delta ferrite content is also suggested; that is, weld V41 with 2.9% delta ferrite has the lowest strength and weld V44 with 13.7% delta ferrite has the highest strength of the series. However, it is probable that the strength differences are a reflection of certain composition differences (e.g., see percent carbon and percent silicon) among the welds. The strength differences are noted to decrease with increasing temperature.

In Table 4.5, the data indicate that the welds also have very similar notch toughness at 75 F (24 C) and at the higher temperatures. At 75 F, for example, the materials exhibit an average DT energy absorption of 625 ft-lb with less than a 10% deviation. Both the D_v and DT data illustrate higher toughness at 500 F (260 C) than at 75 F (24 C) but a comparable toughness at 500 F (260 C) and 900 F (482 C). A higher toughness at 1100 F (593 C) is also found. Significantly, the C_v data for the three primary test temperatures suggest a somewhat lower toughness for weld V43 with 9.9% delta ferrite compared to either weld V41 (2.9% delta ferrite) or weld V44 (13.7% delta ferrite). In contrast, the DT test indicates about equal weld performance. The scatter in DT data at 500 F is larger than that at 75 F but is readily correlated with fracture surface appearance variations among specimens. It is considered that the C_v and DT assessments differ somewhat because of the relative volumes of metal tested in each method (C_v-small, DT-large). In this regard, it is interesting to note that the ratio of C_v to DT energy absorption ranges from about 10.5 to 12.5 for the materials while a much lower ratio of about 8.0 has been observed for several low alloy (ferritic) steels in

Table 4.4. Tensile Properties of Variable Delta Ferrite Content Weld Series

Weld Code	% Delta Ferrite (Magne-Gage)	Yield Strength[a] (0.2% Offset) (ksi) 75F (24C)	500F (260C)	900F[b] (482C)	Tensile Strength[a] (ksi) 75F (24C)	500F (260C)	900F[b] (482C)
V41	2.9	69.3	55.4	47.1	91.1	68.7	62.3
V42	6.7	77.5	60.9	51.9	100.5	75.6	69.3
V43	9.9	75.1	60.2	52.5	99.0	75.5	69.9
V44	13.7	80.8	64.8	54.5	104.2	81.7	75.0

[a] Average of duplicate tests unless indicated otherwise
[b] Single determination

Table 4.5. Charpy-V (C_V) and Dynamic Tear (DT) Notch Ductility of Variable Delta Ferrite Content Weld Series

Weld Code	% Delta Ferrite (Magne-Gage)	C_V Energy (ft-lb) 75F (24C)	500F (260C)	900F (482C)	1100F (593C)	DT Energy (ft-lb) 75F (24C)	500F (260C)	900F (482C)
V41	2.9	62	78	78	82	637	832	-
		65	84	82	87	662	963	-
		(avg) (64)	(81)	(80)	(85)	(650)	(897)	
V42	6.7	53	70	-	-	620	740	-
		60	78	-	-	633	880	-
		(57)	(74)			(627)	(810)	
V43	9.9	47	68	64	75	581	904	949
		50	74	72	77	639	1043	-
		(49)	(71)	(68)	(76)	(610)	(974)	(949)
V44	13.7	54	77	75	78	643	822	-
		64	80	-	90	669	851	-
		(59)	(79)	(75)	(34)	(656)	(837)	

irradiated and unirradiated conditions.[5]

In summary, the results do not indicate a major effect of delta ferrite content on either strength or notch toughness for the unirradiated condition for the temperature range investigated. The observations, however, do not preclude the original concern of a major influence of delta ferrite content on irradiation response. This question will be clarified by continuing investigations.

4.4 THE EFFECT OF AGING ON HOLD-TIME EFFECTS IN SOLUTION ANNEALED TYPE 316 STAINLESS STEEL - H. H. Smith, D. J. Michel, and H. E. Watson

4.4.1 Background

In previous reports[6,7] it has been shown that high temperature thermal aging prior to testing altered the fatigue properties of Type 316 stainless steel (SS). In the most recent report[7] it was shown that for cold-worked Type 316 SS the effects of hold time at 1100 F (593 C) when combined with prior thermal aging are considerably less than in the unaged condition. No comparison of the effect of aging for the annealed steel was possible because of incomplete data. These tests have now been completed and will be presented in the current report. Also, the results of comparisons of single-edged-notched (SEN) and 1/2 T compact tension (CT) specimens of Type 316 stainless steel tested at 1100 F (593 C) will be shown. These unirradiated comparisons were performed to check the feasibility of using CT specimens in place of the larger SEN specimens in current 1200 F (649 C) heat pipe irradiations which are space limited.

4.4.2 Materials and Test Procedures

The effect of hold time was investigated at 1100 F (593 C) for solution annealed Type 316 SS unaged and after thermal aging at 1100 F (593 C) for 5000 hours. The chemical composition of the material, the specimen design, and the general test procedures have been previously reported.[8] Briefly, single-edge-notched cantilever specimens were cycled under zero-to-tension loading in a saw-tooth mode to a constant

maximum load. To examine the fatigue-creep interaction, tension loads were imposed on the test specimen during each cycle by holding the load at the maximum value for times of 0.1 and 1.0 minutes before returning to zero load. The loading and unloading rates remained constant for all hold times.

4.4.3 Results and Discussion

The experimental data were analyzed to yield crack growth rate, da/dN, as a function of the stress intensity factor range, ΔK. The effect of 0.1 and 1.0 minute tensile hold periods on crack growth rate in aged and unaged Type 316 SS at 1100 F (593 C) is shown in Figure 4.7. For the unaged Type 316 SS a small but significant effect of hold time is seen at 1100 F (593 C) with the magnitude of the effect increasing with length at hold time. For the aged steel, a 1.0 minute hold time produced no discernable change in crack growth rate when compared to the results of the zero hold-time test. Thus it appears that aging reduces hold-time effects in annealed Type 316 SS which is consistant with the behavior observed for the cold-worked steel. The small effects of hold time in the annealed steel indicate that the cyclic rather than the static portion of the test produced the majority of the crack growth at 1100 F (593 C). Also, thermal aging has reduced the crack growth rate for all hold times at comparable ΔK's when compared to results for the unaged material.

These data are intended for use as base line controls in pre- and postirradiation material comparisons for high temperature (up to 1200 F, 649 C) advanced reactor designs. In order that the data represent material response relevant to normal advanced reactor operation, it is important that the material is irradiated at the temperature of interest. NRL is presently using heat-pipe reactor assemblies for above ambient reactor temperature irradiations in EBR-II. Because space limitations are inherent in heat-pipe subassemblies, it has become necessary to consider the adoption of the 1/2 T compact tension (CT) specimen design for fatigue crack propagations studies.

Figure 4.8 shows the results of single-edged-notched (SEN) and 1/2 T compact tension crack growth rate evaluations of annealed Type 316 SS at 1100 F (593 C). Both specimen types were nominally 1/2 in. thick and the SEN specimens contained side grooves in contrast to the

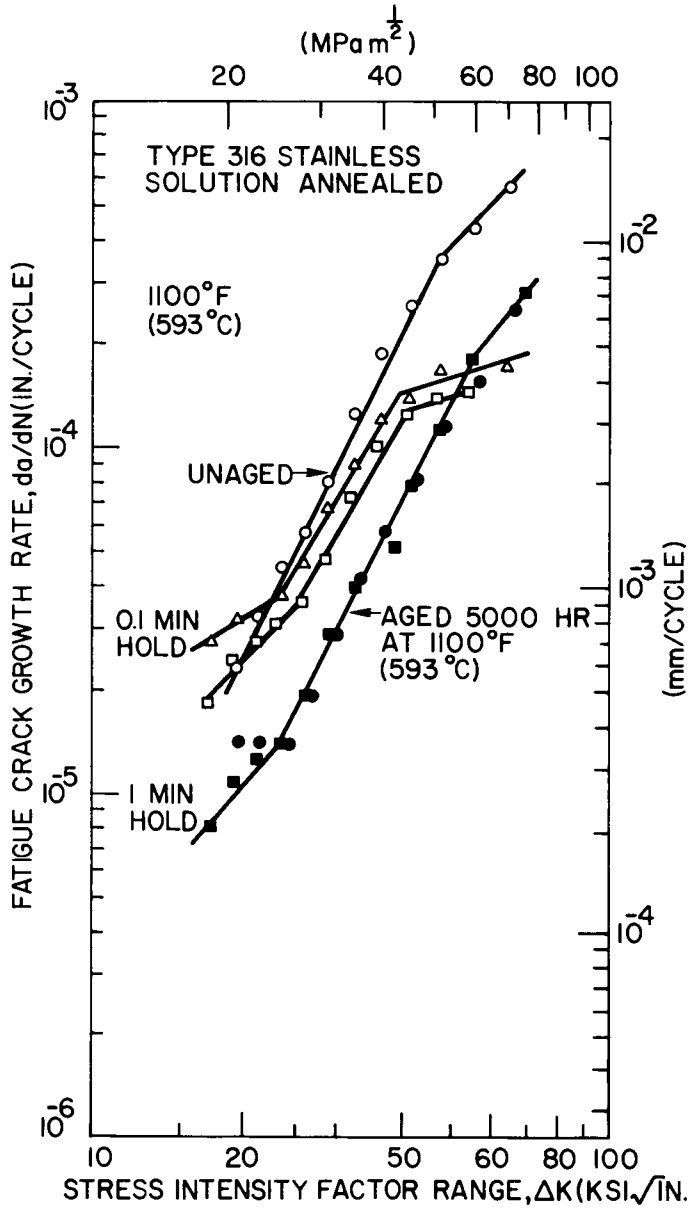

Fig. 4.7. Effect of hold time on fatigue crack growth rates in solution annealed, unaged and thermally aged Type 316 stainless steel as a function of the stress intensity factor range at 1100 F (593 C). Zero, 0.1 minute, and 1.0 minute hold time results are represented by curves drawn through square, triangular, and circular data point symbols, respectively.

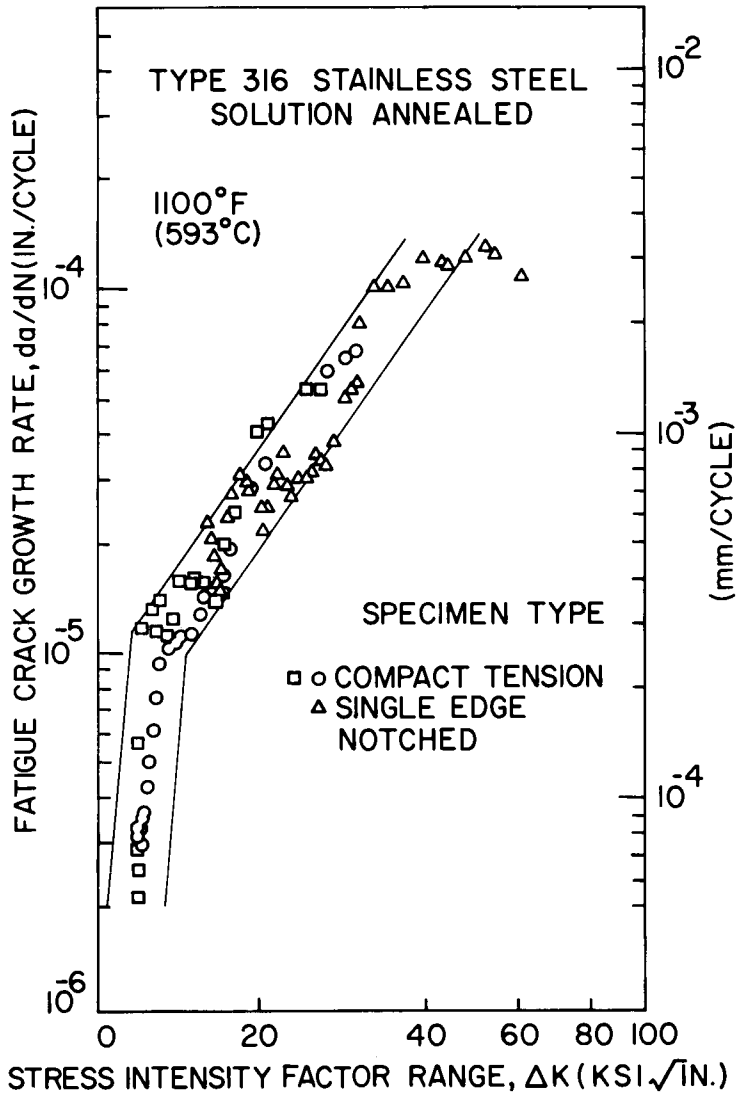

Fig. 4.8. Comparison of fatigue crack growth rate versus stress intensity factor range data for single-edge-notched and 1/2 T compact tension specimen types of solution annealed Type 316 stainless steel at 1100 F (593 C).

CT specimens which were smooth. The tests were conducted on similar fatigue machines with modifications made for differences in gripping. Since the measurement of small crack lengths in the 1/2 T CT specimens is experimentally difficult, the crack length vs cycles data have not been averaged as they have in Figure 4.7. This makes it possible to compare the relative scatter of the data from each specimen type. In Figure 4.8 the data form SEN and 1/2 T CT specimens of Type 316 SS tested at 1100 F (593 C) are seen to fall in a relatively narrow band, with the range of scatter for each specimen type being approximately equal. The preliminary data comparisons appear to be in reasonable agreement but additional tests are planned to further substantiate these findings. Based on these preliminary findings, however, it is expected that 1/2 T CT specimens will be satisfactory for pre- and postirradiation comparisons of Type 316 SS at 1100 F (593 C).

4.5 REFERENCES

1. Loss, F. J. and Gray, R. A., Jr., "Toughness of Irradiated Type 316 Forging and Weld Metal Using the J-Integral," in Irradiation Effects on Reactor Structural Materials, 1 Feb-31 Jul 1974, NRL Memorandum Report 2875, Aug 1974, 23-30; HEDL-TME-74-51, Oct 1974.
2. Rice, J. R., Paris, P. C., and Merkle, J. G., "Some Further Results of J-Integral Analysis and Estimates," ASTM STP 536, 1973, 231-245.
3. Landes, J. D., and Begley, J. A., "Test Results From J-Integral Studies: An Attempt to Establish a J_{Ic} Testing Procedure," ASTM STP 560, 1974, 170-186.
4. Hawthorne, J. R., and Watson, H. E., "Notch Toughness of Austenitic Stainless Steel Weldments with Nuclear Irradiation," Welding Journal Research Supp., June 1973.
5. Loss, F. J., Hawthorne, J. R., and Serpan, C. Z., Jr., "A Reassessment of Fracture-Safe Operating Criteria for Reactor Vessel Steels Based on Charpy-V Performance," Trans. ASME, Vol. 93, Series D, No. 2, 247-258, June 1971; also NRL Report 7152, 8 Sep 1970.
6. Michel, D. J., Smith, H. H., and Watson, H. E., "Fatigue Crack Growth in Thermally Aged Types 304 and 316 Stainless Steel Plate," in Mechanical Properties Test Data for Structural Materials, Quarterly

Progress Report for period ending July 31, 1974, ORNL 4998, Oak Ridge, TN, Sep 1974, 103-110.

7. Michel, D. J., Smith, H. H., and Watson, H. E., "Effect of Hold Time on Fatigue Crack Propagation in Thermally Aged, Solution Annealed and 20% Cold-Worked Type 316 Stainless Steel," in Mechanical Properties Test Data for Structural Materials, Quarterly Progress Report for period ending Jan 31, 1975, ORNL 5104, Oak Ridge National Laboratory, Oak Ridge, TN, Mar 1975, 109-113.

8. Shahinian, P., Watson, H. E., and Smith, H. H., "Effect of Neutron Irradiation on Fatigue Crack Propagation in Types 304 and 316 Stainless Steels at High Temperatures," in Effects of Radiation on Substructure and Mechanical Properties of Metals and Alloys, ASTM STP 529, 1973, 493-508.

5. HANFORD ENGINEERING DEVELOPMENT LABORATORY

Contribution not received in time for inclusion in this issue; it will be included in the subsequent report.

6. WESTINGHOUSE ADVANCED REACTORS DIVISION

E. C. Bishop

6.1 INTRODUCTION

The program being performed at Westinghouse Advanced Reactors Division (ARD) is entitled "Validation of High Temperature Design Methods and Criteria" (189a 04165). Two of the tasks in this program are "Basic Specimen Testing" and "Tubular Specimen Testing." The specimen material for both tasks was supplied from the HNL reference heat of Type 304 stainless steel and future tests will include specimens from the reference heat of Type 316 stainless steel.

The basic specimen tests are performed on plates and bars loaded at 1100°F (593°C). Specimen designs have been selected to provide nonuniform stress distributions (uniaxial, plane stress, and plane strain) and to determine the effects of holes, notches, and welds in various orientations. Uniform and stepped loading is applied at levels sufficient to cause significant creep strain in hundreds of hours and rupture in several thousand hours. Test data are used for: verification of constitutive equations for time-dependent material response, validation of analytical techniques for nonuniform stress states, and investigation of strain limits in base metal, welds, and at geometrical discontinuities.

The tubular specimen tests are being run at 1100°F (593°C) with various combinations of internal pressure and axial load to produce a uniform stress state with a range of biaxiality. Load levels have been selected to determine secondary creep rates in 2000 hours with both steady state and stepped loading. A limited number of tests will be continued to rupture with geometrical discontinuities. The test data are primarily used for verification of constitutive equations and validation of analytical techniques for shells under multiaxial states of stress.

This report covers the work performed during the period from March 1 to May 31, 1975.

6.2 BASIC SPECIMEN TESTING - M. J. Manjoine (Westinghouse Research Laboratories)

The specimen designs selected for this task are shown in Table 6.1 and Figure 6-1. Data obtained to data are presented in Table 6.2.

TABLE 6.1

MODEL TYPES

Specimens From Base Material[a]

Code Designation	Description[b]
A.	Plane Stress Specimen 1/3 x 2/3 x 3 in. (8.5 x 17 x 76.2 mm) gage section.
B.	Plate Specimen 1/3 x 10/3 x 3 in. (8.5 x 85 x 76.2 mm) gage section.
C.	Plate Specimen with Central Hole of 1/3 in. (8.5 mm) Diameter, 1/3 x 10/3 x 3 inc. (8.5 x 85 x 76.2 mm) plate section.
D.	Round Circumferentially Notched Specimen, Major Diameter = 0.96 in. (24.4 mm), Minor Diameter = 0.64 in. (16.2 mm), K_t = 4, Root Radius = 0.018 in. (0.46 mm), Two nearly identical notches in specimen.
E.	Plate Specimen in bending and tension, 1/3 x 10/3 x 2 in. (8.5 x 85 x 50.8 mm) plates section, eccentric load
F.	Designation generally refers to failure or fracture; therefore, it is not used to identify a type of model.
G.	Plane Strain Specimen 1/3 x 10/3 x 1 in. (8.5 x 85 x 25.4 mm) gage section. Ends constrained in transverse direction

Specimen With Welds

BTW - B-type plate specimen with transverse weld at mid-length of gage section.

BAW - B-type plate specimen with axial weld at center of gage section.

CTW - C-type specimen with hole through transverse weld.

CAW - C-type specimen with hole through axial weld.

DTW - D-type specimen with notch root in transverse weld.

DZTW - D-type specimen with notch root at weld fusion line of heat affected zone.

GTW - G-type specimen with transverse weld at mid-gage length.

GAW - G-type specimen with axial weld at center of gage section.

(a) Type 304 SS (HT9T2796) annealed at 2000°F.

(b) Reference Figure 6-1.

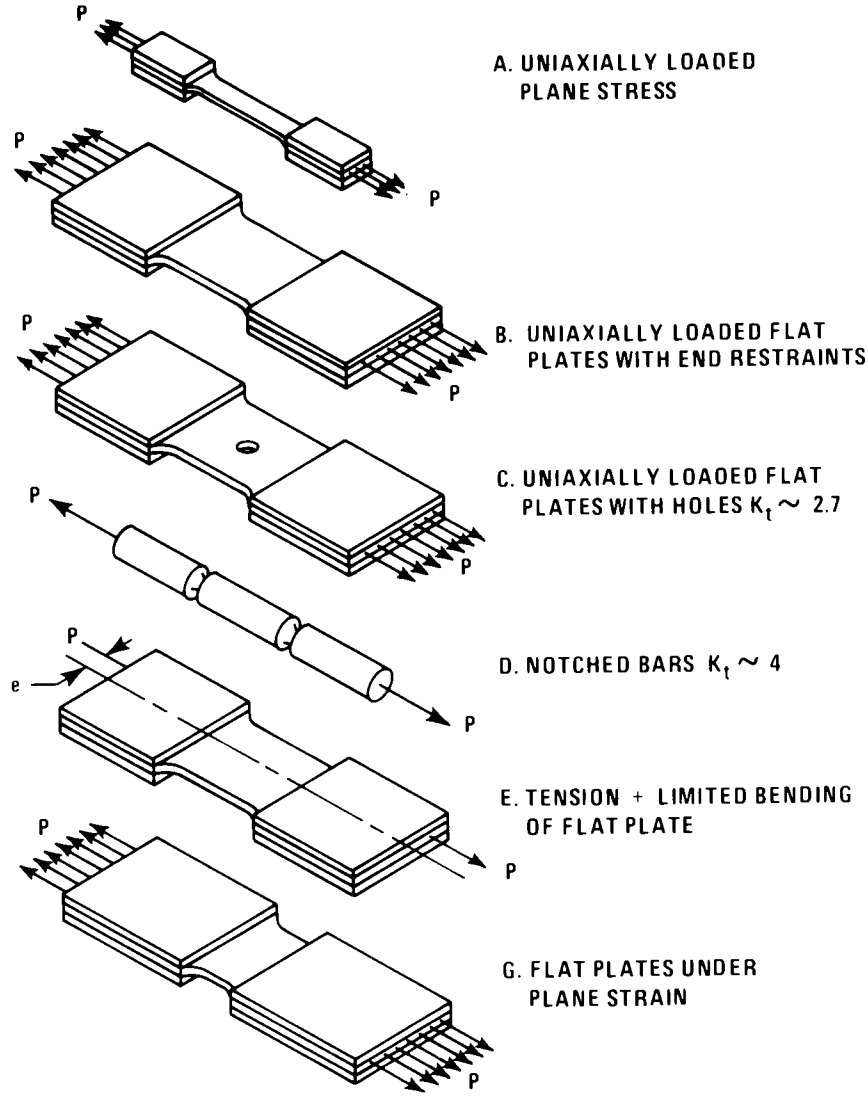

Figure 6-1. Basic Specimen Types

TABLE 6.2

SUMMARY OF CREEP DATA FOR MODELS OF TYPE 304 STAINLESS STEEL* AT 1100°F (593°C)

Loading Data			Creep Data					
				Increment		Accumulated		
Stress (ksi)	(MPa)	Plastic Strain (%)	Creep Rate (% hr)	Strain (%)	Time (hr)	Strain (%)	Time (hr)	Permanent Strain (%)
A1, GAGE SECTION 1/3 x 2/3 x 3 in. (8.5 x 17 x 76.2 mm)								
21.0	144.8	4.66	2.2×10^{-3}	1.10	303	1.10	303[a]	5.76
			2.2×10^{-3}	0.89	403	1.99	706[a]	6.65
						3.47	1250[b]	8.13
						3.65	1270[c]	8.31
						7.34	1826[d]	12.0
A2 (STEP-LOADED TEST)								
10.0	69.95	0.215	8.5×10^{-5}	0.228	2180	0.228	2180[a]	0.443
			6.2×10^{-5}	0.028	405	0.256	2585[e]	0.471
11.0	75.84	0	8.6×10^{-5}	0.124	1349	0.380	3934[e]	0.595
12.5	86.19	0	2.0×10^{-4}	0.213	1002	0.593	4936[e]	0.808
15.0	103.4	0.014	2.5×10^{-4}	0.811	1848	1.40[a]	6784[e]	1.619
21.0	144.8	0.646	4.5×10^{-3}	14.80	2800	16.20	9584	17.07
				1.05[b]	200	17.25	9784	18.12
				12.90	1266[h]	30.15	11050	31.02
						--	4266[m]	--
B1, GAGE SECTION, 1/3 x 10/3 x 3 in. (8.5 x 85 x 76.2 mm)								
21.0	144.8	5.34	1.4×10^{-3}	1.76	666	1.76	666[a]	7.10
			7.6×10^{-4}	1.03	1005	2.79	1671[a]	8.13
			1.7×10^{-3}	--	--	--	3000[c]	--
				1.72	1587	4.51	3258[a]	9.85[g]
						5.33	3487	--
						--	3525[h]	--
B2 (STEP-LOADED TEST)								
10.0	68.95	0.273[i]	8.6×10^{-5}	0.31	1044	0.31	1644[a]	0.58
j			9.0×10^{-5}	0.17	1462	0.45	3106[e]	0.72
11.0	75.84	0	1.1×10^{-4}	0.16	1804	0.61	4910[e]	0.88
12.5	86.19	0	2.0×10^{-4}	0.33	1364	0.94	6274[e]	1.21
15.0	103.4	0.051	4.7×10^{-4}	1.00	1302[a]	1.93	7576[e]	1.98
21.0	144.8	1.880	8.4×10^{-3}	7.50	720	9.43	8296	11.64
				5.28[b]	604	14.71	8900	16.92
				3.69[h]	239	18.40	9139	20.61
				--	--	--	1563[m]	--

Loading Data			Creep Data					
		Plastic	Creep	Increment		Accumulated		Permanent
Stress (ksi)	(MPa)	Strain (%)	Rate (%/hr)	Strain (%)	Time (hr)	Strain (%)	Time (hr)	Strain (%)
G1, GAGE SECTION, 1/3 x 10/3 x 1 in. (8.5 x 85 x 25.4 mm)								
25.0	172.4	4.25	1.8×10^{-2}	2.1	47[a]	2.1	47	6.35
			7.2×10^{-3}	2.8	268[a]	4.9	315	9.1
			1.4×10^{-2}	--	--	6.5	420[c]	10.7
				--	170[a]	7.6	485[g]	11.8
				--	83	11.6	568[h]	--
G1, DATA FROM WELDABLE STRAIN GAGES (Middle, 5/8 in. Gage Section)								
25.0	172.4	2.00	2.6×10^{-2}	0.88	47[a]	0.88	47	2.47
			2.5×10^{-3}	1.12	268[a]	2.00	315	4.00
			7×10^{-3}	0.90	170[a]	2.90[c]	485[g]	4.90
			--	0.65	83	3.55	568[h]	5.60
G2 (STEP-LOADED TEST)								
21.0	144.8	0.43	3.9×10^{-4}	1.34	1195[a]	1.34	1195	1.77
			1×10^{-4}	0.83	5520[a]	2.17	6715[e]	2.60
25.0	172.4	0.01	2.3×10^{-3}	1.80	700	3.97	7415	4.41
			4.6×10^{-3}	2.50	450[c]	4.67	7865	6.90
				4.43	283[a]	6.60	8148	11.33
				--	404	--	8552[d]	--
							1837[m]	
C1, 1/3 x 10/3 x 3 in. (8.5 x 85 x 76.2 mm), CENTRAL HOLE, 1/3 in. (8.5 mm) Dia.								
23.3[k]	160.6	8[n]	1.2×10^{-2n}	1.7[n]	100	1.7[n]	100	8.7[n]
						2.0	125[c]	10.0
							138[d]	
C2, 1/3 x 10/3 x 3 in. (8.5 x 85 x 76.2 mm), CENTRAL HOLE, 1/3 in. (8.5 mm) Dia.								
10.0[k]	68.95	0.14[n]		0.62[n]	2808[a]	0.62	2808[e]	0.76[n]
11.0	75.84	0		0.40	1290	1.02	4098[e]	1.16
12.5	85.68	0		0.50	1300[a]	1.52	5398[e]	1.66
15.0	103.4	0.28		0.82	1148	2.34	6546[e]	2.76
18.0	124.1	0.06		3.31	1630[a]	5.65	8176	6.13
			1.1×10^{-3n}	0.89	791[a]	6.54	8967	7.02
			1.1×10^{-3n}	1.05	944[a]	7.59	9911	8.07
			9.3×10^{-4n}	1.25	1345[a]	8.84	11256	9.32
			2.2×10^{-3n}	1.54	942[c]	10.38	12198	10.86
				5.0	520	15.4	12718[d]	15.9
							6172[m]	
C3, 1/3 x 10/3 x 3 in. (8.5 x 85 x 76.2 mm), CENTRAL HOLE, 1/3 in. (8.5 mm) Dia.								
21.0[k]	144.8	4.4[n]	2.3×10^{-3n}	1.5[n]	310	1.5[n]	310[g]	5.9[n]
				0.3	28	1.8	338[c]	
				2.3	59	4.1	397[h]	8.5

Loading Data			Creep Data					
		Plastic	Creep	Increment		Accumulated		Permanent
Stress (ksi)	(MPa)	Strain (%)	Rate (%/hr)	Strain (%)	Time (hr)	Strain (%)	Time (hr)	Strain (%)
D1-1, NOTCHED BAR D = 0.96 in. (24.4 mm) Dia., d = 0.64 in. (16.2 mm) Dia., r = 0.19 in. (0.46 mm)								
30.0	206.8	2.6[t]		0.3[t]	137	0.3[t]	137	2.9[t]
				0.2	102	0.5	239[g]	3.1[u]
D1-2								
30.0	206.8	2.2[t]		0.26[t]	137	0.26[t]	137	2.46[t]
				0.22	113	0.48	250[c]	2.68
						10.92	305[d]	13.12
D2-1 NOTCHED BAR								
25.0	172.4	0.009[r]				0.006[r]	1371[g]	0.15[r]
							1371	2.17[t]
D2-2								
25.0	172.4	0.009[r]				0.006[r]	1240[c]	
							1371[d]	5.3[t]
D3-1 and 2 NOTCHED BAR								
21.0	144.8	0.002[r]					5499[h]	1.52[t]
D4-1 and 2 NOTCHED BAR								
10.0	68.95	0			406		406[e]	
11.0	75.84				477		883[e]	
12.5	85.68				434		1317[e]	
15.0	103.4				404		1721[e]	
21.0	144.8	0.001[r]		0.004[r]	433		2154[e]	
25.0	172.4	0.003[r]		0.033[r]	1581[g]		3735[u]	1.73[t]
D4-2[u]								
25.0	172.4			0.93[t]	1323		5058	2.66
					2904[m]			
D5-1 NOTCHED BAR								
23.0	158.4				1681[g]		1681[u]	1.8[t]
D5-2								
23.0	158.4				1681		1681	1.69[t]
					150		1831[d]	2.83
D6-1 NOTCHED BAR								
20.0	137.9			1.0[t]	4023[g]	1.0[t]	4023[g]	1.0[t]
D6-2								
20.0	137.9			0.94[t]	4023	0.94[t]	4023[u]	0.94[t]
					5979	0.007[r]	10002	

Loading Data			Creep Data					
		Plastic	Creep	Increment		Accumulated		Permanent
Stress (ksi)	(MPa)	Strain (%)	Rate (%/hr)	Strain (%)	Time (hr)	Strain (%)	Time (hr)	Strain (%)
E1, TENSION PLUS BENDING, 1/3 x 10/3 x 2 in. (8.5 x 85 x 50.8 mm)								
20.0	137.9	8.17[nv]	1.2×10^{-2}	1.1[nv]	94	1.1[nv]	94[a]	8.27[nv]
±13.0[w]	± 89.64		3.5×10^{-3}	2.27	648	3.27	742[s]	11.54
				0.63	167	4.0	909[s]	12.17
				0.58	168	4.58	1077[s]	12.75
				0.57	168	5.15	1245[s]	13.32
				0.46	115	5.16	1360[a]	13.18
				0.79	262	6.40	1622[s]	14.51
			3.0×10^{-3}	0.58	190	6.98	1812[s]	15.15
				0.65	215	7.63	2027[s]	15.80
				0.90	263	8.53	2290[s]	16.70
			2.6×10^{-3}	0.49	190	9.02	2481[s]	17.19
				0.52	171	9.54	2652[s]	17.71
				0.77	237	10.31	2889[s]	18.48
				1.81	238	12.12	3127[h]	20.29
E2, TENSION PLUS BENDING								
18.0	124.1	6.25[nv]		0.47[nv]	23	0.47[nv]	23	6.72[nv]
±11.7[w]	±80.7		1.9×10^{-3}	2.52	1317[a]	2.99	1340	9.24
			8.3×10^{-4}	1.15	1818[a]	4.55	3158	10.8
					1438[f]			
MODELS WITH WELDS								
BAW-1, B-TYPE WITH CENTRAL AXIAL WELD								
25.0	172.4	0.25[n]	8.3×10^{-3}	4.35[n]	477[a]	4.35	477	4.60[g]
			1.1×10^{-2}	8.32	765	12.67	1242	12.92
			1.5×10^{-2}	3.42	216	16.09	1458	16.34
				2.35	71	18.44	1529	18.69
							1532[d]	
CAW-1, C-TYPE WITH CENTRAL AXIAL WELD								
18.0[k]	124.1	0.033[n]	3×10^{-5}	0.95[n]	7319[a]	0.95[n]	7319	0.98[n]
		0.007					8758[f]	
DTW-1, D-TYPE NOTCH AT CENTER OF TRANSVERSE WELD								
29.0	200			0.002[r]	619[f]			
DTW-2								
25.0	172.4			0.003[r]	5183		5183[e]	0.16[t]
28.0	193.0			0.003[t]	3988[f]			
DZTW-1 CIRCUMFERENTIAL NOTCH AT HAZ								
25.0	172.4						978[d]	0.39[t]
							903[d]	
DZTW-2								
22.0	151.7						903[d]	

Loading Data			Creep Data					
		Plastic	Creep	Increment		Accumulated		Permanent
Stress (ksi)	(MPa)	Strain (%)	Rate (%/hr)	Strain (%)	Time (hr)	Strain (%)	Time (hr)	Strain (%)
GAW-1, G-TYPE WITH CENTRAL AXIAL WELD								
23.0	158.6	0.1[n]	5.1×10^{-3}	1.56[n]	188	1.56[n]	188	1.65[n]
			4.2×10^{-3}	1.93	452[a]	3.59	640	3.69[n]
			5.3×10^{-3}	1.64	307[a]	5.13	947	5.23
			5.3×10^{-3}	2.0	379[a]	7.13	1326[g]	7.23
				2.21	456[a]	9.34	1782	9.44
				3.17	576[a]	12.54	2758	12.62
				4.69	528[a]	17.21	2886	17.31
				8.20	210	25.41	3096[d]	25.51
BTW-1, B-TYPE, CENTRAL TRANSVERSE WELD								
21.0	144.8	0.17[n]	3.2×10^{-3}	1.29[n]	339[a]	1.29[n]	339	2.47[n]
			3.2×10^{-3}	2.35	718[a]	3.64	1057[g]	3.82
				1.25	474[a]	4.89	1531	5.07
						5.67	1724	
							1734[d]	
BTW-2								
19.0	131.0	0.08[n]		0.44[n]	622[f]			
GTW-1, G-TYPE, CENTRAL TRANSVERSE WELD								
25.0	172.4	0.09[n]	4.7×10^{-3}	1.62[n]	240[a]	1.62[n]	240	1.71[n]
					208		448[d]	

*HT9T2796, annealed 2000°F (1094°C)

[a]Interrupted for photographic measurement

[b]Transition at 0.2% offset

[c]Transition at double minimum rate

[d]Rupture, R

[e]Stress raised (step-loaded test)

[f]Test in progress

[g]Crack initiated

[h]Test terminated, crack tearing

[i]Strain gage average, bending noted

[j]Specimen rotated 180° to investigate bending

[k]Net section stress

[m]Time at final stress

[n]Average overall strain

[p]Test in preparation

[q]Specimen to be sectioned to determine damage.

[r]Deflection of notch, inches (25.4 mm)

[s]Unloaded and reloaded to determine damage

[t]True strain = $l_n(Ao/A)$

[u]Test interrupted, 1/2 of specimen continued

[v]Peak stress side

[w]Nominal elastic bending stress

6.2.1 Uniaxially Loaded Specimens with Uniform Gage Sections (Types A, B and G)

One purpose of these tests was the determination of the strain distribution of a specimen model for comparison with the output of an analytical program. The verification of the analytical formulation was to be accomplished by measuring the grid lines on the specimens. The test was interrupted at specified strains, and the grid was photographed. The measurements were made from the photographs or directly from the specimen. Since the latter requires removal of the specimen from the test machine, this was done only at the termination of the test. The grid lines, as applied by the Westinghouse method, are readable after 3158 hours of testing at 1100°F (593°C). The strain distributions from the photographs of the specimen have not been completed at this time. Techniques are being developed to improve readability and accuracy and to bypass areas where the grid has been damaged or the photograph is poor. Additional effort will be spent in improving (a) accuracy of master grid which is used to apply grid lines, (b) contrast of grid lines, (c) lighting during photography, (d) photograph reproduction, and (e) techniques for reading the photographs or the enlargements.

The photograph of the grid lines of Specimen A1 at 303 hours was measured to obtain the axial strain distribution. Measurements were made at intervals of one-third inch along the entire length of the specimen. Three sets of readings were taken. The error in strain reading is estimated to be ± 0.2 percent for a technician with no previous experience. The results are plotted in Figure 6-2. The effect of the larger heads is a reduction of strain for a distance nearly equal to the width of test section. The average strain for the middle inch is 5.4 percent at 303 hours, compared with 5.35 percent for the middle two inches, and 5.06 percent for the uniform section length of three inches. The extensometer, however, contains the strain beyond the uniform section and slightly overcompensates for the reduction of the heads. Thus, the overall strain measured by dividing the overall extension of the head by the three-inch uniform section is 5.65 percent, compared to the 5.4 percent measured for the middle inch, and 5.67 percent measured by the extensometer.

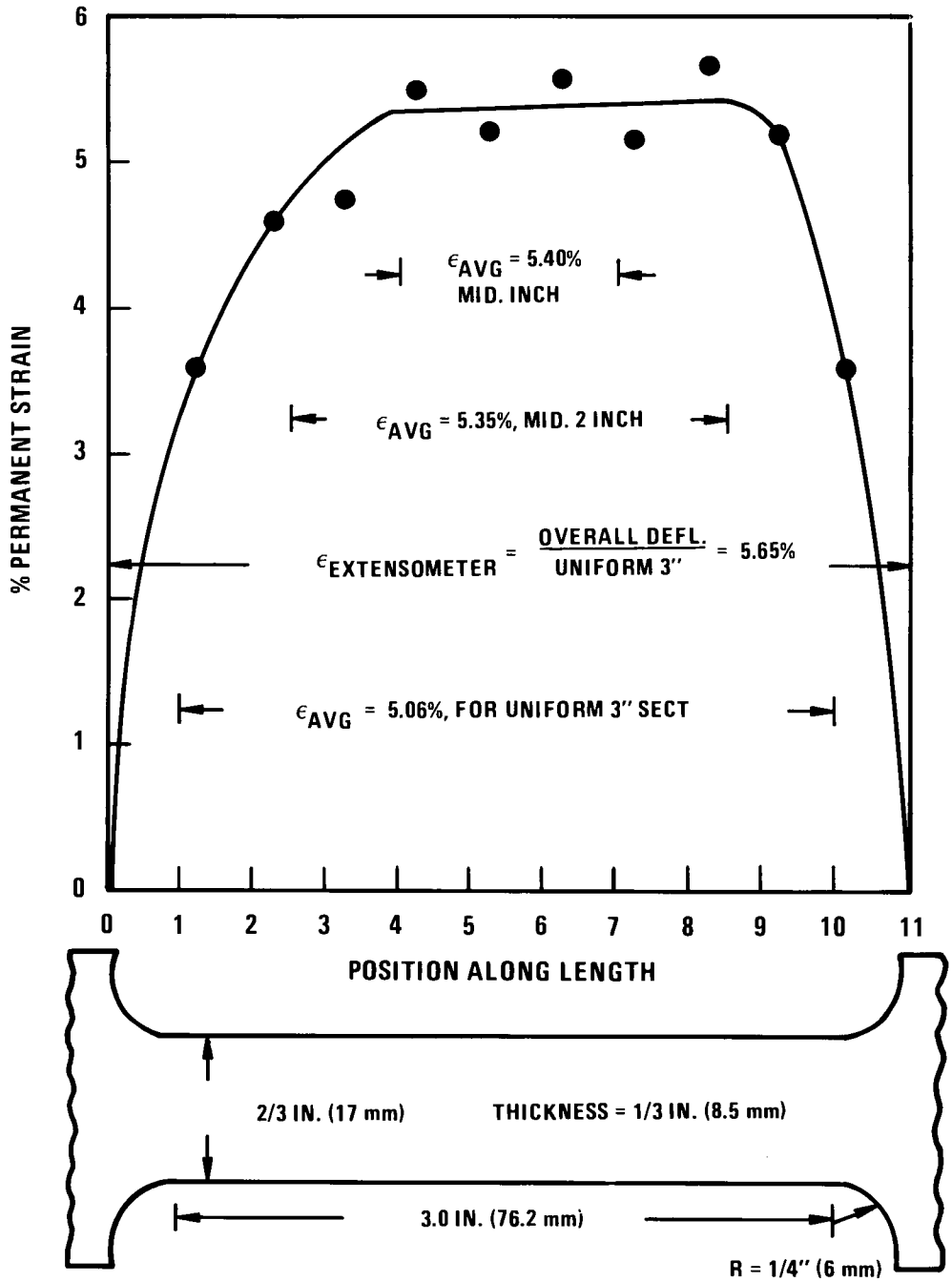

Figure 6-2. Axial Strain Distribution Of A-1 At 303 Hr From Grid Measurements

The data from the measurements of the grid lines have not been compared with analysis and the comparison with the computer calculations will be made at a later date. However, some limited verification of the computer output can be made by comparison with the experimental data at 303 hours. The axial strain from the computer program is given in Figure 6-3. When compared to the experimental data of Figure 6-2, the agreement is very good both for the strain distribution and strain magnitudes. The average strain for the middle two inches is slightly smaller for the computer calculation (5.1 percent) than that for the experimental measurement (5.35 percent), but within the experimental and measurement errors.

The tests of specimens with different degrees of plane strain and various loading histories allow a comparison of strain and stress damage theories in the proposed damage law. Greater emphasis was given to strain damage since this is usually the dominant mechanism for materials with high ductility. A comparison of the strain and stress damage is given in Table 6.3. Only two components of strain damage are summed: the loading strain at a strain rate of about $300\%h^{-1}$ and the creep strain to the transition to third stage or to first cracking. The strain limit for cracking is taken for the minimum creep rate. The stress damage is the sum of the ratios of the time increments at a given stress level to the corresponding rupture time.

The strain damage for the different specimens ranges from 0.98 to 1.08 for the steady loads and from 1.32 to 1.80 for the step-loaded tests.

The stress damage ranges from 0.91 to 1.76 for the steady loads and from 0.8 to 7.35 for the step-loaded tests. The stress damage would give even a larger variation if the maximum principal stress at the point of failure were used.

For noncycling loading, a linear damage law was proposed:

$$\text{Damage} = A\ \Sigma\left(\frac{t}{t_r}\right)\sigma_1 + B\ \Sigma\left(\frac{\varepsilon}{\varepsilon_L}\right)\dot{\varepsilon},\ \sigma_{ij}$$

where the first term is the damage under the history of the maximum principal stress and the second term is the strain damage for the history of the strain rate and stress state.

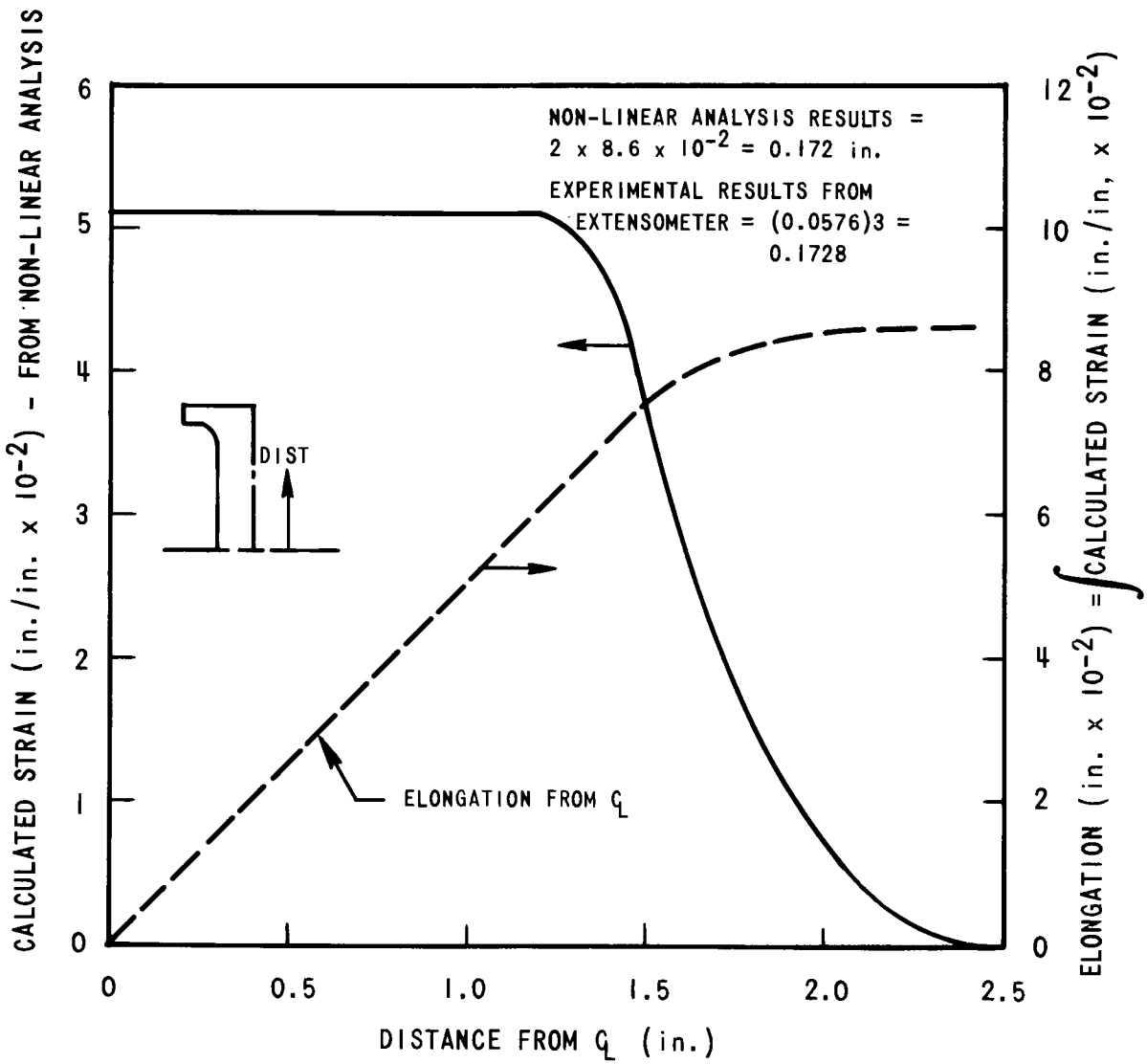

Figure 6-3, Specimen A1, Strains at Time = 303 Hours

7763-3

TABLE 6.3

COMPARISON OF STRAIN AND STRESS DAMAGE

Type of Loading	Monotonic			Step		
Type of Specimen (Figure 6.1)	A	B	G	A	B	G
Specimen Number	A1	B1	G1	A2	B2	G2
Stress, ksi	21	21	25	21	21	25
M Pa	144.8	144.8	172.4	144.8	144.8	172.4
ε_p = Average Overall Loading Strain, %	4.66	5.34	4.20	0.87	2.20	0.44
T.F. x Strain Limit (ε_L) for $\dot{\varepsilon}$ of 300% h^{-1}	39	39	39	39	39	39
T.F. = Triaxiality Factor = Measure of Degree of Plane Strain	1.00	1.30[d]	1.73[a]	1.0	1.30[d]	1.73[a]
ε_L = Strain Limit for $\dot{\varepsilon}$ of 300% h^{-1}	39	30	23	39	30	23
$\frac{\varepsilon_p}{\varepsilon_L}$ = Loading Strain Damage	0.12	0.18	0.18	0.02	0.07	0.02
Minimum Creep Rate, 10^{-3}% h^{-1}	2.20	0.88	7.00	4.50	8.40	2.30
ε_C = Creep Instability Strain at First Indication of Crack or Transition, %	6.7[b]	4.5[b]	4.9[b]	14.8[c]	12.78[c]	4.67[c]
T.F. x Strain Limit (ε_L) for Creep Rate	7.8	7.1	9.4	9.0	10.0	6.2
$\frac{\varepsilon_c}{\varepsilon_L}$ = Creep Strain Damage	0.86	0.83	0.90	1.64	1.73	1.30
Total Strain Damage $\frac{\varepsilon_p}{\varepsilon_L} + \frac{\varepsilon_c}{\varepsilon_L}$	0.98	1.01	1.08	1.66	1.80	1.32
$\frac{t_i}{t_r}$ = Time at Damaging Load	1825	3525	568	4266	1563	6715 1837
t_r = Rupture Time From ORNL Rupture Data TM3845	2000	2000	460	2000	2000	2000 460
Total Stress Damage $\Sigma \frac{t_i}{t_r}$ for all stress levels	0.91	1.76	1.23	2.16	0.80	7.35

(a) T.F. estimate for fillet

(b) Measured from photograph of grid lines

(c) Average transition strain

(d) Derived from finite element analysis where T.F. = $\frac{\text{R Stress} + \text{Z Stress}}{\text{Effective Stress}}$

One of the purposes of the comparisons of the types of damage is the determination of the constant A and B in the damage equation for noncyclic loading. From the current analysis, which did not consider the complete history of maximum principal stress, the optimum values of A and B for this material are A = 0, and B = 1. It is anticipated that at the longer rupture times of service, a consideration of the history of the principal stress will result in a larger value of A where A + B = 1.

6.2.2 Plate Specimens Under Tension and Bending (Type E)

Specimen E2 was interrupted at 3158 hours for photographic measurement. The permanent strain on the higher stressed side was 10.8 percent, but no cracks were detected. The creep rate continued to decrease and was 8×10^{-4} percent per hour on the higher stressed side at this time. The test will be continued until cracking is initiated.

6.2.3 Specimens with Welds

The data from these specimens are summarized in Table 6.2 and Figure 6-4.

6.2.3.1 Transverse Welds in Specimens B and G

From the current tests of Specimens BTW-1 and GTW-1, a comparison can be made between those specimens with transverse welds in reannealed plates and those of the same type from reannealed base plate. The plates with welds have a much higher yield strength. From Table 6.2, the strain on loading to 21 ksi for Specimen BTW-1 is only 0.17 percent compared to 5.34 percent for Specimen B1. Cracks initiated in the heat affected zone (HAZ) of Specimen BTW-1 at 1057 hours at 3.82 percent permanent strain, whereas for B1 this did not occur until 3258 hours at 9.85 percent. The rupture strength of the transverse welded specimens is slightly less than that for the base metal under plane stress (Figure 6-4).

6.2.3.2 Axial Welds in Specimens B and G

The yield strengths for the axially welded models are also higher than for the base plates. Specimen BAW-1, loaded to 25 ksi, had only

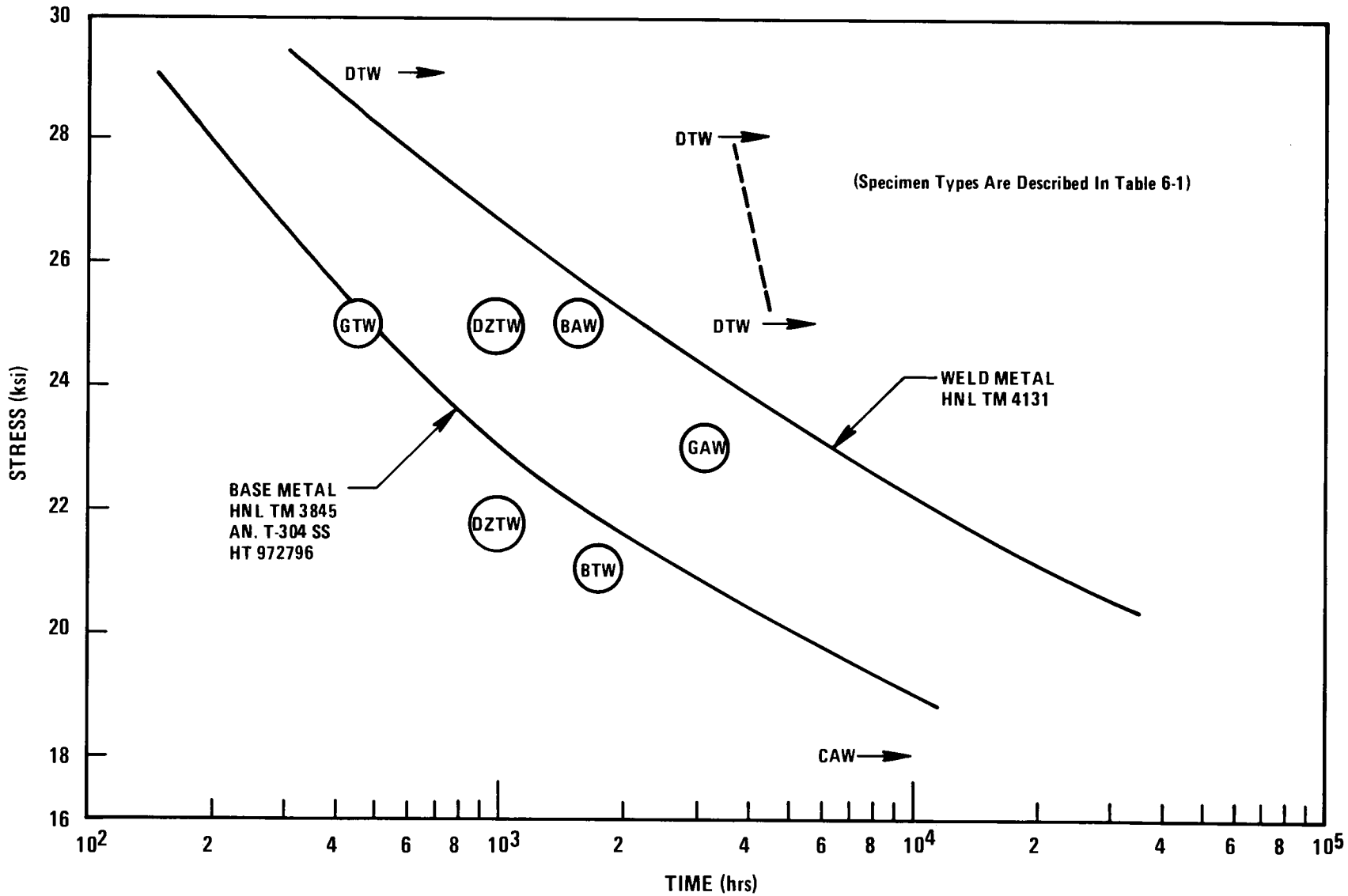

Figure 6-4. Rupture Data For Basic Specimens With Welds

0.25 percent plastic strain (Table 6.2). The rupture strengths of these welded specimens are greater than those of the base metal. The rupture life at comparable stress (Figure 6-4) is about three times that of the base metal and about 60 percent of that of the weld metal samples under plane stress. The axial weld is only one-fifth of the width of the specimens. Based on the law of mixtures and the plane stress strength, this should increase the combined strength only about 3.5 percent. Cracking, however, initiated in the HAZ at about 30 percent of life (Table 6.2). These cracks form along the HAZ in a direction normal to the principal stress and also to the weld.

6.2.3.3 Transverse Weld Specimens with Notches in the Weld

In the DTW specimens, the circumferential notches are located so that the notch is entirely within the weld. To date, none of these have failed, and the life is estimated to be at about ten times that of the all-weld-metal samples under plane stress (Figure 6-4).

6.2.3.4 Transverse Welds with Notches at the HAZ

In the DZTW specimens, the notch was located so that part of the root is at the HAZ. The strength was greatly reduced and the results showed considerable scatter (Figure 6-4). Much of the scatter can be attributed to the location of the root of the notch. Since the transverse weld has a "V" profile, it is difficult to locate the notch with the same amount of HAZ at the root. From the preliminary results, it must be concluded that the HAZ is notch weakened.

6.3 TUBULAR SPECIMEN TESTING - K. C. Thomas, P. C. S. Wu, A. K. Dhalla, C. Daniels

6.3.1 Test Piece Description

The tubular test pieces used in this program to date have been Type 304 stainless steel from the ORNL reference heat (9T2796). The specimens are 8.7 inch in length with a 1.6-inch internal diameter and wall thickness of either 0.1 or 0.05 inch.

6.3.2 Test Matrix

The uniaxial constant-load creep testing of Type 304 stainless steel tubular specimens has been completed according to the test matrix given in Table 6.4. Multiaxial constant-load creep testing is continuing according to the expanded test matrix given in Table 6.5. Test No. 16 was initiated during the current report period. Multiaxial variable-load creep tests are continuing according to the test matrix shown in Table 6.6. Test No. 15 was initiated during the current report period.

The test matrix for Type 316 stainless steel specimens has been prepared as shown in Tables 6.7 and 6.8. Eighteen feet of 2-1/2 inch x 0.56 inch wall Type 316 stainless steel pipe was received from ORNL and has been cut to lengths ready for heat treatment.

The test matrix for the post-test evaluation of Type 304 stainless steel creep specimens is given in Table 6.9 along with the current status.

6.3.3 Test Equipment and Measurement

The multiaxial variable-load creep test No. 15 has been completed, but two malfunctions occurred during the test. In the first stage, the specimen was tested under an effective stress of 10,000 psi (stress ratio of 2.0) for 1150 hours. A temperature excursion occurred 120 hours after initiation of testing. The second stage of testing at 15,000 psi effective stress (stress ratio of 1.5) for 500 hours was accomplished without incident. During the third stage of testing at 20,000 psi effective stress (stress ratio of 1.0), another temperature excursion occurred due to a controller malfunction. The test was therefore terminated in the third stage after 167 hours instead of the intended 200 hours testing.

With the exception of test No. 11, all other tests shown in the post-test matrix (Table 6.9) have been completed. The measurements obtained from these tests are being compiled in the data acquisition system, and data reduction will be initiated during the next report period. The current status of the test matrix is shown in Table 6.9.

A post-test specimen (No. 3C), which was tested under a uniaxial load of 7700 psi for 2000 hours at 1100°F, was tensile tested to provide information on the effect of creep strain on the yield strength of the reference heat (9T2796), Type 304 stainless steel. Eight strain gages were

TABLE 6.4

TYPE 304 TUBULAR SPECIMEN CREEP TESTS - UNIAXIAL CONSTANT LOAD

NOMINAL TEST TEMPERATURE - 1100°F

Test No.	Wall Thickness (0.001 inch)	Axial Stress (psi)	Test Hours Accumulated	Axial Loading Strain (%)	Axial Creep Strain (%)	Total Axial Strain (%)
1B	50	25,000	241.5	0.7988	3.5572	4.3660
2A	100	10,000	2016	0.0490	0.0697	0.1187
2B	100	10,000	2000	0.0780	0.0880	0.1660
3A	100	20,000	336	------	0.9591	------
3B	100	20,000	1990	0.1783	2.7468	2.9251
3C	100	7700	2002	0.0461	0.0534	0.0995
3D	100	5500	1721	0.0253	0.0089	0.0342
3F	100	15,000	1556	0.4855	1.1224	1.1710

TABLE 6.5

MULTIAXIAL CREEP TEST - CONSTANT LOAD NOMINAL TEST TEMPERATURE 1100°F

Test No.	Wall Thickness (10^{-3} in)	Axial Load (lbs)	Nominal Internal Pressure (psi)	Nominal Effective Stress (psi)	Nominal Principal Stress Ratio (σ_θ/σ_z)	Test Time (hours)	Average[a] Loading Strain (%)		Nominal Average Creep Strain			
							Axial	Hoop	Radial	Hoop	Axial	Effective
4A	100	323.0	1209.5	10,000[b]	2.0	1965.7	0.01048	0.02174	-0.12711	0.12466	0.00245	0.1453
5	100	484.0	1814.3	15,000[b]	2.0	1998.0	0.09208	0.08499	-0.57795	0.54670	0.03125	0.6499
6	100	0.0	2716.9	20,000[c]	2.0	762.0	0.13321	2.71103	-2.12850	2.16000	-0.03150	2.4700
7A	100	1211.0	1180.0	10,000[b]	1.5	1648.0	0.04240	0.03521	-0.02101	0.01360	0.00741	0.0211
8	100	1515.0	2000.0	15,000[e]	1.5	2009.3	0.19414	0.80047	-0.84800	0.71900	0.12900	0.9130
9[e]	100	2018.6	2668.4	20,000[c]	1.5	573.4	0.00541	0.02334	-3.74600	3.31000	0.43600	4.0900
10	100	2670.0	1049.4	10,000[b]	1.0	2033.8	0.04363	0.01994	-0.06130	0.03890	0.03330	0.0600
11	100	4005.0	1574.0	15,000[b]	1.0	2012.9	0.03288	0.07339	-0.48900	0.21100	0.27800	0.4720
12[e]	100	5340.7	2353.0	20,000[e]	1.0	1096.5	1.82117	0.99892	-2.82000	1.56000	1.26000	2.7900
16	50	1619.9	757.6	12,500	1.0	2000						
17	50	612.3	859.0	12,500	1.5	2000						
18	50	0.0	874.8	12,500	2.0	2000						
19	50	2267.8	1060.6	17,500	1.0	2000						
20	50	857.1	1202.6	17,500	1.5	2000						
21	50	0.0	1224.6	17,500	2.0	2000						

(a) The axial loading strain is the average of two readings. The hoop strain is the average of three readings.

(b) Effective stress calculated as per thick cylinder formula is given by:

$$\sigma_e = \frac{1}{2}\left[(\sigma_z - \sigma_\theta)^2 + (\sigma_\theta - \sigma_r)^2 + (\sigma_r - \sigma_z)^2\right]^{1/2}$$

where: $\sigma_z = \sigma_{axial} = \frac{L}{A} + p\,\frac{a^2}{b^2-a^2}$

$$\sigma_\theta = \sigma_{hoop} = p\,\frac{a^2(b^2+r^2)}{r^2(b^2-a^2)}$$

$$\sigma_r = \sigma_{radial} = p\,\frac{a^2(b^2-r^2)}{r^2(b^2-a^2)}$$

A = cross-sectional area of the tube

t = tube thickness

a = inside radius of the tube

b = outside radius of the tube

r = radius of the point under consideration

L = axial load

P = internal pressure

(c) Effective stress calculated as per thin cylinder formula is given by:

$$\sigma_e = \left[\sigma_\theta^{\,2} + \sigma_z^{\,2} - \sigma_\theta\sigma_z\right]^{1/2}$$

where: $\sigma_\theta = P\,\frac{r_{av}}{t}$ $\qquad r_{av}$ = average radius of the tube

$$\sigma_z = p\,\frac{r_{av}}{2t} + \frac{P}{2\pi r_{av} t}$$ $\qquad t$ = thickness of the tube

(d) Sample rupture after 808 hours under the test condition.

(e) Test terminated because the sample has already reached tertiary creep stage.

TABLE 6.6

TYPE 304 TUBULAR SPECIMEN CREEP TEST - MULTIAXIAL VARIABLE LOAD

NOMINAL TEST TEMPERATURE 1100°F

Test No.	Wall Thickness (0.001 in)	Effective Stress σ_e^a (psi)	Nominal Principal Stress Ratio $\sigma_{hoop}/\sigma_{axial}$ (σ_θ/σ_z)	Loads to Obtain Nominal Desired Stresses: Int. Pressure p (psi)	Loads to Obtain Nominal Desired Stresses: Axial Load p (lbs)	Nominal Test Duration t (hrs)	Test Status
13	50	10,000	1.5	612.9	436.8	1100	a
13 (Cont'd)	50	15,000	1.5	2000.0	1515.0	500	a
13 (Cont'd)	50	20,000	1.5	2668.4	2018.6	200	a
13 (Cont'd)	50	20,000	1.0	2353.0	5340.7	200	a
14	50	15,000	2.0	930.3	0.0	500	b
14 (Cont'd)	50	15,000	1.5	2000.0	1515.0	500	b
14 (Cont'd)	50	15,000	1.0	832.5	1780.0	500	b
14 (Cont'd)	50	15,000	2.0	930.3	0.0	500	b
15	50	10,000	2.0	620.2	0.0	1150	a
15 (Cont'd)	50	15,000	1.5	2000.0	1515.0	500	a
15 (Cont'd)	50	20,000	1.0	2353.0	5340.7	200	a
15 (Cont'd)	50	15,000	2.0	930.3	0.0	200	c

(a) Test completed.

(b) Test to be initiated.

(c) Due to malfunction of the temperature controller, the test was terminated without the fourth stage testing.

TABLE 6.7

TYPE 316 SS TUBULAR SPECIMEN CREEP TEST - UNIAXIAL CONSTANT LOAD

Test No.	Effective Stress σ_e (a) (psi)	Stress Ratio $\sigma_{hoop}/\sigma_{axial}$ (σ_θ/σ_z)	Loads to Obtain Nominal Desired Stresses: Int. Pressure p (psi)	Loads to Obtain Nominal Desired Stresses: Axial Load p (lbs)	Nominal Test Temperature T (°F)	Nominal Test Duration t (hours)	Test Priority	Remarks
101	25,000	0.0	0.0	6479.5	1100	2000	(b)	Test to Failure
102	20,000	0.0	0.0	5183.6	1100	2000	(d)	
103	15,000	0.0	0.0	3887.7	1100	2000	(b)	
104	10,000	0.0	0.0	2591.8	1100	2000	(b)	Test to Failure with Stepped Loading
105	7700	0.0	0.0	1995.7	1100	2000	(c)	

(a) $\sigma_e = \sigma_z = \frac{P}{2\pi r_{av} t}$

where: r_{av} = average radius of the tube

t = thickness of the tube

(b) These tests should be initiated before tests 102 and 105.

(c) Test 105 can be omitted if machine time is not available.

(d) Test 102 need not be performed. It is given here only as a comparison test for Type 304 stainless steel Test No. 3.

TABLE 6.8

TYPE 316 SS TUBULAR SPECIMEN CREEP TEST - MULTIAXIAL CONSTANT LOAD

Test No.	Effective Stress σ_e (a) (psi)	Stress Ratio $\sigma_{hoop}/\sigma_{axial}$ (σ_θ/σ_z)	Loads to Obtain Nominal Desired Stresses: Int. Pressure p (psi)	Loads to Obtain Nominal Desired Stresses: Axial Load P (lbs)	Nominal Test Temperature T (°F)	Nominal Test Duration t (hours)	Test Priority	Remarks
106	20,000	2.0	1399.6	0.0	1100	2000	(c)	
107	20,000	1.0	1212.1	2591.8	1100	2000	(c)	
108	15,000	2.0	1049.7	0.0	1100	2000	(b)	
109	15,000	1.0	909.1	1943.9	1100	2000	(b)	
110	12,500	2.0	874.8	0.0	1100	2000	(b)	
111	12,500	1.0	757.6	1619.9	1100	2000	(b)	
112	10,000	2.0	699.8	0.0	1100	2000	(b)	Test to Failure with Stepped Loading
113	10,000	1.0	606.1	1295.9	1100	2000	(b)	

(a) Effective stress calculated as per thin cylinder formula is given by:

$$\sigma_e = [\sigma_\theta^2 + \sigma_z^2 - \sigma_\theta\sigma_z]^{1/2}$$

where: $\sigma_\theta = p \frac{r_{av}}{t}$

$\sigma_z = p \frac{r_{av}}{t} + \frac{P}{2\pi r_{av} t}$

r_{av} = average radius of the tube

t = thickness of the tube

(b) These tests should be initiated before tests 106 and 107.

(c) Tests 106 and 107 can be omitted if machine time is not available.

TABLE 6.9

TYPE 304 SS TUBULAR SPECIMEN CREEP TEST - POST-TEST MATRIX*

Test No.	Effective Stress, σ_e (ksi)	Stress Ratio (σ_θ/σ_z)	Specimen History[a] Axial Load (lb)	Internal Pressure (psi)	Post-Test Plan	Current Status
2A	10.0	0.0	5340	0	(b)	(j)
3C	7.7	0.0	4112	0	(b)	(j)
4A	10.0	2.0	323	1209	(c)	(i)
3B	20.0	0.0	10,681	0	(d)	(j)
9	20.0	1.5	2018	2668	(d)	(j)
12	20.0	1.0	5340	2353	(d)	(j)
11	15.0	1.0	4005	1574	(d)	(k)
7A	10.0	1.5	1211	1180	(d)	(j)
2B	10.0	0.0	5340	0	(e)	(j)
3D	5.0	0.0	2670	0	(f)	(j)
	10.0	1.0	2670	1049	(e)	(j)
1A[g]	25.0	0.0	6872	0	(h)	(j)
1B	25.0	0.0	6872	0	(h)	(j)
3A	20.0	0.0	10,681	0	(h)	(j)
4	10.0	2.0	323	1207	(h)	(j)
6	20.0	2.0	0.0	2717	(h)	(j)
7	10.0	1.5	1212	1180	(h)	(j)
8	15.0	1.5	1515	2000	(h)	(j)

* Priority of testing is indicated by the order of listing in the table.
(a) All specimen tested at 1100°F for about 2000 hours.
(b) Tensile test to failure.
(c) Pressurize to failure.
(d) Creep-rupture test under the same prior creep test condition.
(e) Specimen step loaded to effective stress levels of 15 and 20 ksi respectively for a period of 500 hours at each stress level.
(f) Specimen step loaded to effective stress levels of 10, 15 and 20 ksi respectively for a period of 500 hours at each stress level.
(g) Test terminated due to over-temperature.
(h) Microstructural characterization.
(i) To be initiated.
(j) Test completed.
(k) Test in progress.

attached to the tubular sample which was loaded in a Baldwin tensile machine. The results show no significant deviation among the readings taken from the various gages. The 0.2 percent yield strength was determined to be 29 ksi. The same property for the annealed material was determined to be 28 ksi.

Tensile testing on miniature specimens was initiated. These specimens were machined from 2-1/2 inch OD pipe of the HNL reference heat (9T2796), Type 304 stainless steel. The purpose of this testing is to study the annealing effect and possible anisotropy effect on the tensile properties of this material.

6.3.4 Data Reduction

Data reduction continued on the Type 304 stainless steel tubular specimen creep test results. Creep strains derived from measurements obtained previously at various stress levels were analyzed according to the following equation:

$$\varepsilon_c = \varepsilon_t \, (1-e^{-rt}) + \dot{\varepsilon}_m t \qquad (1)$$

where ε_c = creep strain (in/in)

t = time (hour)

ε_t, r, and $\dot{\varepsilon}_m$ are constants

Values of these constants were obtained, according to Equation (1) for all uniaxial creep tests, by using the computer program CREEP-FIT transmitted from ORNL. The effective strain versus time relationships derived from the multiaxial creep measurements were also fitted according to the same equation and the results were reported previously.[1]

During the present report period, master equations with the three terms, ε_t, r and $\dot{\varepsilon}_m$, described as a function of stress were derived for all creep tests conducted previously. For the multiaxial creep testing, a master equation was derived for a given stress ratio throughout the effective stress range. The master equation constants are as follows:

Uniaxial Creep Test (7700 psi to 25,000 psi axial stress)

$\varepsilon_t = \exp\,(2.28 \times 10^{-4}\,\sigma - 5.33)$

$r = \exp\,(1.14 \times 10^{-4}\,\sigma - 6.17)$

$\dot{\varepsilon}_m = \exp\,(3.64 \times 10^{-4}\,\sigma\ 14.06)$

Multiaxial Constant Load Creep Test (10,000 psi to 20,000 psi effective stress)

Stress Ratio of 1.0

$\varepsilon_t = \exp\ (3.3 \log \sigma - 14.5)$

$r = \exp\ (7.33 \log \sigma - 32)$

$\dot{\varepsilon}_m = \exp\ (9 \log \sigma - 4.15)$

Stress Ratio of 1.5

$\varepsilon_t = \exp\ (3.0 \log \sigma - 12.9)$

$r = \exp\ (9.0 \log \sigma - 32)$

$\dot{\varepsilon}_m = \exp\ (9.67 \log \sigma - 44)$

Stress Ratio of 2.0

$\varepsilon_t = \exp\ (1.33 \log \sigma - 6.1)$

$r = \exp\ (6.7 \log \sigma - 27.3)$

$\dot{\varepsilon}_m = \exp\ (8.7 \log \sigma - 40)$

As shown in Figures 6-5 and 6-6, the master equation describes the uniaxial creep test results very well. In Figures 6-7 to 6-9, the effective strain versus time for multiaxial creep tests was fitted by using the master equation derived for the three stress ratios for the effective stresses ranging from 10,000 to 20,000 psi. It is noted that at 15,000 and 20,000 psi effective stresses, the master equations describe the experimental results extremely well. Since Equation (1) does not have a term that describes the tertiary creep strain, it is understandable that the master equations cannot account for the tertial creep strains shown in Figure 6-9. In the case of 10,000 psi, it is noted in Figure 6-7 that the agreement between the experimental results and the derived values based on master equations is not so good in the transient creep range.

Analytically, the calculated effective creep strain should be the same for any stress ratio ($\sigma_{hoop}/\sigma_{axial}$) at a given effective stress level. However, as shown in Figures 6-7 to 6-9, there is a significant difference among the effective creep strains derived for the various

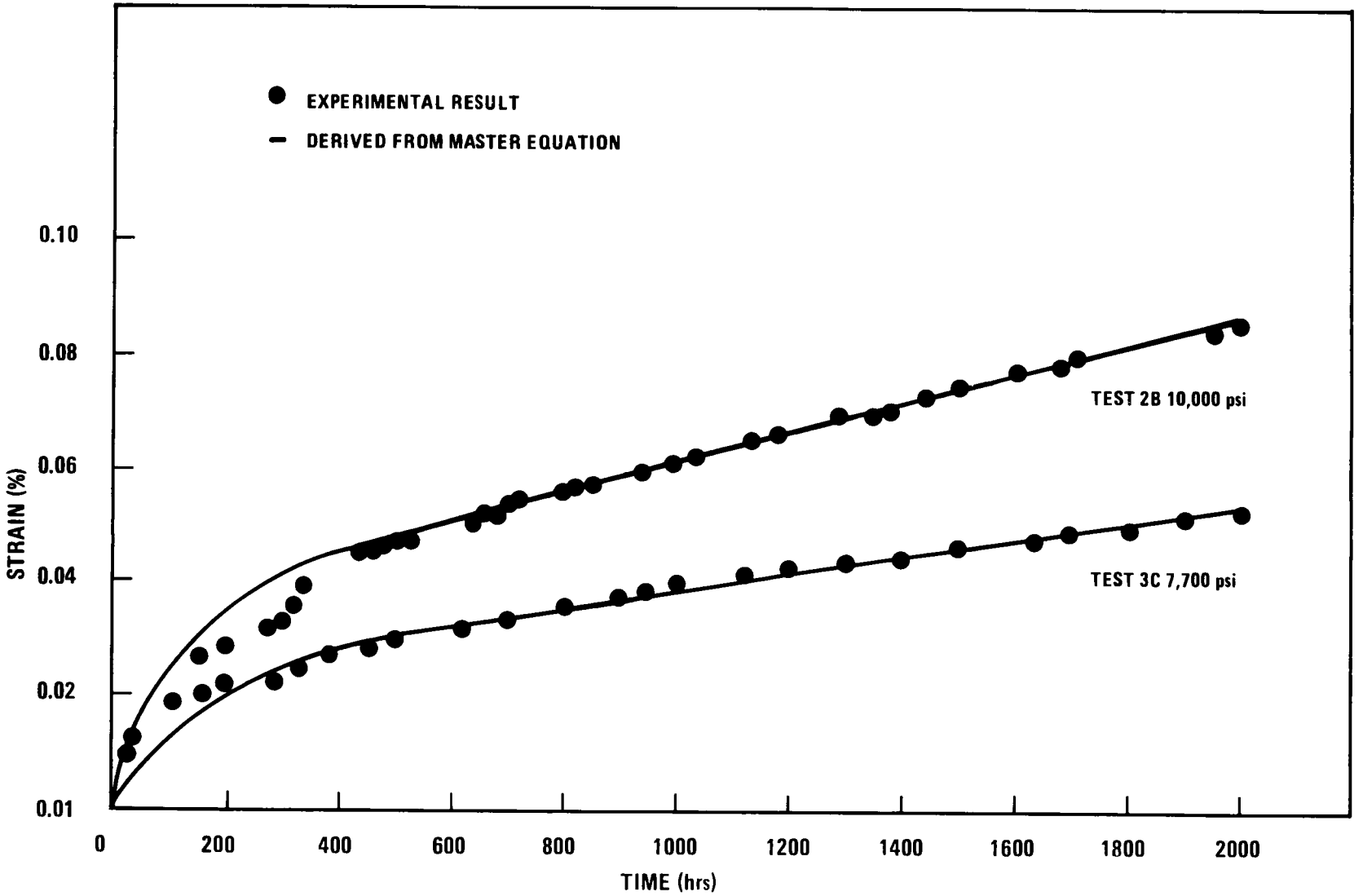

Figure 6-5. Uniaxial Creep Strain Of Type 304 SS (Heat No. 9T2796) At 7700 And 10,000 psi Axial Stress And 1100°F

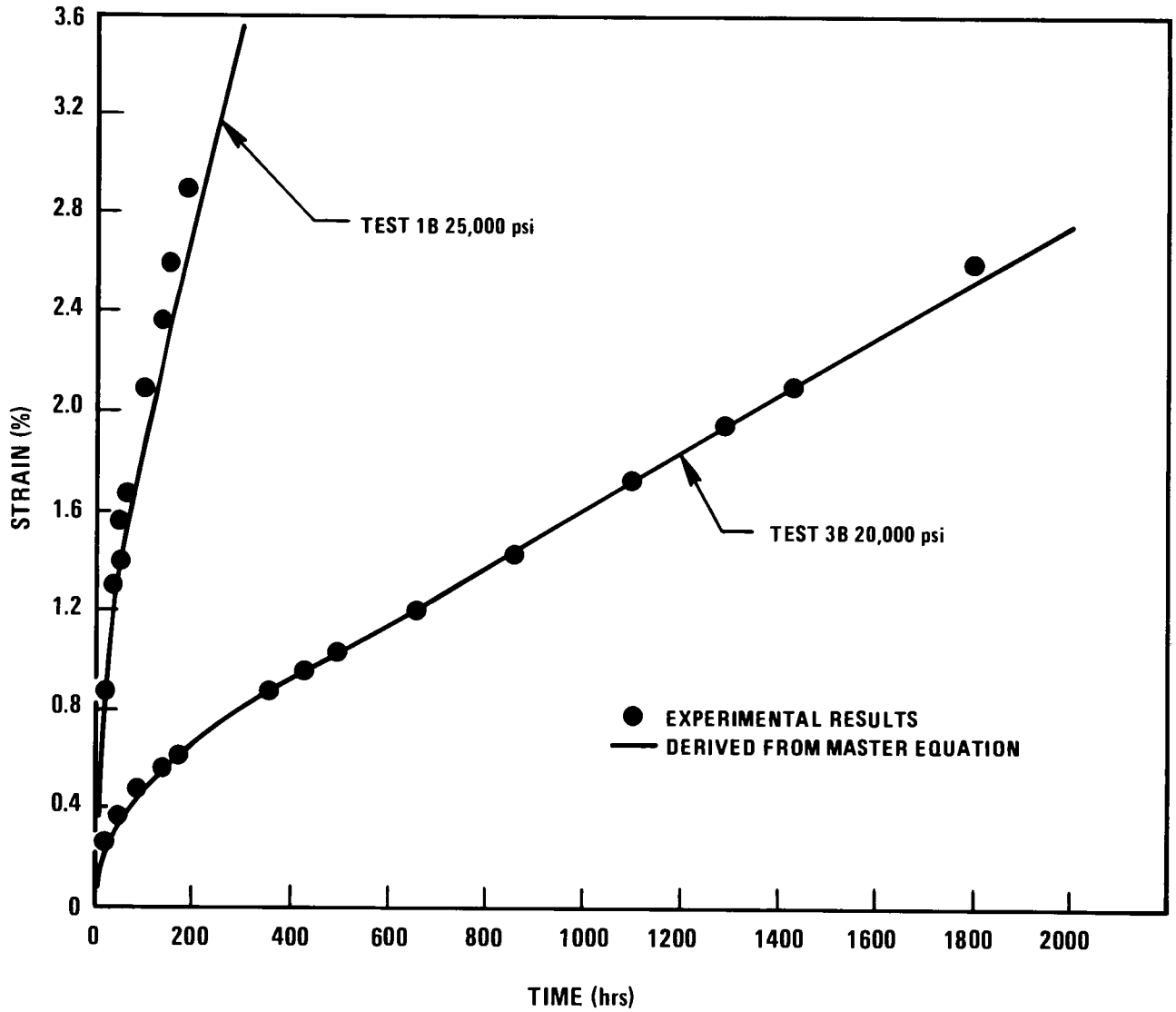

Figure 6-6. Uniaxial Creep Strain Of Type 304 SS (Heat No. 9T2796) At 20,000 And 25,000 psi Axial Stress And 1100°F

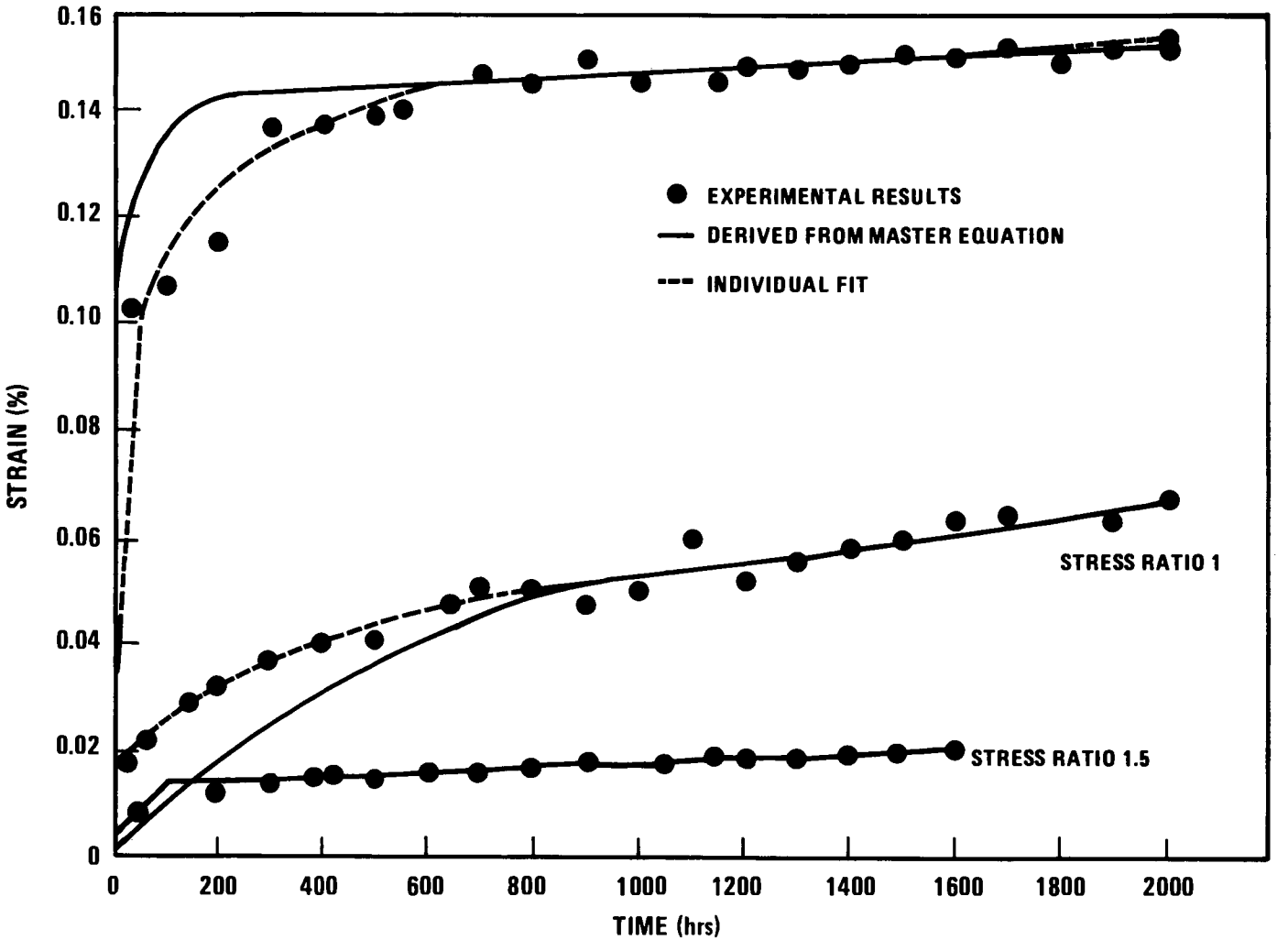

Figure 6-7. Effective Strain Versus Time For Multiaxial Creep With Effective Stress Of 10,000 psi

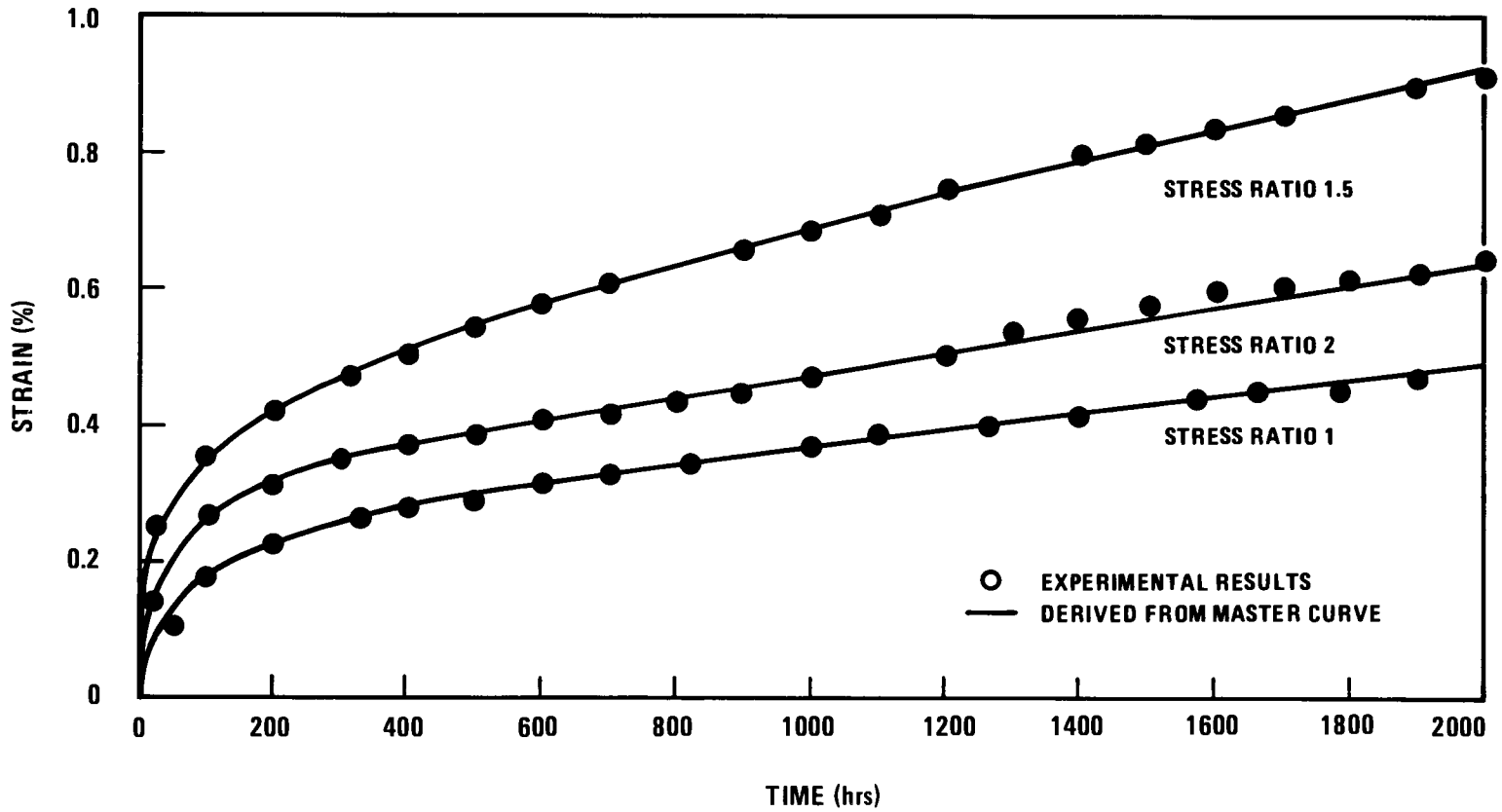

Figure 6-8. Effective Strain Versus Time For Multiaxial Creep With Effective Stress Of 15,000 psi

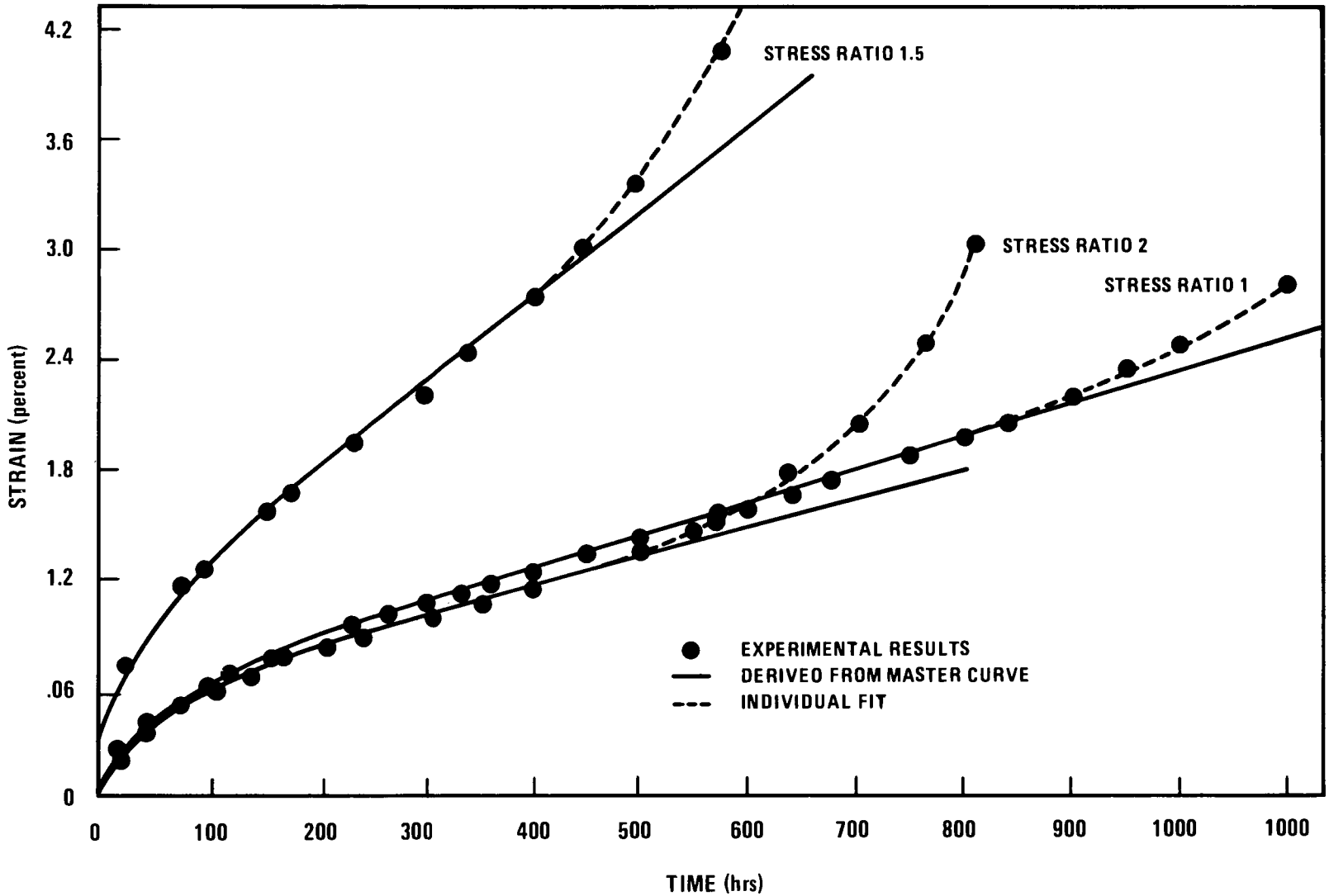

Figure 6-9. Effective Strain Versus Time For Multiaxial Creep With Effective Stress of 20,000 psi

stress ratios. The exact reason for this discrepancy is not yet understood. However, preliminary analysis is currently being conducted by evaluating the following factors:

1. Experimental error introduced into the strain measurements due to either mechanical instability of the extensometers or electronic instability of the SLVC transducers.
2. Anisotropy in the material, hence, the effect of the biaxiality stress ratio.
3. The effect of non-uniform spatial distributions of the stress components and strain components. The assumption of elastic behavior and pressure loading in the present investigation dictates that the effective stress is higher at the inside surface than at the outside surface for the tubular specimens.

The conceptual implications of the nonuniformity of stress and strain is far reaching. The significance of the absence of a single constant effective stress value for the present tubular specimen creep testing needs to be thoroughly investigated in order to derive a more realistic creep behavior model for the alloys investigated.

6.4 REFERENCES

1. Mechanical Properties Test Data for Structural Materials Quarterly Progress Report for Period Ending April 30, 1975, ORNL-5105. (Availability: USERDA Technical Information Center).

7. UNIVERSITIES

7.1 UNIVERSITY OF CINCINNATI — J. Moteff

7.1.1 Introduction

The objective of this program is to (a) evaluate the time, temperature and stress-dependent mechanical properties of reactor structural materials, (b) determine the relationship of these properties to the microstructure and (c) show the contribution of the microstructure to the internal stress fields and the subsequent influence on microcracking and the grain boundary sliding behavior during the normal plastic deformation at elevated temperatures. Special consideration is being given to operating conditions typical of nuclear reactor applications, including the knowledge that the radiation environment can influence the substructure of these metals, a circumstance which can lead to significant changes in the conventional mechanical property behavior.

7.1.2 Experimental Program

Transmission electron microscopy has been used to study the deformation substructure resulting from creep, tensile and fatigue deformation at elevated temperatures. The substructural characteristics for the creep and tensile tested specimens from the ORNL reference heat 9T2796 of AISI 304 stainless steel are now presented. The presence of matrix carbides seemed to influence the formation of

cells or subgrains. A program is initiated to study the morphology of the precipitates and their influence on the deformation of 304 stainless steel. Creep and tensile data from ORNL reference heat 9T2796 was further evaluated through analysis in preparation for the correlation of the macroscopic deformation properties with the corresponding microstructure. Creep tests were conducted on 304 stainless steel specimens in which the stress level was abruptly changed to another value during time on test at elevated temperatures and then subsequently terminated following a given strain and/or steady state creep rate for TEM evaluation of the substructure. The characterization of the dislocation substructure by TEM is underway and results will be presented in the next progress report. The substructural evaluation by TEM was performed on specimens from a 304 stainless steel tested in creep at 704°C. The results are now presented.

A family of fatigue tests on 304 stainless steel (Heat 9T2796) conducted at ANL under a Thesis Parts Program were completed and the evaluation of the dislocation substructure by transmission electron microscopy was also performed. The results are presented. Work on the substructural evaluation in Incoloy 800 tested in the fatigue mode at elevated temperatures is being continued and will be reported in future progress reports.

Work is completed on the creep-rupture studies on three

alloys obtained from the National Alloy Development Program (NADP) and the results will be presented in the NADP Progress Reports.

7.1.2.1 Characterization of the Creep and Tensile Substructure of 304 Stainless Steel, Reference Heat 9T2796 (R. K. Bhargava)

The dislocation substructure of the tensile and creep tested specimens of AISI 304 stainless steel (Reference Heat 9T2796) was evaluated by transmission electron microscopy. The test conditions of these specimens involved a temperature range of 538°C to 816°C and the strain rates varied from 9.7×10^{-9} sec^{-1} to 8.3×10^{-2} sec^{-1}. The stress levels of these specimens varied from 5.27 $kg \cdot mm^{-2}$ (7,500 psi) to 39.23 $kg \cdot mm^{-2}$ (55,800 psi). Some photomicrographs showing the typical dislocation substructure that was developed during creep and tensile tests have been reported previously[1-3]. The typical subgrain substructure that was developed in high temperature creep and slow tension is shown in Figures 7.1 and 7.2. Fig. 7.1 shows the subgrains that were developed during creep at high temperatures 704°C to 816°C. The stress levels of these specimens ranged from 5.72 $kg \cdot mm^{-2}$ (7,500 psi) to 10.55 $kg \cdot mm^{-2}$ (15,000 psi). The substructure developed in creep at 760°C and 816°C and during slow tension at 760°C is shown in Fig. 7.2. The stress levels for these specimens varied from a low of 5.27 $kg \cdot mm^{-2}$ (7,500 psi) to a high of 14.06 $kg \cdot mm^{-2}$ (20,000 psi).

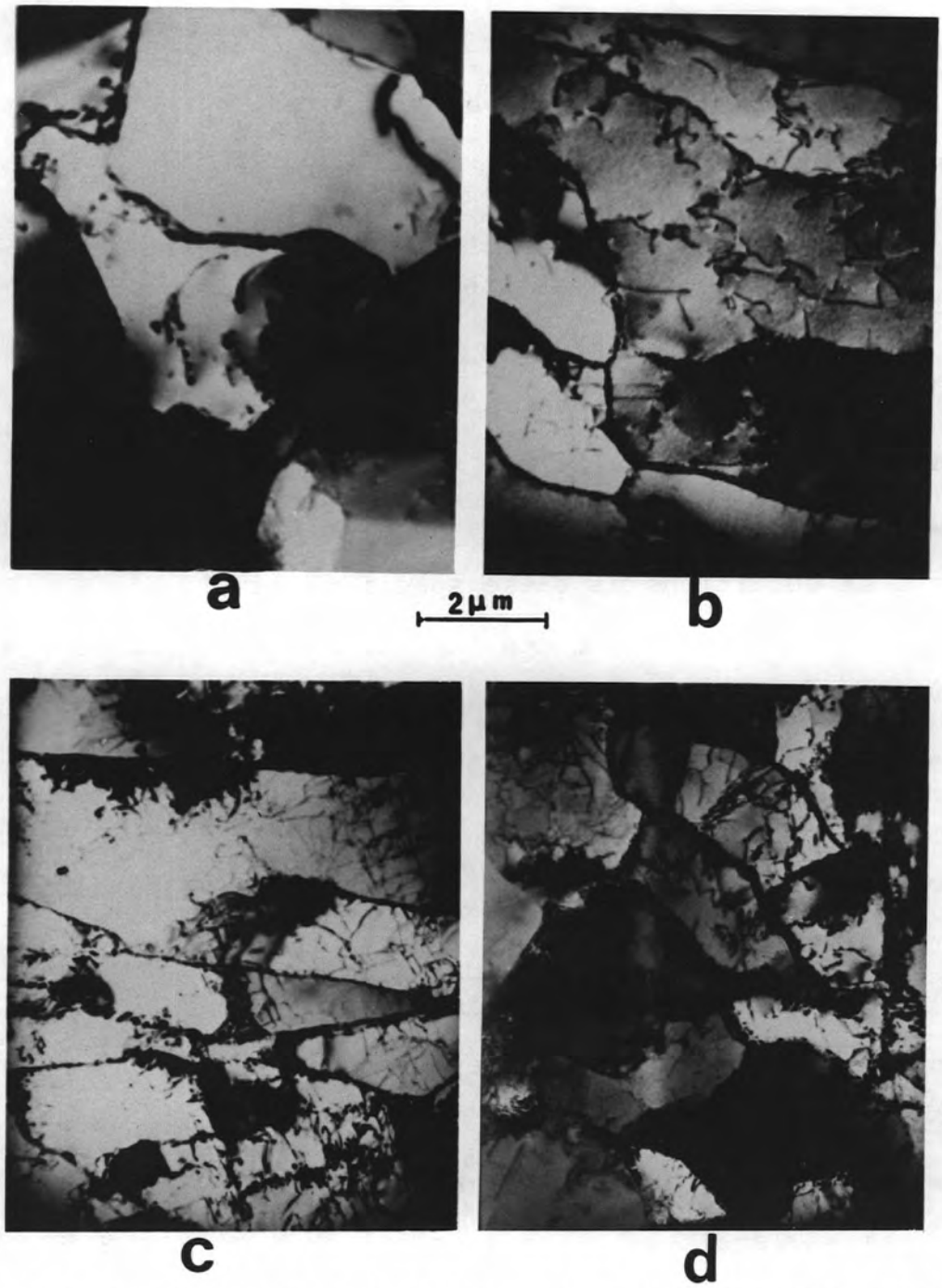

Fig. 7.1 Typical Subgrain Substructure Developed in Creep Tested AISI 304 SS (Heat 9T2796) at (a) 816°C, 5.27 $kg \cdot mm^{-2}$, (b) 760°C, 7.03 $kg \cdot mm^{-2}$, (c) 704°C, 10.55 $kg \cdot mm^{-2}$, and (d) 760°C, 10.55 $kg \cdot mm^{-2}$.

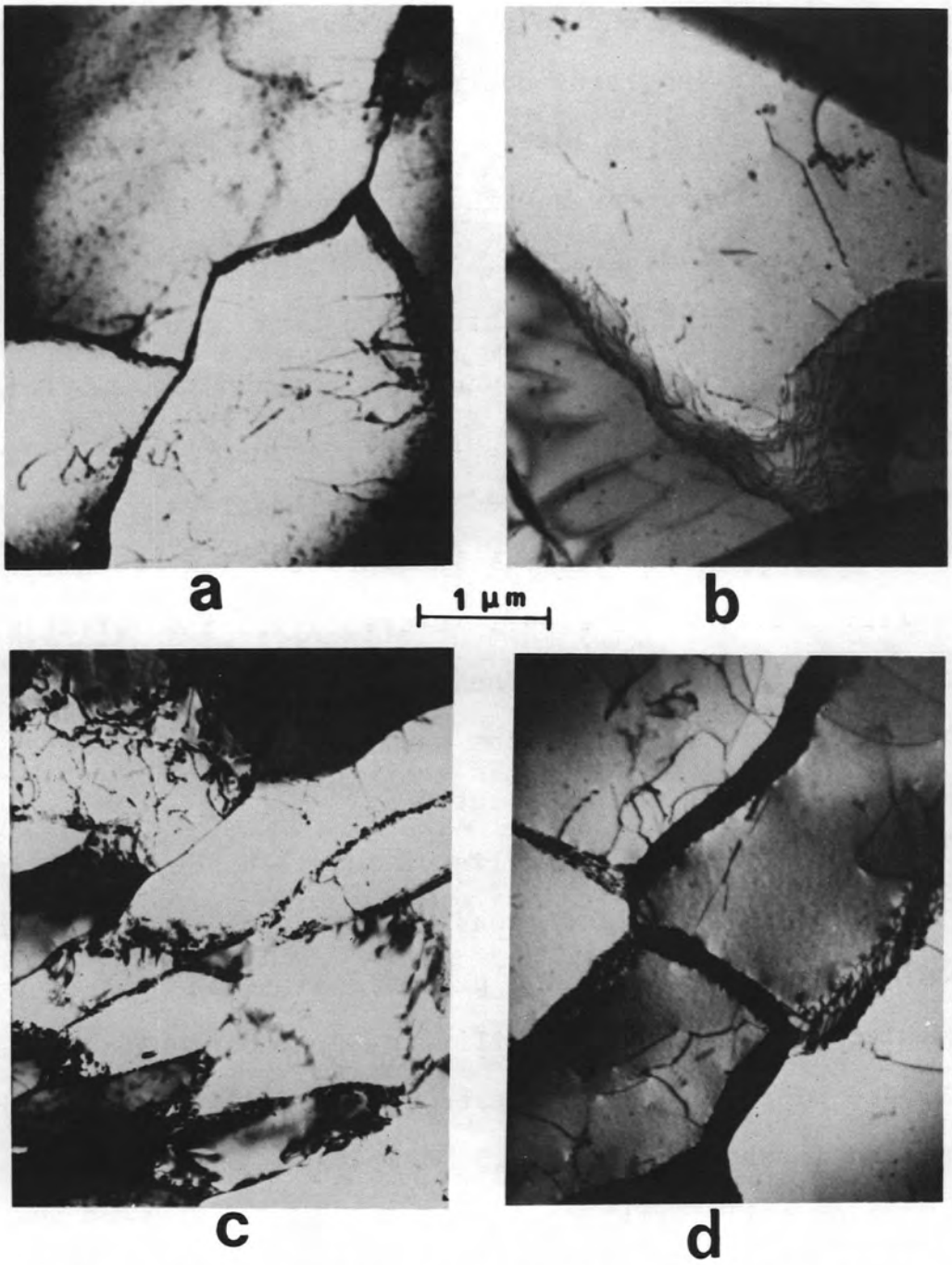

Fig. 7.2 Typical Subgrain Substructure Developed in AISI 304 SS (Heat 9T2796) at (a) 816°C, 7.03 kg·mm^{-2}, Creep, (b) 816°C, 5.27 kg·mm^{-2}, Creep, (c) 760°C, $\dot{\varepsilon} = 6.7 \times 10^{-6}$ sec^{-1}, tensile and (d) 760°C, 14.06 kg·mm^{-2}, Creep.

The substructure developed consisted of subgrains and the size of the subgrains decreased with a corresponding increase in the stress levels. The dislocations within the subgrains were very few and their number increased as the subgrain size became smaller. In fact, some of the dislocations at these high temperatures were part of broken up subgrain boundaries. The boundaries between the subgrains consisted of more or less regular arrays of dislocations. The substructure that resulted from the tests at lower temperatures and higher stresses is characterized by cells. (See Fig. 7.1(a) & (b) p.307, reference 1, Fig. 7.1(a) & (b) p. 325, reference 2). The cell walls consisted of a diffuse tangle of dislocations and the interior of cells was relatively free of any dislocations.

The formation of the cells or subgrains depends mainly on the mobility of dislocations under a combined action of stress and temperature. The presence of second phase particles also influences the mobility of dislocations and the influence of carbide precipitates on the cell or subgrain formation is shown in Fig. 7.3. For tests at 593°C, the subgrain or cell formation was hindered by the profuse precipitation of the second phase. This phase was identified to be a complex carbide of iron and chromium of type $M_{23}C_6$ [4]. Fig. 7.3(b) and 7.3(c) show the interaction of the precipitate particles with the dislocations. The amount of precipitate was proportional to the test duration. RP 7 with a rupture

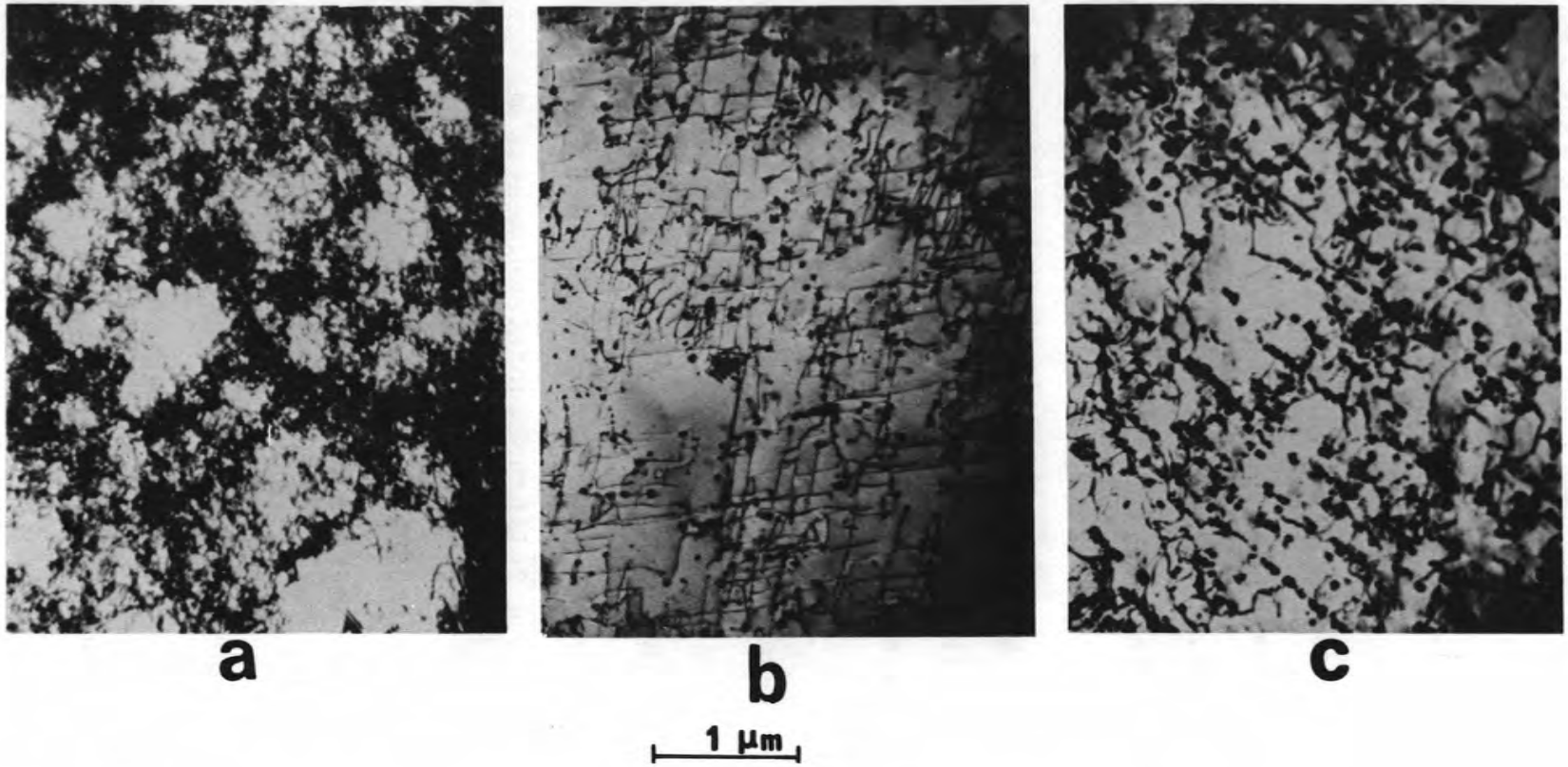

Fig. 7.3 Typical Dislocation Substructure Developed in AISI 304 SS (Heat 9T2796) at (a) 538°C, 24.61 kg·mm^{-2}, Creep (b) 593°C 17.50 kg·mm^{-2}, Creep and (c) 593°C, 15.82 kg·mm^{-2}, Creep. The Influence of Carbide Precipitates is Illustrated in (b) and (c).

life of 440 hours showed a finer precipitate and most of the dislocations were straight. (Fig. 7.3(b)). RP 32 ruptured in 878 hours and the precipitates became more blocky. As a result of this, the resistance to the motion of dislocations became less and the dislocations were observed in their usual curved form. (Fig. 7.3(c)). At 538°C, RP 9 which was tested at 24.61 $kg \cdot mm^{-2}$ (35,000 psi) showed very little carbide precipitation and the dislocations rearranged to form cells (Fig. 7.3(a)).

The quantitative substructural features, viz., the average cell or subgrain intercept size, the dislocation density and the average misorientation across subgrains or cells for specimens tested in creep and tensile modes are listed in Tables 7.1 and 7.2 respectively. The dislocations that were associated with the subgrain boundaries were not included in counting the dislocation density. The misorientation between the adjacent subgrains was measured by using selected area diffraction patterns containing pairs of Kikuchi lines. The misorientation angle was determined by measuring the shift in Kikuchi lines that occurred when a subgrain boundary was traversed across.

Fig. 7.4 shows a plot of the cell or subgrain intercept size, λ, versus the modulus compensated true stress, σ_T/G on a log-log scale. For comparison with the present results, the data obtained by Cuddy[5] for creep substructure in a type 304 stainless steel have also been plotted in the same

TABLE 7.1

SUBSTRUCTURE DATA OF AISI 304 STAINLESS STEEL (REFERENCE HEAT 9T2796) IN CREEP

Specimen Number	Test Temperature °C	True Stress[a] σ_T $kg \cdot mm^{-2}$	Modulus Compensated True Stress $\sigma_{T/E}$	$\sigma_{T/G}$	Average Cell or Subgrain Intercept λ, μm	Average Dislocation Density[c] ρ cm^{-2}	Subgrain or Cell Misorientation θ Degree
RP 8	538	33.3	2.08×10^{-3}	5.37×10^{-3}	0.74 ± 0.10[b]	N.M.	N.M.
RP 9		28.0	1.74×10^{-3}	4.51×10^{-3}	0.84 ± 0.08	N.M.	N.M.
RP 4	593	30.1	1.94×10^{-3}	5.04×10^{-3}	0.82 ± 0.13	$(13.70 \pm 3.43) \times 10^9$	N.M.
RP 7		19.9	1.28×10^{-3}	3.33×10^{-3}	N.O.	$(6.28 \pm 1.76) \times 10^9$	N.M.
RP 32		17.9	1.15×10^{-3}	2.99×10^{-3}	N.O.	$(4.50 \pm 1.13) \times 10^9$	N.M.
RP 1	650	21.3	1.43×10^{-3}	3.69×10^{-3}	1.64 ± 0.16	$(7.36 \pm 3.50) \times 10^9$	0.53 ± 0.08
RP 2		17.1	1.15×10^{-3}	2.97×10^{-3}	1.71 ± 0.48	$(5.81 \pm 1.46) \times 10^9$	0.60 ± 0.34
RP 3		12.0	0.80×10^{-3}	2.08×10^{-3}	1.72 ± 0.19	$(4.99 \pm 1.25) \times 10^9$	N.M.
RP 27	704	12.7	0.88×10^{-3}	2.29×10^{-3}	1.61 ± 0.13	$(5.50 \pm 1.38) \times 10^9$	0.38 ± 0.29
RP 109	760	19.0	1.38×10^{-3}	3.58×10^{-3}	0.81 ± 0.19	$(6.41 \pm 2.68) \times 10^9$	0.45 ± 0.28
RP 118		13.9	1.01×10^{-3}	2.63×10^{-3}	1.55 ± 0.20	$(3.62 \pm 1.04) \times 10^9$	0.33 ± 0.21
RP 30		8.6	0.63×10^{-3}	1.63×10^{-3}	2.49 ± 0.48	$(2.62 \pm 0.67) \times 10^9$	0.36 ± 0.12
RP 84		7.9	0.57×10^{-3}	1.48×10^{-3}	2.52 ± 0.46	$(1.34 \pm 0.40) \times 10^9$	0.67 ± 0.44
RP 81	816	11.1	0.85×10^{-3}	2.20×10^{-3}	1.51 ± 0.28	$(3.94 \pm 1.74) \times 10^9$	0.60 ± 0.22
RP 80		7.3	0.56×10^{-3}	1.45×10^{-3}	2.32 ± 0.57	$(2.54 \pm 1.18) \times 10^9$	0.92 ± 0.57

[a] True Stress $\sigma_T = \sigma_a (1 + e)$ where σ_a is the applied stress and e is calculated from the cross section of the foil for TEM.

[b] The error band indicates the 95 percent confidence level (λ, ρ among the plates and θ among the measurements).

[c] The dislocation density is determined by counting free dislocations which are not associated with subgrain boundaries.

N.O. (Not Observed), N.M. (Not Measured).

TABLE 7.2

SUBSTRUCTURE DATA OF AISI 304 STAINLESS STEEL (REFERENCE HEAT 9T2796) IN TENSION

Specimen Number	Test Temperature °C	True Stress[a] σ_T $kg \cdot mm^{-2}$	Modulus Compensated True Stress $\sigma_{T/E}$	$\sigma_{T/G}$	Average Cell or Subgrain Intercept λ, μm	Average Dislocation Density[c] ρ cm^{-2}	Subgrain or Cell Misorientation θ Degree
RP 14	538	53.8	3.36×10^{-3}	8.67×10^{-3}	0.41 ± 0.08[b]	N.M.	N.M.
RP 201		49.6	3.10×10^{-3}	8.00×10^{-3}	0.28 ± 0.02	N.M.	N.M.
RP 15	593	42.2	2.72×10^{-3}	7.06×10^{-3}	0.50 ± 0.05	N.M.	N.M.
RP 202		46.4	2.98×10^{-3}	7.55×10^{-3}	0.47 ± 0.09	N.M.	N.M.
RP 21	650	26.3	1.77×10^{-3}	4.57×10^{-3}	0.81 ± 0.08	$(12.51 \pm 3.13) \times 10^9$	N.M.
RP 16		33.0	2.21×10^{-3}	5.72×10^{-3}	0.65 ± 0.10	$(14.03 \pm 3.51) \times 10^9$	N.M.
RP 19		38.4	2.58×10^{-3}	6.66×10^{-3}	0.52 ± 0.08	N.M.	N.M.
RP 206		42.4	2.84×10^{-3}	7.36×10^{-3}	0.65 ± 0.22	$(25.91 \pm 6.79) \times 10^9$	N.M.
RP 17	704	25.5	1.77×10^{-3}	4.59×10^{-3}	1.04 ± 0.14	$(9.41 \pm 2.40) \times 10^9$	0.52 ± 0.21
RP 208		38.9	2.70×10^{-3}	6.99×10^{-3}	0.61 ± 0.06	$(25.77 \pm 6.50) \times 10^9$	N.M.
RP 221	760	11.6	0.84×10^{-3}	2.19×10^{-3}	2.17 ± 0.43	$(2.53 \pm 0.64) \times 10^9$	0.49 ± 0.42

[a] True Stress $\sigma_T = \sigma_{UTS}$ (1 + e) where σ_{UTS} is the engineering ultimate tensile strength and e is calculated from the cross section of the foil for TEM.

[b] The error band indicates the 95 percent conficence level (λ, ρ among the plates and θ among the measurements).

[c] The dislocation density is determined by counting free dislocations which are not associated with subgrain boundaries.

N.M. (Not Measured).

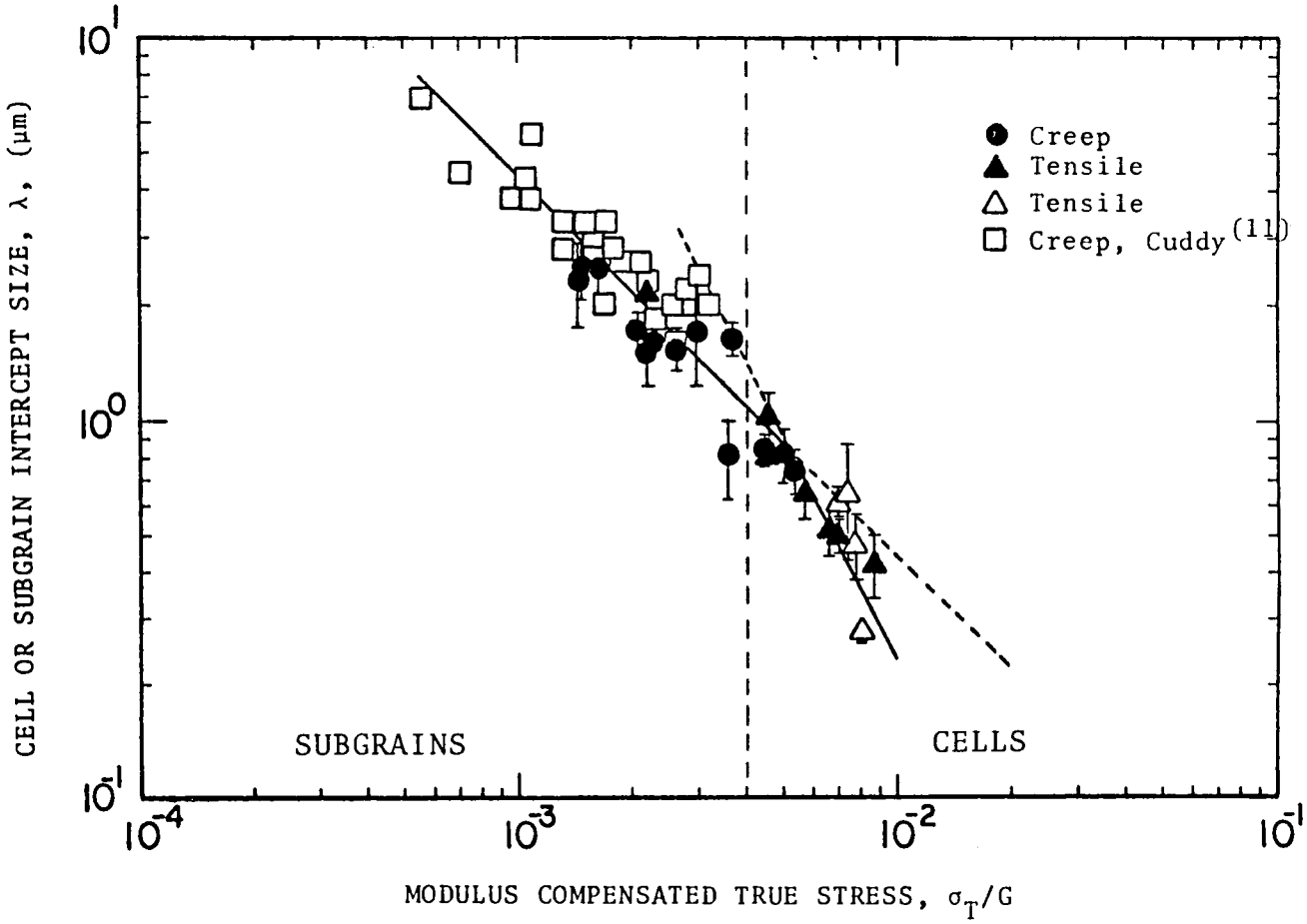

Fig. 7.4 Plot of the Cell of Subgrain Intercept Size, λ, vs. the Modulus Compensated True Stress, σ_T/G on a log-log Scale (AISI 304 SS).

figure. The cell or subgrain size - stress relationships[3] determined for the reference heat 9T2796 seem to provide a very good fit to Cuddy's data. In Fig. 7.5, the modulus compensated true stress, σ_T/G is plotted versus the square root of the dislocation density, $\rho^{0.5}$, on a linear scale. The data can be represented by a straight line confirming the various work hardening theories. The stress - dislocation density relation is given by

$$\sigma_T/G = -\ 6.67 \times 10^{-4} + 1.97\ b\ \rho^{0.5} \qquad [7.1]$$

The constant and the slope were determined by a least square analysis of the data. The misorientation angle across the subgrain boundaries, θ, is plotted versus the cell or subgrain intercept size, λ, in Fig. 7.6. The misorientation angle seems to be independent of the subgrain size.

7.1.2.2 Characterization of the Dislocation Substructure in Creep Mode of AISI 304 Stainless Steel, UC Heat G8607 (R. K. Bhargava)

A set of creep tests were conducted at 704°C and the dislocation substructure evaluation by the transmission electron microscopy was started[6]. The dislocation substructure developed during a set of creep tests at 17.58 $kg \cdot mm^{-2}$ (25,000 psi) which were interrupted at the various stages of the creep curve was reported previously[3]. In Fig. 7.7 the typical subgrains developed during creep tests at 704°C are shown. The subgrain size is shown to be a

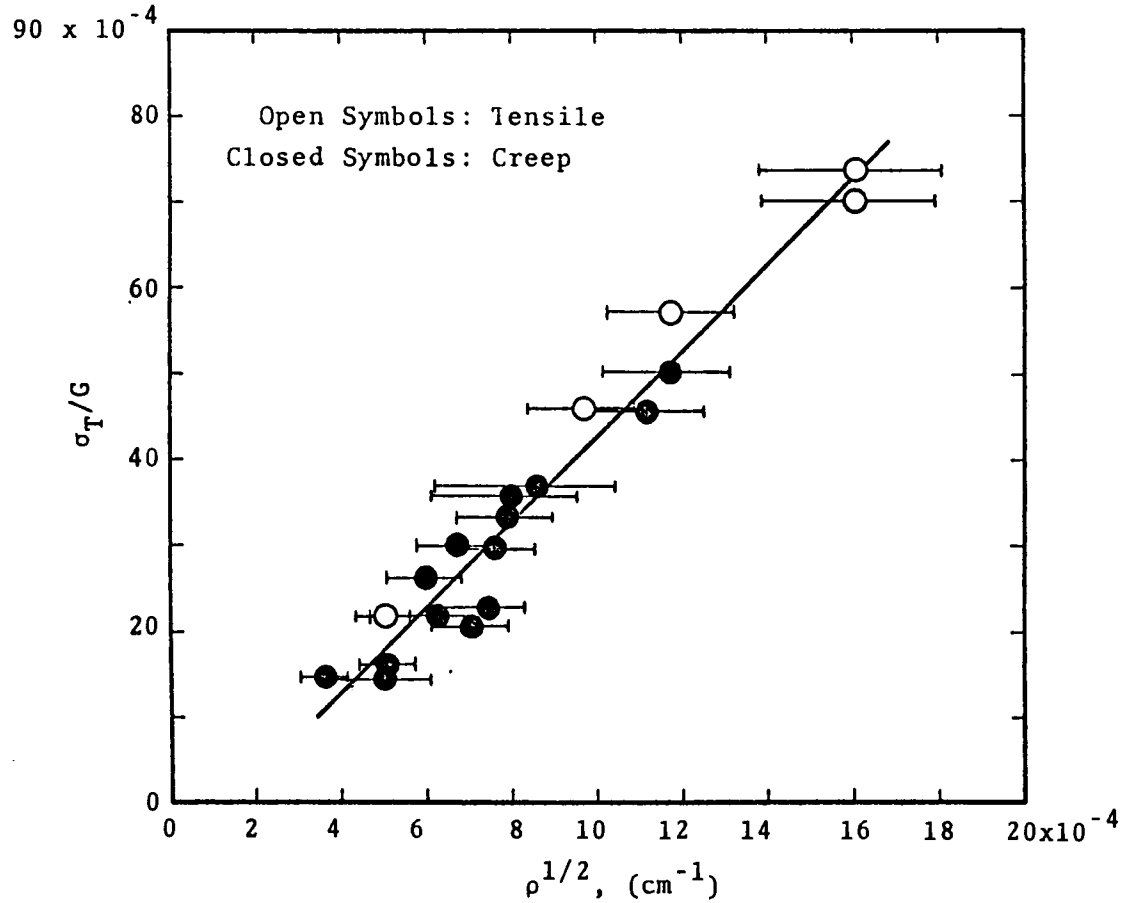

Fig. 7.5 Plot of the Modulus Compensated True Stress, σ_T/G, vs. the Square Root of the Dislocation Density, $\rho^{1/2}$, AISI 304 SS, (Reference Heat 9T2796).

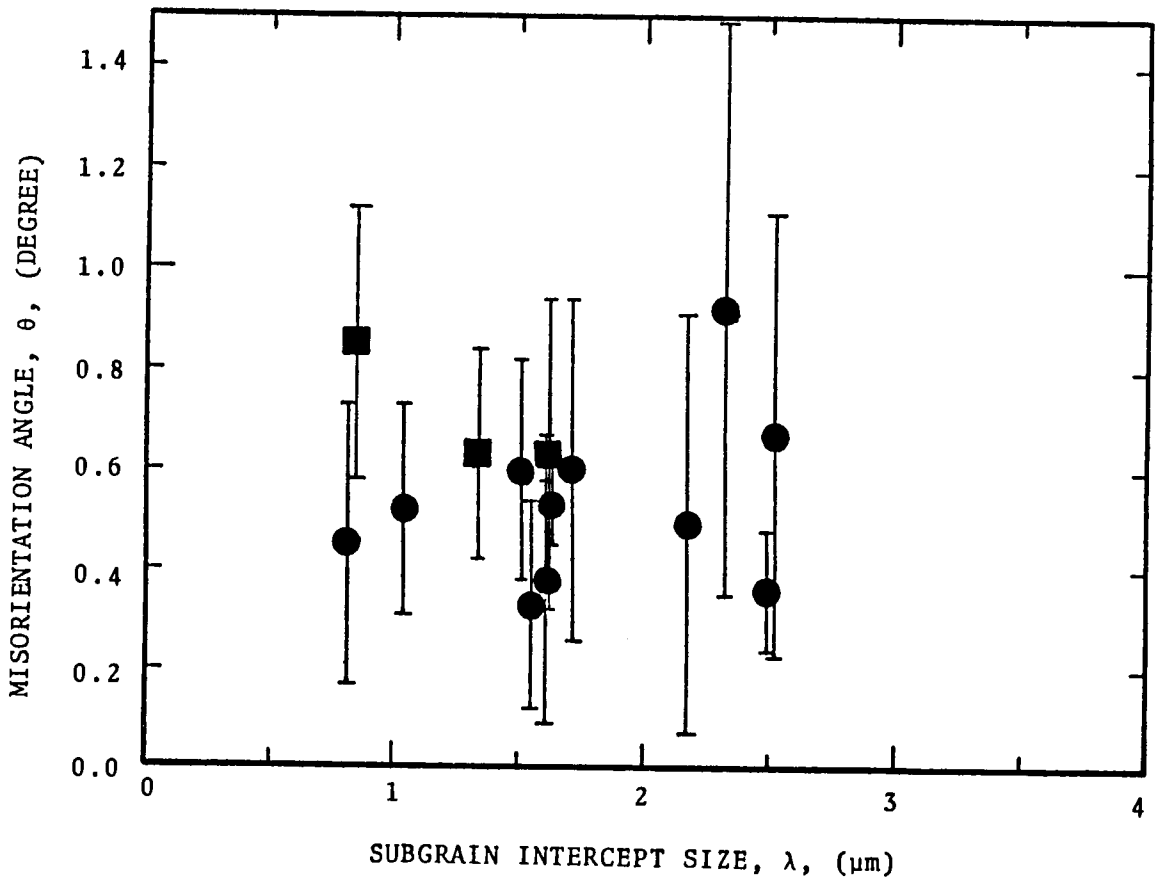

Fig. 7.6 Plot of the Misorientation Angle, θ, vs. the Subgrain Intercept Size, λ (AISI 304 SS).

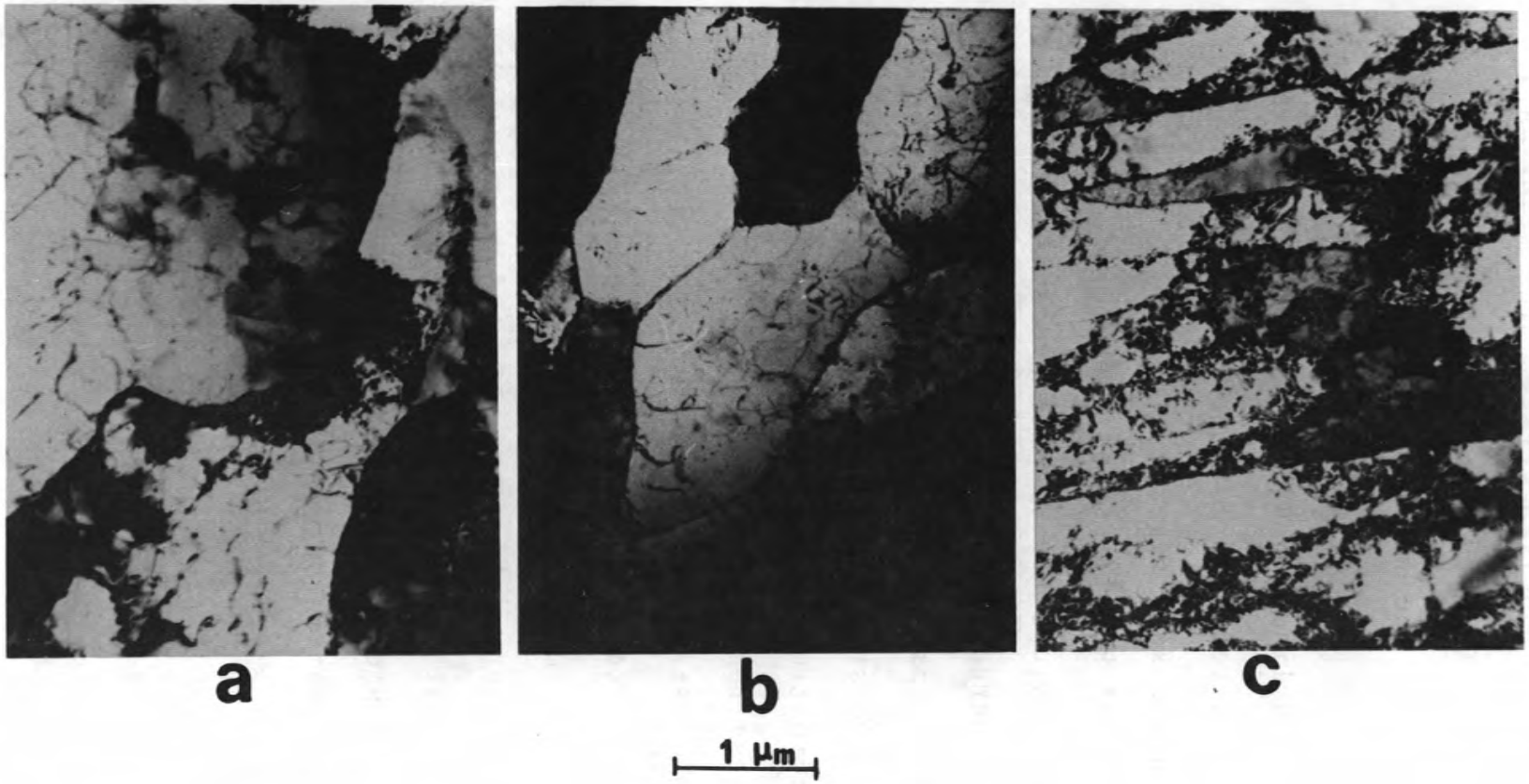

Fig. 7.7 Typical Subgrain Substructure Developed in AISI 304 SS, (Heat G8607) in Creep at 704°C (a) 10.55 $kg \cdot mm^{-2}$, (b) 14.06 $kg \cdot mm^{-2}$, (c) 21.09 $kg \cdot mm^{-2}$.

strong function of the applied stress. The misorientation angle, θ, determined from the specimens has also been plotted in Fig. 7.6. The modulus compensated true stress, σ_T/G, is plotted versus the square root of the dislocation density, $\rho^{0.5}$, on a linear scale in Fig. 7.8. For comparison, the relation determined for the reference heat 9T2796 is also shown in the same figure.

7.1.2.3 Analysis of Relationships of Deformation Rate, Stress and Temperature for 304 Stainless Steel (R. K. Bhargava)

The relationships of deformation rate, stress and temperatute for 304 stainless steel are being analyzed in light of the microstructure and the results will be reported in future progress reports.

7.1.2.4 Change in Stress Experiments on 304 Stainless Steel, Reference Heat 9T2796 (R. K. Bhargava)

A set of stress change creep tests were performed at 650°C and some of the results were reported previously[3]. The substructure that is developed during these conditions is being evaluated and the results will be shortly reported. A preliminary observation suggests that the subgrains or cells remain the same after the stress reductions only for a short period at 650°C.

7.1.2.5 Substructure Development During Low Cycle Fatigue of AISI 304 Stainless Steel at 649°C (H. Nahm)

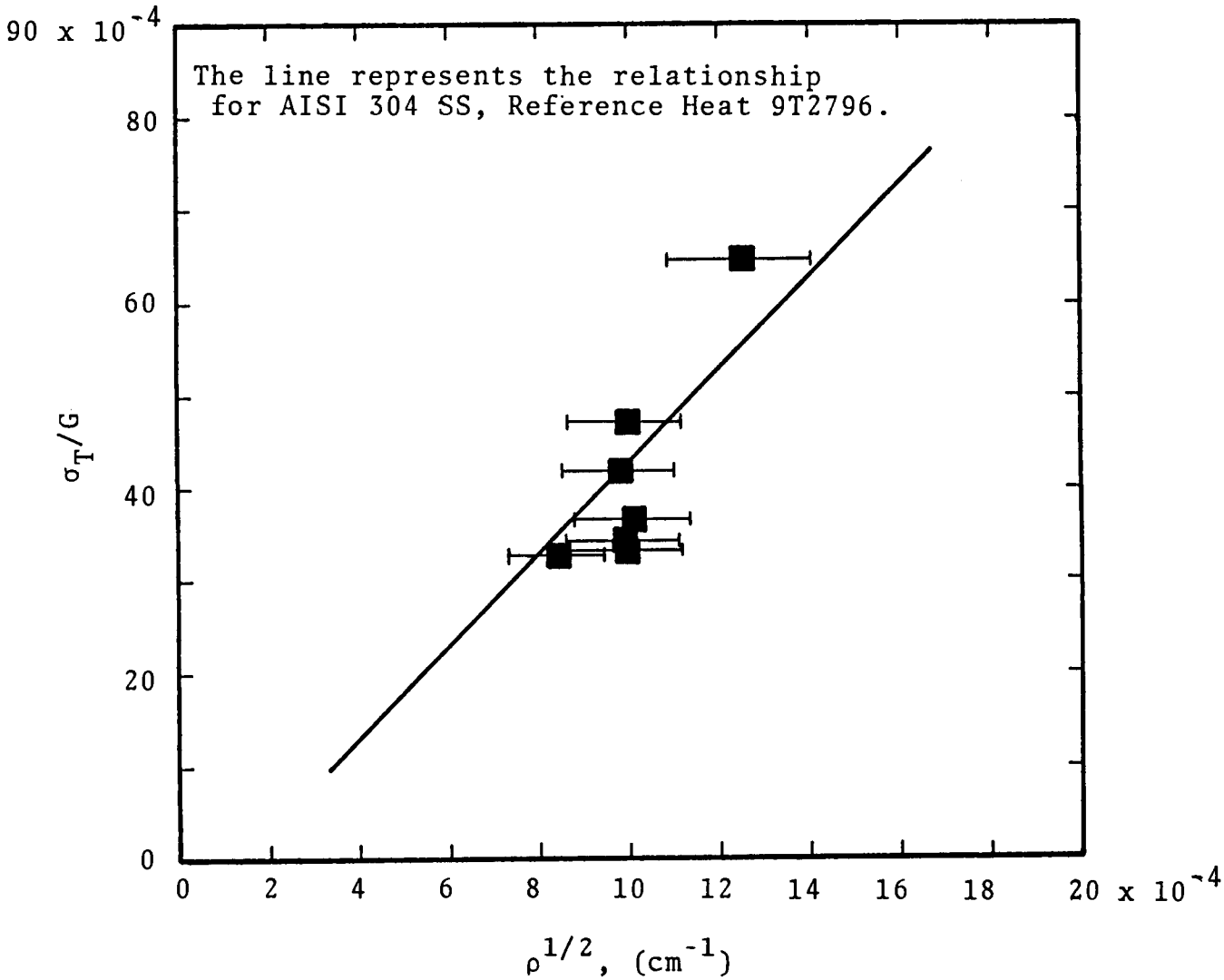

Fig. 7.8 Plot of the Modulus Compensated True Stress, σ_T/G, vs. the Square Root of the Dislocation Density, $\rho^{1/2}$ (AISI 304 SS, Heat G8607).

In an effort to understand the basic principles underlying fatigue, substructure development during fatigue has been investigated by many researchers. However, most investigations have been concerned with fatigue in single crystals at ambient temperatures. It appears that no study is availalbe in the literature on the substructural changes at different stages of fatigue life at elevated temperature where recovery becomes increasingly important. The purpose of the present study is, therefore, to examine the dislocation substructure development in low cycle fatigued AISI type 304 Stainless Steel at 649°C by transmission electron microscopy. Preliminary results were reported in the previous report[6].

A special set of LCF tests were performed at Argonne National Laboratory, Materials Science Division, High Temperature LCF Laboratory under the provisions of a "Thesis Parts Program". The tested specimens of AISI 304 stainless steel (9T2796) were solution treated at 1092°C for half an hour and aged for 1,000 hours at 593°C.

The hour glass type specimens have been tested to different fractions of the fatigue life under the identical testing conditions of temperature (649°C), total strain range (2%) and cyclic strain rate (4×10^{-3} sec^{-1}). The number of cycles at the termination of the respective fatigue tests and their test details are given in Table 7.3. All tests were initiated in the compression cycle and ter-

TABLE 7.3

LOW CYCLE FATIGUE DATA FOR AISI 304 STAINLESS STEEL (9T2796)

TESTED IN AIR AT 649°C - SUBSTRUCTURAL DEVELOPMENT EVALUATIONS

ANL Test Number	Specimen Number	Number of Cycles at Interruption[b] N, Cycles	Fraction of Fatigue Life N/N_f, Percent	Total Strain Range $\Delta\varepsilon t$, Pct.	Plastic Strain Range at Interruption[c] $\Delta\varepsilon p$, Pct.	Elastic Strain Range at Interruption[c] $\Delta\varepsilon p$, Pct.	Stress Response at Interruption[c] σ, psi	σ, MPa
719	T344	1/4	0.04	1.99	1.82	0.17	-17,740	-122.31
717	T343	3/4	0.10	1.99	1.81	0.18	18,830	129.83
713	T339	2 3/4	0.38	1.99	1.70	0.29	30,910	213.12
711	T338	6 3/4	0.94	1.99	1.63	0.36	38,310	264.14
720	T347	80	11.08	2.00	1.61	0.39	41,320	284.89
725	T351	361	50.00	1.97	1.57	0.40	42,060	289.99
709[a]	T337	722	100.00	1.98	1.58	0.40	42,010	289.65

[a] This specimen was tested till failure.

[b] All tests were initiated in the compression mode and interrupted at the peak of tension cycling with the exception of the 1/4 cycle case which was terminated at the end of compressive cycling.

[c] $\Delta\varepsilon p$, $\Delta\varepsilon e$, and σ were determined from the last half cycle where interruption was made except for the case of the specimen T337 where $\Delta\varepsilon p$, $\Delta\varepsilon e$, and σ were taken at one half of the fatigue life. Strain rate $\Delta\varepsilon_t = 4 \times 10^{-3}$ sec^{-1} for all tests.

minated at the peak of tension cycle, with the exception of 1/4 cycle case which was terminated at the peak of compression cycle. Right after the termination of testing, the induction furnace was shut off so that the substructure was preserved. Specimen cooling rate on completion of each test is estimated to be greater than about 90°C per minute from 649°C to about 100°C.

A plot of stress range, $\Delta\sigma$, versus the number of cycles, N, for AISI 304 stainless steel is presented in Fig. 7.9. Several remarks can be made from this figure. Excellent reproducibility of hardening behavior, under identical experimental conditions, is obtained especially at the saturation stage. The difference at the initial stages of hardening is believed to be due to the difference in the initial microstructures that results from the ageing treatment. But the difference decreases as cycling continues so the saturation stresses for each specimen are almost identical. This indicates that the so called "planar slip" materials[7] (low stacking fault energy) such as AISI 304 stainless steel produce "wavy slip" when fatigued at high temperatures.

The rapid hardening stage is finished in around 30 cycles followed by the saturation state where the flow stress remains constant until fatigue failure sets in. Test parameters and fatigue properties are presented in Table 7.3.

The characteristics of the fatigue substructure develop-

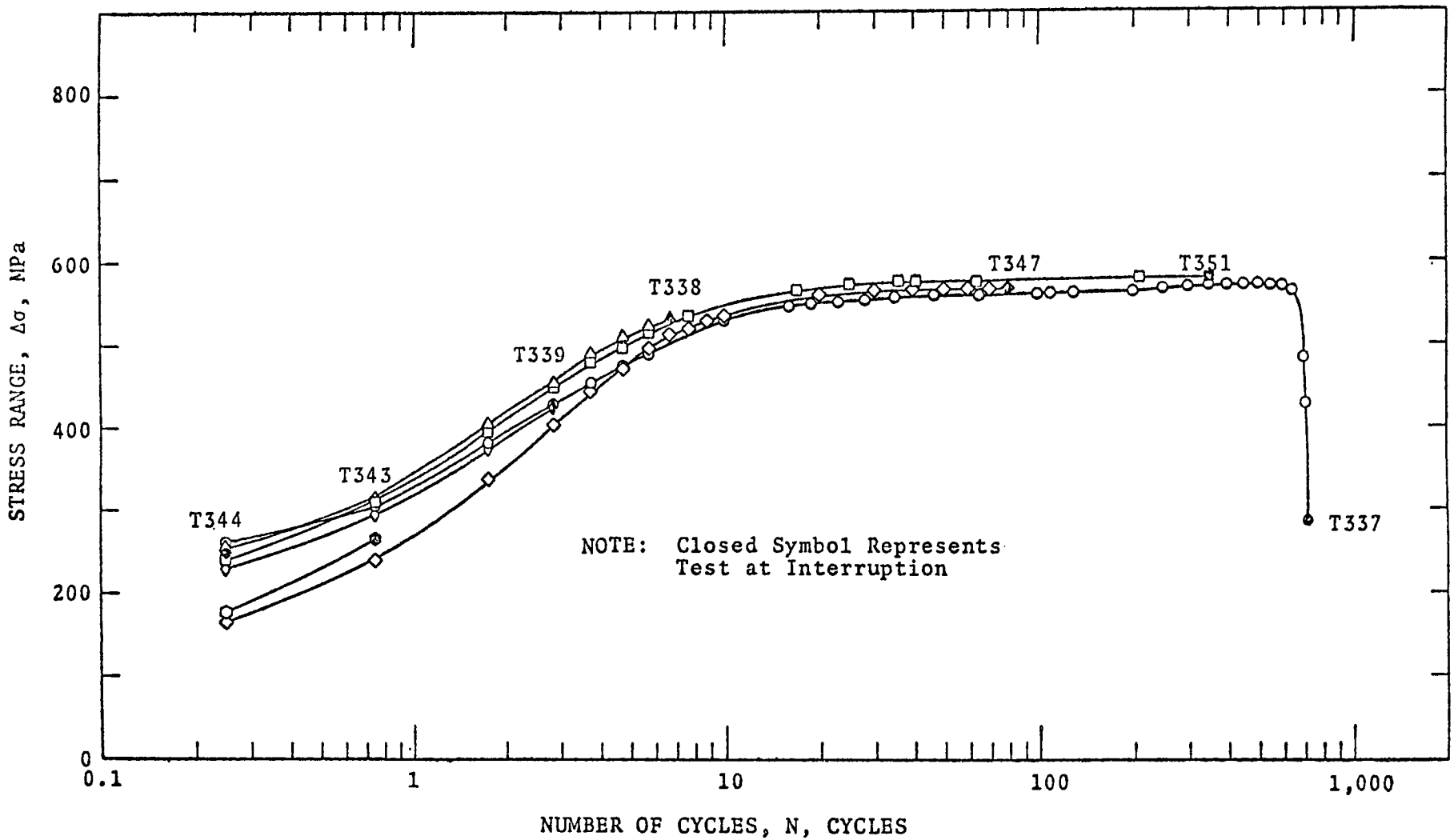

Fig. 7.9 Plot of the Total Stress Range, Δσ, Versus the Number of Cycles, N, for AISI 304 Stainless Steel at 649°C.

ment for AISI 304 stainless steel specimens employed in this study are summarized with a series of micrographs as shown in Fig. 7.10. Each column of micrographs show the variation in substructure that can occur within a given specimen after the indicated number of cycles. It is apparent that the cell intercept size, λ, decreases until the saturation state is reached and the misorientation angle, θ, between adjacent cells and the volume fraction occupied by cells increase throughout the fatigue life.

Cell intercept size, λ, as a function of fatigue life, N/N_f is plotted in Fig. 7.11. The shear modulus compensated cyclic stress amplitude, σ/G, is plotted in Fig. 7.12 as a function of the corrected reciprocal of cell intercept size, b/λ, where b is the Burgers vector taken to be 2.54×10^{-8} cm. An equation of the type

$$\sigma/G = A\ (b/\lambda)^n \qquad [7.2]$$

is obtained, which indicates that the cell size decreases with increasing stress.

A plot of average misorientation angles between adjacent cells, θ, against fractions of fatigue life, N/N_f, is provided in Fig. 7.13, showing that the present result of the misorientation increases throughout fatigue life.

As shown in Fig. 7.10 the early hardening stage is attained through the continuous accumulation of dislocations in the form of dipoles, multipoles, and loops that form

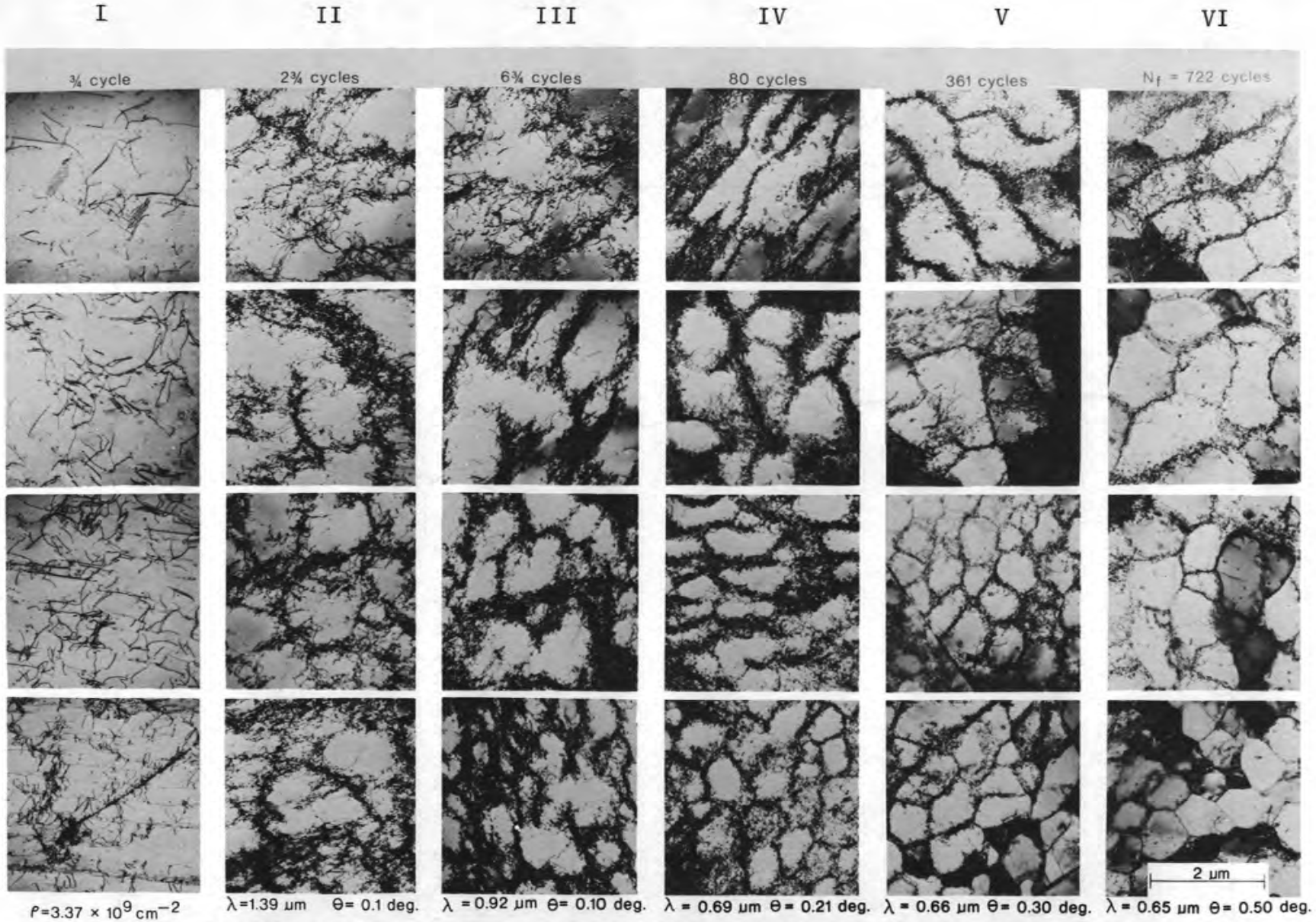

Fig. 7.10 Low Cycle Fatigue Substructure Development in AISI 304 Stainless Steel at 649°C.

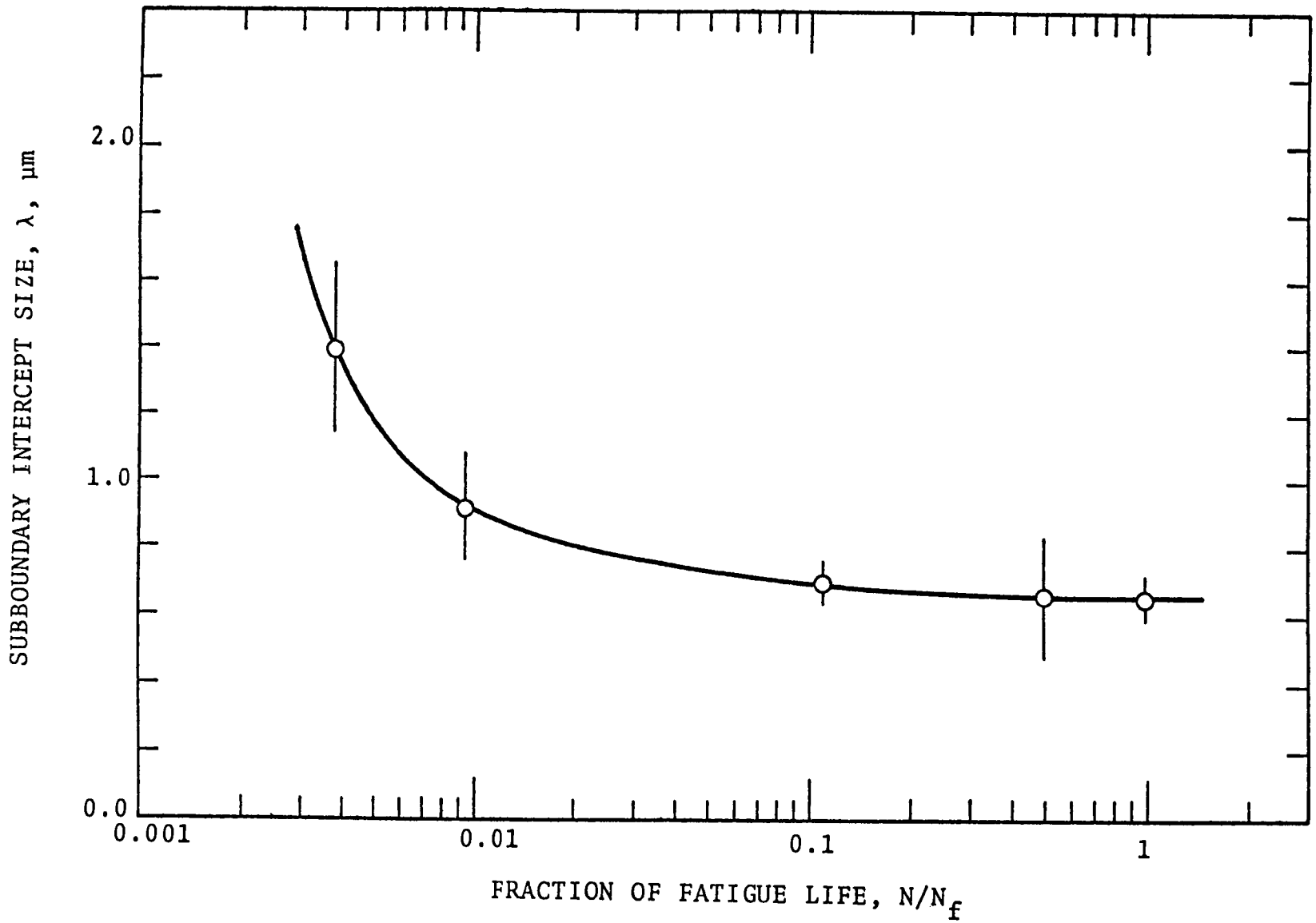

Fig. 7.11 Plot of the Subboundary Intercept Size, λ, Versus the Fraction of Fatigue Life, N/N_f for AISI 304 Stainless Steel at 649°C.

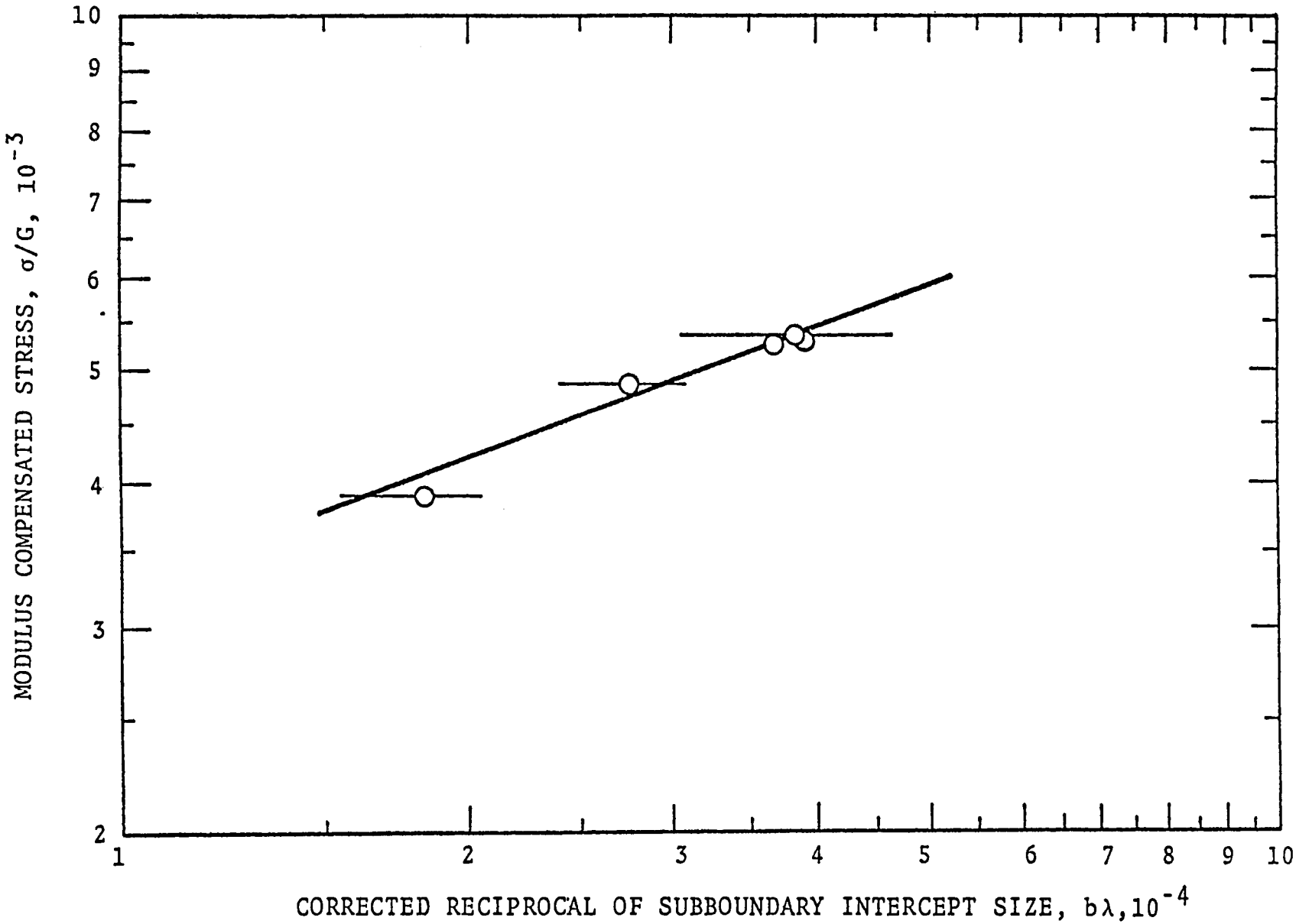

Fig. 7.12 The Shear Modulus Compensated Cyclic Stress Amplitude, σ/G, as a Function of the Corrected Reciprocal of the Subboundary Intercept Size, b/λ, for AISI 304 Stainless Steel at 649°C.

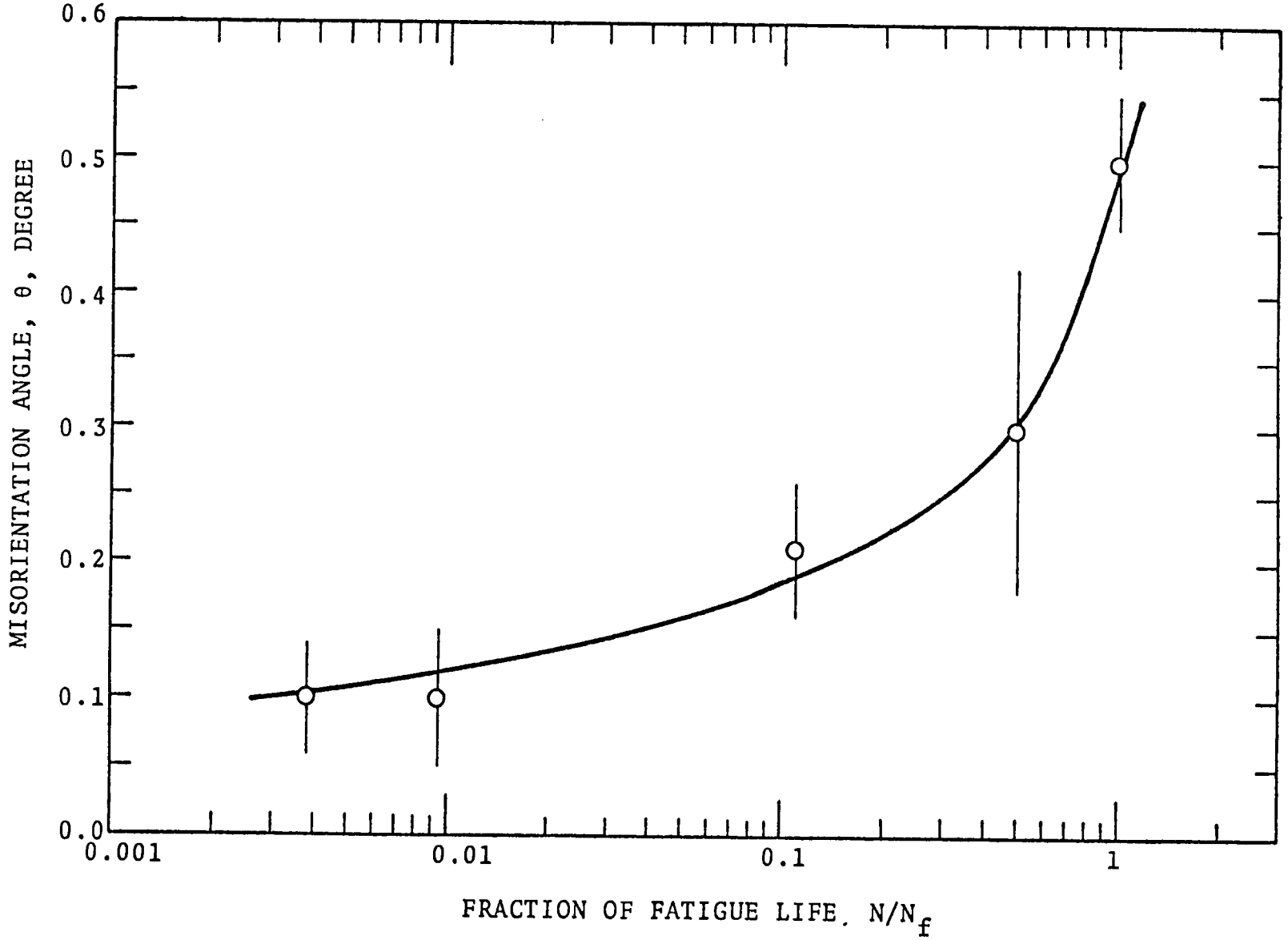

Fig. 7.13 Plot of the Misorientation Angles Between Adjacent Cells, θ, Against the Fraction of Fatigue Life, N/N_f, for AISI 304 Stainless Steel at 649°C.

uncondensed cell walls. The decrease in cell size until the saturation state is another way of dislocation storage contributing to the hardening. During the saturation state, most of the flow stress is gained from either the stress for dislocations to move through the long range stress field set up by subboundaries or the stress needed to bow out dislocations between the dislocation network of subboundary. It is evident that recovery is occurring during the entire fatigue process. This is manifested by the observation that the misorientation angles increase and the uncondensed thick cell walls continuously refine themselves throughout the entire fatigue life.

The dislocation density of cell boundaries, ρ_{SB} was estimated to be 9.4×10^9 cm^{-2} by substituting the experimental values (θ = 0.5 deg., λ' = 0.65 x 1.68 μm). Thus, the saturation stress was calculated to be approximately 210 MPa from the equation

$$\tau_s = Gb/\alpha\, \ell_{SB} \qquad [7.3]$$

where G is the shear modulus

b is the Burgers vector

α is a constant

and ℓ_{SB} is the mesh length of the dislocation network in the subboundary, by using the value of α = 2.

The calculated value is compatible with the observed applied saturation stress of ∿ 290 MPa (G = 7.9×10^6 psi and b =

2.54×10^{-8} cm for AISI 304 stainless steel was used).

It is in order at this point to discuss what mechanisms account for the cyclic strain in fatigue, especially in saturation state. If we assume that "cell shuttling" model[8-10] is operating, a relationship

$$\gamma = \rho b \lambda' \qquad [7.4]$$

should be true, where γ is the shear strain range, b is the Burgers vector, and λ' is the subgrain diameter. Substitution of the present results for AISI 304 stainless steel into equation [7.4] indicates that around 50 shuttling dislocations per cell are needed to accomodate the strain range for each cycle during saturation stage. This is contradictory to the observation that the region inside the subgrain is almost free from dislocations. Therefore, the cell shuttling model does not appear to adequately explain the straining during saturation stage of fatigue. Feltner[11] proposes a similar model in which the "flip-flop" motion of dislocation loops yield the same result as in the case of the cell shuttling model.

Therefore, the preceeding discussions lead to another mechanism - movement of subboundary walls during deformation. Cell walls can bulge out under complex cooperative stress system as suggested by Li[12]. Or cell walls can annihilate each other and/or glide under the proper conditions as proposed by Ashby[13].

It is also possible that the annihilation of dislocations by recovery near or in the subboundary walls may be partly responsible for the cyclic strain, especially in the early hardening stage. The observed transition for cell walls from the thick, uncondensed to condensed, sharp and narrow walls along with the continuous increase in the misorientation angles supports this idea.

7.1.3 References

1. ORNL - 4998, "Mechanical Properties Test Data for Structural Materials", Quarterly Progress Report for Period ending July 31, 1974, pp. 307.

2. ORNL - 5103, "Mechanical Properties Test Data for Structural Materials", Quarterly Progress Report for Period ending October 31, 1974, pp. 325-327.

3. ORNL - 5105, "Mechanical Properties Test Data for Structural Materials", Quarterly Progress Report for Period ending April 30, 1975, pp. 314-321.

4. R. K. Bhargava, Ph.D. Dissertation, University of Cincinnati, 1975.

5. L. J. Cuddy, Met. Trans., Vol. 1, 1970, pp. 395-401.

6. ORNL - 5104, "Mechanical Properties Test Data for Structural Materials", Quarterly Progress Report for Period ending January 31, 1975, pp. 303-309, 320.

7. C. E. Feltner and C. Laird, Acta Met., 15 (1967) 1621.

8. D. F. Watt and R. K. Ham, Nature (London) 211 (1966) 734.

9. S. J. Basinski, Z. S. Basinski and A. Howie, Phil. Mag., 19 (1969) 899.

10. J. R. Hancock and J. C. Grosskreutz, Acta. Met., 17 (1969) 77.

11. C. E. Feltner, Phil. Mag., 12 (1965) 1229.

12. J. C. M. Li, "Electron Microscopy and Strength of Crystals", Edited by G. Thomas, et. al., Interscience, New York (-963) 713.

13. M. F. Ashby and R. A. Verrall, Acta Met., 21 (1973) 149.

7.2 UNIVERSITY OF CALIFORNIA, LOS ANGELES — K. Ono, A. J. Ardell, and A. S. Tetelman

7.2.1 Microstructure and High Temperature Deformation of Cr-Mo Steels for LMFBR Heat Exchanger (S. Y. Hsu and K. Ono)

(1-4)

Creep deformation study of Cr-Mo steels for LMFBR applications has been continued during this report period. Creep rate of low carbon alloy (Alloy M) was determined in step loading tests and conditions of the presence/absence of a strain burst during a stress change was examined as a function of heat treatment and the time interval of stress changes.

Additional creep tests of alloy M in the normalized and tempered condition (1700/1300°F) have been performed. The chemical composition of alloy M is given in Table I. Beside a lower carbon content, the analysis varies little from that of alloy I reported previously.[2] The nitrogen content, although not analyzed yet, is expected to be two to three times lower in alloy M than in alloy I, because of the differences in processing history. In the N & T condition, the creep rate-stress relation of alloy M in the temperature range of 850 to 1000°F, was determined (Fig. 1) and found to be quite similar to that of alloy I reported previously.[3] Creep rate at a given stress level was slightly lower in alloy M tested at 1050°F in comparison to the data of alloy I, corresponding to a difference of creep stress of several ksi.

TABLE I Chemical Analysis of Steels (wt.%)

Material	Cr	Mo	Mn	Ni	Si	Cu	C	S	P
Cr-Mo	2.48	0.99	0.45	0.21	0.19	0.05	0.021	0.021	0.019
304	17.40	0.68	0.88	9.60	0.40	0.43	0.051	0.029	0.028
304L	18.45	0.19	1.67	9.00	0.60	---	< 0.01	0.025	0.017
316	17.30	2.34	1.72	13.55	0.44	---	0.059	0.009	0.016

In contrast to the similarity in the creep-rate stress relations, alloy M showed a much less tendency of strain burst than in alloy I. An example is given in Table II, where the initial creep stress σ_i, stress increment $\Delta\sigma$ and the amount of strain burst $\Delta\epsilon$ are shown for comparable creep tests at 850°F. In alloy I, $\Delta\epsilon$ of a few tenths percent strain was common and $\Delta\epsilon$ reached as high as 2%. In alloy M, on the other hand, $\Delta\epsilon$ was typically below 0.03% and the maximum $\Delta\epsilon$ was 0.6%. At higher test temperatures, $\Delta\epsilon$ for alloy M was typically 0.02% and was no more than 0.08%. Additional tempering of the N & T material suppressed strain burst in alloy M, as has been the case for alloys L and I.[2] When alloy M in the N & T condition was tempered at 1030°F for seven days, $\Delta\epsilon$ at 850°F and 950°F was always less than 0.05% for comparable stress increments. Thus, it appears that a low carbon content alone cannot produce strain burst during a stepwise stress increase. Higher test temperatures and additional tempering tend to eliminate strain burst in the N & T materials.

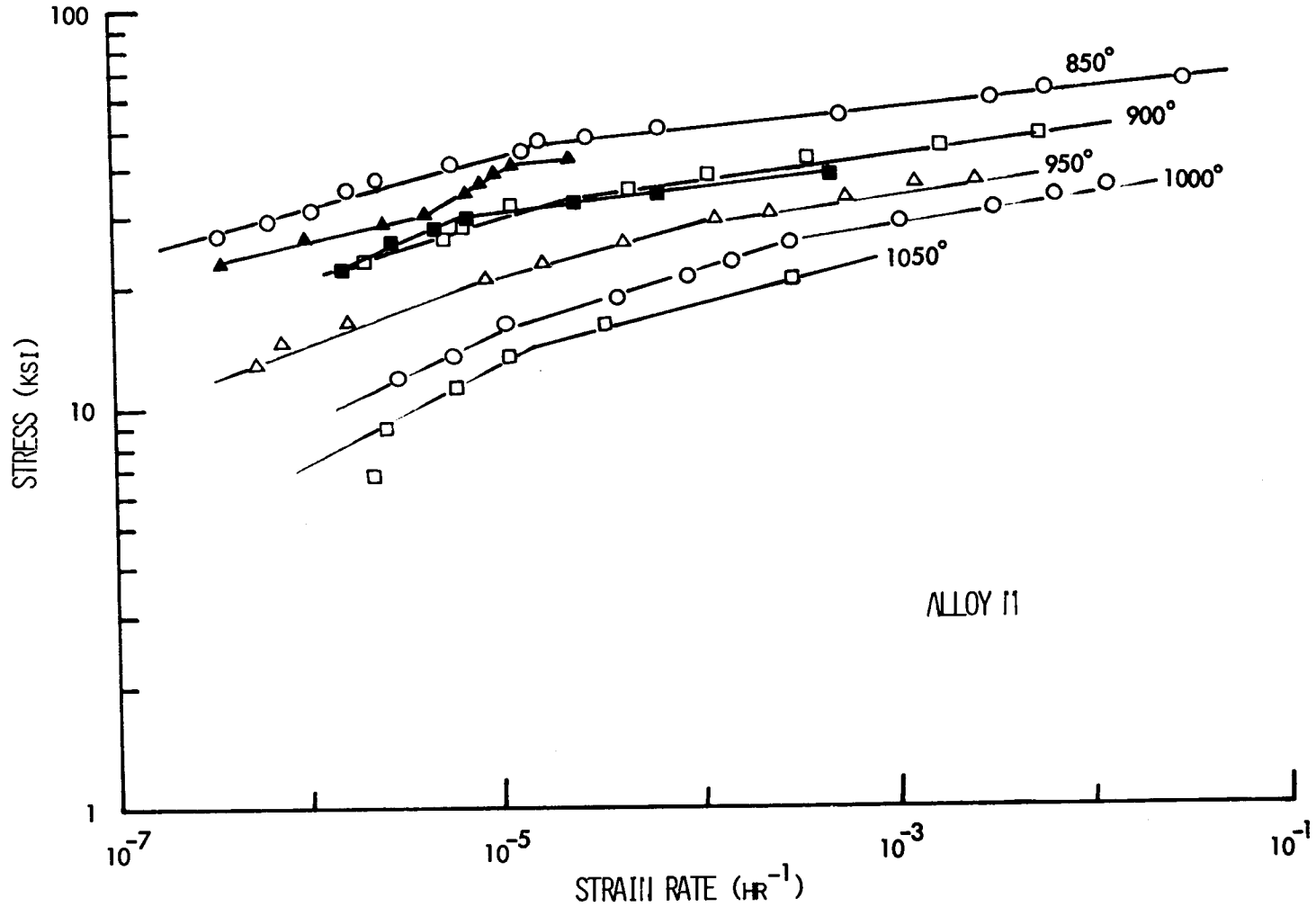

FIG. 1 Creep stress vs. strain rate for alloy M, N & T condition. Test temperatures given in °F

TABLE II Strain Burst in Alloys M and I

Alloy M tested at 850°F			Alloy I tested at 850°F		
σ_i(ksi)	$\Delta\sigma$(ksi)	$\Delta\epsilon$ (%)	σ_i(ksi)	$\Delta\sigma$(ksi)	$\Delta\epsilon$ (%)
29.5	1.40	0.007	29.5	2.4	0.355
30.9	3.0	0.027	31.9	2.1	0.067
34.9	2.7	0.017	34.0	2.4	0.418
37.5	2.7	0.06	36.4	2.1	0.013
40.2	2.4	0.022	38.5	2.2	0.046
42.6	3.5	0.59	40.7	2.3	0.27
49.2	3.9	0.244	46.0	2.2	0.071
53.1	4.5	0.037	48.2	3.4	2.06
			51.6	2.5	0.276

7.2.2 Creep Studies in Stainless Steels
(O. Ajaja and A. J. Ardell)

A series of creep tests have been run on Type 316SS tensile specimens. Testing was done using the six-arm constant stress apparatus which was described in a previous progress report.[1] For each run, six specimens prestrained 0, 2, 4, 6, 8 and 10% were tested concurrently in the same furnace. In all cases, the prior cold work was introduced by prestraining on the Instron tensile machine at room temperature. The furnace temperature was controlled such that temperature fluctuations were limited to within ± 2°F.

A typical set of creep curves plotted from our test data is shown in Fig. 2 for specimens tested at 1300°F and 25,000 psi. The test was discontinued during the steady state creep to enable us to concentrate more on the analysis of primary creep data. However, most of the other tests had continued to rupture. A curve-fitting computer program was run to fit our data into the Garofalo creep equation[2]

$$\epsilon = \epsilon_0 + \dot{\epsilon}_s t + \epsilon_t[1 - e^{-rt}] \qquad (1)$$

where

ϵ = total instantaneous creep strain

ϵ_0 = instantaneous loading strain

$\dot{\epsilon}_s$ = steady state creep rate

ϵ_t = total transient creep strain

r = rate of exhaustion of transient creep

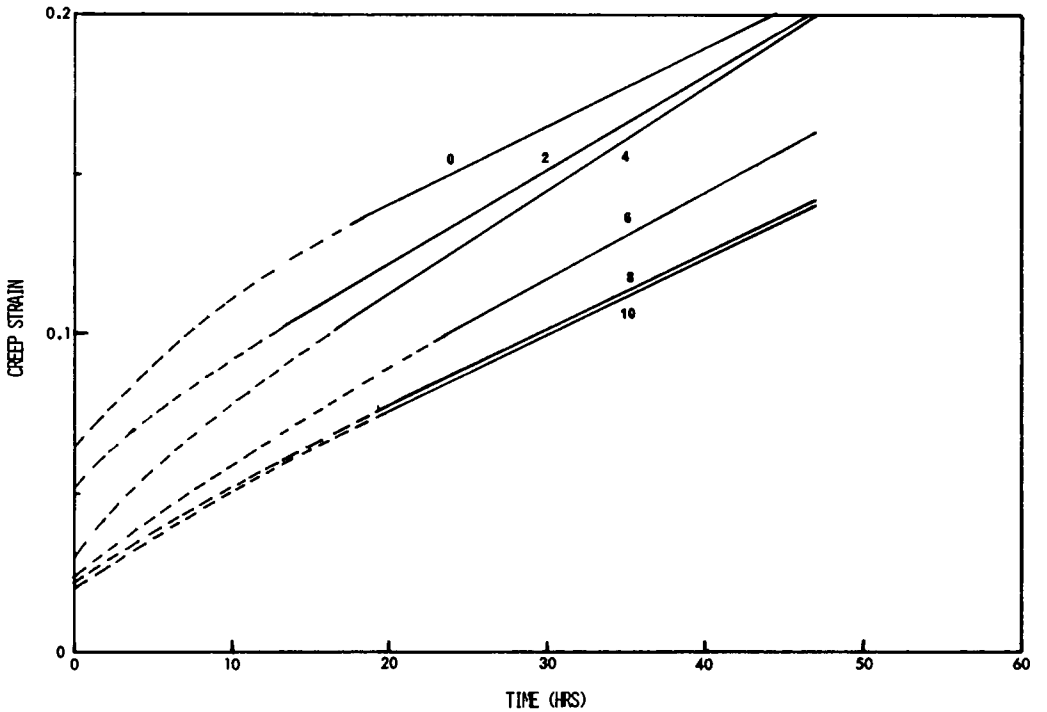

Figure 2 Creep curves for specimens tested at 1300°F and 25,000 psi. Test was discontinued after 47 hours. Broken lines represent the PRIMARY creep state. The number next to each plot shows the amount of prior cold work level.

In all cases where transient creep was exhibited, we obtained excellent agreement between our data and Eq. (1). Table III show the various creep parameters as analyzed for each test.

7.2.2.1 Rupture Life, t_R

Although Table IIIa-f shows that the rupture life varies with initial cold work level, this variation has not been consistent. In this cold work range (0-10%), the observed variation is probably experimental scatter and in general, the rupture life is not strongly dependent on the initial prestraining.

7.2.2.2 Steady State Creep Rate, $\dot{\varepsilon}_s$

In Fig. 2 we observe that all the six creep curves run nearly parallel inthe steady state creep stage. This indicates, as previously observed,[2] that the secondary creep rate, $\dot{\epsilon}_s$ does not vary appreciably in the cold work range of interest. Values of $\dot{\epsilon}_s$ are also indicated in Table III for the different test conditions.

7.2.2.3 Primary Creep

The greatest effect of initial cold work is observed in the primary creep stage which consists of the loading strain, ϵ_0 and the transient creep strain, ϵ_t. The loading strain decreases as the initial cold work level increases. Beyond 4% cold work, the

Table III Creep Data of 316 Stainless Steel

a) Tested at 1200°F, 35 ksi

Cold Work (%)	t_R (hrs.)	ϵ_R	ϵ_o	ϵ_t	$\dot{\epsilon}_s$ ($\times 10^{-3}$)	r
0	174.7	0.370	0.090	0.017	1.41	0.104
2	182.5	0.300	0.078	0.011	1.13	0.142
4	186.5	0.323	0.048	0.033	1.22	0.037
6	174.1	0.294	0.039	0.015	1.24	0.037
8*	--	--	---	---	---	---
10	192.5	0.280	0.029	0.004	1.24	--

*Alignment problem-test data discarded

b) Aged for 25 hrs. at 1200°F and tested at 1200°F, 30 ksi

Cold Work (%)	t_R (hrs.)	ϵ_R	ϵ_o	ϵ_t	$\dot{\epsilon}_s$ ($\times 10^{-3}$)
0	320.1	0.293	0.063	0.012	0.425
2	520.8	0.250	0.046	0.03	0.398
4	387.1	0.218	0.031	0	0.420
6	474.0	0.197	0.038	0	0.411
8	458.9	0.210	0.026	0	0.310
10	348.0	0.186	0.022	0	0.280

t_R = rupture time in hours

ϵ_R = true rupture strain

All other parameters are as defined in the text

c) Aged for 75 hrs. at 1300°F and tested at 1300°F/30 ksi

Cold Work (%)	t_R (hrs.)	ϵ_R	ϵ_o	ϵ_t	$\dot{\epsilon}_s$ (x 10^{-3})	r
0	35.5	0.451	0.057	0.045	9.45	0.304
2	53.4	0.488	0.048	0.052	6.65	0.208
4	38.8	0.424	0.033	0.045	8.05	0.292
6	32.1	0.369	0.027	0.044	8.35	0.282
8*	--	--	--	--	--	--
10	27.0	0.321	0.021	0.032	7.70	0.212

*Alignment problem-test data discarded

d) Tested at 1300°F/25 ksi

Cold Work (%)	*t_R	*ϵ_R	ϵ_o	ϵ_t	$\dot{\epsilon}_s$ (x 10^{-3})	r
0	--	--	0.0641	0.0273	2.45	0.146
2	--	--	0.0515	0.0110	2.95	0.300
4	--	--	0.0290	0.0180	3.23	0.226
6	--	--	0.0244	0.0121	2.70	0.089
8	--	--	0.0226	0.0074	2.38	--
10	--	--	0.0200	0.0072	2.39	--

*Test discontinued after 47 hrs.

**Transient creep strain, ϵ_t is vanishingly small for 8% and 10% cold work

f) Aged for approximately 2 hrs. at 1400°F and tested at 1400°F/20 ksi

Cold Work (%)	t_R (hrs.)	ϵ_R	ϵ_o	ϵ_t	ϵ_s (x 10^{-3})	r
0	39.8	0.411	0.012	0.081	7.90	0.176
2	32.9	0.388	0.017	0.053	8.60	0.236
4	18.0	0.283	0.003	0.052	11.40	0.274
6	37.0	0.350	0.005	0.047	7.50	0.206
8	43.0	0.315	0.001	0.028	6.00	0.380
10	43.4	0.338	0	0.024	6.80	0.228

transient creep strain keeps decreasing with increasing cold work. Between 0 and 4% cold work, there is wide scatter and inconsistency in the variation of ϵ_t. In all cases, it appears that the transient creep can be completely eliminated by imposing higher levels of prestrain. As can be seen from Table III, the transient creep strain increases with increasing test temperature. Table III-b (1200°F, 30,000 psi) shows that transient creep was not observed in specimens with more than 2% cold work. Similarly, the values of ϵ_t observed for specimens tested at 1200°F and 35,000 psi (Table III-a) are generally lower than the corresponding values for tests run at higher temperatures (Tables IIc-f). The variation of r with cold work has not been delineated. This parameter increases with increasing cold work levels up to about 4% and starts decreasing after 6%, apparently going through a broad maximum around 4-6% (Table III).

Most of the scatter observed is probably due to misalignment of some of the six specimen-bearing rods lined up in the same furnace. Secondly, minor elastic deflexions of some parts of the apparatus cause considerable alterations in the cam settings, which consequently introduce errors in the stress levels imposed on the specimens, The creep machine is being slightly modified to take care of these problems. More than sixty tensile specimens have been machined from the 0.25 inch diameter rods of Type 304SS supplied to

us by Atomics International (composition shown in Table I). In the next quarter, we will be performing creep tests mainly on these specimens in order to investigate how the various creep parameters have been influenced by prior cold work.

7.2.3 The Effect of Carbon on the Elevated Temperature Tensile Properties and Fracture Behavior of Type 304L Stainless Steel (P. L. Jones and A. S. Tetelman)

Studies involving the effect of carbon on the elevated temperature mechanical properties and fracture behavior of stainless steel have been extended to Type 304L and the results compared to those obtained using Type 316.[2] Sheet tensile specimens were carburized in a gas reaction furnace using hydrogen and methane. Tensile tests were performed at 760°C (1400°F): yield strength, fracture strength tensile ductility, UTS and fracture mode are compared as a function of volume fraction of carbon case. The model used to describe the fracture behavior of Type 316SS also explains adequately the fracture behavior of Type 304L SS.

A comparison of the chemical compositions of the two steels used in this study is shown in Table I. The Type 316SS (Heat No. 65808) and the Type 304L (Heat No. 67430) were supplied by HEDL and ORNL, respectively. Specimen preparation, mechanical testing, and fractographic procedures have been reported previously.[2,3]

7.2.3.1 Mechanical Properties vs. Volume Fraction of Case

Figs. 3 and 4 graphically compare yield strength, fracture strength, and tensile ductility of the two steels as a function of volume fraction of carbon case. Volume fractions ranged from 0 to 0.628 and 0.654 for Type 316 and Type 304L, respectively. The yield and fracture strength of both steels increase linearly as the volume fraction of carbon case increases. Type 316 generally displays both a higher yield and fracture strength over the entire range of volume fractions considered. Tensile ductility plotted as a function of volume fraction is shown in Fig. 4. The drastic reduction in ductility noted in Type 316SS with increasing volume fraction is also apparent in Type 304L. The only significant difference is at small volume fractions. Type 304L exhibits a significantly larger ductility in the as-normalized condition, but as the volume fraction increases, the ductilities observed for the two steels are essentially the same. This can be explained by considering the lower initial carbon content of the 304L. As the volume fraction increases and cracking of the case becomes the fracture controlling process, as opposed to subsequent normal fracture of the core, the two steels both fail in a brittle manner at relatively low values of tensile ductility.

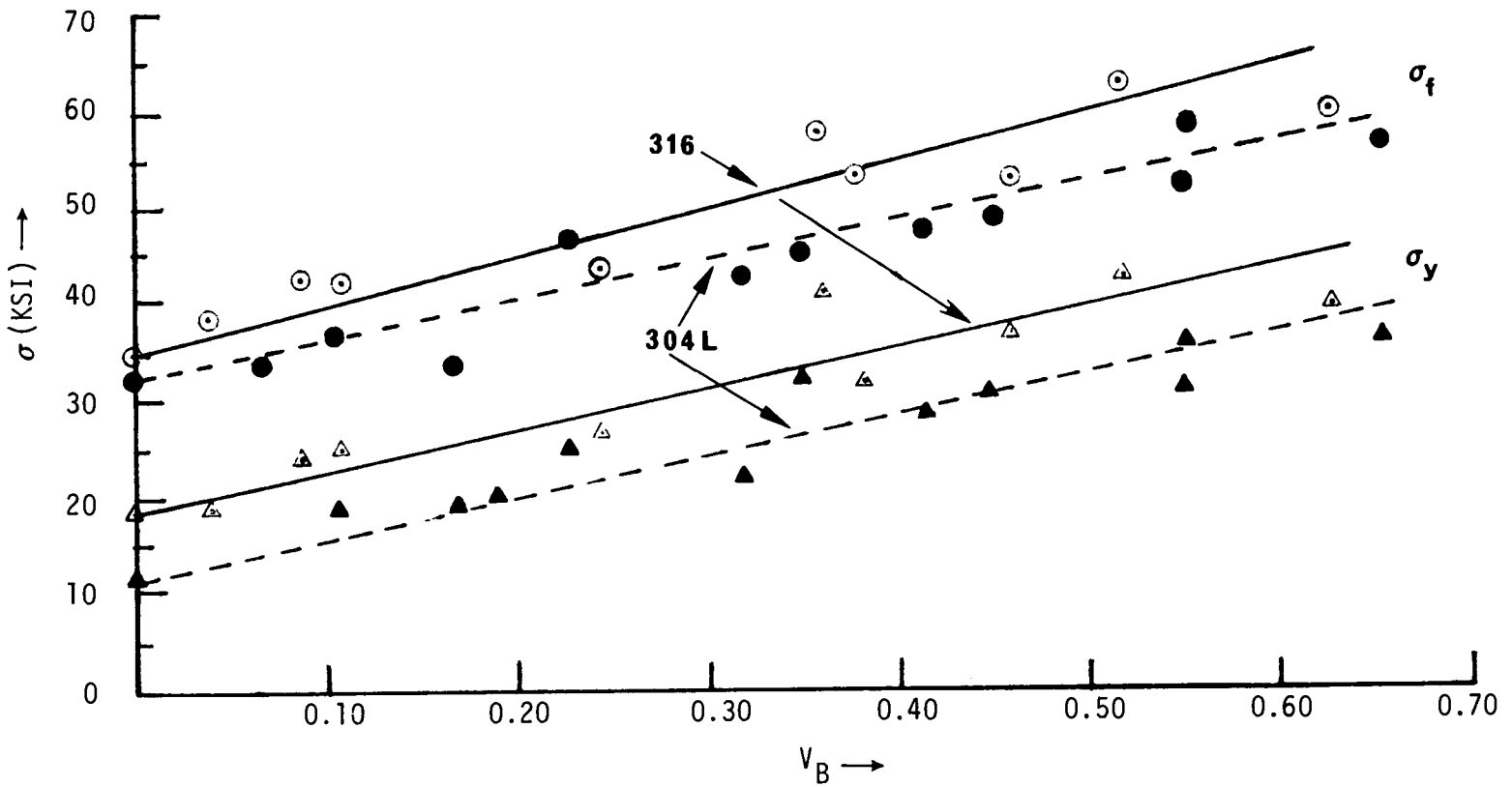

FIG. 3 Yield and fracture strength vs. volume fraction of carbon case

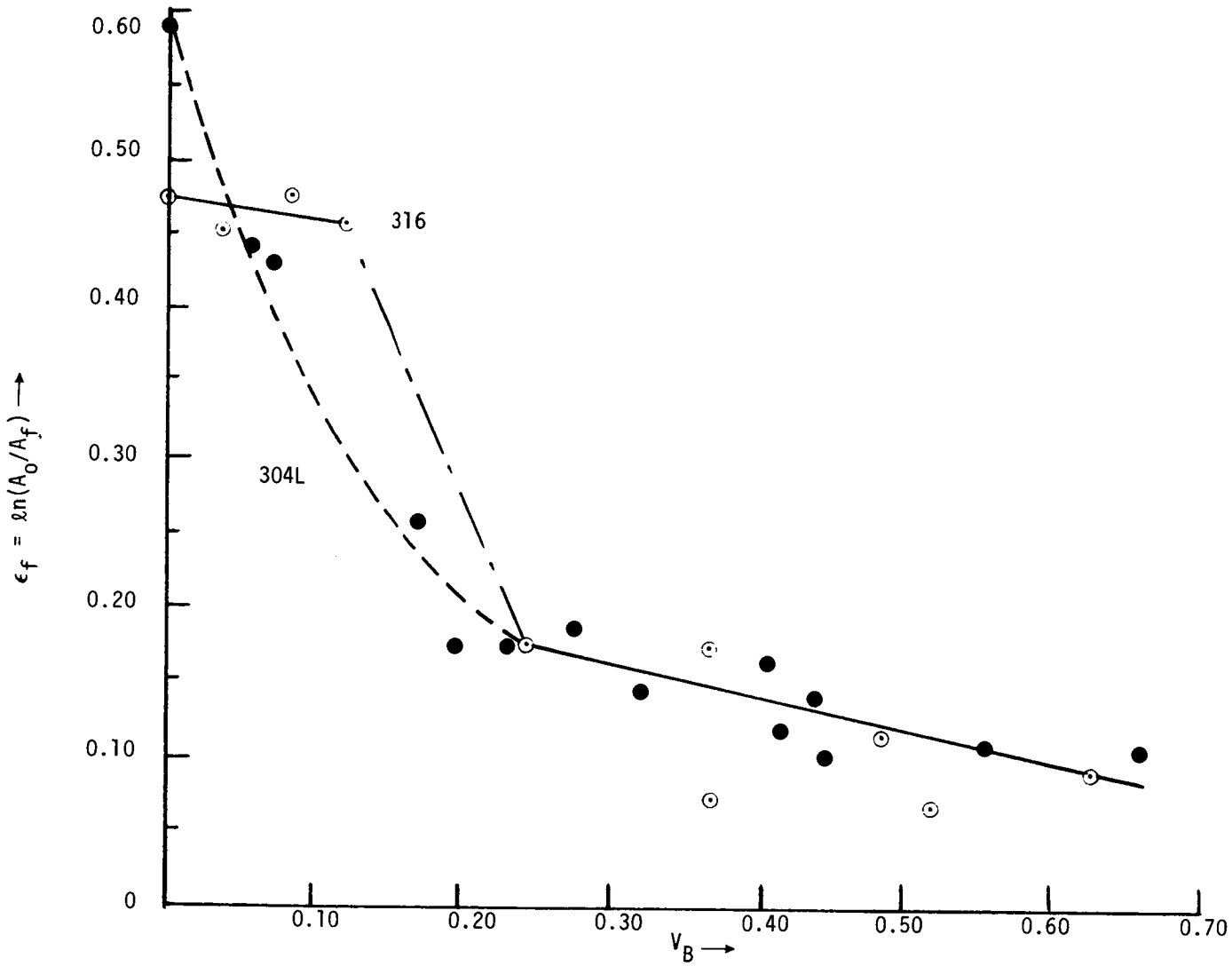

FIG. 4 Tensile ductility vs. volume fraction of carbon case

7.2.3.2 Fracture Model

The continuous fibered composite model[2] used to predict the UTS of carburized Type316SS as a function of volume fraction has been successfully extended to Type 304L. Fig. 5 shows the results of comparing the UTS of Type 316SS and 304L as a function of volume fraction to values predicted using the composite model. As can be seen, the UTS for case carburized 304L is lower and the critical volume fraction of case, $V_{B(crit)}$, smaller. The agreement between the predicted and the actual UTS is very good. Thus, a continuous fibered composite model can be used to estimate the UTS for case carburized Type 304L as well as Type 316SS.

7.2.3.3 Fracture Mode

Fig. 6 displays graphically tensile ductility and observed fracture mode as a function of volume fraction. For both steel specimens exhibiting a relatively large tensile ductility fail transgranularly, while specimens failing at intermediate and low strains display a mixed or entirely intergranular fracture mode. As discussed previously for Type 316SS,[3] the primary cause for this observed transition in fracture mode can be attributed to the increase in the local strain rate acting on the core at the tip of case cracks when failure of the carbon case is the controlling

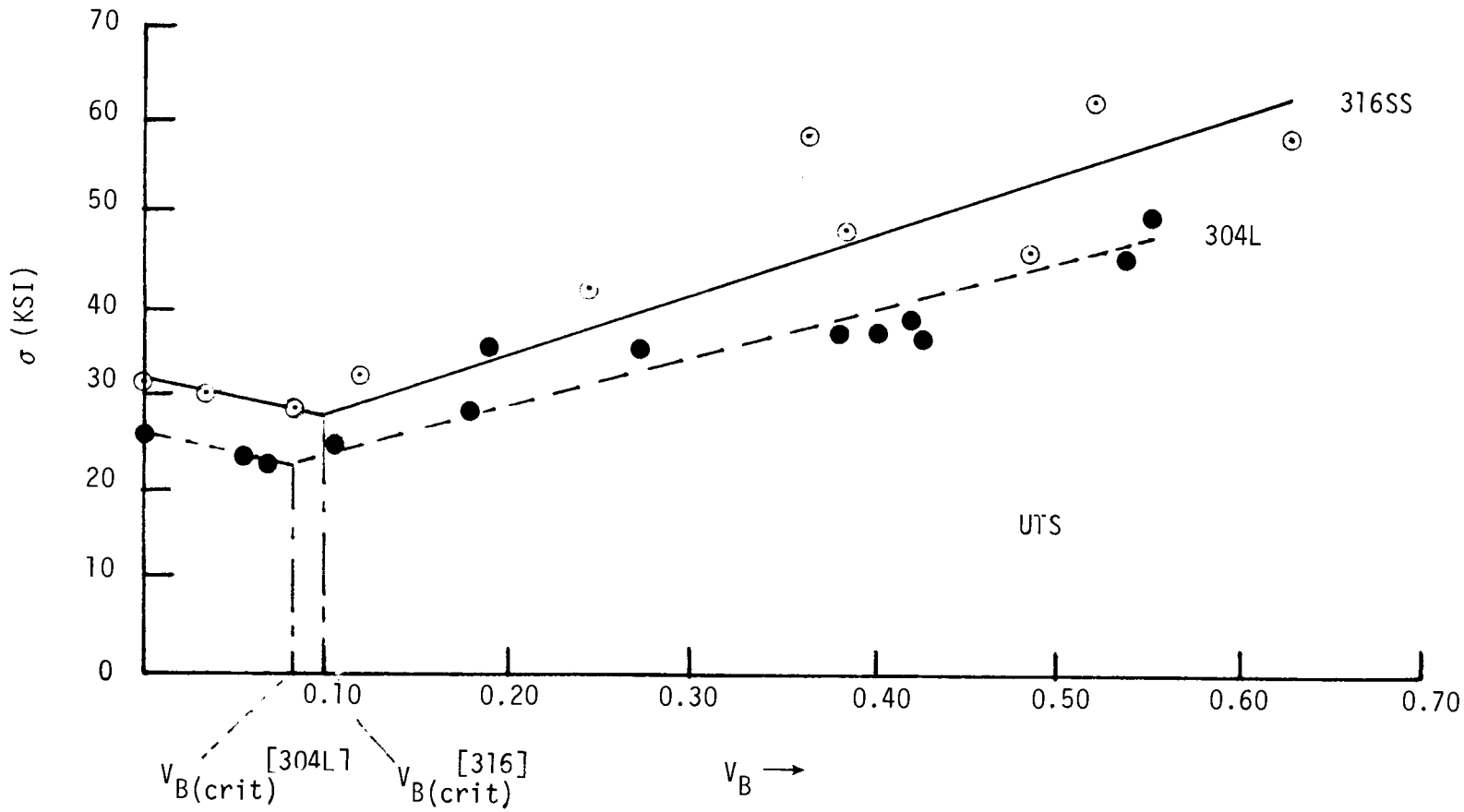

FIG. 5 Comparison of σ_c predicted and σ_{UTS} measured vs. volume fraction at carbon case

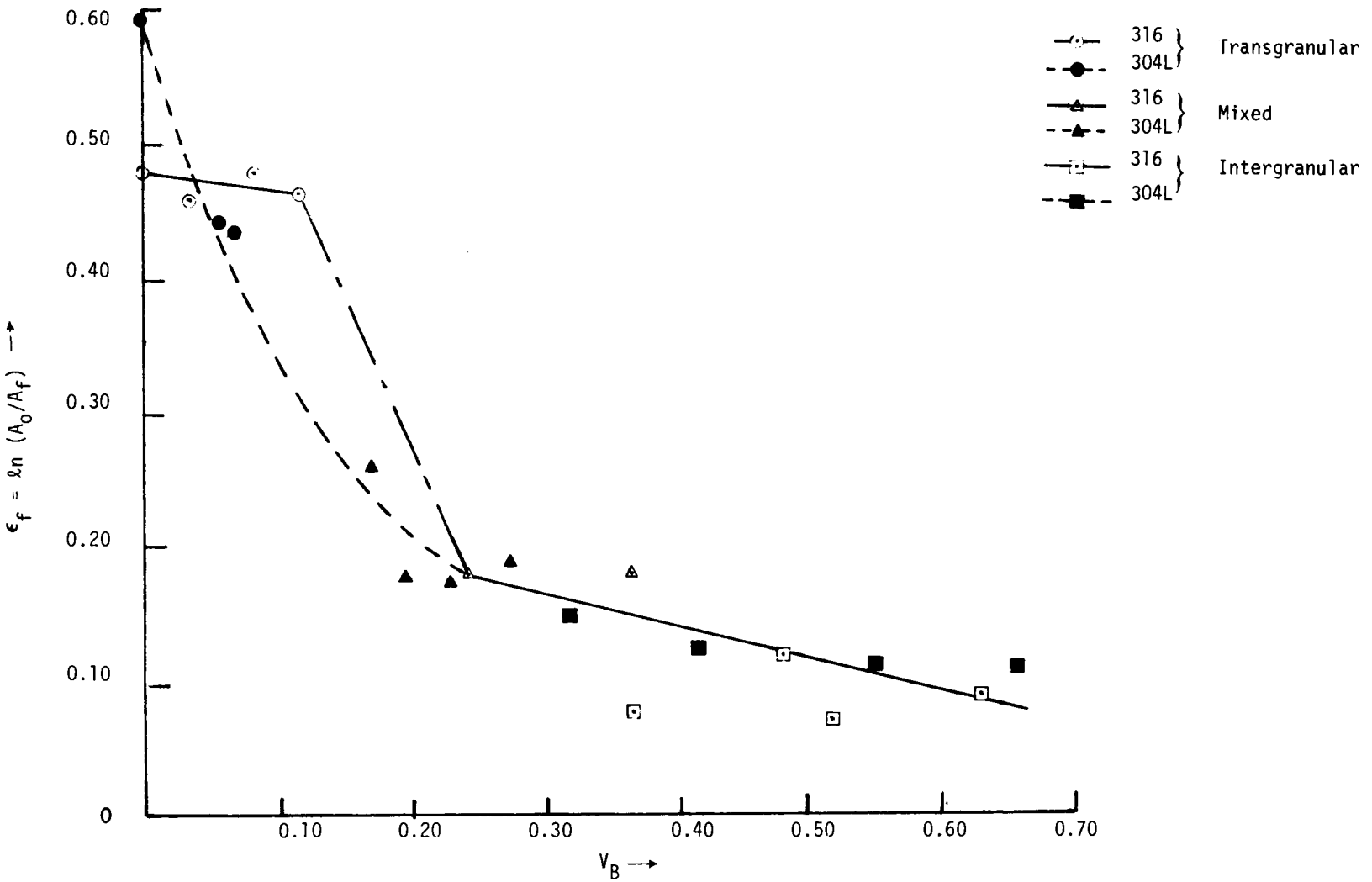

FIG. 6 Tensile ductility and fracture mode vs. volume fraction of carbon case

step in the fracture process, while sensitization and the imposition of a triaxial stress state at the tip of case cracks are contributing factors.

7.2.4 References

1. Ono, K., et al. UCLA-34P177-21, June 1974.
2. Chalco, P.A. and K. Ono, ORNL-4963, June 1974.
3. Ono, K., et al. ORNL-5103, December 1974.
4. Ono, K., et al., "Mechanical Properties Test Data for Structural Mat. Quart. Prog. Report for Period Ending 30 April 1975," ORNL Report May 1975.

8. GENERAL ELECTRIC COMPANY

D. Weinstein

8.1 INTRODUCTION

The principal objective of mechanical properties testing at the General Electric Company is to characterize the behavior of 2¼Cr-1Mo and austenitic stainless steels in sodium environments relevent to LMFBR steam generators and intermediate heat transport systems. Under conditions predicted for the intermediate sodium system of the CRBRP, 2¼Cr-1Mo will lose carbon to the system and be weakened. The carbon will tend to carburize and embrittle stainless steel components in other portions of the system. The effects of a carburizing environment on creep rupture properties of Type 316 stainless steel will be evaluated along with an assessment of creep-fatigue interactions. In addition, studies of fatigue crack propagation rates in carburizing sodium will be performed in order to assess environmental effects under pertinent intermediate sodium loop loading conditions. The loss of carbon from 2¼Cr-1Mo steel components can result in increased creep rates of the decarburized surface layer with the possibility of ratchetting under cyclic straining. These effects will be evaluated for base metal and weld metal in a decarburizing sodium environment.

8.2 MECHANICAL PROPERTIES OF STAINLESS STEEL IN CARBURIZING SODIUM- J. F. Copeland

8.2.1 Background

The objective of this program is to experimentally verify and supplement ASME Code design values for austenitic stainless steels to be used in LMFBR Intermediate Heat Transport Systems (IHTS). The effects of sodium carburization on creep-rupture lives and deformation rates, and the influence of creep-fatigue interaction and tension hold time at peak stresses, will be evaluated. Additionally, the effect of environment and other design-related parameters on the fatigue crack propagation rate will be determined in high carbon sodium using a fracture mechanics approach.

The program includes a study of continuous carburization in sodium at a crack tip during cyclic stressing. These data will be used for assessing the integrity of LMFBR IHTS components in possible carburizing liquid sodium environments.

Type 316 stainless steel is tested at 950°F in carbon-saturated sodium after approximately 1000 hr. specimen pre-exposures. The degree of carburization expected[1] is a case depth of about 5 mils with a surface carbon content of approximately 1-1.5 wt. %. This carburization corresponds to that expected[2] for the 30 year CRBR IHTS design life with a 2¼Cr-1Mo steel carbon source. GE analysis of bimetallic sodium test loops (Steam Generator Test Rig,[3] PA15 Loop 3,[4,5] B&W Model Steam Generator,[6] and EBR II secondary sodium system vent-line[2] has verified that such surface carburization of stainless steel components does occur.

Testing is of two types: (a) tubular creep and creep-fatigue tests that give rupture times, deformation rates, and rupture ductilities, and (b) ASTM E399 fracture mechanics bend tests to give fatigue crack propagation rates. Under (a), specimens are filled with sodium and a carbon source and sealed prior to testing. For part (b), testing will be performed in flowing sodium (Loop A). Control tests will be performed in air. Cyclic frequency will be low and will include the determination of hold-time effects.

8.2.2 Current Progress

The fatigue crack growth test facility is illustrated in Figure 8.1. Two such facilities have been fabricated: one for incorporation into Loop A for sodium tests, and the other for control tests in air. Crack growth rate specimens are 12.7mm (0.5 in.) thick, and three specimens per loading facility can be tested simultaneously in a 3-point bending, load control mode. The constants C and n will be evaluated in the crack growth equation

$$\frac{da}{dN} = C\ (\Delta K_{eff})^n$$

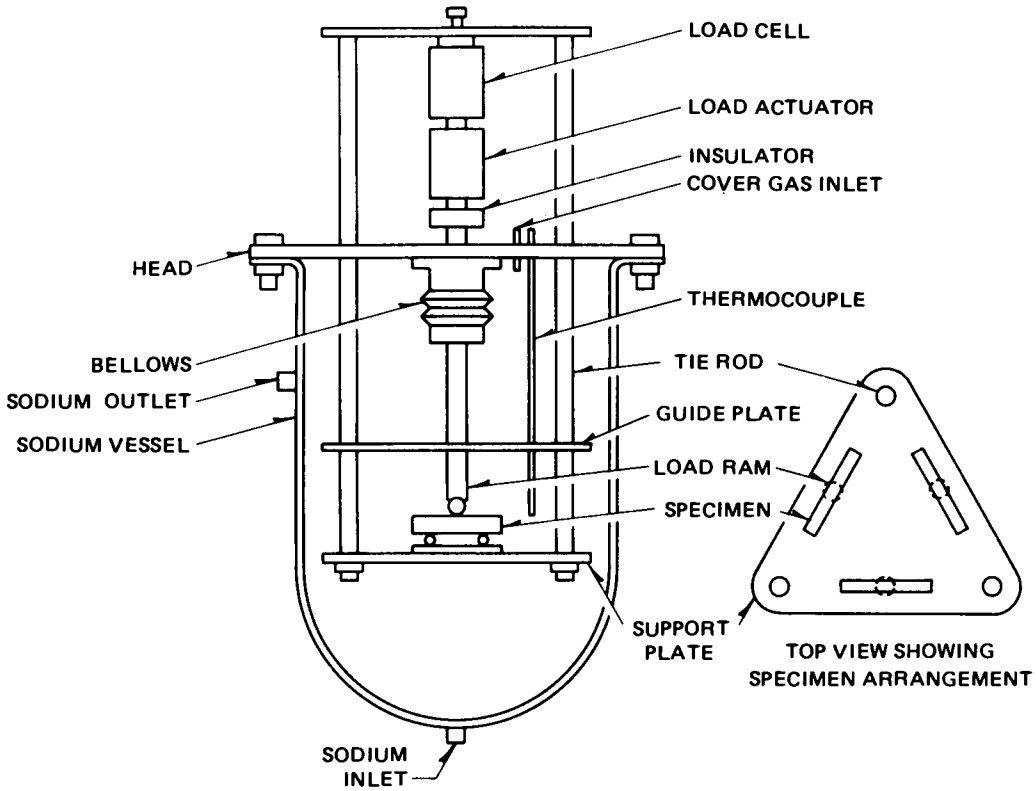

Figure 8.1 Schematic Illustration of Fatigue Test Sodium Pot

where da/dN is the instantaneous crack extension per fatigue cycle and ΔK_{eff} is the effective range of stress intensity factor for each load cycle. The crack growth rate, da/dN will be determined by fatiguing a specimen for approximately 1000 cycles. The specimen is then withdrawn and crack extension, Δa, is measured. For a small Δa, $\Delta a/\Delta N$ approximates da/dN.[7] For each value of da/dN, ΔK_{eff} will be computed based on the initial crack length plus half of the crack extension.[7] The test parameters to be studied are listed in Table 8.1.

Chemical analysis and tensile testing have been completed, and the results are shown in Tables 8.2 and 8.3. Subsequently, 50 bend specimens were machined, and 25 of them were fatigue precracked. Thirteen of the precracked specimens were aged in carbon saturated sodium at 510°C (950°F) for 1000 hours in Loop A. The carbon source, 20 gage sheet AISI-SAE Grade 1050 carbon steel, is shown in its holder in Figure 8.2. Type 304 0.0127mm (5 mil) foil pieces (Figure 8.3) were inserted and studied before loading specimens and were loaded with the specimens to monitor the carburizing potential of the loop. The carburization of these foils indicated proper loop conditions for the required carburization. These specimens have been exposed and are now ready for testing. The remaining 12 precracked specimens were aged for 1000 hours at 510°C (950°F) in air for the control tests.

Test facility fabrication has been completed. Preliminary trials and incorporation of one facility into Loop A remains to be done.

Uniaxial creep-fatigue testing has been in progress since February 1975. The specimen is shown in Figure 8.4. Twenty-four of these Type 316 specimens have been fabricated and aged for 1000 hours at 510°C (950°F). Before aging, 15 specimens were filled with high purity sodium, and a 1095 steel carbon source (wire) was inserted; the remaining specimens were filled with argon (atmospheric pressure at test temperature) for control testing. Material characterization results for the Type 316 stainless steel are shown in Table 8.2 and 8.3. Creep machines were modified to permit automatic load cycling for creep-fatigue and automatic creep data accumulation. The apparatus are shown in Figure 8.5. Again, the major emphasis in this study will be to determine environmental

Table 8.1 Fatigue Crack Growth Test Parameters

Environment	-	C saturated Na and air (in situ)
Temperature	-	510°C (950°F)
Material	-	Annealed Type 316 stainless steel
Frequency	-	0.5 and 0.05 cycles/min.
Hold Time	-	zero and one min.
Load Ratio (R)	-	0.05
Range of ΔK_{eff}	-	About 11 to 44 $MPam^{\frac{1}{2}}$ (10 to 40 ksi. $in.^{\frac{1}{2}}$)
Load Wave Form	-	Sawtooth

Table 8.2 Type 316 Stainless Steel Annealed Test Material Characterization-Chemical Composition (wt. %)

	C	Mn	P	S	Si	Cu	Ni	Cr	Mo	N
					1/4 Schedule 80 pipe [(a) Tests]					
Ladle	0.056	1.63	0.029	0.015	0.56	0.08	13.32	17.24	2.40	-
Check	0.055	1.63	0.018	0.010	0.70	0.05	13.40	17.47	2.67	0.038
					5/8 in. Plate [(b) Tests]					
Ladle	0.042	1.66	0.015	0.008	0.60	-	13.40	17.50	2.69	-
Check	0.053	1.59	0.009	0.013	0.54	0.06	13.37	17.22	2.37	0.050

Table 8.3 Type 316 Stainless Steel Annealed Test Material Characterization-Tensile Tests

	0.2% Y.S. (ksi.)	U.T.S. (ksi.)	% El. (2")	% R.A.
1/4 in. Schedule 80 Pipe [(a) Tests]*				
Room Temperature	39.4	90.4	50.0	55.3
	43.5	88.7	44.0	48.5
950°F	25.1	69.4	28.5	36.3
	24.0	71.2	32.5	36.6
5/8 in. Plate [(b) Tests]**				
Room Temperature	38.0	88.7	45.9	77.0
	39.3	89.4	53.6	77.4
950°F	21.1	70.6	36.5	66.4
	21.8	74.1	41.3	61.3

* 0.34 inch O.D. x 0.020 inch wall x 2 inch reduced section
** 0.25 inch Dia. x 2 inch reduced section

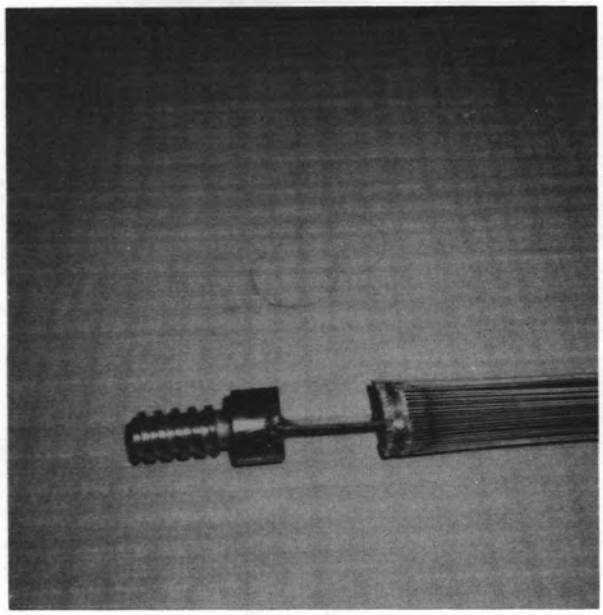

Figure 8.2 Carbon Source (Right Side of Picture) in Holder for Loop A

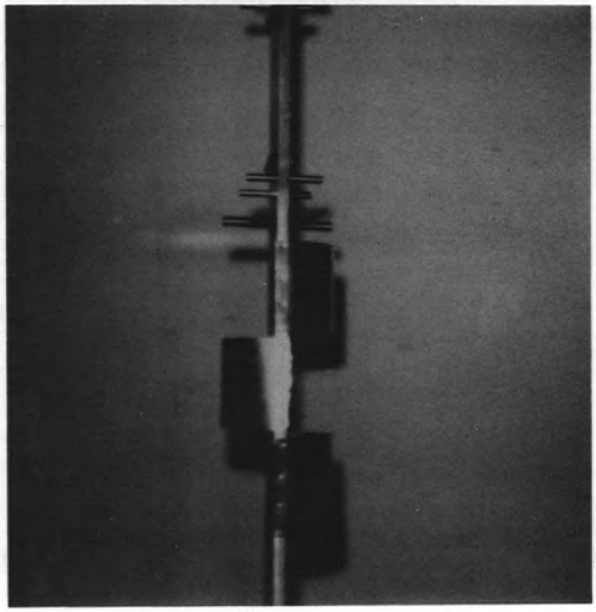

Figure 8.3 Type 304 Foils Mounted on Specimen Holder to Monitor Loop Carburizing Conditions

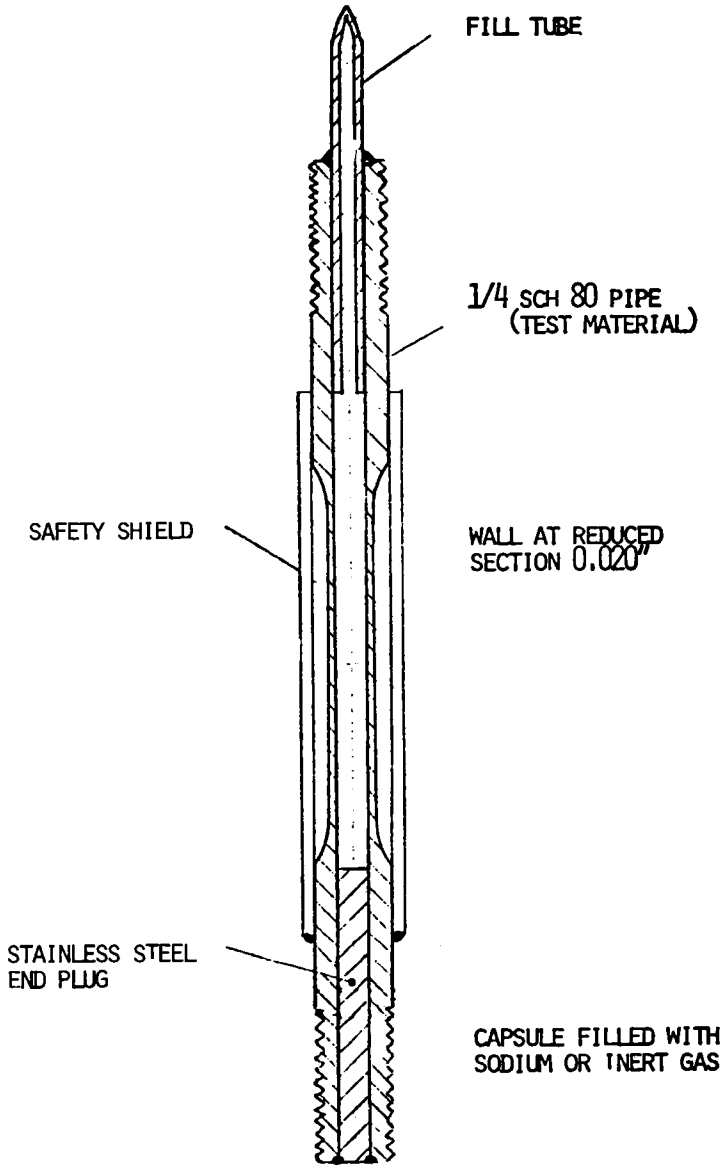

Figure 8.4 Uniaxial Creep/Fatigue Specimen

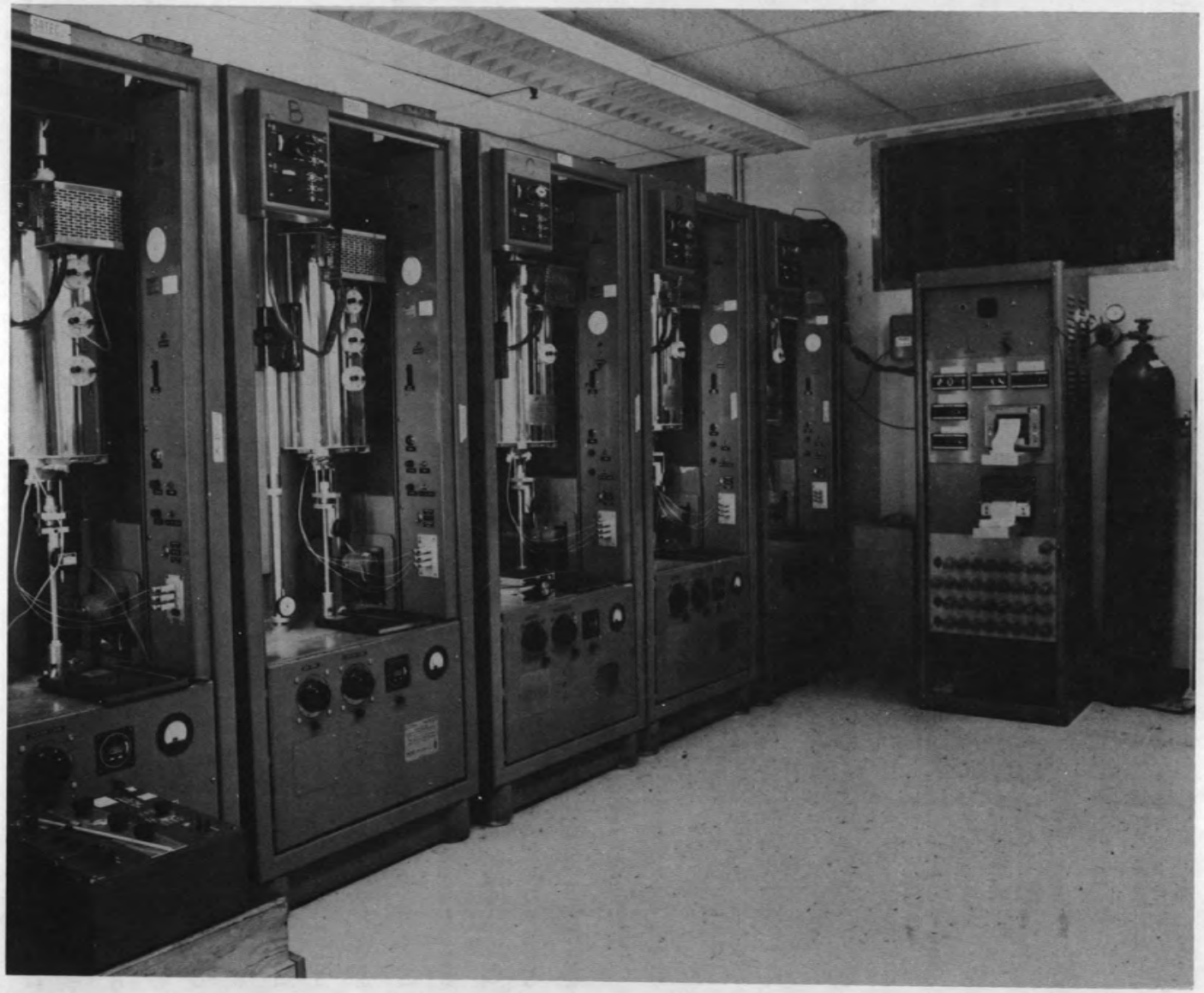

Figure 8.5 Creep Machines Showing Digital Dial Gages and Load Cycle Control and Data Accumulation Panel

effects (carbon saturated sodium). The test parameters being studied are listed in Table IV. Essentially, there are four groups of tests: argon creep-fatigue, Na/C creep-fatigue, Na/C creep-fatigue with hold time, and Na/C creep. The argon creep-fatigue tests are being performed under subcontract to Battelle, Columbus.

Initial stress rupture results are presented in Figure 8.6. The creep rupture data with Na/C fall above the ASME Code Case 1592 minimum stress rupture values. Rupture values for the Na/C creep-fatigue tests with a 30-minute hold time are below those for creep rupture. Control data are not yet available to determine the exact influence of the Na/C environment on stress rupture lives. Testing is continuing, along with an analysis of creep rates and specimen metallography and carburization.

8.3 DECARBURIZATION KINETICS AND DESIGN METHODS VERIFICATION TESTING - L. V. Hampton

8.3.1 Background

The selection of 2¼Cr-1Mo steel as the reference alloy for sodium-heated steam generators was based primarily upon its immunity to stress corrosion cracking in chloride or caustic contaminated environments and its proven fabricability.[8] One of the major concerns with the use of this material for sodium applications is its susceptibility to decarburization during service. Early analyses assumed that relatively thin sections, such as steam generator tubing, would completely decarburize during the LMFBR lifetime, with concomitant severe design stress penalties necessarily imposed.[9] In addition to the assumed carbon losses, the potential for severe carburization of stainless steel components in the loop was also recognized as a potential difficulty.

In the absence of an acceptable theoretical model for decarburization of 2¼Cr-1Mo steel, an approach introduced by Armijo and Krankota[10] was used to analyze the results obtained from many different experiments.[4,11-28] This technique treats carbon loss data as if it were corrosion data; that is, the loss of carbon per unit area is described as a function of time. A parabolic time dependence has been observed which suggests that the decarburization process is diffusion controlled. The decarburization

Table 8.4 Uniaxial Creep-Fatigue Test Parameters

Environment	-	C saturated Na and argon (air on outside) - in situ
Temperature	-	510°C (950°F)
Material	-	Annealed Type 316 stainless steel
Loading Modes	-	Constant load for creep Periodic load increase of 69MPa (10ksi.) for creep-fatigue
Load Increase Frequency	-	1 cycle per hr.
Hold Time at Peak Load	-	Zero and 30 min.

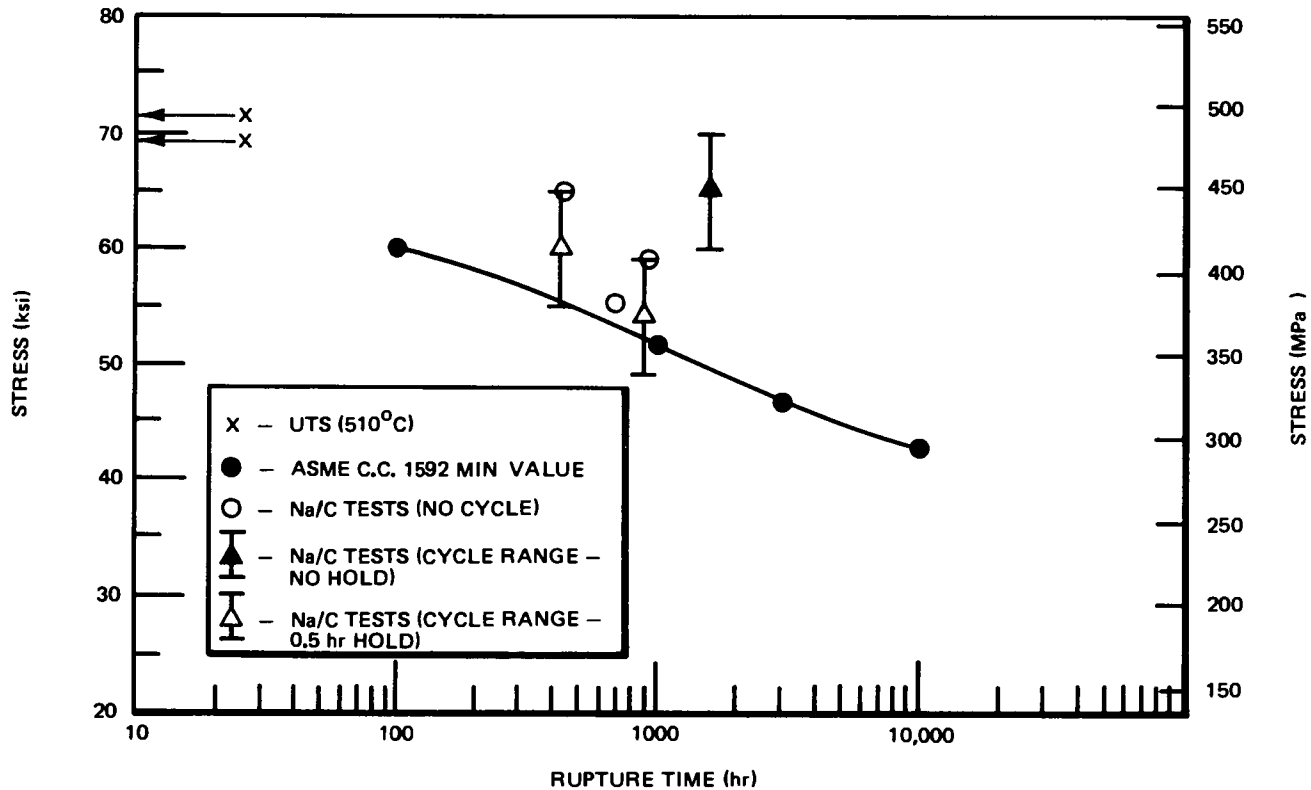

Figure 8.6 Preliminary Stress Rupture and Creep-Fatigue Results for Annealed Type 316 Stainless Steel Tubes at 510°C (950°F) Exposed to High Carbon Sodium Before, and During, the Test

rate constants, K, from all available data were fit to an Arrhenius type expression* for design use. Figure 8.7 shows the results of this analysis. The "data class" and the weighting applied to each class are defined in the NSM Handbook entry for decarburization of 2¼Cr-1Mo steel.[29] Based upon the upper limit curve given in Figure 8.7, estimates of carbon loss and associated design stress penalties can be made for steam generator components. These predictions of decarburization kinetics indicate that steam generator tubes would not be expected to lose more than 300 ppm carbon in the design life of the CRBRP. Only a small design stress penalty (<10%) is associated with this loss. The handbook approach suggests that decarburization kinetics are too slow to yield a carbon loss at end-of-life of greater than 300 ppm for CRBRP steam generator tubing.** WARD experiments, utilizing thin foils, imply that the "equilibrium" carbon content of 2¼Cr-1Mo in 950°F sodium will be approximately 700-900 ppm.[13] The design stress penalty associated with these predictions of carbon loss can be accomodated.

Design analysis for high temperature components requires a consideration of creep/fatigue interaction to accomodate the effects of transient loading. A recent study has provided creep/fatigue interaction information for 2¼Cr-1Mo[30] under conditions of uniform microstructure (i.e. no decarburized surface layer) with no ratcheting strains permitted. Steam generator tubes will experience cyclic loading with the potential to accumulate ratcheting strains, and with a weaker surface layer, as compared to the bulk metal. Interrupted creep tests on 2¼Cr-1Mo pipe, tubing, and weld metal are being undertaken to assess the effects of such loading on partially decarburized material. Uniaxial tests will be

---

*K is defined by:

$$K = \frac{gm^c}{cm^2 - sec^{\frac{1}{2}}}$$

$$M \quad \left(\frac{gm^c}{2}\right) = Kt^{\frac{1}{2}}$$

**Tubing specification sets initial carbon levels of 700-1200 ppm.

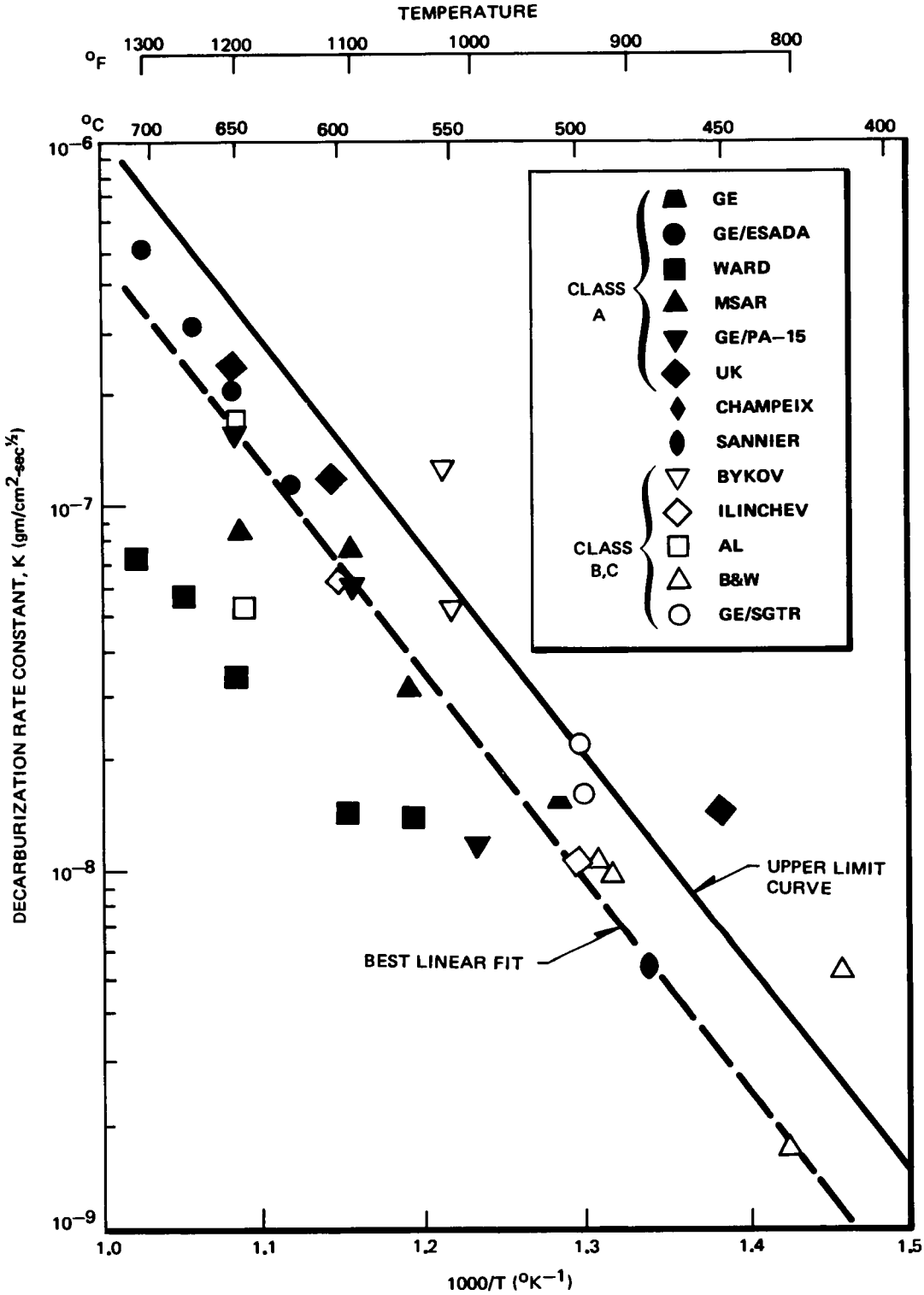

Figure 8.7 Decarburization Rate Constants for All Investigations

performed on sodium-filled and inert gas-filled pipe samples in order to characterize the effect of stress cycling on creep strains. Tubing and all-weld-metal tubes will be internally pressurized in sodium and argon environments to assess the effects of creep/fatigue on rupture life in a decarburizing environment. Description of the samples, test facilities, and test matrix was included in earlier reports.[31,32]

8.3.2 Current Progress

Decarburization studies on 2¼Cr-1Mo base metal samples have been completed. These samples have accumulated 10,000 hours exposure to 950°F sodium in Decarb Pot #1. The samples are currently being analyzed, and the results will be applied to Figure 8.7. At the same time, the weld metal samples in Decarb Pot #1 have amassed a total exposure time of 4500 hours. They require another 2500 hours in order to complete the 7000 hour total exposure time.

Biaxial creep-fatigue interaction testing in 950°F sodium is continuing in Decarb Pot #2. Initial runs in this pot indicated that the planned stress levels (40 and 45 ksi) were too high for the specimens being tested. Random ruptures occurred in both weld and base metal samples within a 15 hour period. This situation led to a lowering of the stress levels to 32.5 and 36.3 ksi for the previous 40 and 45 ksi design specimens, respectively. Thus far there has been one failure in the base metal specimen at 32.5 ksi. The ruptue time for this test was 98.2 hours. Another failure occurred at 108 hours, but it is impossible at this time to tell which sample failed.

Initial uniaxial testing has indicated the need for some specimen modifications. Of the four tests already completed in this investigation, only one has led to a failure within the specimen gage section. Other failures have occurred at the fillet of the specimen gage to the specimen shoulder (Figure 8.4) and in the thread of the specimen shoulder. These results are believed to result from undercutting in these regions during fabrication. The balance of the uniaxial specimens will be tested in hopes of gaining good creep data; those tests leading to abnormal ruptures will be repeated using more carefully machined specimens.

8.4 REFERENCES

1. "LMFBR Heat Exchanger Materials Development Program". Second Quarterly Report, September-November 1972, AEC Contract AT(04-3)-189, PA-60, December 1972 (GEAP-13919-2).
2. R. B. Snyder, K. Natesan, and T. F. Kassner, "A Generalized Method of Computing Carbon-Diffusion Profiles in Austenitic Stainless Steels Exposed to a Sodium Environment", ANL-8015, AEC Contract W-31-109-Eng-38, June 1973.
3. J. L. Krankota, "Carburization of Stainless Steel Rupture Discs in SGTR," GE letter report, August 1, 1974.
4. M. C. Rowland and D. E. Plumlee, "Sodium Mass Transfer: XXII - Metallurgical Examination of the Test Loops," GEAP-4838, October 1965.
5. Summary Report - Sodium Mass Transfer Program: "Effects of Sodium Exposure on the Corrosion and Strength of Stainless Steel", GEAP-10394, August 1971.
6. D. W. Koch and P. J. Kovach, "Materials Examination of a Model Sodium Heated Steam Generator", BAW-1280-37, June 1966.
7. L. A. James, "Fatigue-Crack Propagation Behavior of Incoloy 800 at Elevated Temperatures", ASME Paper No. 74-Mat-7, Presented at ASME Pressure Vessel and Piping Conference in Miami Beach, Fla., June 24-28, 1974.
8. G. J. Licina and J. F. Copeland, "A Review of 2¼Cr-1Mo Steel for Steam Generator Applications in the Clinch River Breeder Reactor," GEAP-20589, August 1974.
9. "Task VI Final Report, Vol. 4, Steam Generator Development," NEDC-13655, October 1970.
10. J. L. Krankota and J. S. Armijo, "Decarburization Kinetics of Low Alloy Ferritic Steels in Sodium," Met Trans., 3, pp. 2515-2523, September 1972.
11. J. M. Scott, et. al., "Sodium Heated Steam Generator Model Tests at SGTR: Volume 1," GEAP-10580-1, June 1972.
12. J. L. Krankota and J. S. Armijo, "The Kinetics of Decarburization of 2¼%Cr-1%Mo Steel in Sodium," Nuc Tech., 24, November 1974.
13. "Sodium Technology Program - Component Materials Compatibility," WARD-NA-3045-11, August 1974.

14. D. E. Plumlee, R. W. Lockhart, and L. E. Pohl, "Sodium Mass Transfer: XVIII - Studies of Carbon Movement in Pumped Sodium Test Loops," GEAP-4834, June 1965.

15. M. C. Rowland, et al., "Sodium Mass Transfer: XIX - Long-Term Exposure Effects in a Bimetallic Type 316 Stainless Steel - 2¼Cr Test Loop," GEAP 4835, April 1965.

16. L. H. Kirschler, R. H. Hiltz, and S. J. Rodgers, MSAR 64-81, July 1964.

17. L. H. Kirschler, R. H. Hiltz, and S. J. Rodgers, MSAR 69-42, April 1969.

18. L. H. Kirschler, R. H. Hiltz, and S. J. Rodgers, MSAR 69-207, October 1969.

19. L. Champeix and O. Konovaltschikoff, Proceedings of the International Conference on Sodium Technology, pp. 93-103, ANL-USAEC Report ANL-7520-Part 1, November 1968.

20. J. Sannier, et al., Report on BNES Conference on Corrosion and Effects of Environment on Materials Properties in Nuclear Systems, pp. 137-147, London, July 1971.

21. G. Ilinchev, CEMA Symposium of Atomic Power Stations with Fast Reactors - Volume I (Obninsk), pp. 462-477, Joint Publications Research Service, Washington, D. C., July 1969.

22. W. J. Anderson, G. J. Sheffield, and J. Birkle, NAA-SR-7544, November 1963.

23. L. H. Kirschler, R. H. Hiltz, and S. J. Rodgers, MSAR 72-286, December 1972.

24. V. N. Bykov, et al., "The Problems of Corrosion Resistance of Structural Materials In Sodium," CEMA Symposium of Atomic Power Stations with Fast Reactors (Obninsk) Volume I, pp. 426-461, July 1969.

25. A. Thorley, B. Longson, and J. Prescott, "Effect of Exposure to Sodium on the Mechanical Properties and Structure of Some Ferritic, Austenitic and High Nickel Alloys," TRG Report 1909 C (1969).

26. D. W. Koch, P. J. Kovach, BAW-1280-37, June 1966.

27. S. Ohta, "2¼Cr-1Mo-Nb Steel: A New Steel for Steam Generator Tubes of Sodium Cooled Fast Breeder Reactors," Central Research Lab Kobe Steel. Ltd. (in Reactor Steels Studies in Japan UCLA-34, pp. 177-179).

28. J. Motz, Zeit. Fur Metallkunde, Vol. 55, pp. 489-494, (1964).

29. Nuclear Systems Materials Handbook, Decarburization of 2¼Cr-1Mo Steel, January 1975.

30. R. M. Curran and B. M. Wundt, "A Study of Low-Cycle Fatigue and creep Interactions in Steels at Elevated Temperatures," to be published.

31. Steam Generator Materials Engineering - First Quarterly Report, GEAP 14029-1, October 1974.

32. Steam Generator Materials Engineering - Second Quarterly Report, GEAP 14029-2, January 1975.

INDEX

Test	Material	Page
Chemical Analysis Data		
	type 308 SS welds.	207–216
Creep Test Data		
Base-Line		
	type 304 SS bar	226–233
	type 304 SS plate	41–50; 226–239
	type 304 SS tube	241–255
	type 304 SS welded bar	241
	type 304 SS welded plate	239–241
	type 316 SS plate.	64
	type 316 SS tube	245–246; 307–321
	2 1/4 Cr-1 Mo.	287–290; 307–321
Correlations		
	type 304 SS	41–50; 65–72; 87–95; 174–175
	type 316 SS	65–72; 87–95
	alloy 718	87–95
	2 1/4 Cr-1 Mo.	87–95; 155–165
Creep Plasticity		
	2 1/4 Cr-1 Mo	180–185
Cyclic Tests		
	type 304 SS	178–179
Effect of Aging		
	type 304 SS.	82–86
Effect of Carbon Case		
	type 304L and 316 SS	298–305
Effect of Cold Work		
	Type 316 SS.	291–298

Test	Material	Page
Creep Test Data (Continued)		
Effect of Cycling		
	type 316 SS tube	307–321
	2 1/4 Cr-1 Mo	180–185
	2 1/4 Cr-1 Mo tube	307–321
	2 1/4 Cr-1 Mo weld metal	307–321
Effect of Environment		
	2 1/4 Cr-1 Mo	187–188
	9 Cr-1 Mo	187–188
	Hastelloy X	187–188
Effect of Heat Treatment		
	alloy 718	14–16
	type 316 SS	291–298
Effect of Hold Time		
	type 316 SS	307–321
Effect of Sodium Exposure		
	type 316 SS tube (carburizing)	307–321
	2 1/4 Cr-1 Mo weld metal	307–321
Precipitate-Dislocation Interactions		
	type 304 SS	262–266
Elastic Constants		
Dynamic Measurements		
	2 1/4 Cr-1 Mo	104–109
Static Measurements		
	2 1/4 Cr-1 Mo	105–111
	type 308 SS weld metal	112–114
Fatigue Test Data		
Crack Growth Rate Data		
	2 1/4 Cr-1 Mo	147–157
	type 316 SS plate	307–321
	type 316 SS welds	216–221
Effect of Aging and Hold Time		
	type 316 SS welds	216–221

Test	Material	Page
Fatigue Test Data (Continued)		
Effect of Heat Treatment		
	alloy 718 weld metal	2–14
Effect of High-Temperature Sodium Environment		
	types 304 and 316 SS	20–24
Effect of Sodium Testing Environment		
	type 304 SS	8–10
Effect of Thermal Aging		
	types 308 SS weld metal	2–4
Interrupted Tests		
	type 304 SS	272–285
Statistical Analysis of Data Scatter		
	type 304 SS	3–7
Substructure Development		
	type 304 SS	272–285
Fracture Toughness		
	type 316 SS forging	197–207
Hardness Data		
Effect of Heat Treatment		
	type 316 SS	52
Impact Test Data		
Effect of Delta Ferrite		
	type 304 SS welds (C_v, DT)	207–216
Effect of Heat Treatment		
	alloy 718 weld metal	2–12
Effect of Test Temperature		
	type 308 SS weld	207–216
Microstructure		
	type 304–308 SS weld metal, creep tested	157–171
	type 304 SS, creep tested	259–272
	type 304 SS, tensile tested	259–272
	type 304 SS, fatigue tested.	272–285
	type 316 SS	54–60

Test	Material	Page
Relaxation		
	2 1/4 Cr-1 Mo	179–183
Tensile Test Data		
Base-Line Data		
	type 316 SS	53, 62–63
	type 308 SS welds.	207–216
	Hastelloy S	185–186
Correlations		
	type 304 SS.	64–65
	type 316 SS.	64–65
	type 308 SS welds	207–216
Effect of Aging		
	types 304 and 316 SS	72–78
Effect of Corrosion		
	types 304 and 316 SS, aged	74–83
Effect of Delta Ferrite		
	type 308 SS welds	207–216
Effect of Heat Treatment		
	alloy 718 weld metal	2–10
	alloy 718.	15
	2 1/4 Cr-1 Mo	131–142
Effect of Product Form		
	type 304 SS	171–172
Effect of Sodium Exposure		
	types 304 and 316 SS	7–19
Effect of Strain Rate		
	2 1/4 Cr-1 Mo.	121–131
Effect of Test Temperature		
	type 308 SS welds	207–216

ORNL-5106
UC-79b, -h, -k
(Liquid Metal Fast
Breeder Reactors)

INTERNAL DISTRIBUTION

(3) Central Research Library
ORNL — Y-12 Technical Library
Document Reference Section
(8) Laboratory Records Department
Laboratory Records, ORNL RC
ORNL Patent Office
R. J. Beaver
R. G. Berggren
J. J. Blass
M. K. Booker
C. R. Brinkman
D. A. Canonico
J. Corum
W. R. Corwin
F. L. Culler
J. E. Cunningham
J. H. DeVan
D. P. Edmonds
G. Fee
M. H. Fontana
W. R. Gall
B. L. Greenstreet
J. C. Griess, Jr.
J. P. Hammond
W. O. Harms
R. L. Heestand
(5) M. R. Hill
D. O. Hobson
F. J. Homan
H. Inouye
P. R. Kasten
J. F. King
R. T. King
R. L. Klueh
K. C. Liu
(20) C. T. Liu
A. L. Lotts
W. R. Martin
W. J. McAfee
H. E. McCoy
H. C. McCurdy
C. J. McHargue
J. Merkle
P. Patriarca
S. Peterson
H. Postma
C. E. Pugh
P. L. Rittenhouse
D. N. Robinson
T. Roche
J. L. Scott
Myrtleen Sheldon
V. K. Sikka
G. M. Slaughter
W. J. Stelzman
J. P. Strizak
R. W. Swindeman
D. B. Trauger
T. N. Washburn
J. R. Weir, Jr.
G. D. Whitman
T. Yahr
W. C. Leslie (consultant)
John Moteff (consultant)
Hayne Palmour III (consultant)
J. W. Prados (consultant)
N. E. Promisel (consultant)
G. V. Smith (consultant)
D. F. Stein (consultant)

EXTERNAL DISTRIBUTION

USERDA DIVISION OF REACTOR RESEARCH AND DEVELOPMENT, Washington, DC 20545

(2) Director

USERDA OAK RIDGE OPERATIONS OFFICE, P.O. Box E, Oak Ridge, TN 37830

Research and Technical Support Division
Director, Reactor Division

USERDA TECHNICAL INFORMATION CENTER, Office of Information Services, P.O. Box 62, Oak Ridge, TN 37830

(309) For distribution as shown in TID-4500 Distribution Category, UC-79b (Fuels and Materials Engineering Development); UC-79h (Structural Materials and Design Engineering); UC-79k (Components)

U.S. GOVERNMENT PRINTING OFFICE: 1975-748-189/73